Development of TACTIC: a novel detector for nuclear astrophysics

Soham Chakraborty

PhD

University of York

School of Physics, Engineering and Technology

December 2023

Abstract

Active-target detectors play a significant role in low-energy nuclear physics. The ability to utilise low intensity radioactive beams and a flexible choice of target gas enable these detectors to make direct measurements of a variety of nuclear reactions. This thesis focuses on the development and commissioning of TACTIC, a cylindrical active-target TPC. The design of TACTIC is suitable for the cross section measurement of alpha-induced charged particle reactions at low centre of mass energies. The measurements rely on the identification of charged particles by means of differential energy loss in the detection medium. In order to detect the reaction products over a wide range of energies, the novel μ-RWELL (micro-Resistive WELL) detectors are used as the gas multiplication stage. A unique concentric cathode cage configuration is also used to trap the ionisation electrons from the unreacted beam ions, which enables TACTIC to accommodate higher beam intensities ($> 10^6$ pps), compared to other active target detectors. Furthermore, an adjustable extended gas target allows simultaneous cross section measurements at multiple centre of mass energies. A detailed characterisation of the detector and the first successful cross section measurement at the TRIUMF ISAC-I facility are documented in this work. The astrophysically important ^{23}Na(α, p)^{26}Mg reaction was studied in inverse kinematics as a commissioning experiment.

This thesis also includes the study of the μ-RWELL detectors with the test chamber, which is a planar analogue of TACTIC. A series of alpha and ^{55}Fe X-ray source tests were used to study the performance and optimum operating conditions of the μ-RWELL detectors in terms of gas gain and energy resolution achievable as well as the low-energy detection capability ($\sim$ few keV) in different gas mixtures of interest. The installation marked the very first integration of the state-of-the-art μ-RWELL technology inside a cylindrical geometry for charged particle tracking.

To my mother.

Acknowledgements

I must start by mentioning that all the work related to this thesis was made possible by the collective effort of many and their sincere dedication to science. I am grateful for the opportunity I had to work with and learn so much from each and every one of them. Firstly, I would like to thank my supervisor, Prof. Alison Laird. It is almost impossible for me to muster the adequate words that would rightfully express her role in my four-year long doctoral journey. Nevertheless, I am truly grateful to her for having faith in me and providing constant guidance, support, and encouragement. I am hopeful that after sixteen long years, we were finally able to set TACTIC free from the shackles.

I must also mention that this thesis would not have been possible without the financial support from the School of Physics, Engineering, and Technology at the University of York and the Physical Sciences Division at TRIUMF, in the form of my tuition fees, stipend, and travel grants.

A sincere thanks to my thesis advisory panel members at the University of York, Dr. Chris Murphy and Dr. Christian Diget, for keeping track of my thesis progress as well as offering important guidance and advice. A lot of credit goes to Dr. Warren Lynch, a fellow member of the "TACTIC crew." During his time at the University of York, he played a key role in the testing and development of the test chamber and TACTIC. I have learned so much from him about gas-filled detectors, coding, and, more importantly, life, during the lengthy lab hours, late evening clean room visits, and most importantly, at the familiar tables of Charles XII. On that note, I must thank the "TACTIC veteran," Dr. Lars Martin, for all his support. Despite being occupied with scientific endeavours of his own, he went out of his way to help me get TACTIC in shape for the experiments. I also give thanks to Bob Hide and Dr. Pankaj Joshi for their invaluable contributions to the project. Furthermore, a big thank you to Dr. Giovanni Bencivenni and Dr. Davide Raspino for their expert guidance and help related to the important μ-RWELL tests.

My deepest thanks to my TRIUMF supervisor, Dr. Chris Ruiz, for securing the important beam time for the TACTIC experiments and his constant support. I also sincerely thank Peter Machule, Dr. Annika Lennarz, and Dr. Martin Alcorta Moreno for all the advice and support they provided in making the TACTIC experiments possible. Additional thanks goes to everyone at TRIUMF who collaborated on the TACTIC experiments. I could not possibly list everyone, but a specific mention should be made of Pierre-André Amaudruz and Konstantin Olchanski from the DAQ group, Spencer R. Kiy along with the ISAC beam delivery group, Rick Maharaj from the Detector group, and Gelo Remon from the Controls group.

Although I had to spend most of my days in York cooped up amidst the Covid-19 woes, the fellow members of the Nuclear Physics group at the University of York and my flatmates at Student Castle made the time I spent there truly memorable and fulfilling. Thanking people individually is never easy, as I am bound to leave some out. Therefore, a warm thanks to all the students and postdocs, past and present, whom I have had the pleasure of knowing and befriending over the course of my time in York and Vancouver.

A very special thank you goes to my family for their undying love and faith throughout all these years. Finding the right words to convey my gratitude is beyond my capabilities. Thus, simply put, it would have been impossible for me to arrive at this juncture of life without their support.

Last but certainly not least, Debarati, thank you for being such a constant throughout and for walking by my side through thick and thin.

Declaration of authorship

I declare that this thesis is a presentation of original work and I am the sole author. This work has not previously been presented for a degree or other qualification at this University or elsewhere. All sources are acknowledged as references.

Contents

List of Figures

List of Tables

Chapter 1

Introduction

1.1. Astrophysical motivation

In the grand scheme of the universe as we know it, stars can very well be imagined as giant factories. Throughout their lifespan, during different stages of evolution, stars synthesise a variety of chemical elements via numerous nuclear processes. Thus, a thorough understanding of the nuclear processes in different astrophysical environments is of prime importance in order to model the chemical evolution of the universe. The study of the key nuclear reactions driving nucleosynthesis in a particular astrophysical environment improves the understanding of the composition and enrichment of the same, as well as the galactic chemical evolution (GCE), improving the existing stellar and GCE models. The measurement of such nuclear reactions can be performed either directly or indirectly. A *direct* measurement, as the name suggests, involves using the reactants of interest. This is usually performed by bombarding a heavy target nucleus with a lighter beam nucleus. An *indirect* measurement is performed by using a different nuclear reaction in order to extract information on the reaction or reaction products of interest. The *direct* measurements can also be performed in *inverse kinematics*, i.e., the projectile is a heavy and the target is a light nucleus. This technique is useful where the heavy ion is radioactive with a short half-life, e.g., 1.66 s for ^{18}Ne, which renders the production of an enriched target impractical.

Hydrogen (^{1}H) and helium (^{4}He) are by far the most abundant chemical elements in the universe, boasting solar system abundances of 71.1% and 27.4%, respectively [1]. Therefore a majority of nuclear reactions with astrophysical significance involve either of these nuclei. Such reactions can be classified as *capture* and *charged particle* reactions. In case of *capture* reactions, i.e., (α, γ) and (p, γ), the photon is only able to carry a small portion of the momentum compared to the heavy reaction product or the *recoil*. Hence the recoil can be identified using recoil separators such as DRAGON [2]. In such experiments, the momentum of the heavy recoil is almost similar to that of the reactant beam particle. Examples of such reactions are $^{17}\mathrm{O}(\alpha, \gamma)^{21}\mathrm{Ne}$ relevant to the s-process nucleosynthesis and $^{23}\mathrm{Mg}(p, \gamma)^{24}\mathrm{Al}$ in classical novae. In *charged particle* reactions, the reaction products usually are a heavy *recoil* and a lighter *ejectile*. Detectors like TUDA [3], which is a cylindrical chamber with an arrangement of silicon detectors, can be used for studying *charged particle* reactions such as $^{23}\mathrm{Na}(\alpha, p)^{26}\mathrm{Mg}$ playing an important role in Type Ia supernovae and $^{18}\mathrm{F}(p, \alpha)^{15}\mathrm{O}$ in classical novae.

The motivation behind this thesis was the development and commissioning of a novel detector dedicated to the study of *direct charged particle* reactions. Measurements of such reactions often pose significant challenges, which arise from low reaction cross section at astrophysically important energies, low intensity of the available radioactive beams etc. Over the past decade, the development of radioactive beam facilities all over the world has led to the availability of a wide range of high intensity radioactive beams [4, 5]. As a result, the study of many nuclear reactions in inverse kinematics has become feasible. However, many such measurements still remain challenging at relevant energies with conventional silicon detector and ionisation chamber setups. This is mainly due to the energy loss of the reaction products inside the dead layer of silicon detectors, or the "window" separating the target and detection volumes in an ionisation chamber setup. Both of which can significantly impact the detection efficiency of reaction products by means of *differential energy loss*, depending on specific reactions and the corresponding energy region of interest. In order to minimise or eliminate the energy loss inside the material separating the target and the detection volumes, the concept of *active target* detectors was perceived. In *active target* detectors, the target material itself also acts as the detection medium. This concept is discussed in detail in the later chapters.

TRIUMF **A**nnular **C**hamber for **T**racking and **I**dentification of **C**harged particles (TACTIC) [6], which is the main focus of this thesis, was developed to study alpha-induced *charged particle* reactions with astrophysical significance. TACTIC is a cylindrical *active target* time projection chamber (TPC), which can be used to track and identify the reaction products of interest. It can only detect charged particles by means of differential energy loss ($-dE/dx$) in the detection medium. The focus of the recent studies was on the (α, p) and (p, α) reactions. The heavy recoils (A $>$ 10) for such reactions have small forward angles, which makes the detection of both reaction products in coincidence challenging in the TACTIC geometry. This is due the presence of the cathode cage, which shields the majority of the heavy recoils with lab angle of $\lesssim 10°$ from detection. Thus, the aim was to develop a robust detection scheme for the light ejectiles, e.g., p or α, (singles measurement) by utilising the low energy detection capability ($\approx$ 5.9 keV) of TACTIC to estimate reaction cross sections. The astrophysically important and well-constrained ^{23}Na$(\alpha, p)^{26}$Mg reaction was studied and re-investigated with TACTIC as a commissioning experiment. The reaction was identified to have a significant contribution to the nucleosysnthesis in Type Ia supernovae during the explosive Ne/C burning ($T = 2.3$ GK) and in massive stars during the convective shell C/Ne burning ($T = 1.4$ GK). In massive stars, the ^{23}Na$(\alpha, p)^{26}$Mg reaction was found to influence the production of ^{26}Al, which is an important isotope for γ-ray astronomy. The half-life of ^{26}Al is 7.2×10^5 years, which is small compared to the GCE time scales ($\approx 10^{10}$ years). Thus, traces of ^{26}Al in the interstellar medium point towards the relatively recent nucleosynthesis in the galaxies. The reaction of interest acts as a source of protons for the ^{25}Mg$(p, \gamma)^{26}$Al reaction. In the recent work by Hubbard et al. [9], a combined reaction rate for ^{23}Na$(\alpha, p)^{26}$Mg was calculated. All the recent individual studies of the reaction and the Hauser-Feshbach models [10] were found to be consistent within 30% in the relevant energy range of E_{cm} = 1.7-3.0 MeV (see Fig. 1.1). The ^{23}Na$(\alpha, p)^{26}$Mg reaction was studied in the energy range of $E_{cm} \approx$ 1.0-4.5 MeV with TACTIC. The

energy range was chosen in order to study the *Gamow window* corresponding to the temperatures for explosive Ne/C burning ($E_{cm} \approx$ 1.7-3.4 MeV) and convective shell C/Ne burning ($E_{cm} \approx$ 1.2-2.4 MeV). The *Gamow window* represents the energy range over which a nuclear reaction is more probable in a specific stellar environment and is discussed further in the later chapters. As shown in Fig. 1.1, the reaction still lacks experimental data in the energy region below $E_{cm} \approx$ 1.8 MeV, study of which is important for ^{26}Al production in the C/Ne convective shell of massive stars during the pre-supernova stages [10] as well as to verify the accuracy of the existing statistical models.

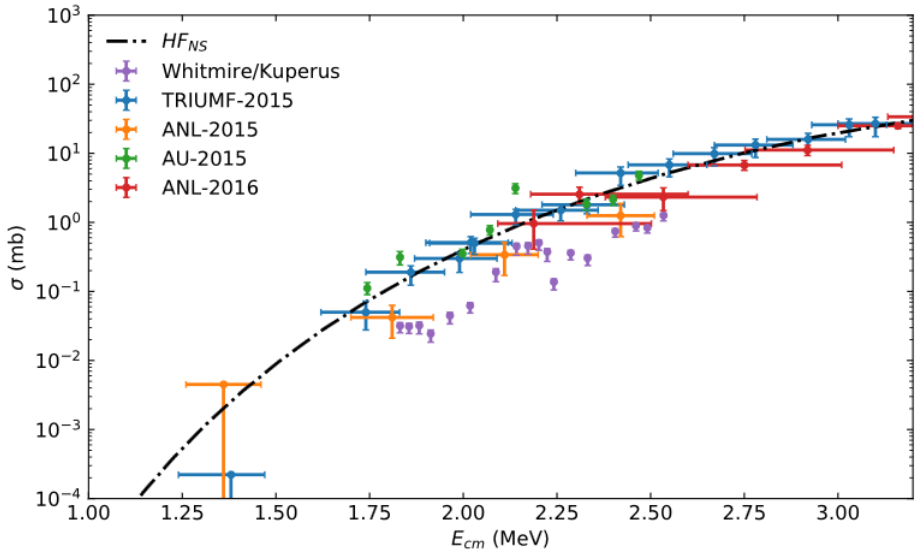

Figure 1.1: Total cross sections of the non-resonant ^{23}Na$(\alpha, p)^{26}$Mg reaction [9].

1.2. Thesis outline

Multiple campaigns have been undertaken in the past to test TACTIC with alpha sources as well as different ion beams. The information on the test setups and results was published and presented alongside prior PhD dissertations [7, 8, 11, 12] focused on the detector design and its characterisation. The detailed studies of the detector setup highlighted several challenges, including high electronic noise and the lack of uniformity in the detector channel responses, which mainly originated from the gas electron multiplier (GEM) used as the electron multiplication stage. Furthermore, the low gas gain from the GEM and the VF48 data acquisition system used was not suited for an efficient detection of low energy deposition ($<$ 100 keV) in the detection medium and the wide range of deposited energy (tens of keV to a few MeV) by the different reaction products. Both of which limited the number of nuclear reactions that could be studied with TACTIC.

In light of the past difficulties, several major changes and modifications were recently made to the old TACTIC setup. The gas electron multiplier (GEM) was replaced by the μ-RWELL detector as the electron multiplication stage, following the successful studies with the test chamber at the University of York (Chapter 5). A detailed characterisation was performed using the test chamber setup, a part of

which was published during the time span of this work [13]. The discussions on both GEM and μ-RWELL are included in Chapter 3. As discussed in Chapters 5 and 7, the novel μ-RWELL was tested for the first time in He-based gas mixtures and cylindrical geometry. Furthermore, the dedicated TACTIC preamplifiers were also modified (discussed in Section 6.2.3) and the previously used VF48 data acquisition system was replaced by the CAEN V1740 digitiser [14]. A dedicated Geant4-based NPTool simulation was also developed for the test chamber and TACTIC (discussed in Chapter 4). Chapters 2 and 3 contain brief descriptions of the key concepts and literary references used in the later chapters. The simulation was rigorously used alongside the data analysis in Chapter 7, towards achieving a better understanding of the experimental data from the source and stable beam tests. Chapter 7 includes the investigation of the particle identification capability, the tracking accuracy of TACTIC, and the verification of the experimental method (discussed in Chapter 6) using both alpha source and stable beam data. Furthermore, it includes the cross section measurement of the $^{23}\mathrm{Na}(\alpha, p)^{26}\mathrm{Mg}$ reaction at the TRIUMF research facility. The analysis of the stable beam data was focused on the proton detection efficiency, the vertex energy resolution, and background suppression. All the relevant experimental and simulation data analysis codes were developed by the author.

Chapter 2

Nuclear reactions

Thermonuclear reactions fuel the stars and drive the chemical evolution of the universe. Therefore comprehensive studies of important reactions are key to understanding the relevant astrophysical sites, the present day chemical abundances and moreover the physical world around us. This chapter will detail the crucial concepts and definitions of the parameters related to nuclear reactions.

2.1. Energetics of nuclear reactions

A nuclear reaction can be symbolically represented as,

$$0 + 1 \rightarrow 2 + 3, \tag{2.1}$$

or,

$$0(1,2)3, \tag{2.2}$$

where 0 and 1 represent the nuclei taking part in the reaction, while 2 and 3 represent the reaction products. If species 0 and 1 are identical to species 2 and 3, then the interaction is called elastic or inelastic scattering; otherwise it refers to a nuclear reaction. For charged particle reactions, the reaction products usually have different masses. The heavier and the lighter reaction products are commonly known as recoils and ejectiles, respectively. Furthermore, if all species involved in a nuclear reaction have rest masses, the total relativistic energy in a nuclear reaction must be conserved. Therefore,

$$Q_{01\rightarrow 23} \equiv m_0c^2 + m_1c^2 - m_2c^2 - m_3c^2 = E_2 + E_3 - E_0 - E_1, \tag{2.3}$$

where E_i and m_i are the kinetic energies and the nuclear masses of the species involved in the nuclear reaction. The difference in masses before and after the nuclear reaction or the difference in kinetic energies after and before the reaction is known as the reaction Q-value. If the Q-value is positive, then the reaction is exothermic, i.e., the reaction releases energy, and if the Q-value is negative, then the reaction consumes energy and is called endothermic. Eq. 2.3 allows the calculation of the Q-value of a nuclear reaction by using appropriate nuclear masses. It must be noted that the direct measurements of nuclear masses are difficult due to the presence of

the atomic electrons. However, the atomic masses can be precisely measured. The atomic and the nuclear masses are related by,

$$m_a(A,Z) = m_{nuc}(A,Z) + Zm_e - B_e(Z), \tag{2.4}$$

where m_e and B_e are the electron mass and the electron binding energy in the atom. As the electron binding energy is much smaller than the nuclear mass differences, the term B_e can be ignored. As the nuclear reactions conserve the total charge, the nuclear masses can be replaced by atomic masses since the same number of electron rest masses is added on both sides of a reaction equation. The quantity atomic mass excess (in units of energy) can be defined as,

$$M.E. \equiv (m_a - Am_u)c^2, \tag{2.5}$$

where A is the mass number of the atom and the quantity m_u is the atomic mass unit, u. The reaction Q-value can be expressed in terms of the mass excess as shown in Eq. 2.8. From the definition in Eq. 2.3,

$$Q_{01\to23} = m_{a0}c^2 + m_{a1}c^2 - m_{a2}c^2 - m_{a3}c^2. \tag{2.6}$$

If m_{ai} and A_i are the atomic masses and mass numbers, respectively, of the species involved in the nuclear reaction and since $(A_0 + A_1) = (A_2 + A_3)$,

$$\begin{aligned} Q_{01\to23} = &(m_{a0}c^2 + m_{a1}c^2 - m_{a2}c^2 - m_{a3}c^2) \\ &+ (A_2m_uc^2 + A_3m_uc^2 - A_0m_uc^2 - A_1m_uc^2), \end{aligned} \tag{2.7}$$

$$Q_{01\to23} = (M.E.)_0 + (M.E.)_1 - (M.E.)_2 - (M.E.)_3. \tag{2.8}$$

It can immediately be inferred from Eq. 2.6 and 2.8 that using atomic masses or atomic mass excesses gives the same result for the calculation of reaction Q-value.

2.2. Cross sections

The cross section (σ), is a quantitative measure of the probability that a nuclear interaction will take place. For a typical nuclear physics experimental setup with incident beam ions (N_b) and the target area density (N_t/A), the cross section can be defined as,

$$\sigma = \frac{N_R/t}{(N_b/t)(N_t/A)}, \tag{2.9}$$

where N_R/t is the number of reactions taking place per unit time, also called the reaction yield (Y) per unit time. Eq. 2.9 holds true when the target area is larger than the beam area. The differential cross section can be defined as,

$$\left(\frac{d\sigma}{d\Omega}\right) = \frac{N_R^{d\Omega}/t}{(N_b/t)(N_t/A)}\frac{1}{d\Omega}, \tag{2.10}$$

where dΩ is the solid angle covered by the detector and $N_R^{d\Omega}/t$ is the number of reactions corresponding to dΩ per unit time. The quantities σ and $\left(\frac{d\sigma}{d\Omega}\right)$ are related by,

$$\sigma = \int \left(\frac{d\sigma}{d\Omega}\right) d\Omega \tag{2.11}$$

Eq. 2.9 indicates that cross section has the units of area, commonly expressed as barn (b) or milibarn (mb). 1 b $\equiv 10^{-24}$ cm^2 $= 10^{-28}$ m^2.

2.3. Elastic scattering

Elastic scattering can be considered as the simplest form of nuclear interaction, where two nuclei interact without any loss of kinetic energy. If a beam of monoenergetic particles is incident on a stationary target along the z-direction, the value and the uncertainty of the z-component of the linear momentum are given by $p_z =$ constant and $\Delta p_z = 0$, respectively. Furthermore, under the assumption $p_x = p_y = 0$, the incoming particles can be represented by an incident plane wave, e^{ikz}, i.e., a wave of very large wavelength in the x- and y-directions. Therefore, stationary scattering problem can be described by the time-independent Schrödinger equation [1, 15],

$$\left[-\frac{\hbar^2}{2m}\nabla^2 + V(\vec{r})\right]\psi(\vec{r}) = E\psi(\vec{r}), \tag{2.12}$$

where $V(\vec{r})$ is the central potential defining the average interaction between the incident and target nuclei. At the position of the target nucleus, the total wave function cannot be specified without assuming an explicit nuclear potential. However, far from the scattering centre, the total wave function ($\psi_T(\vec{r})$) can be expressed as the sum of an incoming stationary plane wave travelling in the z-direction (represented by the term containing $e^{i\vec{k}\vec{r}}$) and an outgoing stationary spherical wave (represented by the term containing e^{ikr}) [1].

$$\psi_T(\vec{r}) = N\left[e^{i\vec{k}\vec{r}} + f(\theta)\frac{e^{ikr}}{r}\right], \quad r \to \infty, \tag{2.13}$$

where N is an overall normalisation factor, $f(\theta)$ is the scattering amplitude. The factor $1/r$ signifies that the scattered intensity obeys an inverse square law. A relationship between the differential cross section defined in Eq. 2.10 and the scattering amplitude can be established as [1],

$$\left(\frac{d\sigma}{d\Omega}\right) = |f(\theta)|^2. \tag{2.14}$$

If the z-axis is chosen along $\vec{k}$, the plane wave term from Eq. 2.13 can be expressed as,

$$e^{i\vec{k}\vec{r}} = e^{ikr\cos\theta} = e^{ikrz/r} = e^{ikz}. \tag{2.15}$$

For $V(\vec{r}) \neq 0$, $f(\theta) \neq 0$, the total wave function from Eq. 2.13 can be expanded into partial waves,

$$\psi_T = e^{ikz} + f(\theta)\frac{e^{ikr}}{r} = \sum_{\ell=0}^{\infty} b_\ell \frac{u_\ell(kr)}{kr} P_\ell(\cos\theta). \tag{2.16}$$

By substituting $b_\ell = (2\ell{+}1)i^\ell e^{i\delta_\ell}$ and the radial wave function $u_\ell = \sin(kr{-}\ell\pi/2{+}\delta_\ell)$ $(r \to \infty)$,

$$\psi_T = e^{ikz}{+}f(\theta)\frac{e^{ikr}}{r} = \sum_{\ell=0}^{\infty}(2\ell{+}1)i^\ell e^{i\delta_\ell}\frac{\sin(kr-\ell\pi/2+\delta_\ell)}{kr}P_\ell(\cos\theta),\ r\to\infty. \tag{2.17}$$

Using $\sin x = (i/2)(e^{-ix} - e^{ix})$ in Eq. 2.17,

$$\psi_T = e^{ikz}{+}f(\theta)\frac{e^{ikr}}{r} = \frac{1}{2kr}\sum_{\ell=0}^{\infty}(2\ell{+}1)i^{\ell+1}[e^{-i(kr-\ell\pi/2}{-}e^{2i\delta_\ell}e^{i(kr-\ell\pi/2)}]P_\ell(\cos\theta),\ r\to\infty, \tag{2.18}$$

where $P_\ell(\cos\theta)$ is the Legendre polynomial and δ_ℓ is the phase shift between the incoming and outgoing waves. The scattering amplitude $f(\theta)$ can be obtained from solving the following [1],

$$f(\theta)\frac{e^{ikr}}{r} = \psi_T - \psi_T^{f.p.}, \tag{2.19}$$

where $\psi_T^{f.p.}$ is the wave function under the free particle consideration $(V(\vec{r}) = 0, f(\theta) = 0)$ and can be expressed as [1],

$$\psi_T^{f.p.} = e^{ikz} = \frac{1}{2kr}\sum_{\ell=0}^{\infty}(2\ell+1)i^{\ell+1}[e^{-i(kr-\ell\pi/2} - e^{i(kr-\ell\pi/2)}]P_\ell(\cos\theta),\ r\to\infty. \tag{2.20}$$

Therefore, Eq. 2.18, 2.19 and 2.20 can be used in conjunction to obtain the following expression for $f(\theta)$ [1],

$$f(\theta) = \frac{1}{k}\sum_{\ell=0}^{\infty}(2\ell+1)e^{i\delta_\ell}\sin\delta_\ell P_\ell(\cos\theta). \tag{2.21}$$

The differential elastic scattering cross section can be written as [1],

$$\left(\frac{d\sigma}{d\Omega}\right)_{el} = |f(\theta)|^2 = f^*(\theta)f(\theta) = \frac{1}{k^2}|\sum_{\ell=0}^{\infty}(2\ell+1)\sin\delta_\ell P_\ell(\cos\theta)|^2. \tag{2.22}$$

The above equation indicates that the differential scattering cross section is dependent on the energy of the incoming particle, angular momentum and the scattering

angle. So far an assumption that at least one particle participating in the interaction is uncharged. If both the nuclei are charged, then then the phase shift δ_ℓ needs to be replaced by $\delta_\ell + \sigma_\ell$. σ_ℓ is the phase shift caused by the long-range Coulomb potential. Therefore the scattering amplitude in this case can be expressed as,

$$f(\theta) = \frac{i}{2k}\sum_{\ell=0}^{\infty}(2\ell+1)(1-e^{2i\sigma_\ell})P_\ell(\cos\theta)+\frac{i}{2k}\sum_{\ell=0}^{\infty}(2\ell+1)e^{2i\sigma_\ell}(1-e^{2i\delta_\ell}P_\ell(\cos\theta)). \quad (2.23)$$

In Eq. 2.23, the first term describes the scattering from a pure Coulomb field, also called Rutherford scattering. The second term corresponds to scattering from both the nuclear and the Coulomb potential. For the Rutherford or Coulomb scattering between two nuclei, it can be shown using the conservation of energy and angular momentum [15], that the differential cross section corresponding to a solid angle, $d\Omega$ ($=2\pi\sin\theta d\theta$), at a plane angle θ is,

$$\frac{d\sigma}{d\Omega} = \left(\frac{Z_1 Z_2 e^2}{4T_p^{cm}}\right)^2 \frac{1}{\sin^4\left(\frac{\theta}{2}\right)}, \quad (2.24)$$

where Z_1 and Z_2 are the charges corresponding to interacting nuclei, T_p^{cm} is the projectile energy in the centre of mass frame. Eq. 2.24 shows that Rutherford scattering cross section has a strong dependence on the scattering angle (θ). Furthermore, Rutherford scattering is not a nuclear reaction as it does not involve the nuclear force, however it accompanies nuclear reactions involving charged particles, giving rise to background from scattered particles at forward angles. Fig. 2.1 shows the dependence of Rutherford scattering cross section on scattering angle for projectile ^{23}Na and targets ^{4}He (α), ^{12}C, ^{16}O.

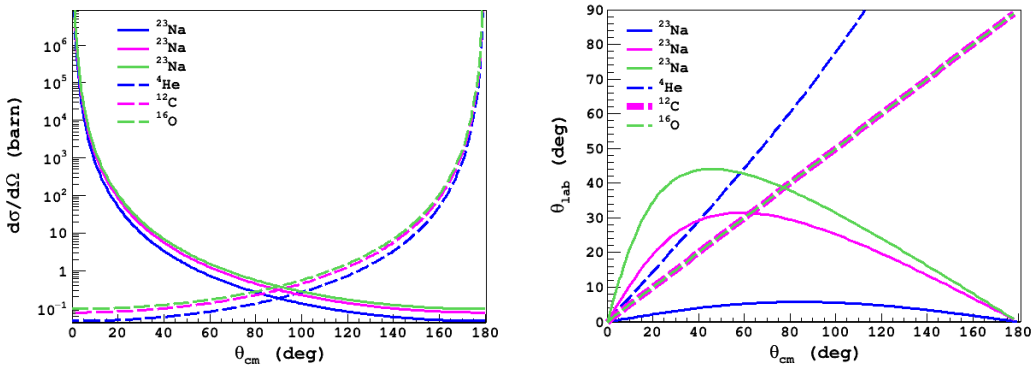

Figure 2.1: Angular dependence of differential cross section for different elastic scattering interactions, i.e., ^{4}He(^{23}Na, ^{4}He)^{23}Na, ^{12}C(^{23}Na, ^{12}C)^{23}Na, ^{16}O(^{23}Na, ^{16}O)^{23}Na. The projectile (^{23}Na) energy in the lab frame was considered to be, $T_p^{lab} = 25$ MeV.

2.4. Transmission through barrier

The probability for transmission of a particle through a potential barrier is obtained by solving the Schrödinger equation explicitly for the simple case of s-wave. In order

to develop a simple model for nuclear reactions, a one-dimensional constant barrier potential of height V_1 and a constant square well potential that steps down to -V_0 can be considered. The quantity transmission coefficient ($\hat{T}$) is used to define the probability that an individual particle will be transmitted through a barrier from the outer to the inner region. For a square-barrier potential illustrated in Fig. 2.2 [1], $\hat{T}$ can be expressed as,

$$\frac{1}{\hat{T}} = \frac{1}{\sqrt{E(E+V_0}}\left\{\left[2E+V_0+2\sqrt{E(E+V_0)}\right]\right. \\ \left. + \left[E+V_0+V_1+\frac{E(E+V_0)}{V_1-E}\right]\sinh^2\left[\sqrt{(2m/\hbar^2)(V_1-E)}\Delta\right]\right\}. \tag{2.25}$$

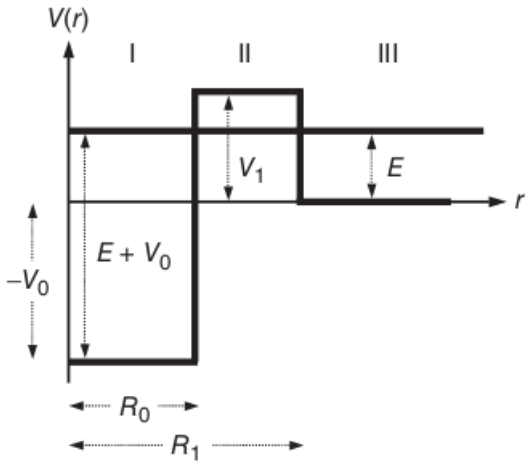

Figure 2.2: Three-dimensional square-well potential of radius R_0, potential depth V_0 and the repulsive square-barrier potential of thickness $\Delta \equiv R_1 - R_0$, height V_1. The incoming particle energy is E ($< V_1$) [1].

Eq. 2.25 shows that the particle approaching the potential barrier from the right-hand side can reach the left-hand side even if its energy is less than the barrier height. This is known as the *tunneling effect*, which plays a key role in charged particle reactions in different stellar environments. Eq. 2.25 can also be written as,

$$\hat{T} \approx 4\frac{\sqrt{E(E+V_0)}(V_1-E)}{V_1(V_0+V_1)}e^{-(2/\hbar)\sqrt{2m(V_1-E)}(R_1-R_0)}. \tag{2.26}$$

The first term in the above equation is dimensionless and can be considered as unity for the physically reasonable values of E, V_0 and V_1, therefore,

$$\hat{T} \approx e^{-(2/\hbar)\sqrt{2m(V_1-E)}(R_1-R_0)}. \tag{2.27}$$

This result only applies to the s-wave ($\ell = 0$) scattering of neutral and spinless particles under the constant potential consideration. In order for a nuclear reaction to take place, the Coulomb barrier between the two charged particles must be overcome. The transmission coefficient in Eq. 2.27 can be generalised. It is possible to

divide a potential barrier of arbitrary shape into thin slices of width dr. The total s-wave transmission coefficient can be expressed as the product of the transmission coefficients for each slice,

$$\hat{T} = \hat{T}_1\hat{T}_2...\hat{T}_n \approx \exp\left[-\frac{2}{\hbar}\sum_i \sqrt{2m(V_i - E)}(R_{i+1} - R_i)\right]. \tag{2.28}$$

For a large number of slices Eq. 2.28 can be written as,

$$\hat{T} \approx \exp\left[-\frac{2}{\hbar}\int_{R_0}^{R_c} \sqrt{2m(V(r) - E)}dr\right]. \tag{2.29}$$

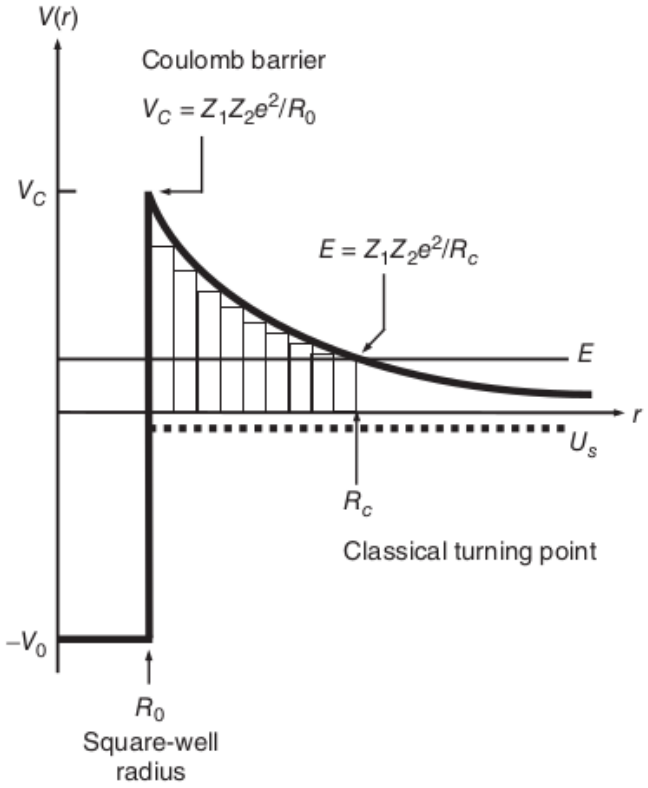

Figure 2.3: $r < R_0$: region governed by the attractive nuclear square-well potential, $r < R_0$: region governed by the repulsive Coulomb potential. The transmission coefficient can be calculated by dividing the Coulomb barrier into infinitesimally thin slices of square-barrier potentials [1].

For the Coulomb barrier consideration, $V(r)$ in Eq. 2.29 can be replaced by,

$$V(r) = \frac{Z_0Z_1e^2}{r}, \tag{2.30}$$

where Z_0 and Z_1 are the charges of the two nuclei involved in the interaction, $V_C = Z_0Z_1e^2/R_0$ is the height of the Coulomb barrier with R_0 is the radius of the square-well potential. R_0 is commonly expressed in units of femtometers. Furthermore, R_c is the distance at which the incoming particle would get reflected classically, called the *classical turning point* and is defined by $E = Z_0Z_1e^2/R_c$. By substituting

$V(r)$ from Eq. 2.30 into Eq. 2.29 and solving it analytically [1], the s-wave Coulomb barrier transmission coefficient ($E < V_C$) can be obtained,

$$\hat{T} \approx exp\left(-\frac{2\pi}{\hbar}\sqrt{\frac{m}{2E}}Z_0 Z_1 e^2\right) \equiv e^{-2\pi\eta}. \tag{2.31}$$

In the above equation, $e^{-2\pi\eta}$ is called the *Gamow factor* and η is the *Sommerfeld parameter*, which is a dimensionless quantity defined as,

$$\eta = \frac{Z_0 Z_1 e^2}{\hbar}\sqrt{\frac{m}{2E}}, \tag{2.32}$$

where m is the reduced mass of the target and incident particles.

2.5. Charged particle induced reactions

In case of a nuclear reaction ($0 + 1 = 2 + 3$), following Eq. 2.9, with the definition $r_{01} \equiv N_R/(Vt)$, the reaction rate per unit volume can be expressed as,

$$r_{01} = N_0 N_1 v\sigma(v), \tag{2.33}$$

where $N_0 \equiv N_t/V$ and $N_1 \equiv N_b/V$ are the number densities of the interacting nuclei. In the stellar environment at thermodynamic equilibrium, the relative velocity of the interacting nuclei (0 and 1) does not remain constant. Their relative velocities follow a distribution instead and can be defined by the probability function $P(v)$ and $P(v)dv$ is the probability that the relative velocity of the interacting nuclei is in the range between v and $v + dv$,

$$\int_0^\infty P(v)dv = 1. \tag{2.34}$$

Therefore the reaction rate can also be expressed as,

$$r_{01} = N_0 N_1 \int_0^\infty vP(v)\sigma(v)dv \equiv N_0 N_1 \langle\sigma v\rangle_{01}, \tag{2.35}$$

$$r_{01} = \frac{N_0 N_1 \langle\sigma v\rangle_{01}}{(1 + \delta_{01})}, \tag{2.36}$$

where $\langle\sigma v\rangle_{01}$ is the reaction rate per particle pair, δ_{01} is the Kronecker symbol and $N_0 N_1$ is the total number density of pairs of nonidentical nuclei 0 and 1. For identical particles the total number density of pairs is given by $N_0^2/2$. In a stellar environment, the kinetic energy available to nuclei comes from their thermal motion ($kT \approx$ 1-100 keV). Under the consideration of non-relativistic and non-degenerate motion of the stellar plasma, the velocities of nuclei can be expressed by a Maxwell-Boltzmann distribution,

$$P(v)dv = \left(\frac{m_{01}}{2\pi kT}\right)^{3/2} e^{-m_{01}v^2/(2kT)} 4\pi v^2 dv, \tag{2.37}$$

where $k = 8.6173\times10^{-5}$ eV/K is the Boltzmann constant, T is the temperature of the stellar environment, and m_{01} is the reduced mass $m_{01} = m_0m_1/(m_0 + m_1)$ of the interacting nuclei. By using the expressions $E = m_{01}v^2/2$ and $dE/dv = m_{01}v$, Eq. 2.37 can be written in terms of energy distribution,

$$P(v)dv = P(E)dE = \frac{2}{\sqrt{\pi}}\frac{1}{(kT)^{3/2}}\sqrt{E}e^{-E/kT}dE. \tag{2.38}$$

Considering the energy distribution has a maximum at $E = kT/2$, from Eq. 2.35 the reaction rate per particle pair [1],

$$\langle\sigma v\rangle_{01} = \left(\frac{8}{\pi m_{01}}\right)^{1/2}\frac{1}{(kT)^{3/2}}\int_0^\infty E\sigma(E)e^{-E/kT}dE, \tag{2.39}$$

The reaction rate at temperature T can be expressed as [1],

$$N_A\langle\sigma v\rangle_{01} = \frac{3.7318\times10^{10}}{T_9^{3/2}}\sqrt{\frac{M_0+M_1}{M_0M_1}}\int_0^\infty E\sigma(E)e^{-11.605E/T_9}dE, \tag{2.40}$$

where N_A is the Avogadro constant, the centre of mass energy E is in units of MeV, the temperature T_9 in GK ($T_9 \equiv T/10^9K$), the relative atomic masses M_0 and M_1 are in amu, and the cross section σ in barn. It can be inferred from Eq. 2.40, that the reaction rate depends primarily on the cross section. The reaction rate $N_A\langle\sigma v\rangle_{01}$ can be determined by solving Eq. 2.39 once the reaction cross section has either been measured or been theoretically estimated. Based on the energy dependence of cross sections, two extreme cases can arise, i.e., the first case, where the cross sections vary smoothly with energy (non-resonant cross sections) (see Fig. 1.1) and in the second case, the cross sections vary strongly at and around particular energies (resonant cross sections) (see Fig. 2.4). The results presented in Chapter 7, involve the direct measurement of the non-resonant reaction ^{23}Na$(\alpha, p)^{26}$Mg.

2.5.1. Non-resonant reactions

As shown in Fig. 1.1 for a non-resonant reaction, the cross sections vary smoothly with energy and at lower energies, a significant drop in the cross sections can be observed as a result of the decreasing transmission probability through the Coulomb barrier as per Eq. 2.31. The astrophysical S-factor, $S(E)$, is defined as [1],

$$\sigma(E) \equiv \frac{1}{E}e^{-2\pi\eta}S(E), \tag{2.41}$$

where $\sigma(E)$ is the reaction cross section at energy E and $e^{-2\pi\eta}$ is the Gamow factor. Using the above definition and Eq. 2.31, Eq. 2.39 can be expressed as,

$$N_A\langle\sigma v\rangle_{01} = \left(\frac{8}{\pi m_{01}}\right)^{1/2}\frac{N_A}{(kT)^{3/2}}\int_0^\infty e^{-2\pi\eta}S(E)e^{-E/kT}dE, \tag{2.42}$$

or,

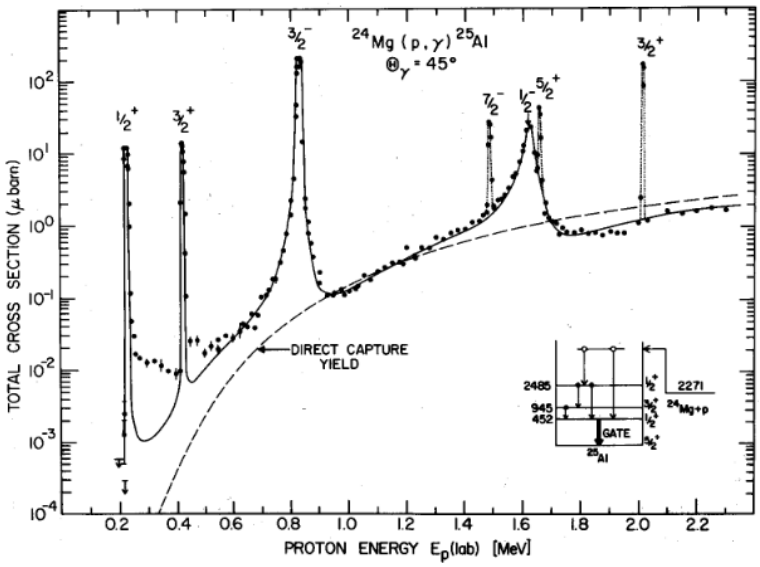

Figure 2.4: Total cross sections at different energies for the resonant ^{24}Mg(p, γ)^{25}Al [16]. Resonance peaks are clearly visible at multiple energies.

$$N_A\langle\sigma v\rangle_{01} = \left(\frac{8}{\pi m_{01}}\right)^{1/2} \frac{N_A}{(kT)^{3/2}} \int_0^\infty \exp\left(\frac{-2\pi}{\hbar}\sqrt{\frac{m_{01}}{2E}} Z_0 Z_1 e^2\right) S(E) e^{-E/kT} dE, \tag{2.43}$$

where Z_0 and Z_1 represent the charges of the target and projectile. If the astrophysical S-factor is considered as a constant, i.e., $S(E) = S_0$, Eq. 2.42 can be expressed as,

$$N_A\langle\sigma v\rangle_{01} = \left(\frac{8}{\pi m_{01}}\right)^{1/2} \frac{N_A}{(kT)^{3/2}} S_0 \int_0^\infty e^{-2\pi\eta} e^{-E/kT} dE, \tag{2.44}$$

where following Eq. 2.31,

$$2\pi\eta = 0.98951013 \cdot Z_0 Z_1 \sqrt{\frac{M_0 M_1}{M_0 + M_1} \frac{1}{E}}, \tag{2.45}$$

where M_0, M_1 are atomic masses and E is the energy in units of amu and MeV, respectively. The integrand in Eq. 2.44 depends on the term $e^{-E/kT}$, originating from the Maxwell-Boltzmann distribution, approaches zero at large energies and the term $e^{-2\pi\eta}$ or $e^{-1/\sqrt{E}}$, follows from the Gamow factor, approaches zero at small energies. The major contribution to the reaction rate come from the energies where the integrand is at maximum. As the Gamow factor shifts the integrand to higher temperatures, i.e., the high energy tail of the Maxwell-Boltzmann distribution, the integrand is commonly referred to as the Gamow peak (Fig. 2.5). The Gamow peak represents the narrow energy range over which a nuclear reaction is most probable in the stellar environment. The location of the maximum of the Gamow peak or the most effective energy (E_0) and the width of the Gamow peak (Δ) can be obtained and expressed as,

$$E_0 = 0.1220\left(Z_0^2 Z_1^2 \frac{M_0 M_1}{M_0 + M_1} T_9^2\right)^{1/3} \text{(MeV)}, \tag{2.46}$$

$$\Delta = 0.2368\left(Z_0^2 Z_1^2 \frac{M_0 M_1}{M_0 + M_1} T_9^5\right)^{1/6} \text{(MeV)}. \tag{2.47}$$

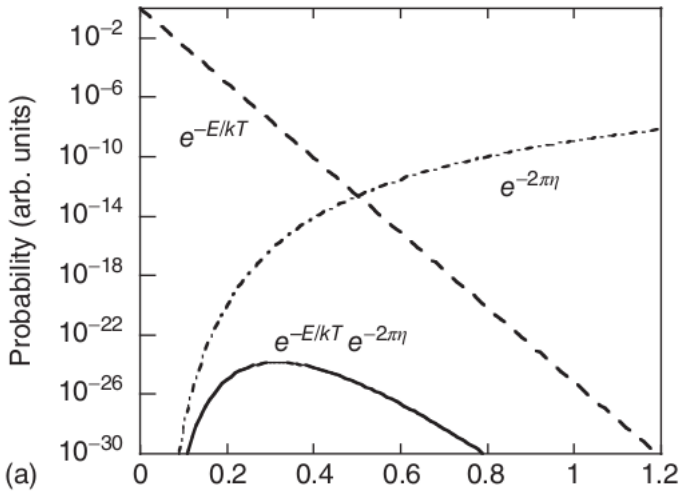

Figure 2.5: Maxwell-Boltzmann factor ($e^{-E/kT}$; dashed line) and Gamow factor ($e^{-2\pi\eta}$; dashed-dotted line) versus energy for the $^{12}C(\alpha,\gamma)^{16}O$ reaction at $T = 0.2$ GK. The product $e^{-E/kT}e^{-2\pi\eta}$, referred to as the Gamow peak, is shown as solid line [1].

Thermonuclear reactions mainly occur over an energy range between $E_0 - \Delta/2$ and $E_0 + \Delta/2$, known as the Gamow window. Eq. 2.46 shows that the Gamow peak shifts to higher temperatures with increasing target and projectile charges. Furthermore, the area under the Gamow peak decreases and the width of the Gamow peak broadens. This is important in order to understand the thermonuclear burning in stars, as in the stellar plasma, the reactions involving particles with the smallest Coulomb barrier will account for most of the nuclear energy generation. Eq. 2.44 can be expressed in terms of E_0 and Δ under the Gaussian approximation of the Gamow peak,

$$N_A\langle\sigma v\rangle = \frac{1}{3}\left(\frac{4}{3}\right)^{3/2} \frac{\hbar}{\pi} \frac{N_A}{m_{01} Z_0 Z_1 e^2} S_0 \tau^2 e^{-\tau}, \tag{2.48}$$

where $\tau \equiv 3E_0/kT$. Thermonuclear reaction rates alongside the Gamow peak features show a major dependency on temperature. In cases where the astrophysical S-factor is not constant, but varies with energy (Eq. 2.49), S_0 in Eq. 2.48 needs to be replaced by an effective S-factor (S_{eff}).

$$S(E) \approx S(0) + S'(0)E + \frac{1}{2}S''(0)E^2. \tag{2.49}$$

Therefore Eq. 2.48 can be expressed as,

$$N_A\langle\sigma v\rangle = \frac{1}{3}\left(\frac{4}{3}\right)^{3/2}\frac{\hbar}{\pi}\frac{N_A}{m_{01}Z_0Z_1e^2}S_{\text{eff}}\tau^2e^{-\tau}, \tag{2.50}$$

where,

$$S_{\text{eff}}(E_0) = S(0)\left[1+\frac{5}{12\tau}+\frac{S'(0)}{S(0)}\left(E_0+\frac{35}{36}kT\right)+\frac{1}{2}\frac{S''(0)}{S(0)}\left(E_0^2+\frac{89}{36}E_0kT\right)\right]. \tag{2.51}$$

The first two terms in the square bracket in Eq. 2.51 correspond to the correction factor, $F(\tau)$, signifying the deviation of the Gamow peak from the Gaussian approximation.

2.5.2. Resonant reactions

Many reaction cross sections exhibit complex and strongly varying dependency on energy caused by resonances, unlike the non-resonant reaction cross sections discussed in the previous section. Isolated and narrow resonance can be considered the simplest case, which occurs when the energy of the projectile in the centre of mass frame matches the energy state, E_r of the compound nucleus (Fig. 2.6). The term "isolated" implies that the level density of a compound nucleus is relatively small. Thus, the resonances do not overlap significantly in amplitude. For a particular reaction the Q-value is a constant. Therefore the reaction can take place when the total centre of mass energy E_R satisfies Eq. 2.52. Since the reaction occurs at fixed values of E_R corresponding to specific excited states of the compound nuclei, the process is referred to as a resonant reaction.

$$E_R = E_r - Q. \tag{2.52}$$

If the excited state E_r decays by γ-emission to a state E_f at a lower energy, the reaction cross section can be represented as the product of two matrix elements,

$$\sigma_\gamma \propto |\langle E_f|H_\gamma|E_r\rangle|^2|\langle E_r|H_f|A+x\rangle|^2, \tag{2.53}$$

where the matrix element with the operator H_f represents the formation of the compound state E_r and the other one represents the subsequent γ-decay. Hence resonant reactions are basically two step processes compared to non-resonant reactions, which are assumed to involve a single step. Near the resonant total centre of mass energies (E_R), the cross section increases significantly. The matrix elements in Eq. 2.53, represent the probability of formation and decay of the excited state, E_r in the compound nucleus into the desired channel. Eq. 2.53 can be rewritten in terms of energy-dependent partial widths:

$$\sigma_\gamma \propto \Gamma_a\Gamma_b, \tag{2.54}$$

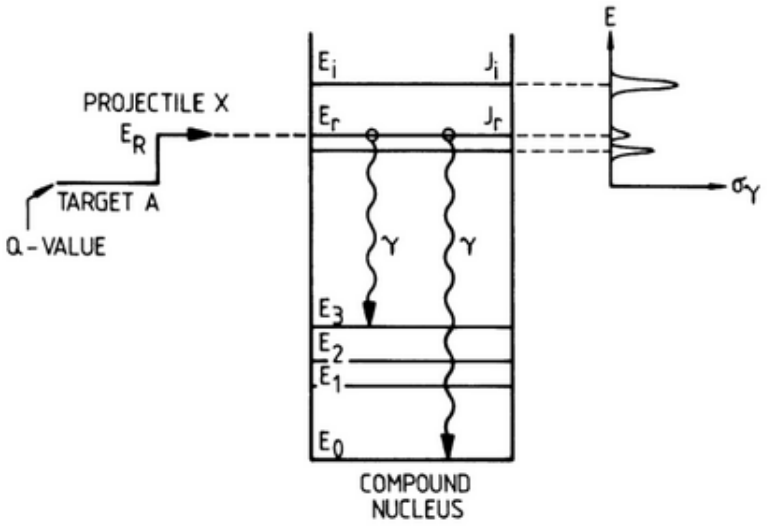

Figure 2.6: Illustrated is a capture reaction A(x, γ)B. The interacting particles A and x in the entrance channel forms an excited state E_r, which decays to lower lying levels through γ emission [17].

where Γ_a is the partial width for the formation of the compound state and Γ_b is the decay with, which can refer to either a particle or a γ-emission, depending on the nuclear reaction mechanism. An isolated resonance can be described by the one-level Breit-Wigner formula [1].

$$\sigma_{BW}(E) = \pi\lambda^2\omega(1+\delta_{12})\frac{\Gamma_a\Gamma_b}{(E-E_R)^2+(\Gamma/2)^2}, \tag{2.55}$$

where Γ is the total energy width given by the sum of the partial widths of all energetically allowed decay channels following Eq. 2.52.

$$\Gamma = \Gamma_a + \Gamma_b + \cdots . \tag{2.56}$$

The geometrical cross section of a nuclear interaction can be expressed by the quantity $\pi\lambda^2$, where λ is the de Broglie wavelength. Thus, the maximum cross section can be expressed as,

$$\sigma_{max} = \pi\lambda^2\omega(1+\delta_{12}). \tag{2.57}$$

where,

$$\omega = \frac{2J+1}{(2J_1+1)(2J_2+1)}, \tag{2.58}$$

In Eq. 2.58, ω is the statistical factor, J is the spin of the compound nucleus, J_1 and J_2 are the spins of the projectile and the target nucleus and δ_{12} is the Kronecker symbol. For an isolated ($\Gamma << E_R$) and narrow resonance (the partial widths are approximately constant over the total resonance width or, Γ less than a few keV [1]), the stellar reaction rate per particle pair can be expressed by using Eq. 2.39,

$$\langle \sigma v \rangle_{01} = \left(\frac{8}{\pi m_{01}} \right)^{1/2} \frac{1}{(kT)^{3/2}} \int_0^\infty E \sigma_{BW}(E) e^{-E/kT} dE, \tag{2.59}$$

where $\sigma_{BW}(E)$ is the Breit-Wigner cross section (Eq. 2.55). As for a narrow resonance, the change in the Maxwell-Boltzmann function, $Ee^{-E/kT}$ can be considered negligible over the resonance region. Therefore, at $E = E_R$,

$$\langle \sigma v \rangle_{01} = \left(\frac{8}{\pi m_{01}} \right)^{1/2} \frac{1}{(kT)^{3/2}} E_R e^{-E_R/kT} \int_0^\infty \sigma_{BW}(E) dE. \tag{2.60}$$

Using Eq. 2.55 and considering negligible energy dependence of the partial and the total widths,

$$\int_0^\infty \sigma_{BW}(E) dE = 2\pi^2 \lambda_R^2 (\omega\gamma), \tag{2.61}$$

where,

$$\gamma = \frac{\Gamma_a \Gamma_b}{\Gamma}. \tag{2.62}$$

The quantity $\omega\gamma$ is commonly termed as the resonance strength and can be deduced from the nuclear properties of a particular resonance. Eq. 2.60 can be expressed in terms of the resonance strength as,

$$\langle \sigma v \rangle_{01} = \left(\frac{2\pi}{m_{01} kT} \right)^{3/2} \hbar^2 (\omega\gamma) E_R e^{-E_R/kT}, \tag{2.63}$$

which is the stellar reaction rate per particle pair for an isolated and narrow resonance. For a nuclear reaction with several narrow resonances, the contributions can be simply summed to estimate the cross section.

Chapter 3

Gas-filled detectors

3.1. Overview

Gas-filled detectors [24] are among the oldest and most extensively used tools for radiation detection. Their operation relies on the effects produced when a charged particle passes through a gaseous medium. The charged particle interactions primarily involve ionisation and excitation of gas molecules along the length of the track in the gaseous detection medium. The electron-ion pairs formed within the gas filling the detector are responsible for producing the electronic output signal from the detector. Gas-filled detectors can be used in either current mode, in which the average rate of ion formation within the detector is measured, or in pulse mode in which each separate radiation quanta of deposited energy gives rise to a distinguishable signal pulse. Pulse mode operation offers significant advantages in sensitivity or the ability to measure the energy of the incident radiation. The majority of gas-filled detectors, based on the principle of sensing the direct ionisation produced by the passage of the ionising radiation are operated in pulse mode. This chapter will detail the basic characteristics, background physics and discuss the important parameters related to gas-filled detectors alongside several examples of the same.

3.2. Regions of operation

Based on the response corresponding to the applied voltage or electric field, gas-filled detectors can be categorised into different types (Fig. 3.1). The electric field inside the detector is responsible for moving the electrons and ions towards the respective collection electrode. At low voltages, the field is inadequate to prevent recombination of the original electron-ion pairs. As the voltage is raised, recombination is suppressed and the region of ion saturation is achieved. This is the normal mode of operation for *ionisation chambers* [26]. With further increase in the voltage, the threshold field at which gas multiplication (section 3.8.1) begins is reached. The collected charge then begins to multiply, and the observed pulse amplitude will increase. Over some region of the electric field, the gas multiplication will be linear, and the collected charge will be proportional to the number of original ion pairs created by the incident radiation. This is the region of true proportionality and represents the mode of operation of conventional *proportional counters*. If the voltage is increased even further, non-linear effects are introduced. The space charge effect

from the slow, positive ions alters the electric field inside the detector giving rise to the *region of limited proportionality*. If the voltage is increased even further, the space charge will dominate reducing the electric field required for gas multiplication. The information of the number of initial ion pairs is lost. This region of operation is called the *Geiger-Mueller region* [27]. For our purpose as discussed in the chapters 5 and 7, we are interested in the region of proportionality. Also, different variants of the proportional counter are discussed in section 3.8.

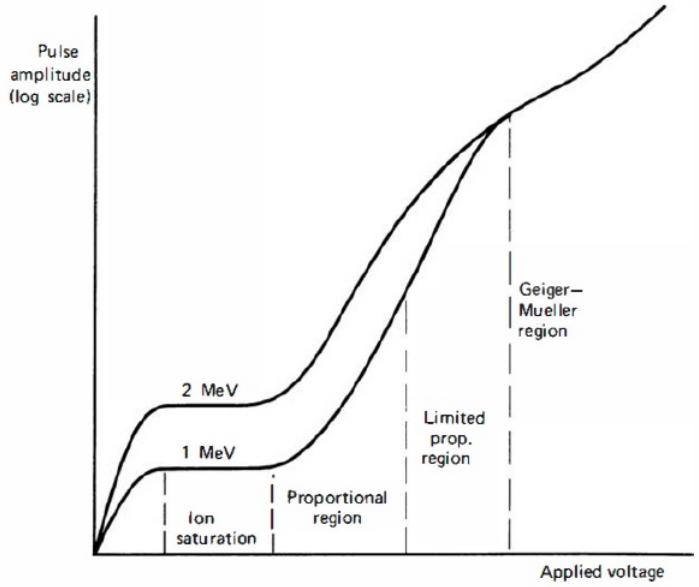

Figure 3.1: The different regions of operation of gas-filled detectors. The observed pulse amplitude is plotted for events depositing two different amounts of energy within the gas [24].

3.3. Diffusion and recombination

Diffusion and recombination of the electron-ion pairs produced by the ionisation process play a pivotal role in determining the performance of the gas-filled detectors. The atoms and the molecules of a gas are always in constant thermal motion. The mean free path ranges between 10^{-6} - 10^{-8}m. The free electrons and positive ions also exhibit this random thermal motion and tend to diffuse away from the regions of high density. This is more severe in case of electrons as they are lighter compared to heavier ions. A point-like collection of free electrons will spread about the original point into a Gaussian spatial distribution whose width will increase with time. If σ is the standard deviation of this distribution as projected onto an arbitrary orthogonal axis, and t be the elapsed time, then it can be shown that [25]:

$$\sigma = \sqrt{Dt}, \tag{3.1}$$

where D is the diffusion coefficient.

Collisions between the free electrons and positive ions can cause them to recombine and return to a charge neutral state. In addition to this a collision between a

negative and positive ion can result in a transfer of electron from the negative to the positive ion. The rate of recombination can be expressed as:

$$\frac{dn^-}{dt} = \frac{dn^+}{dt} = -\alpha\ n^- n^+, \tag{3.2}$$

where n^- and n^+ are the number densities of the negative and positive species. α is the recombination coefficient. It is several orders of magnitude larger between positive and negative ions compared to positive ions and free electrons.

3.4. W-value

In order for ionisaton to take place in a gas the charged particles must transfer a minimum amount of energy to the gas molecule. This minimum energy is termed as the ionisaton energy of the gas. However, all the energy lost by the charged particle in a gas does not contribute solely to the ionisation process. There are other mechanisms through which the charged particle may lose energy, i.e., excitation processes where an electron is elevated to a higher bound state. Thus, the energy lost by the ionising charged particle per ion pair formed is known as the W-value of the gas. The W-value is higher than the ionisation energy of the gas. In table 3.1 W-values and ionisation energies of various gases and gas mixtures are listed. These values are calculated using Garfield [28].

Table 3.1: First ionisation potentials and W-values of various gases and gas mixtures. Gas mixture percentages mentioned are by mass.

Gas	**First ionisation potential (eV)**	**W-value (eV)**
Ar	15.7	26.3
He	24.5	42.7
CO_2	13.7	33.0
CH_4	15.2	28.0
i-C_4H_{10}	10.6	23.0
Air	-	35.1
Ar:CH_4 90:10	-	26.5
He:CO_2 90:10	-	39.2
He:CO_2 97:3	-	40.5

3.5. Energy loss and straggling

While moving through a medium charged particles lose energy via various interactions. The stopping power of a particle in a material depends on the energy of the particle and is defined as $-dE/dx$. The energy loss can be due to the interaction with target electrons (*electronic stopping*) or target nuclei (*nuclear stopping*). The latter becomes important at low energies (< 10 keV), thus can be ignored for typical energy ranges of nuclear physics experiments. If an ion is moving too quickly to pick up electrons from the target and thus change its own effective charge, its stopping power for non-relativistic energies is given by the Bethe formula [29]:

$$-\frac{dE}{dx} = \frac{4\pi e^4 z^2}{m_0 v^2} NB, \tag{3.3}$$

where,

$$B = Z\left[\ln\frac{2m_0v^2}{I} - \ln\left(1-\frac{v^2}{c^2}\right) - \frac{v^2}{c^2}\right], \tag{3.4}$$

where v and ze are the velocity and charge of the ion, N and Z are number density and atomic number of the absorber atoms, m_0 is the electron rest mass, and e is the electronic charge. The parameter I represents the average excitation and ionization potential of the absorber. In the case of a compound material, if the individual stopping powers of the the constituents are known, Bragg's rule [30] states that the stopping power of the compound can be estimated by simple stoichiometric addition of the constituent stopping powers, although the accuracy of that estimate depends on the molecular bonds in the compound. Ziegler and Manoyan [31] investigated this for various compounds leading to the development of SRIM [32]. SRIM has become one of the standard software programs for predicting the interaction of ions with matter.

Measurement of the energy loss of a charged particle over the entire stopping process leads to a specific energy loss curve known as a Bragg curve. An example is shown in Fig. 3.2. Not all electronic energy loss lead to the creation of electron-ion pairs. Some of it can lead to excitation of atoms or molecules. In case the transferred energy is less than the ionisation energy of an atom or molecule, instead of ionizing, the atom or molecule will assume an excited state. Thus, the number of ionisations (N_{ion}) is obtained by dividing the energy by W-value of the gas (discussed in section 3.4), in place of the ionisation energy. W-value is slightly higher compared to the ionisation energy.

$$N_{ion}(E) = \frac{E}{W}, \tag{3.5}$$

where E is the total energy deposited by the charged particle in the gas and W is the W-value of the gas. The energy loss of a monoenergetic charged particle in a particular medium is a statistical process. Therefore the total number of electron-ion pairs created are not always the same. In a simple model, the probability of ionisation occurring can be considered as small and constant, and can be treated as a Poisson process. This variance in the number of ion pairs created places a constraint on the energy resolution achievable with a detector. The Fano factor (F) is used to quantify the departure of the observed statistical fluctuations in the number of ion pairs produced from pure Poisson statistics and is defined as:

$$F = \frac{observed\ variance}{Poisson\ predicted\ variance}. \tag{3.6}$$

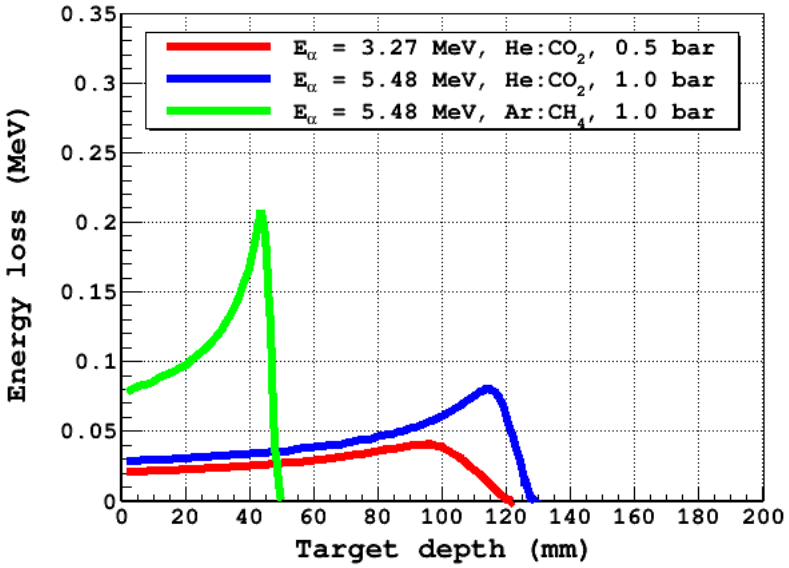

Figure 3.2: Energy loss with target depth or range plot for 3.27 MeV and 5.48 MeV α-particles in He:CO_2 90:10 and Ar:CH_4 90:10 gas mixtures using SRIM [32]. The energy loss or Bragg curves exhibit a plateau region and a maxima known as the Bragg peak, immediately followed by a sharp drop.

The Fano factor is always less than unity in proportional counters. The monoenergetic charged particles exhibit a distribution or a spread in energies while traversing the a medium. This spread of the energy distribution is the measure of energy straggling. The range of a particle in a gaseous medium is dependent on the mass and charge of the particle and composition and pressure of the gas or gas mixture. As an example, the range of an alpha particle in a particular medium can be defined using the curve in Fig. 3.3. The mean range (R_m) is defined as the medium or absorber thickness that reduces the charged particle count to exactly half of its value in the absence of the medium or absorber. The extrapolated range (R_e) is obtained by extrapolating the linear portion of the end of the curve in discussion to zero. Range straggling is defined as the fluctuation in path length for individual mono-energetic particles. The degree of range straggling is determined by the sharpness of the cutoff at the end of energy loss curve in Fig. 3.2.

3.5.1. Angular straggling

The term angular straggling refers to the deviation of the trajectory of a charged particle from its initial direction due to the statistical effects of multiple Coulomb scattering. The exact treatment of multiple scattering requires involved calculations. However, a general estimation formula is given in [33]. The angular distribution of multiple Coulomb scattering has a much wider tail compared to a Gaussian distribution, but a standard deviation σ_θ can be obtained,

$$\Delta\theta = \frac{14.1MeV}{2E/z}\sqrt{\frac{l}{L_R}}\left(1+\frac{1}{9}\log_{10}\left(10\frac{l}{L_R}\right)\right), \tag{3.7}$$

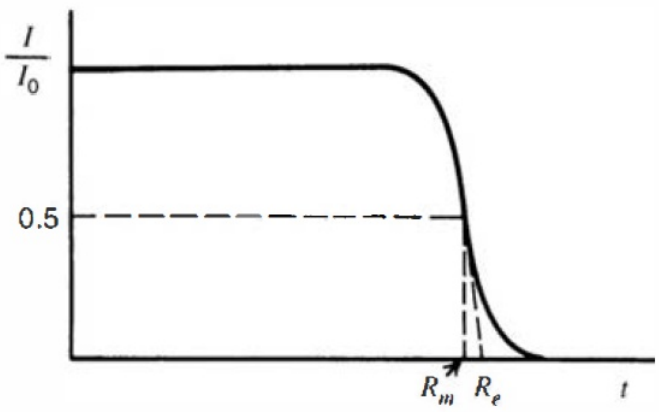

Figure 3.3: An alpha particle transmission experiment. I is the detected number of alpha particles through an absorber thickness t, whereas I_0 is the number detected without the absorber. The mean range R_m and extrapolated range R_e are indicated. [24].

where E is the particle energy, z is the charge state, l is the traversed target distance in g·cm^{-2} and L_R is the radiation length of the target material. The formula was originally developed for high energy particles and thin targets, thus it assumes the projectile energy will remain constant over the entire distance. For thick targets, E decreases leading to a larger $\Delta\theta$ towards the end of the track. Fig. 3.4 shows $\Delta\theta$ for full energy alphas from ^{148}Gd as well as for alphas having experienced full energy loss over the plotted distance.

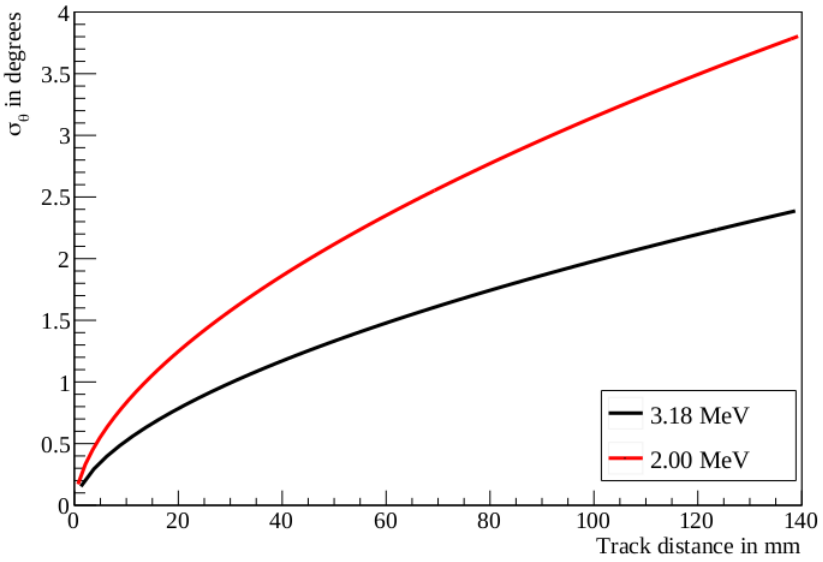

Figure 3.4: Angular straggling according to Eq. 3.7 in He:CO_2 90:10 (P = 200 mbar) for alpha particles at the full energy of 3.18 MeV and at 2 MeV, the approximate remaining energy after 140 mm [7]. Over the plotted range the standard deviation or the angular straggling (σ_θ) increases with track length.

3.6. Photon interactions in matter

The behaviour of electromagnetic radiations or photons (γ-rays, X-rays) in matter are different from that of charged particles due to their lack of an electric charge. A γ-ray gets emitted from the nucleus of a radioactive atom. An X-ray emanates from outside the nucleus of a radioactive atom, or from an electron as it changes direction when passing an atomic nucleus. All are collectively referred to as ionising photons. The main interactions of photons in matter are the photoelectric effect, Compton scattering and pair production. These processes do not result in a gradual degradation of energy as it passes through a matter similar to ions, only the intensity, i.e., the number of photons gets attenuated. This attenuation of a photon beam intensity is exponential to the thickness of the attenuating medium, i.e.,

$$I(x) = I_0 e^{-\mu x}, \tag{3.8}$$

where I_0 is the incident beam intensity, x is the thickness of the attenuating medium and μ is the linear attenuation coefficient. The absorption coefficient is a quantity which is characteristic of the medium and is directly related to the total interaction cross section. The total interaction cross-section, i.e., probability that a photon will undergo an interaction with matter is largely dependent on the atomic number (Z) of the medium or the absorber material and the photon energy.

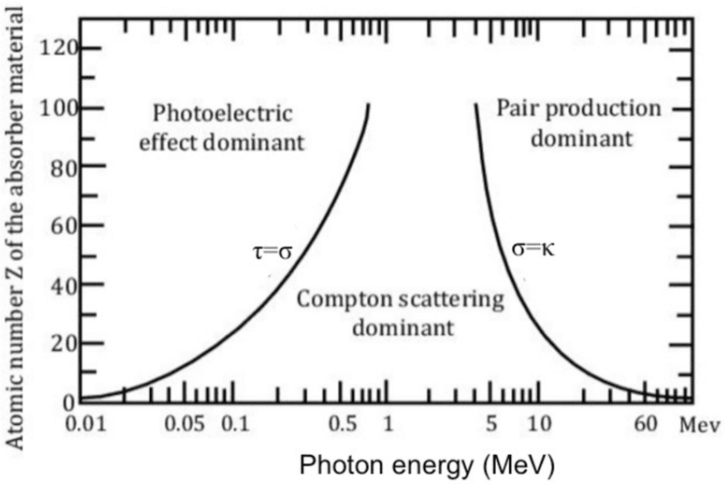

Figure 3.5: Three major types of photon interaction with matter [34]. The curves demarcate the regions where each effect is dominant.

3.6.1. Photoelectric effect

The photoelectric effect occurs predominantly at lower energies (Fig. 3.5) when a photon is absorbed by an inner shell electron causing the electron to gain sufficient energy to be ejected from the atom. After ejection of the inner shell electron, the missing electron must be replaced by an outer shell electron. For this to happen, the outer shell electrons must lose energy by emission of a characteristic X-ray and/or an Auger Electron. For this process to take place, the photon energy must be equal to or higher than the binding energy of the orbital electron. The energy of the outgoing electron is then,

$$E = h\nu - \text{B.E.}, \tag{3.9}$$

where B.E. is the binding energy of the orbital electron and $W = h\nu$ is the photon energy. Since a free electron cannot absorb a photon and also conserve momentum, the photoelectric effect always occurs on bound orbital electrons with the nucleus absorbing the recoil momentum. Fig. 3.6 shows the typical photoabsorption cross section as a function of photon energies. As can be seen, at energies above the highest electron binding energy of the atom (the K- shell), the cross section is small but increases rapidly as the K-shell energy is approached. Right after this point, the cross section drops sharply as the K-shell electrons are not available for the photo-electric effect. This drop is called the K absorption edge. For argon, the K-edge is at 3.2 keV. Similarly L and M absorption edges can be observed for argon. Therefore, the photoelectric effect exhibits a threshold phenomenon in which photons with energy close to the binding energy of an electron greatly increase the probability of interaction ($\propto Z^3/W^3$).

The electrons liberated by the photoelectric effect, i.e., photo-electrons can have different energies depending on the incident photon energy and the shell location. In cases where the energy of a photon is sufficiently high , e.g., $\geq$ 3.2 keV for a K-shell electron in argon, it can liberate an inner shell electron. As a result, the excited atom emits a fluorescence characteristic X-ray photon, which mostly gets reabsorbed instantaneously. The term "characteristic" is used because the photon energy is tied to the quantised energy levels between atomic orbitals causing the X-ray energy spectrum to be unique to a given element. The ionisation caused by the photo-electrons can be detected using proportional counters discussed in secion 3.8. In a detector setup, if the fluorescence photon escapes the absorption or the detector volume, the energy it carries is lost, which often results in an escape peak at a lower energy compared to the main photo-peak in the detected energy spectrum.

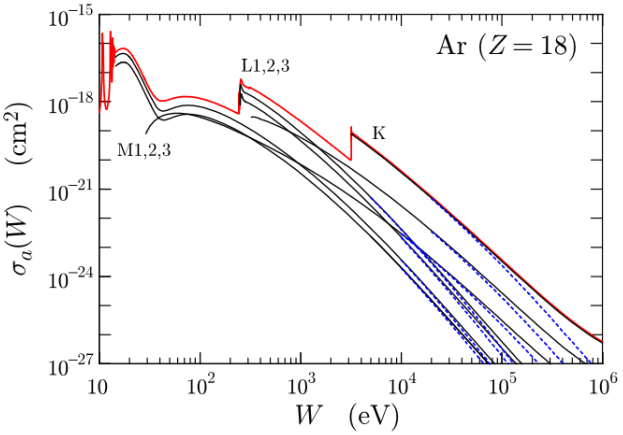

Figure 3.6: The theoretical cross sections for photoabsorption (excitation and ionization) in the sub-shells of argon atoms as functions of the photon energy W (thin solid curves). The thick solid curve (red online) represents the theoretical total atomic cross section. Dashed curves (blue online) are cross sections obtained from the dipole approximation [35].

3.6.2. Compton scattering

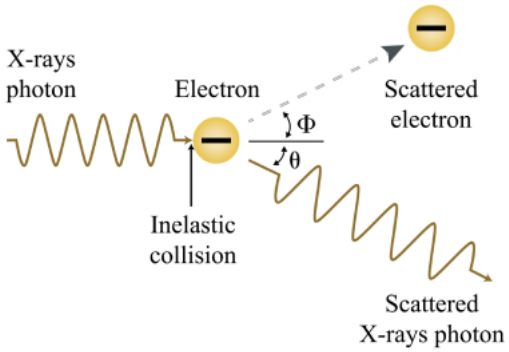

Figure 3.7: Kinematics of Compton scattering.

Compton scattering is an inelastic scattering process in which the photons interact with free electrons. In matter, electrons are bound to the atomic nuclei. If the photon energy is high compared to the binding energy, the latter energy can be ignored and electrons can be essentially considered as free. Because the interaction is inelastic, the photon transfers some of its energy to the electron during the interaction. This causes the electron to be ejected from its orbital. Scattering angle and energy change are governed by conservation of energy and momentum. After scattering, the energy is shared between the electron and the scattered photon. The energy of the scattered photon in terms of scattering angle can be expressed as [24]:

$$h\nu' = \frac{h\nu}{1 + \gamma(1 - \cos\theta)}, \tag{3.10}$$

where $h\nu' = W'$ and $h\nu = W$ are the energies of photon after and before the interaction, θ is the scattering angle of the photon and $\gamma = h\nu/m_e c^2$. Compton scattering involves interaction of a photon with a single electron, therefore electron density is the most important material property for Compton scattering interaction cross section. However, for light elements other than hydrogen, the electron density is roughly constant. Therefore, the probability of Compton scattering is nearly independent of effective atomic number and is proportional to $1/W$.

3.6.3. Pair production

The process of pair production involves the transformation of a photon into an electron-positron pair. This process can only occur in presence of a third body, i.e., an atomic nucleus as it must absorb the recoil energy to conserve momentum. In order to create an electron-positron pair the photon must at least have an energy 1.022 MeV. The probability of the process depends on both atomic number of the absorber material and incident photon energy ($\propto Z \cdot \ln(W)$).

3.7. Signal induction

The drift of electrons in a gas given a constant electric field is a constant of the gas, as the electron acceleration gets balanced by collisions with the gas molecules. The

drift velocity v_D of an electron in a gas with pressure p and with electron mobility μ experiencing a constant electric field E is given by:

$$v_D = \frac{\mu E}{p}. \tag{3.11}$$

For complex geometries the drift velocity $v_D = \frac{dr}{dt}$ is a function of the drift distance. Therefore, the equation 3.11 takes the following form:

$$\frac{dr}{dt} = \frac{\mu E(r)}{p}, \tag{3.12}$$

$$r(t) = \frac{\mu}{p} \int_0^t E(r(t))dt. \tag{3.13}$$

After an ionisation process takes place, the charge carriers generated start to move towards the electrodes and as a result an output pulse begins to form. Once the last charge carrier arrives at the collection electrode, the process of charge induction ends and the output pulse is developed fully. The time evolution of the pulse and the pulse shape is important for understanding the timing characteristics of detectors and predicting the location of radiation interactions inside for tracking. A particle of net charge q drifting in the electric field of an electrode will induce a current I, on the electrode. This instantaneous current is given by the Shockley-Ramo theorem [36]:

$$I = -qW_E v_D, \tag{3.14}$$

where v_D is the drift velocity of in the medium and W_E is the weighting field of the readout electrode defined as [37]:

$$-W_E = \nabla(V_m/V_E), \tag{3.15}$$

where V_m is the potential due to the charge, and V_E is the potential due to the electrode. W_E is the component of the E-field in the direction of v that would exist at the ions instantaneous position in case the ion was removed, the readout electrode was set to unit potential and all other conductors were grounded. It is clear from the definition of the weighting field, that it is possible to isolate the readout electrode from the rest of the detector simply by the adding more electrodes. Such an electrode, known as a Frisch Grid [38], must be transparent for the electrons to drift through.

The case of a planar detector with no boundaries can be considered in pulse mode. The anode is coupled to a RC circuit in an ionisation chamber with Frisch grid. The signal pulse produced from a single event depends on the input characteristics of the circuit to which the detector is connected. Mostly, the time-dependent voltage $V(t)$ across the load resistance, R, is the fundamental signal voltage on which pulse mode operation is based. The time needed for the pulse to reach its maximum value is determined by the charge collection time within the detector. On the other

hand, the decay time of the pulses, or the time required to restore the signal voltage to zero, is determined by the time constant of the load circuit. Furthermore, the maximum signal height can be calculated using [24]:

$$V_{max} = \frac{Q}{C}, \tag{3.16}$$

where $Q = n_0 e$ and C is the capacitance of the RC circuit in use. n_0 is the number of electron-ion pairs produced by ionisation process. For a given induction field there is a minimum rise time for generated pulse which depends on the induction distance. For charged particles entering the ionisation chamber at angles, the rise time of the pulse will tend to this minimum rise time.

3.8. Proportional counters

As discussed in section 3.2, proportional counters utilise the gas multiplication process to amplify the primary ionisation produced by the ionising radiation [39]. This makes them suitable for the detection of low energy depositions in the gas. It is very difficult to detect such low signals with pulse-type ionisation chambers. Proportional counters are usually operated in pulse mode and much higher electric fields compared to the traditional ion chambers. Proportional counters are versatile and can be used to detect different kinds of radiation, e.g., charged particles, X-rays, γ-rays, neutrons.

3.8.1. Gas multiplication

When the electric field inside a gas-filled detector achieves a certain threshold value, secondary ionisation process is triggered. Free electrons have higher mobility compared to the much heavier positive or negative ions. When accelerated by an electric field they are capable of achieving high enough kinetic energy to produce secondary ionisation through collision with neutral gas molecules. The electrons produced in the secondary ionisation process again gets accelerated under the influence of the same electric field resulting in additional ionisation of the gas molecules. The gas multiplication process therefore takes the form of a cascade, known as *Townsend avalanche*. The fractional increase in the number of electrons per unit length can be mathematically expressed by the Townsend equation:

$$\frac{dn}{n} = \alpha \, dx, \tag{3.17}$$

Here α is called the first Townsend coefficient for the gas. Its value is zero for electric field values below the threshold and generally increases with increasing field strength above this minimum. For a spatially constant field (as in parallel plate geometry), α is a constant. The solution of the equation indicates that the increase of the electron density is exponential with distance:

$$n(x) = n(0) \, e^{\alpha x}. \tag{3.18}$$

This increase can be much steeper in cylindrical geometry if the non-uniform electric

field increases in the direction that the avalanche progresses. This phenomenon can be utilised for improvement of the signal to noise ratio in proportional counters. The operation of the proportional counter can be characterised by the average gas amplification factor (M). If the single-electron response of a counter is known, the space charge effects are not large enough to distort the electric field and each avalanche is independent, then M can be defined by the equation 3.19. The single-electron response is expressed as the total charge generated in the gas multiplication process if the avalanche is generated by a single electron from the primary ionisation.

$$Q = n_0 e M, \tag{3.19}$$

where Q is the total charge generated by n_0 original electron-ion pairs. M relies on factors such as gas pressure, applied voltage and electrode configuration specific to a proportional counter. Theoretically, it seems as if M can increase without limit (exponentially). However, physically it is limited to about $M < 10^8$ or $\alpha x < 20$ (defined in the equation 3.18). This threshold is known as the Raether limit [40]. It is dependent on various factors, e.g., gas or gas mixture used, gas pressure, electric field strength. The pulse amplitude from a detector is proportional to Q [24], which is subject to fluctuations even for equal energy depositions by the incident radiation. This is a result of the inherent variations in n_0 and M. Thus, the expected relative variation in Q can be expressed as,

$$\left(\frac{\sigma_Q}{Q}\right)^2 = \left(\frac{\sigma_M}{M}\right)^2 + \left(\frac{\sigma_{n_0}}{n_0}\right)^2. \tag{3.20}$$

The quantity σ_Q can be used to define the energy resolution of a proportional counter and can be further defined as [24],

$$\frac{\sigma_Q}{Q} = \sqrt{\frac{W(F+b)}{E}}, \tag{3.21}$$

where F is the Fano factor (typical value of 0.05-0.20) and b is the parameter from Polya distribution that characterises the avalanche statistics (typical value of 0.4-0.7). For a specific gas mixture, the quantities F, W and b are constants. Thus, the variance in Q or the energy resolution is inversely proportional to the energy deposited by the ionizing radiation, E.

3.8.2. Space charge effect

In proportional counters during the avalanche process positive ions are also created alongside electrons. Due to the presence of the electric field the electrons are collected quickly (usually within a few nanoseconds) on the anode. The much heavier positive ions slowly drift towards the cathode. The space charge represented by these positive ions can, under some circumstances appreciably distort the applied electric field. Depending on the magnitude of the effect, it can reduce the size of the anode output pulse and introduces non-linearity to the proportional counter operation. Also, depending on the detailed track geometry of the original ionising radiation, the amount of space charge effect varies. This has an adverse effect on

the energy resolution of the proportional counter as discussed below:

Self-induced effect: In this case the gas gain is high enough to create a large number of positive ions from a single avalanche that can alter the electric field and hinder the future gas multiplication process. This effect depends on the proportional counter geometry and the magnitude of gas multiplication.

General space charge effect: This is the cumulative effect of positive ions created from multiple avalanche processes. The positive ions cause a change in the electric field affecting further gas multiplication. This effect becomes increasingly severe with the increase in the rate of events inside the counter.

Minimum suitable level of gas multiplication and gas mixtures with high ion drift velocity is used to address the signal reduction and non-linearity in detector response introduced by the space charge effects.

3.8.3. Fill Gases and quenching

The gas multiplication process in proportional counters is heavily dependent on the ionisation electrons. Therefore the fill gas used inside these detectors needs to have a substantially low electron attachment coefficient. Air has a high electron attachment coefficient so an atmospheric leak is detrimental to the operation of such detectors. In order to maintain the purity of the fill gas either a vacuum tight vessel or a continuous flow of gas or a combination of both is often used.

In addition to ionisation, the collision of electrons with neutral gas molecules can result in the excitation of the latter. These molecules in their excited state do not contribute to the avalanche process but they de-excite by emitting a visible or ultraviolet photon. These photons are capable of producing ionisation of the fill gas anywhere inside the detector volume through photoelectric interactions with the loosely bound electron shells or could produce electrons through interactions with the walls and electrode surfaces of the detector. This hinders the operation of a proportional counter by producing spurious signals. Studies show that some poly-atomic gases, such as methane (CH_4), carbon di-oxide (CO_2), when mixed in small amounts with fill gases, suppress the photon-induced effects by absorbing the photons. Most mono-atomic fill gases thus require the use of such a poly-atomic stabilising additive. This component is called the quench gas [41].

Noble gases, such as argon, helium, are preferred as fill gases because of their low electron attachment coefficient. This ensures the minimum loss of primary ionisation electrons in the gas. However, to achieve high gas amplification, low diffusion and to minimise the space charge effect a quench gas is required to be used along with the actual fill gas [42]. P-10, which is a mixture of 90% argon and 10% methane, is one of the most widely used detector gases because of its high stopping power and low electron attachment coefficient. Depending on the application, the choice of the fill gas and the quench gases vary.

3.9. Variants of proportional counter

Proportional counters are favoured across different fields of study for a wide range of applications, e.g., dosimetry of γ-rays and neutrons, heavy charged particle detection, position sensitive fast timing detectors with very large surface area [43]. The following sections detail a few such examples.

3.9.1. Multiwire proportional counter (MWPC)

This variety of proportional counters with a very large surface area are constructed by placing a grid of anode wires between two large flat cathode plates either side of the counter (Fig. 3.8) [44]. Ionisation electrons drift inward under the influence of the electric field and get accelerated toward the nearest anode wire into the surrounding high-field region where avalanches are formed. The multiplied negative charge is collected on the anode wire and the surrounding anodes register small positive responses. Therefore the signals from the preamplifiers connected to each anode wire can be used to localise the event to the nearest wire. The position resolution is dependent on the separation of the anode wires. Independent signals are derived from each anode. Multiwire proportional counters were adopted and successfully used in particle physics experiments and several other fields of application. However the space charge effect affecting the performance of the detectors, insufficient multi-hit position resolution and fast degradation of the anode wires for high ionising fluxes ($\approx 10^4 \text{mm}^{-2}$) [45, 46] necessitated the need for a better alternative.

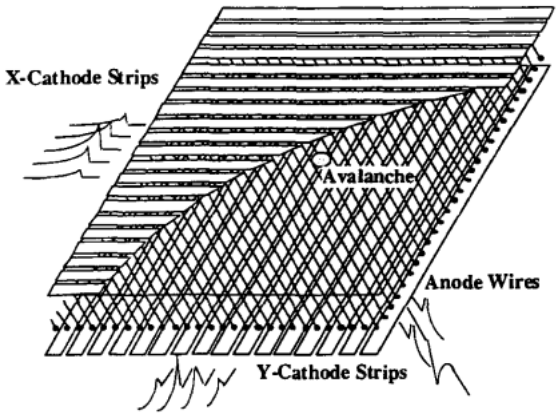

Figure 3.8: Sketch of a two-dimensional position-sensing multiwire proportional counter [24].

3.9.2. Microstrip gas chamber (MSGC)

Microstrip gas chambers [47] are multi-anode gas-filled detectors designed to overcome the shortcomings of multiwire proprtinal counters. They are constructed by etching metal electrodes on a insulating substrate. An example is shown in Fig. 3.9. Instead of anode wires, these detectors use strips as anode structures. The primary ionisation takes place in the fill gas between the drift plane and anode strips. The ionisation electrons drift towards the anode under the influence of the electric field and gas multiplication takes place in the immediate vicinity of the anode strips. The spacing between the anode structures is much narrower (typically 200 μm)

compared to multiwire proportional counters (typically 1-2 mm) providing better position resolution. Another advantage of these detectors is that most positive ions created in the avalanche are collected at the nearby cathodes rather than having to drift from the anode structure to a much distant cathode plane. This significantly reduces the space charge build-up inside the detector improving detector operation especially at higher event rates.

The microstrip gas chamber provides much better two-dimensional position sensing and particle tracking capability compared to the MWPC [47]. Signal is generated on the anode strip close to which the avalanche takes place. The second coordinate is obtained from the backplane, which is the conducting bottom surface of the strips. When an event occurs at the anode, a signal is induced on the backplane. The backplane can be designed as strips running perpendicular to the anode, allowing the second coordinate measurement from the centroid of the induced charges. Despite the advantages, one of the significant drawbacks of these detectors is discharges due to close proximity of the cathode and anode structures. Such discharges leads to irreversible degradation of the detector capabilities [48].

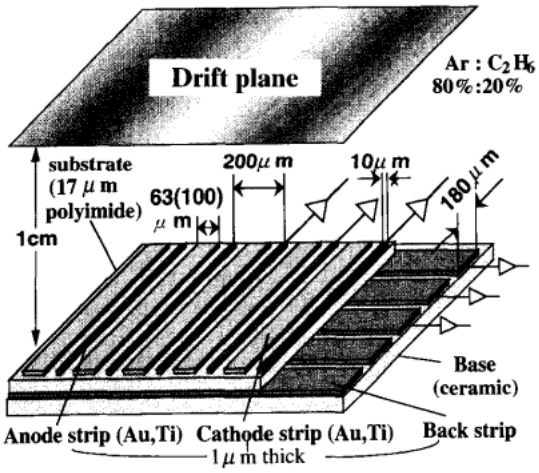

Figure 3.9: Structure of a two-dimensional position-sensing multistrip gas chamber [24].

3.9.3. Micro pattern gaseous detector (MPGD)

The need to overcome the shortcomings of the multiwire proportional counters and multistrip gas chambers resulted in the development of a new breed of detectors collectively known as micro pattern gaseous detectors [49]. Due to their design, these detectors are robust against discharges with high event rate and multi-track capabilities. These properties make them suitable for the use in various fields of study, e.g., nuclear physics, particle physics, dark matter physics along with a wide range of medical and security applications [50, 51]. In this section two different varieties of micro pattern gaseous detectors are discussed, i.e., gas electron multiplier and μ-RWELL.

Gas electron multiplier

Gas electron multiplier (GEM) [52, 53] was an impactful addition to the family of the micro pattern gaseous detectors. The GEM is a versatile amplification element offering fast detection. It is used as the gas multiplication stage at various experimental facilities, e.g., COMPASS [54] and Bordeaux TPC [55]. Although initially designed for high energy particle physics experiments, the high rate capability and the robustness makes it suitable for low-energy nuclear physics.

The GEM is essentially a polymer foil, metal-coated on both sides, containing a high density of holes, approximately 50-100 mm^{-2} (Fig. 3.10). The GEM foils are inserted between the drift and charge collection electrodes. When appropriate potential difference is applied on the faces, GEM develops field lines and equipotentials near the holes (Fig. 3.11). The potential difference applied between the two sides of the GEM, which are separated by a very thin layer of dielectric material (typically tens of micrometers) results in very high fields inside the holes. Electrons are released in the upper region drift towards the holes and acquires sufficient energy to cause ionisation in the gas, eventually resulting an avalanche. A large fraction of electrons produced in the avalanche leave the multiplication region inside the holes and continue on to the collection electrode or a second multiplying region. The negative signal on the anode is generated by the collection of electrons, without any contribution from the positive ions, making the device fast and minimising space charge build-up problems. The low field gap between the multiplying and sensing electrodes reduces the probability of propagation of discharge to the sensitive readout electronics.

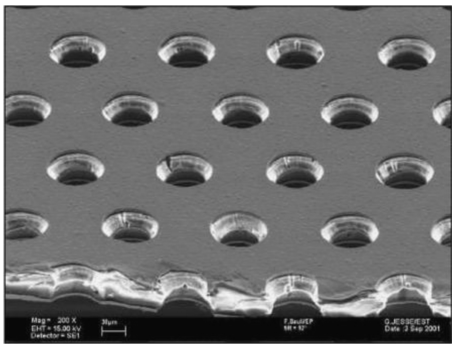

Figure 3.10: An electron microscope picture of a section of typical GEM electrode, 50 µm thick. The holes pitch and diameter are 140 and 70 µm, respectively [52].

The gas gains achievable with the GEM is highly dependent on the voltage applied, i.e., the potential difference between the top and bottom part (Fig. 3.11). An accurate modeling of GEM amplification needs to include charge accumulation on the kapton surfaces in the holes. The electron transparency of the GEM is around 50% and heavily dependent on the drift field [53] and charge-up effect [56, 57]. During the electron multiplication process inside the GEM holes, charged particles can get trapped on the dielectric polymer part of the GEM. Since polymer has a high resistance, charged particles remain there for a longer time and change the electric field locally. This is also known as the "charging-up effect". Many publications claim that the charging-up effect is responsible for a change of the effective gain in the

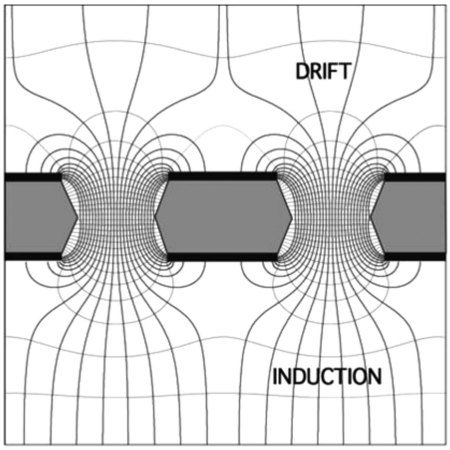

Figure 3.11: Electric field in the region of the holes of a GEM electrode [52].

beginning of a measurement and a steady state is reached after a certain amount of time [56, 57]. This effect is believed to include two sub-processes, i.e., polarisation of the dielectric and accumulation of charges on the dielectric. The charging-up effect is dependent on multiple factors, e.g., rate and duration of radiation, dielectric material [57] and can be unique to a particular MPGD. Detector setups using GEM-like MPGDs are used in a large number of applications. Therefore it is important to quantify the charging-up effect towards achieving a thorough understanding of detector operation and energy calibration.

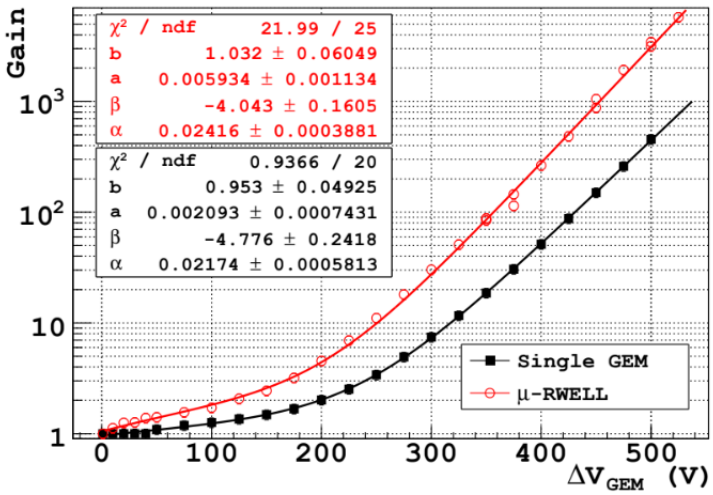

Figure 3.12: Comparison of gas gain as a function of voltage in Ar:CO_2 70:30 mixture for single GEM and μ-RWELL [58].

Micro-resistive WELL

The micro-resistive WELL (μ-RWELL) [58] is a state of the art micro pattern gaseous detector with a single amplification stage. Similar to other MPGDs (GEM, TH-GEM [53] etc.), μ-RWELL can be used as the electron amplification stage in gaseous detectors, which is robust against discharges to achieve high gas gain [58], high rate capability and operational stability [59, 60]. Despite their structural robustness the operating ranges of MPGDs have the tendency to be limited due to

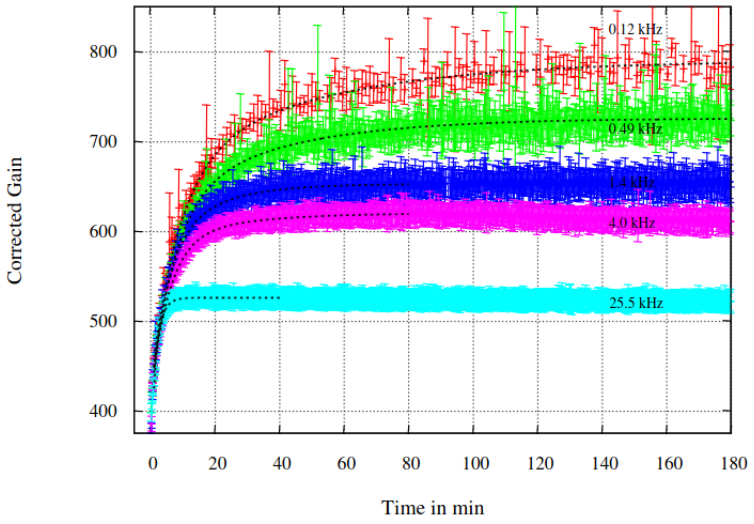

Figure 3.13: Combined effect of dielectric polarization and radiation charging-up effect for different source rates [57].

discharges. Reducing the probability and effect of the discharges is one of the key areas of focus in MPGD development [61]. For μ-RWELL, this issue is dealt with by eliminating the induction gap as the μ-RWELL electrodes are capacitively coupled to the readout plane through a layer of highly resistive material. Another unique advantage of μ-RWELL is its simple assembly and minimum number of components making it very compact.

The μ-RWELL is realised by merging an etched GEM foil with the readout PCB plane coated with a resistive deposition (Fig. 3.14). The copper dots on the bottom side of the foil and copper layer on the top of the WELL structure construct the bottom and top μ-RWELL electrodes, across which a potential difference is applied for the gas multiplication process. The pitch of the WELLs, diameter and thickness of the dielectric kapton determining the depth of the WELLs are typically in the order of tens of micrometers. The ionization electrons produced in the gas, travel towards the μ-RWELL under the influence of the drift field and enter the microscopic holes or WELLs. Inside the holes secondary ionisation is produced via the avalanche process, which is subsequently collected at the resistive layer. The resistive layer is capacitively coupled to the anode pads where the signal is generated. Compared to a conventional single-GEM detector, μ-RWELL exhibit a gas gain at least an order of magnitude higher (Fig. 3.13). Due to the absence of the induction gap, μ-RWELL detectors are robust against discharges providing a very stable operation. The capacitive coupling and absence of the induction gap also ensures that almost 100% of the electrons produced inside the WELLs during the amplification process get collected on the resistive layer through the copper dot, which is a major improvement compared to a typical single-GEM detector, where only 50% of the amplification electrons from the holes are collected on the readout anode contributing to the signal formation [58]. Chapters 5 and 7 detail the performance study of μ-RWELL detectors in planar and cylindrical geometries.

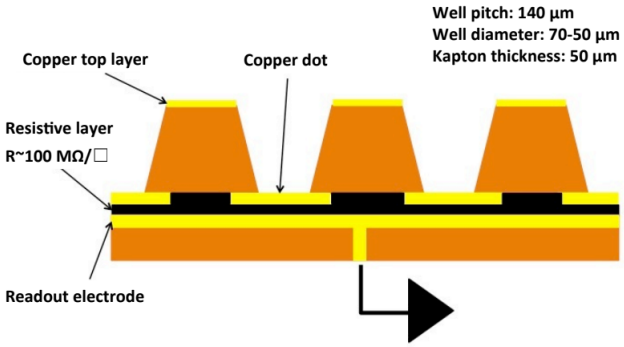

Figure 3.14: Schematic drawing of the μ-RWELL PCB [58].

3.10. Time projection chamber

The concept of the time projection chamber (TPC) was developed at CERN for particle physics research [62]. However, their versatility have made them popular across different fields of study. Fundamentally they are ionisation chambers that can be used for tracking a particle, as it passes through the gas inside the chamber by means of segmented electrodes and electron drift time measurements, allowing the extraction of information about the location of particles in three dimensions at various times, which in turn enables tracking. The initial and final positions of the particle, as well as the trajectory can be determined.

3.10.1. Working principle

The ionisation electrons produced by the passage of a charged particle in the gas, move under the influence of an electric field before they are collected at the anode. As the electrons move, they induce electric signals at the electrodes. Therefore the shape of the signal is highly dependent on the starting position of the electrons. In order to nullify this position dependence of the signal shape, Frisch grid or GEM like electrodes are used. They shield the anode from the induction taking place by the movement of charges in the drift region (Fig. 3.15), limiting the signal induction to the induction region, i.e., region between the grid and anode. As the starting position of all the ionisation electrons is the grid, the variation in signal shape is largely reduced. Time projection chambers usually have multiple planes at the readout with different anode pad or wire orientations, which allow a two-dimensional ion track reconstruction. The third dimension is derived from the drift times of the ionisation electrons, i.e., the drift distance providing a complete three-dimensional reconstruction of an ion track. Examples of few different time projection chambers are described in Section 3.11.1.

3.11. Active target detectors

An active target detector is a novel gas-filled detector concept where the detector gas or the fill gas also serves as the target gas for nuclear interactions. Therefore the detection and the target regions are not physically separated. The working prin-

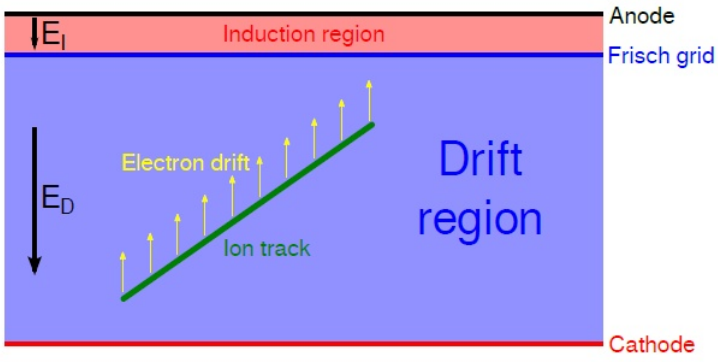

Figure 3.15: Schematic diagram of a basic TPC. Ionisation electrons in drift region move towards the signal anode under the influence of the drift field E_D. In the induction the movement is due to the induction field E_I.

ciple of the active target detector is based on the time projection chamber (TPC) discussed in section 3.10. Such detectors are at present being widely used to study a wide range of nuclear reactions utilising ion beams at multiple accelerator facilities. In order to achieve a better understanding of two-body nuclear reactions, it is important to efficiently detect the reaction products (recoil, ejectile) as they carry significant amounts of reaction information (energy, momentum). In conventional detector setups (solid-state detectors, recoil separators), a significant amount of information carried by the recoil or ejectile is lost in the dead layer or the window separating the target and the detection medium. This makes the measurement of small reaction cross-sections and detection of low energy reaction products challenging. Some experiments address this problem by using higher beam energies. However, using high beam energies can cause several difficulties, e.g., the loss in angular resolution due to the compression of solid angle in the forward direction, opening of additional reaction channels which increase background and most importantly makes it more challenging to measure small cross-sections in the lower energy region of astrophysical interest. Also, the reaction products with low energy makes particle identification by means of differential energy loss difficult in the conventional detector setups.

Ionisation chambers provide a better alternative for identification of particles by means of differential energy loss at low energies compared to a solid-state detector. However, in a traditional setup, the detection volume is usually separated from the target volume by a window. The energy loss in the window is similar to that in the dead layer of a solid-state detector. The best approach is to minimise the amount of material between the target and detection volumes. An extreme application of this concept resulted in development of active target detectors, where there is no physical separation between the target and detection regions. This attribute paired with charged particle tracking capabilities enable active target detectors to make direct measurements of small reaction cross-sections by means of efficient detection reaction products with a wide range of energies, e.g., tens of keV to a few MeV. Another advantage of using active target detectors is that they are basically thick or extended targets, which means that the ion beam loses a significant amount of its kinetic energy while traversing the target region, providing a direct relationship

between the z-position of the reaction vertex and the beam energy in that position. Thus a track reconstruction allows measurement of the reaction at different energies, which is analogous to many thin targets over an extended energy range. Therefore a region of the excitation function for a particular reaction can be measured with a single beam energy.

3.11.1. Examples

MAYA [63], an active target time projection chamber with planar geometry was developed at GANIL, France. The internal design of MAYA (Fig. 3.16) can be divided into three main parts, e.g., an active volume with target gas where the reactions takes place, a detection area where the electrons are amplified and recorded and the ancillary detectors wall placed at the back side for detecting escaping particles.

The active volume is 283 mm long, 258 mm wide and 200 mm high. On the top side there is a stainless steel cathode and on the bottom a Frisch grid separates the active volume from detection area. Below the Frisch grid a plane of proportional wires is used to induce signal on the readout cathode plane beneath. The active volume is surrounded by printed circuit boards, mounted on the front and side panels, with Cu-strips for assuring the homogeneity of the electric field applied between the upper cathode and Frish grid. The readout cathode plane is segmented in 37×35 hexagonal pads with 5 mm sides, from which 32×32 pads are used for charge collection. The signals induced on the cathode pads are collected and delivered to the acquisition system by GASSIPLEX chips. For the three dimensional reconstruction of the track, the $x-$ and $y-$coordinates are extracted from the signal induced in the pads on the cathode plane and $z-$coordinate (perpendicular to the beam direction) is estimated using the electron drift time. From the projection of the beam and the reaction products on the cathode plane, recoil and ejectile angles can be obtained.

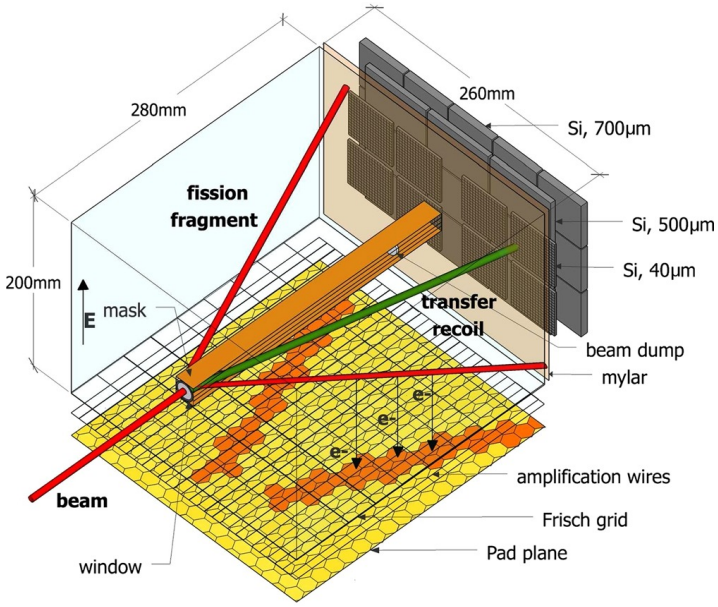

Figure 3.16: Transfer-induced fission event reconstruction inside MAYA [83].

MUSIC is a large area (30 cm×10 cm×20 cm) planar TPC, designed for high-efficiency measurements of fusion reactions utilising radioactive beams. The chamber can be filled with a suitable counting gas, which also acts as the target gas. Depending on the reaction of interest different target gases (CH_4, He, Ne, Ar) can be used. The anode is segmented parallel to the beam direction into 18 strips as shown in the Fig. 3.17, with each strip being 1.58 cm long. The segmentation and the arrangement of the anodes does not provide charged particle tracking capabilities. However, the reactions of interest can be separated from the background elastic and inelastic scattering based on multiplicity [64]. The MUSIC detector uses an extended target, which allows the measurement of the reaction cross-section at different energies utilising a single beam energy. The main disadvantage is the maximum beam intensity the MUSIC detector can tolerate is quite low (≈ 5000 pps) due to the pile-up effects [64]. This constraint affects the small cross-section measurements where much higher beam intensity is desired for better statistics. A wide range of charged particle reactions, e.g., (α, p), (α, n) and fusion reactions can be studied with the MUSIC detector [66].

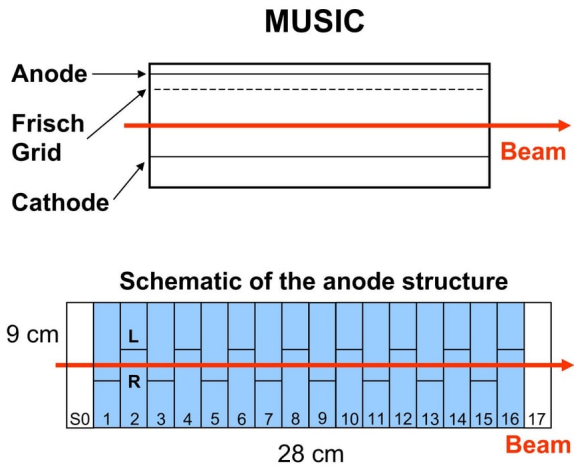

Figure 3.17: Schematic diagram of MUSIC [64].

The Active-Target Time Projection Chamber (AT-TPC) was developed and commissioned at NSCL, MSU [66]. The goal of AT-TPC is to track and identify charged particles to study a variety of charged particle reactions of interest [67]. AT-TPC has a cylindrical geometry with active volume of length 1 m and radius 29.2 cm (Fig. 3.18). The active volume sits inside a concentric shielding. The choice of detector gas depends on the reaction of interest (hydrogen, helium). The detector operates inside a solenoidal magnetic field. The magnetic field is used to bend the trajectories of the charged particles. The bending of the tracks aids in the particle identification by increasing the track length especially for light charged particles, providing more information about their energy. The extended target, near-4π solid angle coverage of the detector are suitable for experiments with low energy and low intensity beams. Micromegas [68] is used as the gas amplification stage in order to efficiently detect light charged particles, e.g., protons. The ionisation electrons migrate towards the anode pads under the influence of the electric field and are amplified by micromegas before getting collected on the anode plane. The anode plane consists of 10240 gold-plated triangular pads. The signal induced in these pads are read out by AGET chips, which are custom ASICs that preamplify and shape the

signals.

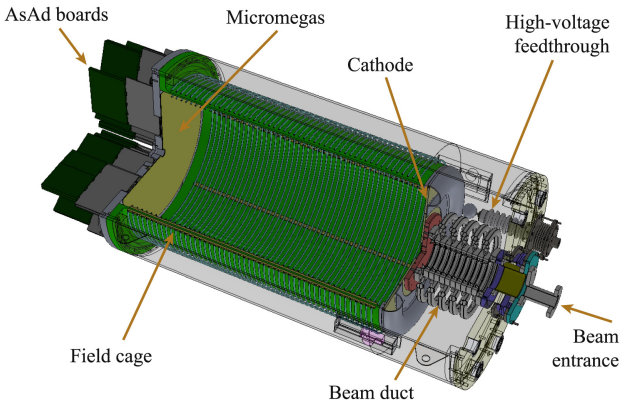

Figure 3.18: Schematic diagram of AT-TPC [66].

Chapter 4

Detector simulation

A new detector simulation framework for TACTIC and the test chamber was developed using the Nuclear Physics Tool (NPTool) [74] by Warren Lynch. The purpose was to achieve a detailed understanding of the capabilities and performance of the detector. The simulation was used to identify the optimum operating condition for detector operation by varying different parameters, e.g., gas composition and pressure, beam energy, etc.

4.1. Overview

NPTool is an open-source data analysis and Monte Carlo simulation framework that has been developed for low-energy nuclear physics experiments with an emphasis on radioactive beam experiments [74]. NPTool development started in 2009 as an analysis tool for the MUST2 charged particle array. Since then, NPTool has been modified and used successfully for the simulation and analysis of experiments at facilities like TRIUMF, GANIL, and RIKEN. The most commonly used simulation toolkit Geant4 [75] was originally designed for high energy particle physics experiments and does not provide a good approximation of the energy loss of heavy ions in matter, especially at low energies. In recent times, with multiple radioactive ion beam facilities coming online and substantial advances in the design of efficient and versatile detector systems, the field of low-energy nuclear physics is thriving. Thus, there is a natural need for a framework adapted to low-energy nuclear physics that will be able to couple both analysis and simulation codes and can support different detector setups. Based on the Geant4 Monte Carlo simulation toolkit and the ROOT [76] data analysis framework and developed in C++, NPTool is tailor-made for this purpose.

4.2. Architecture

The NPTool framework has a layered architecture (Fig. 4.1). The core layer, NPLib defines the necessary tools and features for the framework. Its functions include providing all the generic aspects of the framework and detector libraries required to store data, apply the physics analysis specific to a detector, and generate spectra. The core layer also provides some physics tools, e.g., relativistic kinematics, energy loss calculations etc. The application layer provides the two main NPTool executable files, i.e., *npsimulation* and *npanalysis*. The executable *npsimulation* in

particular depends on the Geant4 toolkit. The NPSimulation directory hence includes all the Geant4-related files required to define the detector geometries and the event generators. The user layer allows the analysis of the Monte Carlo simulation files generated by *npsimulation* or data files from an experiment. The user can choose to use either ROOT macros or build the libNPAnalysis library.

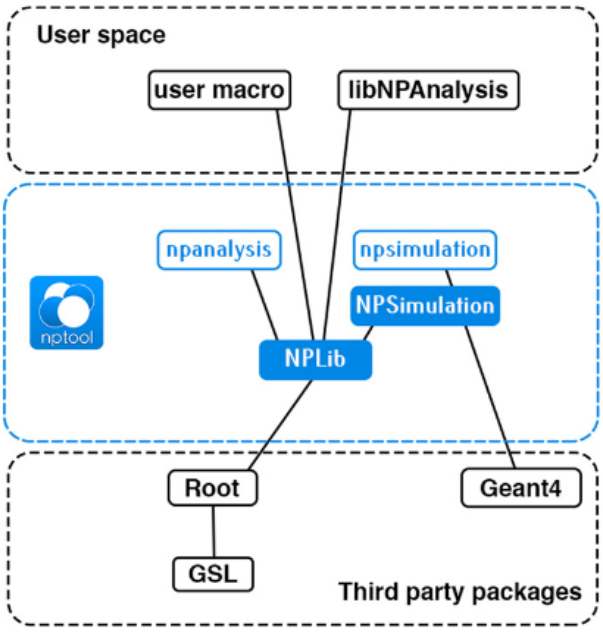

Figure 4.1: Schematic diagram of NPTool framework architecture and dependencies [74].

4.3. Framework details

In the NPTool framework, users are able to generate the primary particles using an event generator. The primary particles propagate through the defined experimental setup and interact with the a target volume, depending on the physics list selected by the user. Based on the selected physical processes, secondary particles are created and tracked.

4.3.1. Physics list

A modular physics list is used in the NPTool framework. The default physics list used is Geant4 standard Electromagnetic (emstandard_opt4), which uses the most accurate low-energy models. This can be replaced by other low-energy electromagnetic models (livermore or penelope) depending on the user preference. The *npsimulation* utility generates an energy loss table depending on the charged particles defined in the event generator and the material defined in the geometry, based on Geant4. This ensures consistency with *npanalysis*.

4.3.2. Event generators

Event generators are used to define different aspects of a particular simulation, e.g., the primary beam particle, two body reactions, particle and γ-ray decays. The event generators can be customised according to the user requirements and easily daisy chained, so the output from one event generator becomes the initial condition for another one. Examples of a few event generators are listed below.

Beam: The Beam event generator fully characterises the beam emittance and energy profile and is required when the primary particle interacts with the target material. The beam emittance and energy profile can be defined in the event generator as a Gaussian analytical model, where the mean and standard deviation of the profile can be passed as arguments, or using distribution files in standard ASCII or ROOT format. The former approach is suitable for the easy simulation of the experimental setup and was used to simulate two-body reactions of interest for TACTIC (Fig. 4.2). The simulation generates a beam energy, a beam direction, and impact position at the entrance of the target volume for every event. The primary beam particle then propagates through the target volume defined by the user and is slowed down using Geant4 energy loss tables to an interaction layer, which is chosen according to a flat distribution within the target thickness. The event generator file shown in Fig. 4.2 defines both beam (^{23}Na) properties and the two-body reaction of interest, ^{23}Na$(\alpha, p)^{26}$Mg simulated using TACTIC geometry. The event generator file allows the user to specify the beam species ($Particle$), beam energy ($Energy$), standard deviation in beam energy ($SigmaEnergy$), beam profile charecteristics ($SigmaX$, $SigmaY$, $SigmaThetaX$, $SigmaPhiY$, $MeanThetaX$, $MeanPhiY$, $MeanX$, $MeanY$). The beam properties can be defined (see Fig. 4.2) and for the simulations discussed in this work, a square monoenergetic beam profile was chosen with no angular deviation at the entrance.

Two-body reactions: The TwoBodyReaction event generator (example in Fig. 4.2) is used to describe the nuclear reactions between the primary beam particle ($Beam$) defined by the Beam event generator and a target nucleus ($Target$) with two nuclei in the exit channel ($Light$, $Heavy$), i.e., reaction products. The nuclei in the exit channel can be produced either in their ground or excited states. The example in Fig. 4.2 shows both reaction products are produced in their ground state ($ExcitationEnergyHeavy = 0.0$, $ExcitationEnergyLight = 0.0$). Any two-body reaction that obeys mass and charge conservation can be simulated. The reaction Q-value is calculated using tabulated masses, and the kinematic calculation is relativistic. Starting with a centre-of-mass angle, the calculation, consistent with laws of momentum and energy conservation, derives the relevant kinematic information (energy and emission angle with respect to the beam direction) of the reaction products. Finally, the emission angles of the reaction products get transformed in the laboratory frame. The reaction mechanism can be defined with a differential cross section file containing reaction cross-sections as a function of the centre of mass angle ($CrossSectionPath$). For TACTIC simulations $flat.txt$ file was used for simplicity, which defines a flat distribution of cross section as a function of centre of mass angle within the entire target thickness. The user can choose to output information on either the light ($ShootLight = 1$, $ShootHeavy = 0$) or the heavy ($ShootLight = 0$, $ShootHeavy = 1$) or both ($ShootLight = 1$, $ShootHeavy = 1$) reaction products.

```
%%%%%%%%%%  Reaction file for 23Na(alpha,p)26Mg reaction  %%%%%%%%%%

Beam
   Particle= 23Na
   Energy= 35 MeV
   SigmaEnergy= 0 MeV
   SigmaX= 1 mm
   SigmaY= 1 mm
   SigmaThetaX= 0 deg
   SigmaPhiY= 0 deg
   MeanThetaX= 0 deg
   MeanPhiY= 0 deg
   MeanX= 0 mm
   MeanY= 0 mm

TwoBodyReaction
   Beam= 23Na
   Target= 4He
   Light= 4He
   Heavy= 26Mg
   ExcitationEnergyHeavy= 0.0
   ExcitationEnergyLight= 0.0
   CrossSectionPath= flat.txt CS
   ShootLight= 1
   ShootHeavy= 1
```

Figure 4.2: Example of beam and two-body reaction event generator file for TACTIC.

4.3.3. Geometry

The detector geometry for a specific experiment is defined in the Geant4 files under the *npsimulation* utility, i.e., NPSimulation directory of the distribution. While running the simulation, a particular detector geometry can be called, and the desired target composition (gas mixture in case of TACTIC and the test chamber) can be selected by using the geometry file shown in the example (Fig. 4.3). TACTIC simulation was designed to be used for both TACTIC and the test chamber. In order to select the desired Geant4 detector geometry for a particular simulation, *Shape* needs to be defined in the geometry file, i.e., *Cylindrical* for TACTIC and *Long_Chamber* for the test chamber. The detailed Geant4 geometries of TACTIC and the test chamber is illustrated in Fig. 4.4 and 4.5. The gas mixture composition, ratio of the components, gas pressure and temperature needs to be defined through *GasMaterial_n* (n=1,2,...), *GasFraction_n* (n=1,2,...), *Pressure* and *Temperature* respectively. In the example shown in Fig. 4.3, a mixture of He:CO_2 90:10 at 1 bar pressure and room temperature was selected. The geometry file also allows the user to select the primary particle interaction volume (either the detector gas volume or the entrance window) for the simulation of ion beam experiments in TACTIC via the *Active* option. Furthermore, the values of the coefficients of the polynomial ($p0$, $p1$, $p2$ and $p3$) can be obtained from Garfield [28] and specified in order to output the arrival times of the electrons in the simulation output file. This is required to simulate the trigger time of an event and the rise time of a signal. The coefficients depend on the specific gas mixture compositions, and the ratio of the components as well as the gas pressure.

```
TACTIC
 POS= 0 0 0 mm
 Shape= Cylindrical
% Shape = Long_Chamber
% GasMaterial_1 = P10_gas
 GasMaterial_1 = G4_He
% GasMaterial_1 = G4_Ar
 GasMaterial_2 = G4_CARBON_DIOXIDE
% GasMaterial_2 = G4_METHANE
 GasFraction_1 = 90
 GasFraction_2 = 10
 Temperature = 293.15 kelvin
 Pressure = 1.0 bar
 %Pressure = 0.8 bar
 Active = gas
 %Active = windows
  p0 = 0
  p1 = 0
  p2 = 0
  p3 = 0
```

Figure 4.3: Example of geometry file for TACTIC and the test chamber.

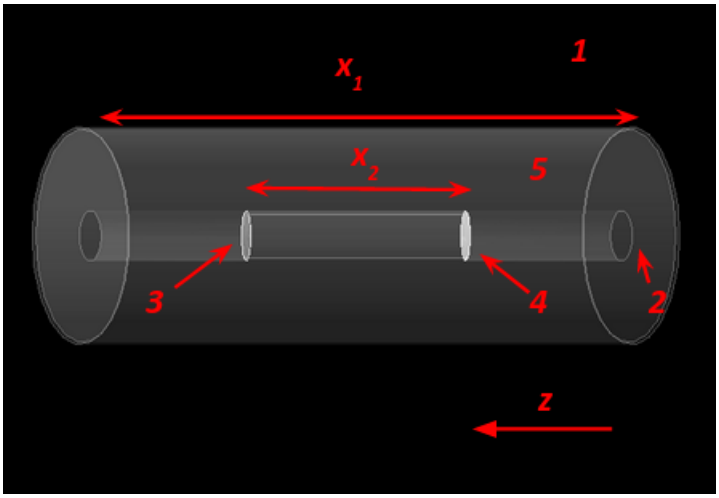

Figure 4.4: Geant4 geometry of TACTIC. 1: vacuum region, 2: hole with circular cross section in the cylinder between window and vacuum region (radius = 12 mm), 3 and 4: exit and entrance windows (radius = 12 mm, thickness = 2.5 μm, 5: gas filled copper cylinder (r = 50 mm), x_1: length of the detection region (251.9 mm), x_2: length of the target region (adjustable by changing window positions).

4.4. TACTIC simulation process: Stepping and scoring

Each simulated event in TACTIC and the test chamber corresponds to a charged particle track from a nuclear reaction or radioactive decay. A simulated track progresses along its trajectory in 0.1 mm steps. The current status of the track is accessed after each step, and information such as the track position, track length, energy loss, across the step is processed by a script called *TACTICScorer.cc*. The

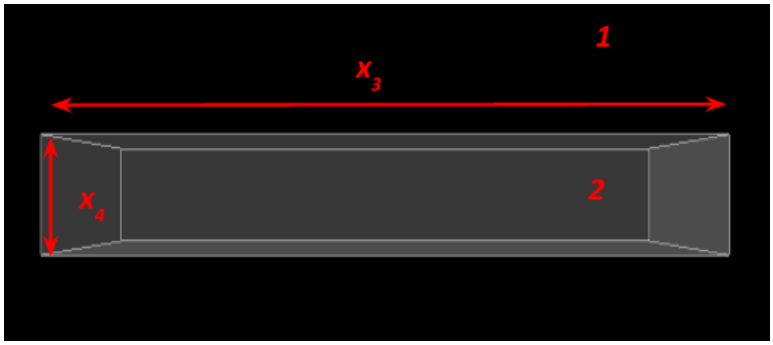

Figure 4.5: Geant4 geometry of the test chamber. 1: vacuum region, 2: gas filled rectangular chamber, x_3: length of the detection region (251.9 mm), x_4: separation between cathode and μ-RWELL, i.e., drift gap (30 mm).

script splits the outer copper cylinder of TACTIC (top part of the rectangular chamber for the test chamber) into 60 horizontal segments to simulate the anode pads. However, for simplicity, only one sector containing 60 anode pads is simulated (utilising the cylindrical symmetry of TACTIC). The script calculates a pad number using the current track position and records the track information for that pad. For example, for each step that occurs across a certain pad number, the scorer accumulates the energy loss (to ionisation) across that pad. For information such as track length, z-position and radius (r), the latest information (from the final step across the pad) is recorded. The scorer also records information such as the vertex position and angle. As this stays the same regardless of the track position, it is simply repeated for each pad. Fig. 4.6 shows an example of an output file created by the stepping action and scorer script for a single alpha event inside TACTIC.

Event No	Track No	Particle ID	time (s)	E_kin (MeV)	E_depo_Ionize (MeV)	Pad	z (mm)	R (mm)	vertex pos (mm)	vertex E_kin (MeV)	vertex theta (deg)	track length (mm)
0	1	3	0.305212	5.0342	0.207046	31	4.16438	2.3869	0	5.23958	29.5983	4.9
0	1	3	0.616819	4.82554	0.210348	32	8.31122	4.80397	0	5.23958	29.5983	9.7
0	1	3	0.941353	4.63539	0.191027	33	12.5889	7.19216	0	5.23958	29.5983	14.6
0	1	3	1.2593	4.43342	0.201055	34	16.7194	9.4338	0	5.23958	29.5983	19.3
0	1	3	1.59139	4.24321	0.189972	35	20.9355	11.7279	0	5.23958	29.5983	24.1
0	1	3	1.93154	4.01988	0.222536	36	25.1458	14.0329	0	5.23958	29.5983	28.9
0	1	3	2.28091	3.79786	0.225245	37	29.3363	16.3737	0	5.23958	29.5983	33.7
0	1	3	2.64834	3.5779	0.215985	38	33.5602	18.8568	0	5.23958	29.5983	38.6
0	1	3	3.02803	3.33776	0.242962	39	37.7594	21.3817	0	5.23958	29.5983	43.5
0	1	3	3.42167	3.08668	0.248003	40	41.9519	23.9179	0	5.23958	29.5983	48.4
0	1	3	3.83197	2.83486	0.253229	41	46.1534	26.4389	0	5.23958	29.5983	53.3
0	1	3	4.2614	2.56155	0.277955	42	50.3724	28.9294	0	5.23958	29.5983	58.2
0	1	3	4.71577	2.27519	0.285151	43	54.5755	31.4457	0	5.23958	29.5983	63.1
0	1	3	5.20127	1.95812	0.314492	44	58.7708	33.9732	0	5.23958	29.5983	68
0	1	3	5.73042	1.60607	0.352254	45	62.9641	36.507	0	5.23958	29.5983	72.9
0	1	3	6.32527	1.2085	0.399515	46	67.1358	39.0764	0	5.23958	29.5983	77.8
0	1	3	7.02671	0.746351	0.459585	47	71.2863	41.4828	0	5.23958	29.5983	82.6
0	1	3	8.03157	0.297165	0.449726	48	75.4938	43.9804	0	5.23958	29.5983	87.5
0	1	3	13.0984	0.00309855	0.279314	49	79.423	48.3435	0	5.23958	29.5983	94.8

Figure 4.6: Example of an output file (out.dat) generated by the *npsimulation* utility.

Chapter 5

Test chamber

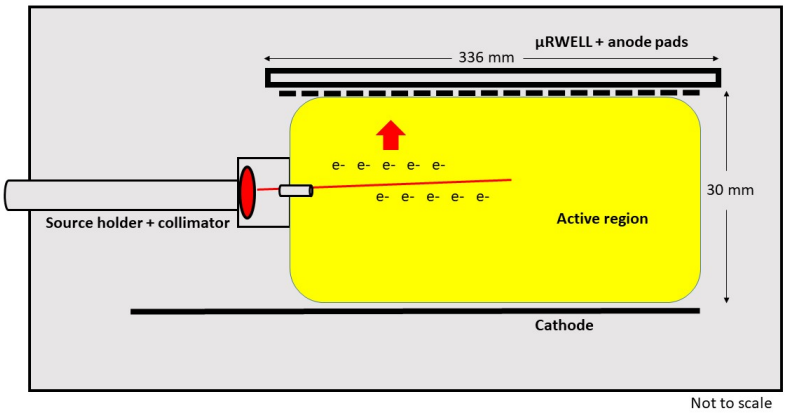

Figure 5.1: Schematic diagram of the test chamber.

The test chamber was built at the University of York as a planar analogue of TACTIC [69]. It can be used to study different micro pattern gaseous detectors, e.g., GEM, μ-RWELL and signal processing electronics, enabling alterations to be made without the need to reconfigure TACTIC, a time consuming and delicate procedure due to the relative complexity of the TACTIC design. The μ-RWELL (discussed in section 3.9.3) was installed as the gas multiplication stage inside TACTIC following successful studies in the test chamber configuration (Fig. 5.1). The focus of these studies was to quantify the gas gains and energy resolutions achievable with the μ-RWELL configuration in different gas mixtures, e.g., Ar:CH_4, He:CO_2. The ranges of alpha particles in the aforementioned gas mixtures, gas gain dependence on pressure and the charging-up effect was also studied. One of the primary objectives was to characterise the μ-RWELL in helium (^{4}He) based gas mixtures, as helium is one of the most common target gases used for nuclear astrophysics to study alpha-induced reactions [22, 23]. This chapter details the test chamber configuration and the test results.

5.1. Experimental arrangement

The electrode separations inside the test chamber were chosen to mimic the TACTIC electrode configuration. The test chamber electrode arrangement included a metal cathode and the μ-RWELL detector with a separation of 3 cm, which constitutes both the drift and the detection region (Fig. 5.1). The μ-RWELL structure included 60 segmented anode pads on the readout PCB plane and had an active area of 35.0 $\times$ 251.9 mm^2 (Fig. 5.2). The induction gap is absent and the resistive layer (sheet resistance $\approx$ 25 M$\Omega/\square$) protects the detector from discharges. The anode pad dimensions were 4.1 mm $\times$ 34.7 mm with pitch 0.1 mm. The electrode arrangement was placed inside a rectangular stainless steel housing. Based on the requirement, the chamber can be operated with a static fill or a constant flow of gas. The gas flow and in-situ gas mixing were controlled with MKS 647C MGC (Multi Gas Controller) and 1179A mass-flo Controller modules [70, 71]. The pressure, temperature and humidity were monitored during tests to maintain desired operating conditions. For this purpose, a diagnostics box was used (Fig. 5.3). The gas mixture in use flows through the diagnostics box, which houses the humidity and the temperature sensors before entering the test chamber. Electrodes were biased using a mesytec MHV-4 programmable power supply [72]. Customised charge-sensitive preamplifiers (gain $\approx$ 2.3 mV/fC) were used to amplify the anode pad signals (discussed in Section 6.2.3), which were fed to a 64-channel CAEN V1740 digitiser [14].

Figure 5.2: The μ-RWELL detector used for the test chamber studies with visible active area.

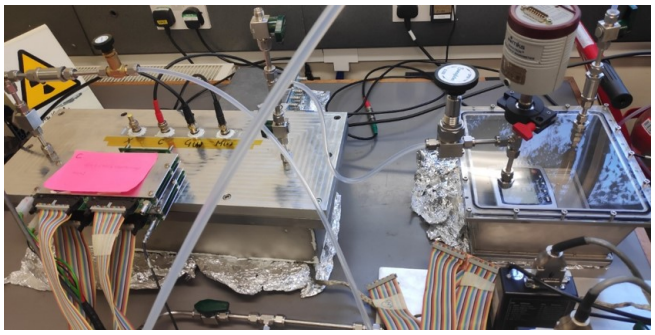

Figure 5.3: The test chamber (**left**) and the diagnostics box (**right**) setup in the lab.

The gas gains and resolutions achievable in Ar:CH_4 and He:CO_2 gas mixtures were studied by irradiating the detector with a collimated 3α source (activity $\approx$ 6.0 kBq). Similar studies were also performed by using ^{55}Fe X-ray source (activity

≈ 0.4 MBq). During the application of bias to the electrodes, current drawn by the μ-RWELL was constantly monitored. It was mostly stable (< 2 nA), with occasional sparks of amplitude ≈ 50-100 nA, especially near the upper limits of μ-RWELL operation. The drift fields (V_d) used for these tests were gas dependent and chosen to maximise the collection efficiency of the primary electrons into the WELLs (holes). Although the optimum drift field recommended in ref [58] for Ar-based mixtures is ≈ 3 kV/cm, the maximum drift field achievable in this work was limited to 450 V/cm by the experimental setup used. The primary limitation in achieving higher drift fields arose from the maximum applicable cathode voltage ≈ -1.8 kV, which was observed to be independent of gas mixture used. A constant cathode discharge was observed above this limit.

5.2. Calibration

Two 32-channel customised charge-sensitive preamplifiers were used to extract signal from the 60 anode pads. The preamplifiers used for this purpose are discussed in detail under section 6.2.3. The pulser walk-through method was used for the calibration of the signal processing electronics, i.e., application of known voltage signals from a pulser to the preamplifier channels through corresponding test input capacitances (≈ 1.6 pF). The application of a voltage signal through a capacitor produces a known charge on the input of the preamplifier channel following Eq. 3.16 and a subsequent response at the corresponding digitiser output channel. Fig. 5.4 shows the pulse height (PH) of signals recorded with the digitiser from multiple pulser inputs for a specific preamplifier channel (channel 0). Each pulse height peak corresponds to a specific voltage input.

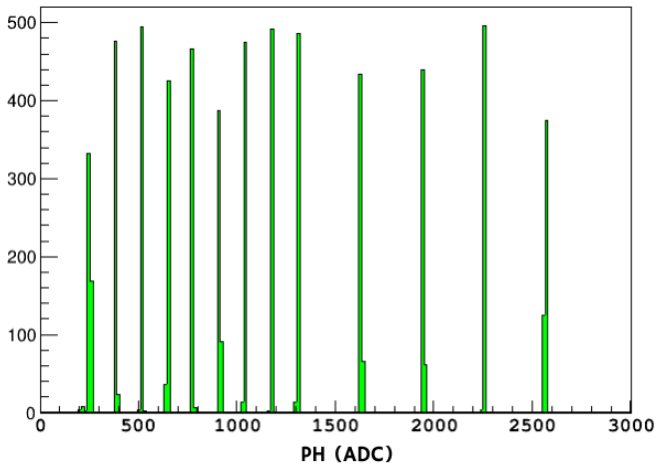

Figure 5.4: Pulse height (ADC) recorded with the digitiser for different voltage inputs. Each peak corresponds to a specific pulser input.

The calibration plots were produced for the individual channels by plotting ADC responses against corresponding voltage input and fitting the data points. Fig. 5.5 shows the calibration plot for channel 0 which corresponds to the first anode pad. The ADC offset and slope (gain) were then calculated from the intercept and gradient of the fit. The fit values were used to perform an offset calibration (Eq.

5.1) or a conversion of ADC channel to energy (Eq. 5.3). Eq. 5.2 and 5.3 were derived by rearranging and modifying Eq. 3.16, where voltage (V) was replaced by the equivalent ADC channel from the liner fit from the calibration plot for the corresponding preamplifier channel.

$$y' = y - p_0, \tag{5.1}$$

$$\frac{Q}{e} = \frac{VC_{test}}{e} = \frac{(y - p_0)}{p_1}\frac{C_{test}}{e}, \tag{5.2}$$

$$E_f = \frac{QW}{e} = \frac{(y - p_0)}{p_1}\frac{C_{test}W}{e}, \tag{5.3}$$

where E_f is the energy equivalent of the total charge in eV after the gas amplification stage, y and y' are the raw and adjusted ADC values respectively, p_0 and p_1 are the offset and slope respectively from the calibration plot, C_{test} is the test input capacitance, W is the work function of the gas in eV and e is the electron charge. Fig. 5.6 shows the variation in the fit parameters p_0 and p_1 across all 64 preamplifier channels for a specific calibration data set. The systematic and alternating nature of the variation is believed to be a result of the relative differences in the test input circuit components and their tolerances. Therefore, the calculation of E_f (Eq. 5.3) using the test input method was used conservatively and solely as an approximation to estimate the gas gains in Section 5.3.3. Channel 52 was found to be anomalous with a large negative offset (p_0 = -641.12) and was not used. A possible reason for this can be a relatively higher electronic noise level arising from the test input circuit components specific to this channel. It must be noted that the pulser calibration is not a true energy calibration, for which a monoenergetic calibration source can be used in the future. However, the pulser calibration can be used reliably to find the ADC offset for each preamplifier channel, and the offset calibration was applied to all experimental data presented in this thesis unless stated otherwise.

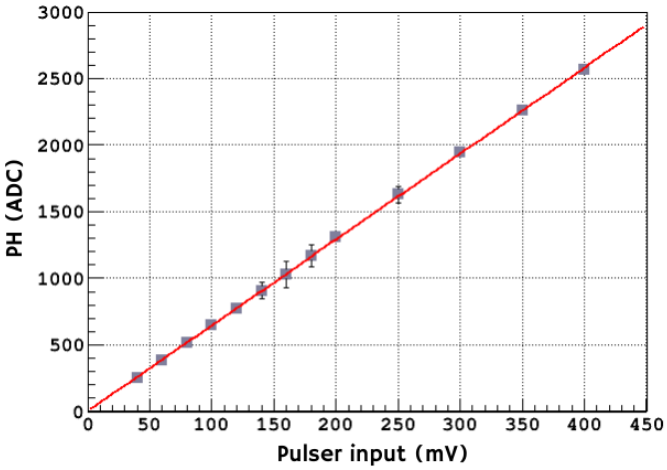

Figure 5.5: Pulser calibration plot, i.e., pulse height (ADC) versus pulser voltage input (mV), with a first order polynomial fit for a single preamplifier channel (channel 0). Fit parameters: $p_0 = 5.71$, $p_1 = 6.45$.

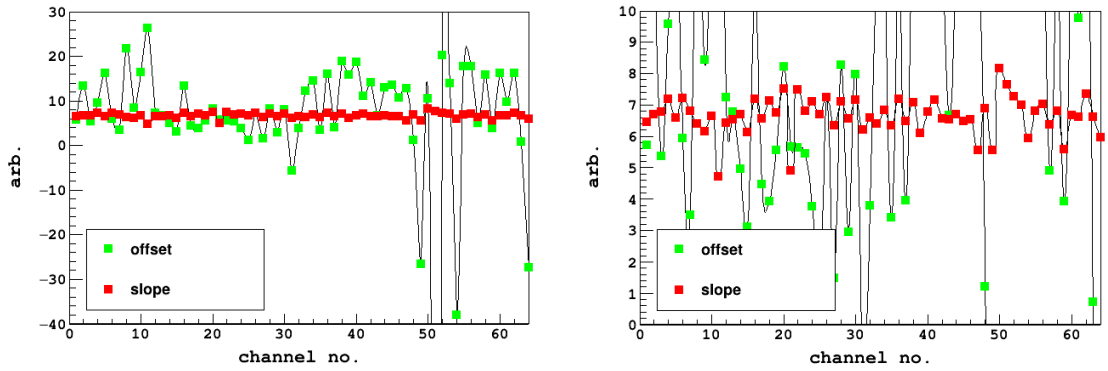

Figure 5.6: The fit parameters p_0 (offset) and p_1 (slope) corresponding to 64 preamplifier channels. The right hand plot was made by adjusting the vertical axis range to highlight the slope (p_1) variation.

5.3. Results

5.3.1. Alpha source studies

In order to study the response of the anode pads, the detector was irradiated with a collimated 3α source. It emits alpha particles at three different energies, 5.155 MeV (^{239}Pu), 5.486 MeV (^{241}Am) and 5.805 MeV (^{244}Cm). The source was positioned against the back wall of the collimator arrangement (Fig. 5.1) approximately 2.8 cm away the collimator opening and the first anode pad. A constant flow of gas mixture Ar:CH_4 90:10 at a pressure 200 mbar was used. The SRIM [32] predicted range for the highest energy alpha particle (E = 5.805 MeV) in the said mixture was calculated to be 255 $\pm$ 3 mm equivalent to 62 anode pads. Fig. 5.7 shows the pulse heights across 60 anode pads triggering above a set threshold. The maximum range obtained from the data ($\approx$ 56 anode pads). The discrepancy between the observed and the calculated ranges can be attributed to the positioning of the source, which resulted in the loss of a part of the track from detection (Fig. 5.1). Fig. 5.7 also shows some unresponsive channels. The unresponsive channels corresponding to pads 31-34 did not have a physical anode pad connection. This is due to four extra preamplifier channels (two on each preamplifier) that were not used. However, a few channels in use were also found to be unresponsive. This was investigated by switching preamplifier positions and DAQ connections. Neither was effective in addressing the unresponsive channels. Thus it is believed, there might be an issue with the anode pad connections, which is intrinsic to the specific μ-RWELL used for the tests and the way the pads were coupled to the readout, which needs to investigated further in the future. Hence, to avoid additional uncertainties arising from using the unresponsive pads, the studies were restricted to a maximum pad number 37 and planned accordingly.

The energy resolution was estimated using the 3α source. The source was collimated to restrict the forward emission angle of the alpha particles to a minimum value ($<$ 6 degrees). This ensured that most of the alpha particle tracks are parallel to the cathode and the anode plane. The energy resolution was studied in two different gas mixtures, i.e., Ar:CH_4 90:10 and He:CO_2 90:10. The parameters used for these tests are listed in table 5.1.

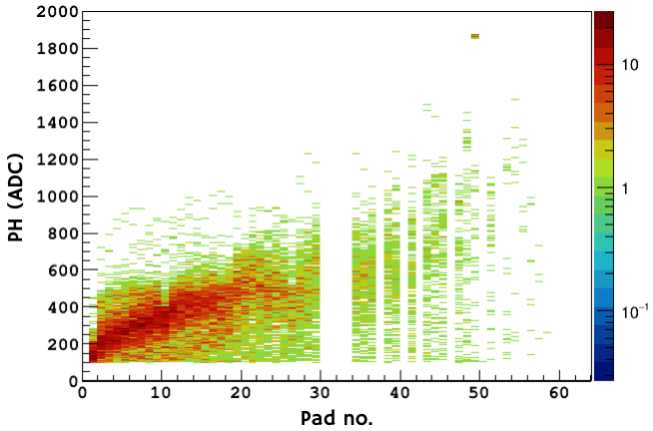

Figure 5.7: Pulse heights across 60 anode pads in Ar:CH_4 90:10 gas mixture (pressure = 200 mbar) after the application of offset calibration to the raw data. The range of the alpha particles agree well with SRIM predicted range. Several unresponsive anode pads were also identified (pad no. 38, 41, 43, 47, 51 and 53).

Table 5.1: List of test parameters in different gas mixtures. The gas pressures used were chosen in order to restrict the range of the alpha particle tracks based on the aforementioned anode pad response study. Furthermore, the maximum applicable μ-RWELL bias was limited by signal saturation at the data acquisition system. The signals show an exponential growth with increasing μ-RWELL bias (discussed in section 5.3.3).

Parameters	**Ar:CH_4 90:10**	**He:CO_2 90:10**
Pressure	0.5 bar	1 bar
Drift field (V_d)	-130 V/cm	-166 V/cm
μ-RWELL bias (ΔV)	-310 V	-450 V

Fig. 5.8 shows the pulse heights across the triggered anode pads for the two different gas mixtures. The ADC thresholds used affect the initial pad triggers. Therefore no signals were observed on the initial pads for both Ar:CH_4 and He:CO_2 gas mixtures. The amplitude traces indicate that the detected ranges (R_d) of the highest energy alpha particles are 19 pads ($\approx$ 8 cm) in Ar:CH_4 90:10 (pressure = 500 mbar) and 23 pads ($\approx$ 10 cm) in He:CO_2 90:10 (pressure = 1 bar). The SRIM predicted ranges (R_{SRIM}) of 5.805 MeV alpha particles are is shown in Fig. 5.9. Due to the position of the source, $\approx$ 2.8 cm of the alpha tracks were outside detection region, which is equivalent to $\approx$ 7 anode pads. The adjusted (R_a) and predicted ranges agree well if the source position is taken into account (table 5.2).

Table 5.2: Range comparison of 5.805 MeV alpha particles. R_{SRIM}, R_d and R_a are the SRIM predicted, detected and adjusted ranges respectively.

Gas mixture	**R_{SRIM}**	**R_d**	**$R_a = R_d$+7**
Ar:CH_4 90:10	25 pads	19 pads	26 pads
He:CO_2 90:10	32 pads	23 pads	30 pads

As discussed in Section 5.2, an equivalence can be drawn between the pulse height and energy. The summed pulse height (PH_{sum}), i.e. the sum of the pulse heights (PH) from all triggered pads in an event or a track was considered to be analogous to the total deposited energy in the detection medium. Fig. 5.10 shows that the shorter tracks with multiplicity, i.e., the number of anode pads triggering in an event over a set energy threshold lower than 12 deposit considerably less energy in the detection volume. These alpha particle tracks are believed to be terminating at the side walls of the detector without depositing the full energy in the detection volume. Therefore in order to estimate the energy resolution, an event selection criteria of a minimum multiplicity of 12 was used for Ar:CH_4 and He:CO_2 gas configurations respectively to eliminate short tracks. By applying Gaussian fits to the 5.155 MeV ^{239}Pu peak in the energy spectrum for each gas configuration, resolutions 4.4% (FWHM) and 7.8% (FWHM) were calculated for the respective gas configurations (Fig. 5.11). The spectra were obtained by applying an offset calibration (discussed in section 5.2) to the raw data.

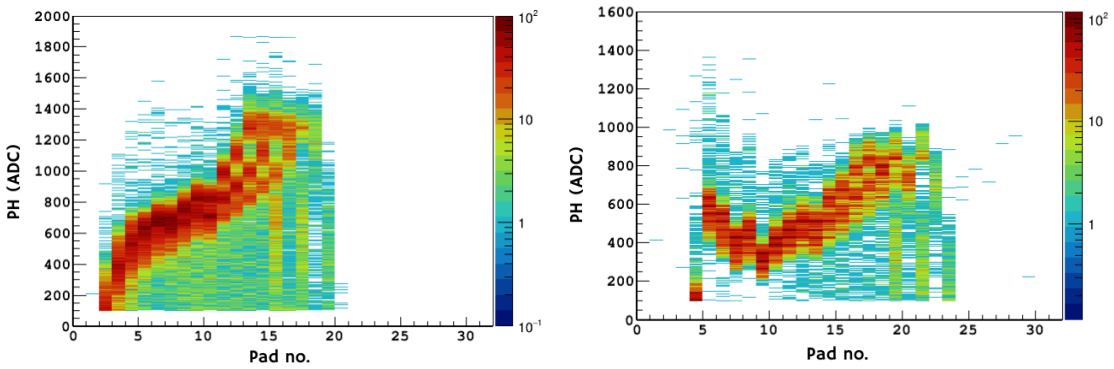

Figure 5.8: Pulse heights across the triggered anode pads showing the detected ranges in Ar:CH_4 90:10 (**left**) and He:CO_2 90:10 (**right**) gas mixtures. No signal on the initial pads is a result of the energy thresholds used.

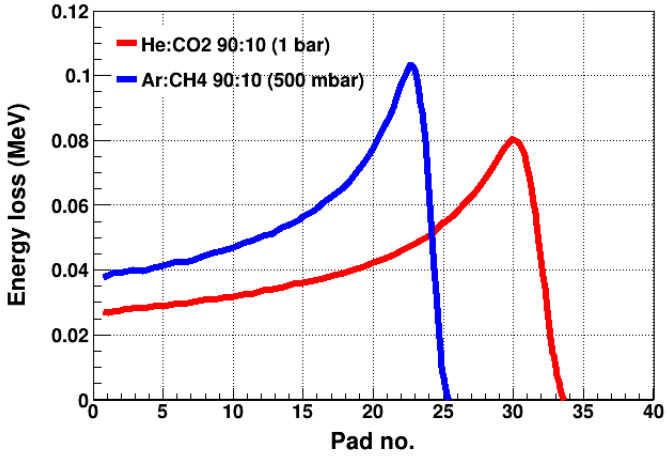

Figure 5.9: SRIM predicted ranges of 5.805 MeV alpha particles in different gas mixtures. The energy loss profiles are consistent with the experimental data shown in Fig. 5.8 after range adjustment (see Table 5.2).

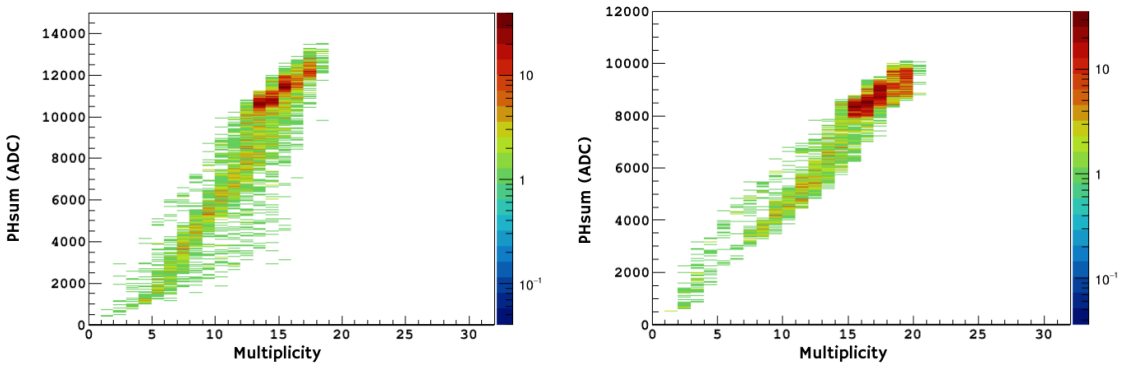

Figure 5.10: Summed pulse height versus multiplicity of the alpha tracks in Ar:CH_4 90:10 (**left**) and He:CO_2 90:10 (**right**) gas mixtures. Tracks with lower multiplicity deposit relatively less amount of energy.

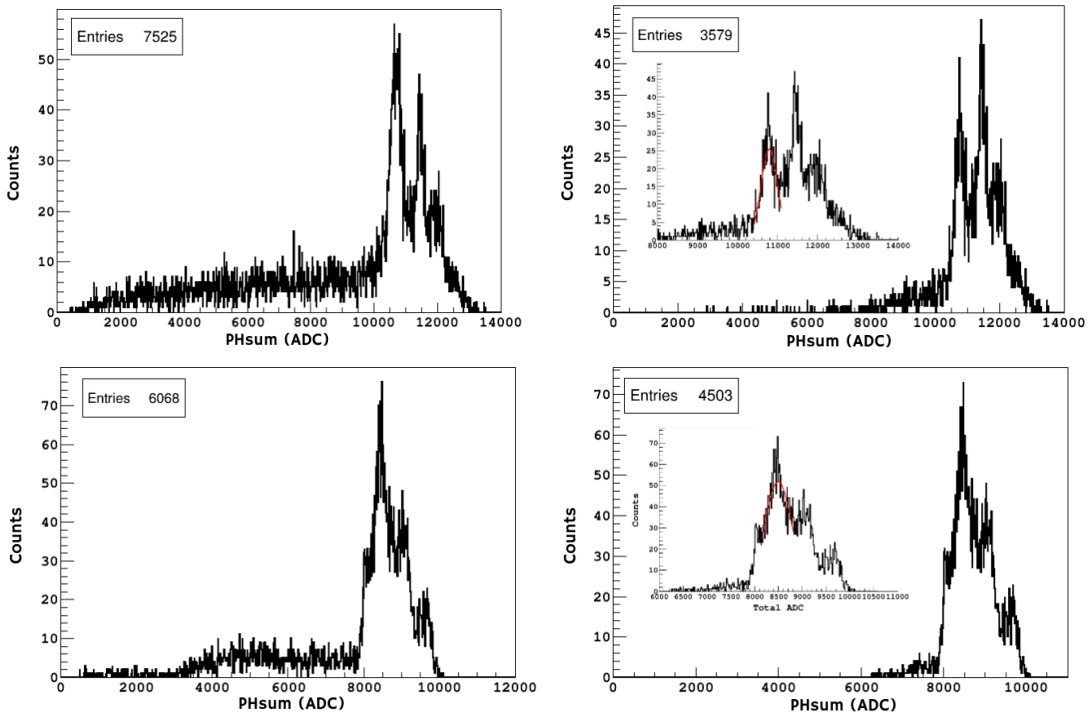

Figure 5.11: 3α spectra with (**right**) and without (**left**) multiplicity cut in Ar:CH_4 90:10 (**top**) and He:CO_2 90:10 (**bottom**) gas mixtures. The 5.155 MeV ^{239}Pu peaks were fitted using a Gaussian function.

5.3.2. X-ray source studies

The test chamber performance at low energies was studied with an ^{55}Fe X-ray source. ^{55}Fe decays through the electron capture process emitting Auger electrons of 5.18 keV, $K_{\alpha 1}$ X-rays of 5.89 keV, $K_{\alpha 2}$ X-rays of 5.88 keV and K_{β} X-rays of 6.49 keV. Since the energies of the two K_{α} X-rays are similar, they are considered as a mono-energetic radiation of 5.9 keV. Upon absorption of these low energy X-rays by the gas atoms, as a result of the photoelectric effect, an outer or an inner shell electron is liberated, causing the primary ionisation of the gas. Fig. 5.12 shows the ^{55}Fe spectra in Ar:CH_4 and He:CO_2 gas mixtures. Both spectra exhibit well defined K_{α} peaks, which were fitted using Gaussian and Crystal Ball functions [73]. The

Crystal Ball function represents the spectra in He-based gas mixture well, with a Gaussian core portion and a low energy tail. From the K_α peak fits, resolutions 24.5% (FWHM) and 32.7% (FWHM) were calculated for Ar:CH_4 and He:CO_2 gas mixtures respectively. The parameters used for these tests are listed in table 5.3. The K_α peak in the ^{55}Fe spectra is sometimes accompanied by an escape peak as discussed in section 3.6.1. The ^{55}Fe spectrum for the Ar-based gas mixture (Fig. 5.12) shows the Ar escape peak corresponding to an energy of 2.7 keV. The energy resolution obtained using the ^{55}Fe X-ray source was found to be worse compared to that achievable with the 3α source as discussed in Section 5.3.1, which was a direct consequence of the difference in the number of primary ionisation electrons liberated or the energy deposited per pad by the ionizing radiation (see Eq. 3.21). For the 3α source, the number of primary ionisation electrons is at least three orders of magnitude higher for the same gas mixture used, which significantly reduces the statistical variance and improves the energy resolution.

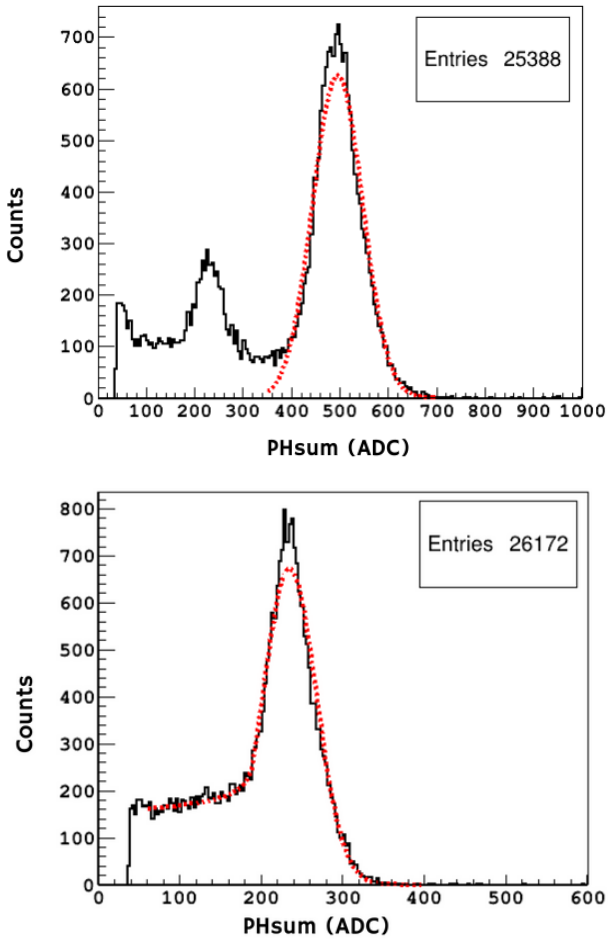

Figure 5.12: ^{55}Fe spectra in Ar:CH_4 90:10 (**top**): $\mu = 495.08$ ADC, $\sigma = 51.54$ ADC, and He:CO_2 90:10 (**bottom**): $\mu = 234.63$ ADC, $\sigma = 32.71$ ADC.

The energy deposition of the photoelectrons inside the gas volume is highly localised and their interaction with the gas can be considered as point-like. The point-like interactions of the photoelectrons were used to estimate the relative variation in the anode pad responses in Ar:CH_4 90:10 gas mixture under the similar operating

Table 5.3: List of test parameters in different gas mixtures. The gas pressures used were chosen in way that the X-ray interactions predominantly take place within the first 37 pads, based on the anode pad response study in Section 5.3.1. Furthermore, the μ-RWELL biases used were selected based on the studies in section 5.3.3 to ensure the optimum detector performance.

Parameters	**Ar:CH_4 90:10**	**He:CO_2 90:10**
Pressure	1 bar	1 bar
Drift field (V_d)	-150 V/cm	-300 V/cm
μ-RWELL bias (ΔV)	-460 V	-540 V

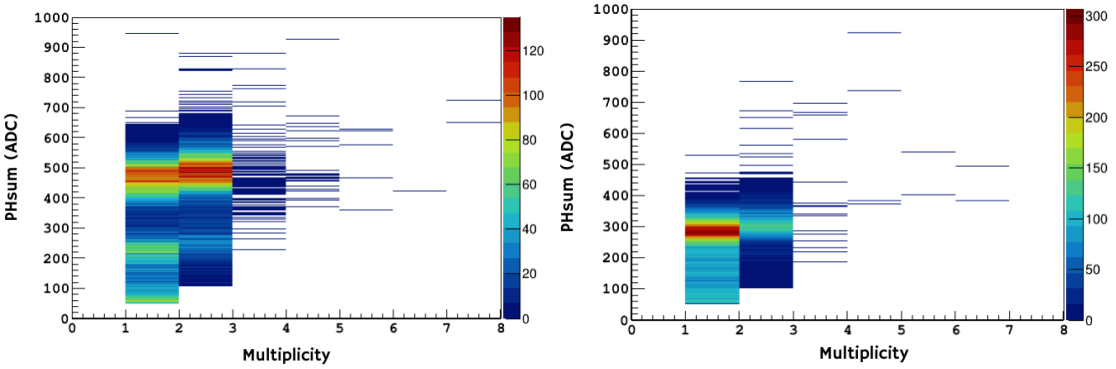

Figure 5.13: Summed pulse height vs multiplicity for Ar:CH_4 90:10 (**left**) and He:CO_2 90:10 (**right**) gas mixtures. The difference in the mean amplitudes originate from the different gas gain values at which the tests were performed for the respective gas mixtures.

parameters listed in table 5.3. Fig. 5.13 shows the primary ionisation produced by the photoelectrons can also be shared between two or more anode pads. In order to better constrain the relative anode pad response study, two specific event selection criteria were chosen:

- Events with multiplicity of 1, to isolate individual pads.
- Events with $PH_{sum} > 300$, to utilise the well defined mono-energetic K_α peak in the X-ray spectrum (Fig. 5.12). By doing so the effects of the low energy noise and the escape peak were negated.

Fig. 5.14 shows the pulse heights across the anode pads before and after applying the multiplicity and summed pulse height cuts. The five black horizontal dotted lines indicate the mean (m_t), standard deviation (σ_t) and FWHM derived from fitting the K_α peak of the Ar:CH_4 90:10 spectrum in Fig. 5.12.

The plot with cuts in Fig. 5.14 show that the variations in the individual anode pad responses are predominantly within a 24.5% range with respect to m_t. The mean values for the each individual anode pad (m_i) are different compared to m_t, which was further quantified using the parameter m_{di} defined in equation 5.4.

$$m_{di} = (m_t - m_i)/m_t, \quad i = 0, 1, 2, ...60 \tag{5.4}$$

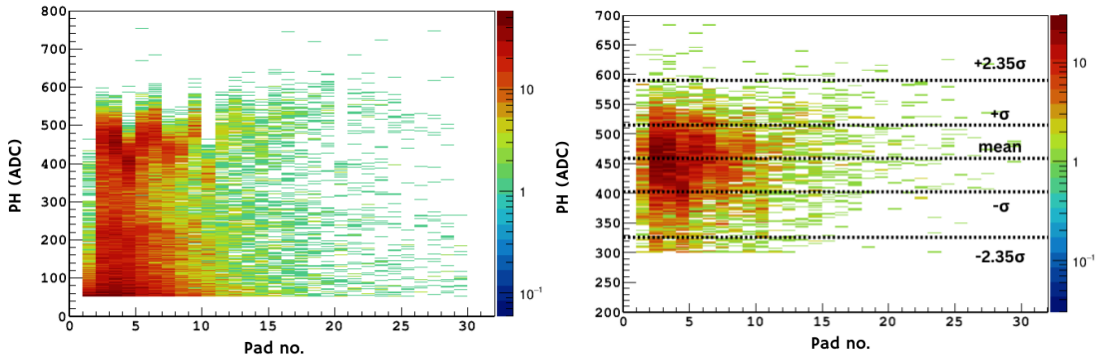

Figure 5.14: Pulse heights across the anode pads from the ^{55}Fe X-ray interactions in Ar:CH_4 90:10 without (**left**) and with selection criteria or data cuts (**right**). The right hand plot includes only the events with multiplicity = 1 and $PH_{sum} > 300$.

where m_{di} is deviation of the mean of the amplitude (ADC) distribution for a pad from the same for the whole detector. Fig. 5.15 shows a comparison of m_{di} values and individual pad resolutions across the anode pads used for $m_t = 495.08$ ADC (see Fig. 5.12). Due to the lack of statistics in the latter pads the comparison was limited to pad 20. The lower statistics in the latter pads is a result of the range of X-rays specific to the source activity, gas mixture and pressure selected for this study. Comparably higher uncertainty arising from low statistics was noticed for pad 1 and pad 14 onwards. For the pads between 2 and 14, the individual resolutions and the m_{di} values fluctuate to a maximum of 30% and 10%, respectively.

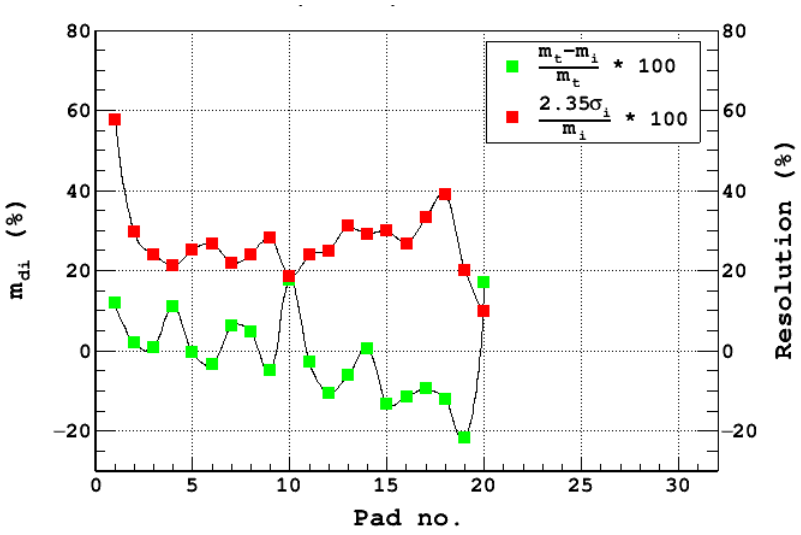

Figure 5.15: Comparison of m_{di} values and individual pad resolutions in Ar:CH_4 90:10 (P = 1 bar). The quantity m_{di} was used to understand the local variations in gas gain and resolution arising from the μ-RWELL structure as well as the variation in preamplifier channel responses. The Crystal Ball fit for pad 5 is shown in Fig. 5.16. The uncertainties in m_i and σ_i were estimated to be small ($< 3\%$) and thus do not visibly appear in the plots.

The variations observed in the anode pad responses can have multiple poten-

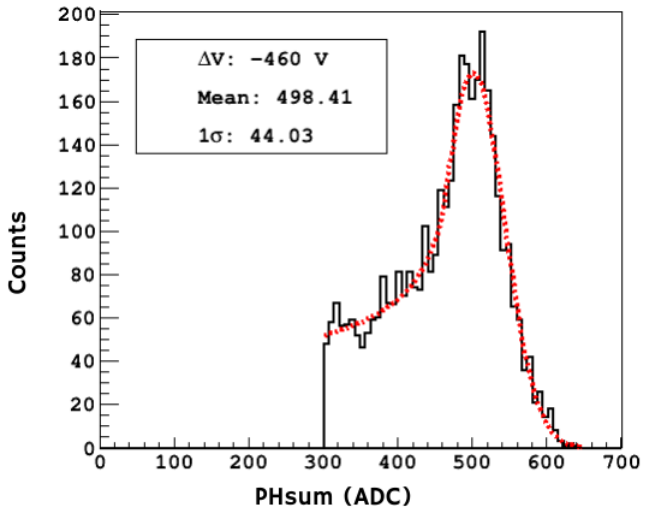

Figure 5.16: ^{55}Fe spectrum in Ar:CH_4 90:10 for pad 5 with cuts: multiplicity = 1, ADC > 300. The fit parameters yield, m_{di} = -0.6% and resolution = 20.8%.

tial sources, e.g., collection efficiency of the primary ionisation at the anode pads, uncertainty in the number of primary ionisation electrons produced, differences in the preamplifier channels arising from circuit component tolerances and inhomogeneous gain from the μ-RWELL structure. The gain variation from μ-RWELL structure is expected as each anode pad collects multiplied electrons from hundreds of individual WELLs. Slight variations in the WELL dimensions can significantly alter the avalanche field and the number of secondary electrons produced by the multiplication process, i.e., the gas gain. Therefore, it is important to estimate the contribution of the μ-RWELL structure in the energy resolution. The results in Fig. 5.15 were obtained by performing an offset calibration on the raw data. In addition to this, a mono-energetic X-ray source and the events with a defined K_α peak triggering on a single anode pad were selected to minimise the uncertainty arising from the variation in the number of primary ionisation electrons. Therefore, the variation in the anode pad responses in Fig. 5.15 is believed to be resulting from the gain inhomogeneity of the μ-RWELL structure and the gain variation between the individual preamplifier channels arising from the circuit component tolerances. The contribution of the preamplifier in the estimation of the gain inhomogeneity could not be eliminated as the test input calibration method introduces additional systematic uncertainty (see Fig. 5.6). However, the quantity m_{di} can be used to identify and normalise any variation in the preamplifier responses originating from both μ-WELL structure and the differences in the circuit components.

5.3.3. Gas gain studies

As discussed in Section 3.8.1, MPGDs such as the μ-RWELL use the gas multiplication process in order to detect ionising radiations over a range of energies. The gas multiplication process is commonly quantified with gas gain (G), a dimensionless physical quantity defined in equation 5.5. It is the ratio of the number of amplified electrons (n_{ea}) to the number of primary electrons (n_{np}).

$$G = \frac{n_{ea}}{n_{np}} = \frac{E_a}{E_p}, \tag{5.5}$$

where E_a is the mean from fitting the K_α peak of the calibrated spectrum in keV. E_a is same as E_f and can be obtained by using Eq. 5.3. E_p is the 5.9 keV X-ray photon energy. As described in Section 5.2, the energy calibration was performed and Eq. 5.3 was used to estimate E_a. An equivalence can be drawn between the number of electrons (n_e) corresponding to an energy (E), i.e., $n_e = E/W$, where W is the work function of the gas. The K_α peaks of the ^{55}Fe X-ray spectra were fitted to quantify the gas gain (see Fig. 5.17) and the associated resolution (see Fig. 5.18) for different gas mixtures over a range of μ-RWELL biases. The charging up effect studied in Section 5.3.4 was taken into account during the tests discussed in this section and the detector was allowed to reach a stable operating condition before each measurement. The gas gain as a function of μ-RWELL bias (ΔV) for different gas mixtures was studied. Figure 5.17 shows a comparison between the results from the test chamber and those reported by Bencivenni et al. [58]. Despite the difference in the test setups and gas mixtures used, the maximum achievable gas gains observed agree well ($G \approx 8\text{x}10^3$) in Ar-based gas mixtures for similar pressure values. The maximum gas gain achievable in He:CO_2 90:10 mixture was also found to be $G \approx 8\text{x}10^3$. In the case of He:CO_2 97:3 mixture, the maximum gas gain achieved was higher ($G \approx 10^4$). For these tests, maximum operating voltages of the μ-RWELL (ΔV) in the different gas mixtures were determined by the operational stability of the setup. The operating voltage range of the μ-RWELL was found to be specific to the gas mixture used, as expected. Similar observations were reported by Sauli [52]. Moreover, the maximum gas gain achievable with the μ-RWELL was found to be much higher compared to the standard single GEM [52].

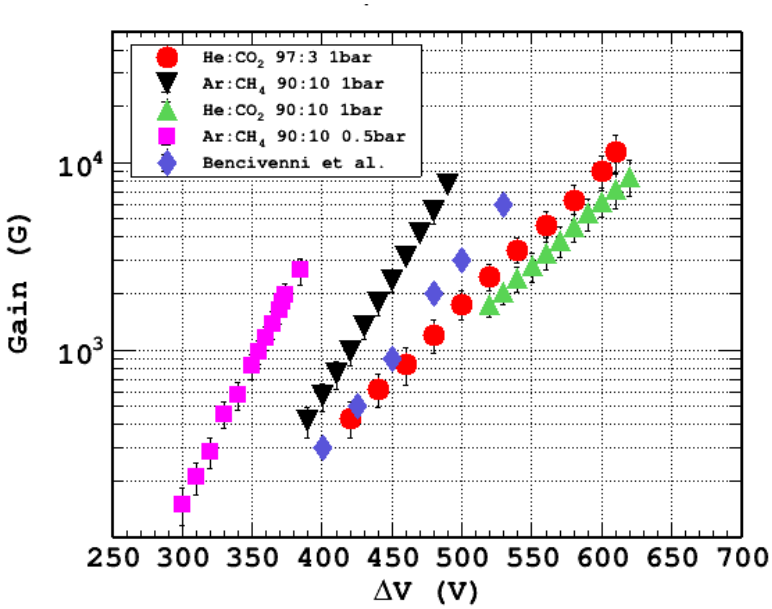

Figure 5.17: Calculated gas gain as a function of μ-RWELL bias for different gas mixtures and results reported by Bencivenni et al. [58]. The gas gain (G) grows exponentially with increasing μ-RWELL bias (ΔV).

Fig. 5.17 also shows that the lower percentage of quench gas does not affect the performance of the μ-RWELL in terms of the range of gas gain achievable. This study is especially important for the future TACTIC experiments. A reduction in the amount of quench gas in the mixture will significantly reduce the amount of background from scattering reactions as well as increasing the yield per unit time for the reaction of interest since the number of target nuclei (^{4}He) will increase. Furthermore, the gas gain studies were also extended to lower pressures in Ar:CH_4 gas mixture. Fig. 5.17 shows that the maximum gas gain achievable at P = 0.5 bar is lower compared to the same mixture at P = 1 bar. This is believed to originate from the higher percentage of impurities in the gas mixture at lower pressures. The inflow of atmospheric impurities changes the W-value of the mixture, which affects the upper limit of the detector operation in terms of the maximum gas gain achievable, i.e., the point at which the Raether limit [40] is exceeded. The test chamber had a leak rate $\approx$ 6 mbar hour^{-1}. Although a constant flow of gas was used during the tests, at lower pressures the higher relative percentage of atmospheric impurities leaking in was believed to have affected the studies. This problem can be addressed by improving on the leak rate of the test chamber or increasing the gas flow rate for the faster recycle of the gas volume. The parameters used for the gas gain studies discussed in this section are listed in table 5.4.

Table 5.4: List of test parameters in different gas mixtures. The upper limit of the μ-RWELL operating bias range was determined by the operational stability of the setup and the lower limit was dictated by the energy threshold used and intrinsic detector noise levels.

Parameters	**Ar:CH_4 90:10**	**He:CO_2 90:10**	**He:CO_2 97:3**
Pressure	1, 0.5 bar	1 bar	1 bar
Drift field (V_d)	-150, -150 V/cm	-300 V/cm	-340 V/cm
μ-RWELL bias range	(-)300-500 V	(-)520-620 V	(-)420-610 V

Fig. 5.18 shows a comparison of the energy resolutions (FWHM) achievable in different gas mixtures. The best energy resolution ($\approx$ 24.5%) was achieved in Ar:CH_4 90:10 at pressure 1 bar. For the He-based gas mixtures, it was found to be between 32-35%. A significant improvement was observed around the mid-range of the μ-RWELL operation in terms of the applied bias (ΔV). At the extremities of the operational bias range, the resolution was found to be worse, believed to be a result of the relatively high statistical uncertainties. At higher bias voltages, the avalanche fields inside the WELLs increase drastically and the small localised variations (discussed in Section 5.3.2) in the amplification process increase, worsening the energy resolution. For the lower regions of operation the resolution from the K_α peak gets affected by the electronic noise, as the output signals are very close to the intrinsic noise levels of the detector. Fig. 5.19 includes the ^{55}Fe X-ray spectra in He:CO_2 97:3 at four different μ-RWELL biases for the same drift field.

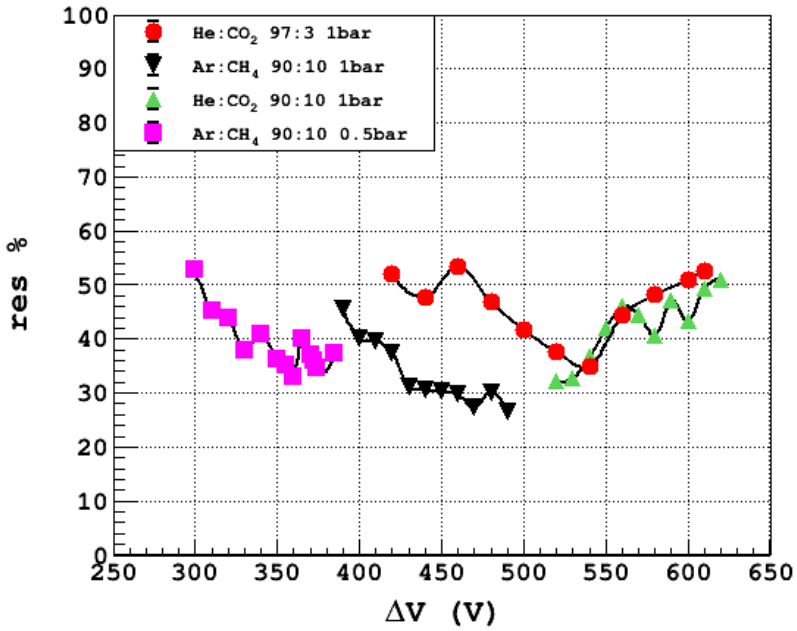

Figure 5.18: Comparison between the resolutions achieved in different gas mixtures. The resolution was found to be particularly worse at the extremities of the μ-RWELL operating bias range. Fig. 5.19 shows the ^{55}Fe spectra at different ΔV for He:CO_2 97:3 gas mixture. The uncertainties in the resolution were estimated to be small ($< 3\%$) and thus do not visibly appear in the plots.

5.3.4. Charging up effect studies

As discussed in Section 3.9.3, it is important to quantify the charging up effect for achieving optimum and stable detector operating condition. Figure 5.20 illustrates charging up effect study in the test chamber using He:CO_2 97:3 and Ar:CH_4 gas mixture with a 0.14 MBq ^{55}Fe X-ray source without collimation. The parameters used for these tests are listed in table 5.5. The fluctuation in the ambient temperature and gas pressure were small (<2%) during these studies. Therefore, any contribution from these parameters is believed to be negligible. To ensure that the μ-RWELL dielectric is completely unpolarised, the detector was kept without bias for several days before the tests. The charging up studies performed in the test chamber were a combination of both polarisation and radiation charging up effects [56]. The individual effects were not studied separately as for the gas gain and resolution measurement both effects need to be considered cumulatively.

Table 5.5: List of test parameters in different gas mixtures. The μ-RWELL biases were chosen in accordance with the studies in Section 5.3.3 for optimum resolution.

Parameters	**Ar:CH_4 90:10**	**He:CO_2 97:3**
Pressure	1 bar	1 bar
Drift field (V_d)	-150 V/cm	-320 V/cm
μ-RWELL bias (ΔV)	-480 V, -490 V	-520 V

After the application of bias (ramp-up rate = 5 V/s), gas gain plateaued and steady state was achieved approximately at t = 180 minutes (Fig. 5.20) in He:CO_2

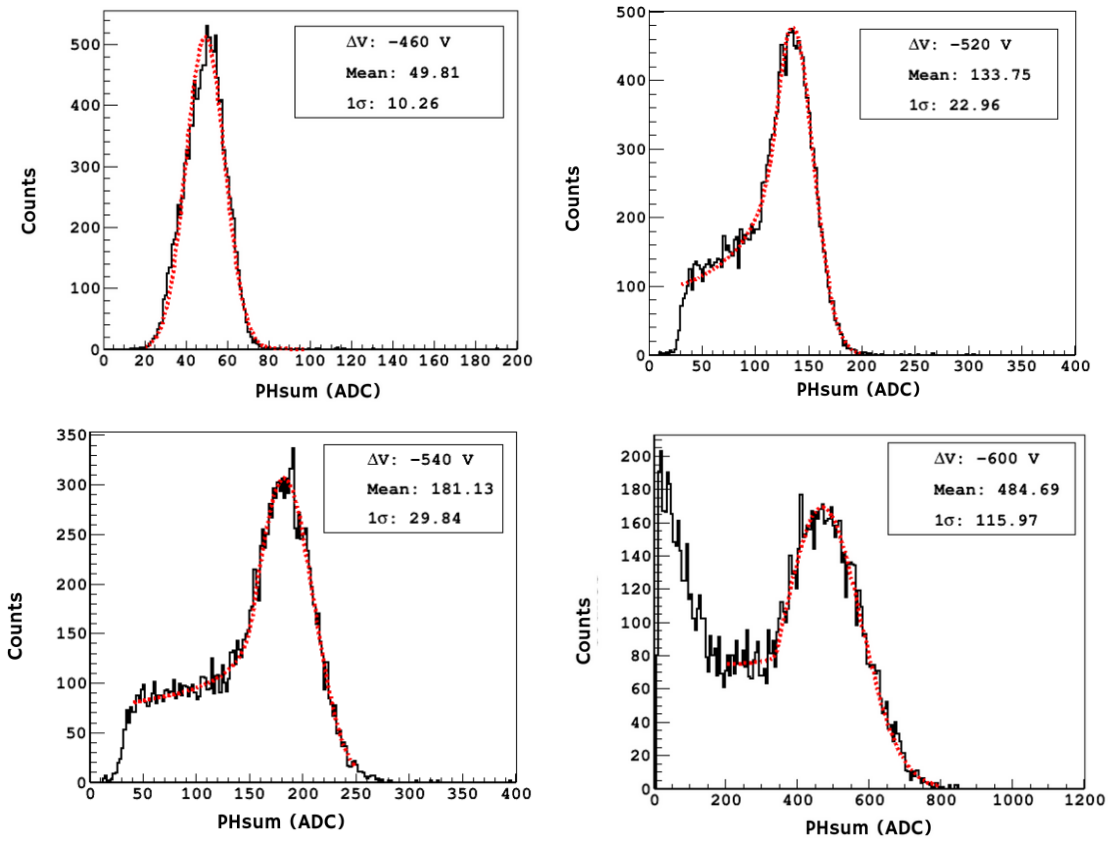

Figure 5.19: ^{55}Fe spectra in He:CO_2 97:3 gas mixture (pressure = 1 bar) for different μ-RWELL bias (ΔV).

97:3. During this time, the gas gain increased by $\approx$ 30%. This charging up time agrees well with the charging up study included in Fig. 3.13 for source rate 0.12 kHz. Although the ^{55}Fe source used for this study had a rate approximately 10^2 times higher, the entirety of the μ-RWELL surface was not subjected to the same rate due to the detector setup. This is evident from the Fig. 5.14. The source rate drops off with distance which can be explained through equation 3.8. Therefore the charging-up effect in Fig. 5.20 is an average over all the pads involved in the study. The two key parameters for determining the charging-up characteristics, the dielectric material and the WELL dimensions of the μ-RWELL used for this work, are similar to the GEM dielectric material and the hole dimensions used in [56]. Therefore some agreement in the results was within expectations. However, the maximum gas gain ($G \approx 700$) and the relative increase in the gas gain during charging-up reported in their work is different from the results of this study. This variation can be attributed to the structural differences between the single GEM and the μ-RWELL, as well as the differences in the active areas and the irradiation rates used. Fig. 5.20, in conjunction with Fig. 5.21 shows that the energy resolution obtained by fitting the K_α peak significantly improves from the initial value of $\approx$ 75%, stabilising around 35% in He:CO_2 97:3 over time.

The charging-up effect was also studied in Ar:CH_4 90:10. However, approximately 70 minutes into the study the μ-RWELL bias (ΔV) was reduced from -490 V to -480 V to ensure detector stability as few sparks were observed at ΔV = -490 V, which is close to the upper limits of μ-RWELL operation according to the studies

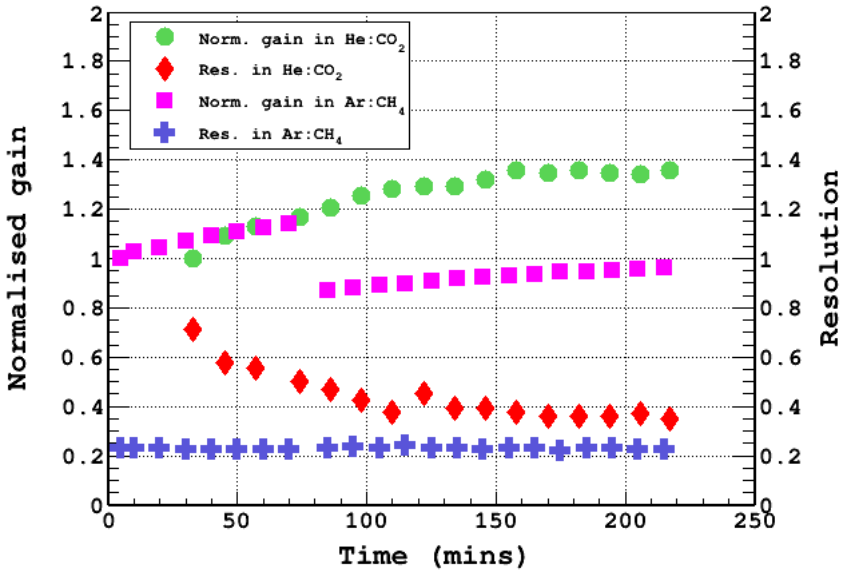

Figure 5.20: Charging up effect study in He:CO_2 97:3 and Ar:CH_4 90:10 gas mixtures. The plots show the time evolution of normalised gain and corresponding resolution (FWHM). Normalised gain plateaus around t = 180 minutes after the bias application, signifying stable operating condition. The gain drop in case of He:CO_2 resulted from a change in operating conditions, i.e. the μ-RWELL bias was lowered by 10 V.

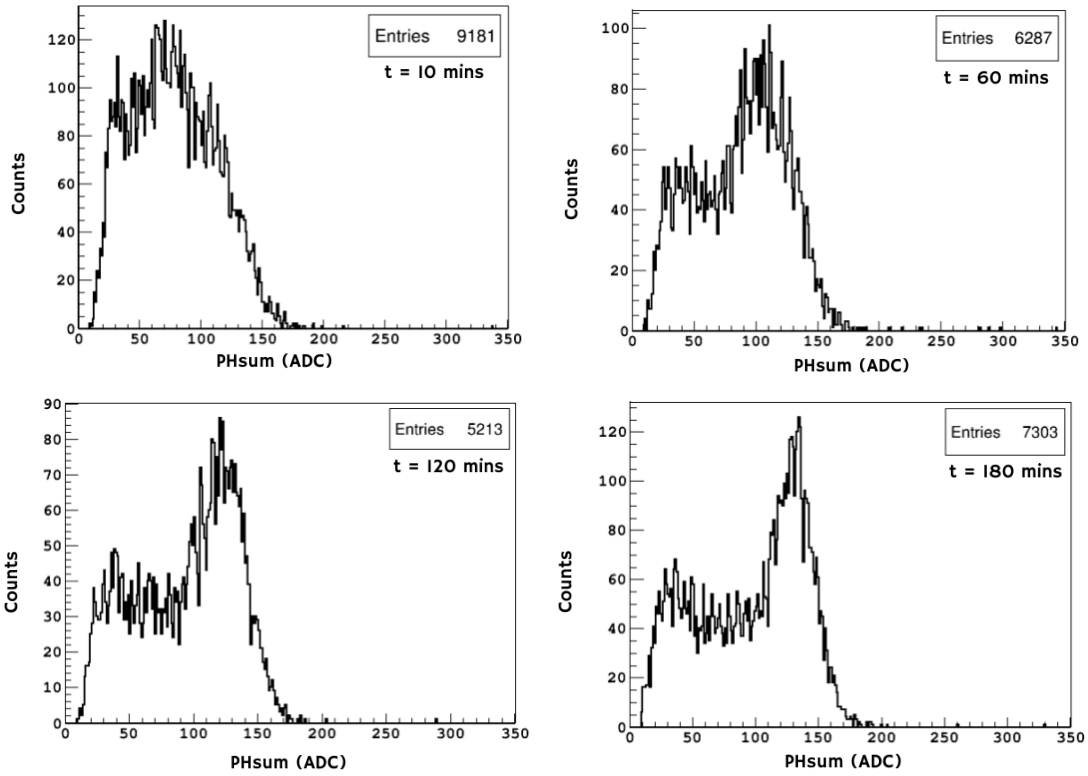

Figure 5.21: ^{55}Fe spectra in He:CO_2 97:3 gas mixture at different time intervals, i.e., t = 10, 60, 120, 180 minutes into the charging up effect study. The resolution improves significantly $\approx$ 180 minutes into the study.

in section 5.3.3. This resulted in a gain drop at t ≈ 70 minutes. Fig. 5.20 shows that after t = 70 minutes, the gas gain increased by ≈ 11% and started to plateau at t ≈ 180 minutes. It is noteworthy that compared to the similar study in He:CO_2 97:3 mixture, the resolution was found to be better throughout around 23%, which can be attributed to ≈ 1.5 times lower W-value of Ar:CH_4 90:10 mixture (table 3.1), resulting in the production of a relatively higher number of primary ionisation electrons in Ar:CH_4 mixture. This was believed to have improved the statistical uncertainty associated with the electron multiplication process. It must be noted that a gradual improvement in resolution with time was observed in the He:CO_2 study compared to the Ar:CH_4 study. This needs to be investigated in the future.

5.4. Discussion

A detailed study of the novel μ-RWELL detector was performed using the test chamber before their installation in TACTIC. The studies showed that the detector is capable of detecting low energy depositions in the order of a few keV from ionising charged particles. This low energy detection capability is important for detection of the reaction protons, as discussed in Chapter 7. The μ-RWELL detector was also studied for the first time in He-based gas mixtures. Helium serves as the key component of the target gas mixture for studying alpha-induced nuclear reactions. A gas mixture optimisation study by varying the amount of quench gas (CO_2) in the mixture was also performed. Reducing the amount of the quench gas from 10% to 3% did not have a major impact on the gas gain and energy resolutions achievable. The maximum achievable gain was found to be approximately 5% higher in the lower quench gas configuration. The best possible resolution was also found to be similar (≈ 32%). This result has a major implication for the application of μ-RWELL in TACTIC. The quench gas acts as an additional source of elastic scattering. The lowest possible percentage in the He-based target gas mixture is optimum for lowering the scattering background. It is noteworthy that an attempt was made to further lower the quench gas percentage to 1%. However, high gas gains ($G > 200$) could not be achieved with the He:CO_2 99:1 gas mixture as frequent sparks were observed at higher μ-RWELL biases ($\Delta V > 500$ V).

A bias (ΔV) dependent gas gain study in Ar- and He-based gas mixtures was performed. The maximum gas gain achievable in all the gas mixtures was found to be in the order of 10^3 and agrees well with the gas gains reported by Bencivenni et al. [58]. An exact match was not expected as the gas mixtures used in this work were different as well as the experimental arrangement. The operating range of ΔV was found to be specific to the gas mixture used. This was also within expectations, as the gas gain is dependent on the W-value, which is unique to a specific gas mixture. Similar observations were reported by Sauli [52] for both single and triple GEM. The lower and upper limits of ΔV in each gas mixture were determined by the DAQ energy threshold and operational stability of the μ-RWELL, respectively. Furthermore, the maximum gas gain achievable was found to be much higher than the standard single GEM [52]. The high gas gain is important for the efficient detection of light charged particles like protons in TACTIC, which deposit a small amount of energy per pad (a few keV to tens of keV) in the detection volume.

A 3α source was also used to study the range of alpha particles in the detection volume of the test chamber. This study was important in order to compare the experimentally obtained and simulated (SRIM, Geant4) range of ions in different gas mixtures. The experimentally obtained and simulated ranges predicted by Geant4 and SRIM were found to be in agreement within 10%. For the charged particle tracking inside TACTIC, calculated track length and track angle are the two most important parameters, which have a direct dependence on the range. Furthermore, the energy resolution achieved in both Ar- and He-based gas mixtures with the 3α source showed approximately a $5-$fold improvement compared to the ^{55}Fe source. The number of primary electrons per pad is $\approx 9-40$ times higher for the 3α source, i.e. $\approx$ 50-120 keV/pad for the 3α source, and $\approx$ 3-6 keV/pad for the ^{55}Fe source used. This significantly improves the statistical uncertainty arising from the amplification process.

The charging up effect was also studied in different gas mixtures. The time required to achieve a stable gain after the bias application was found to be similar ($\approx$ 3 hrs.) in both Ar- and He-based gas mixtures. As a low ionising X-ray source was used for these studies, the charging up time obtained serves as the upper limit for alpha source and beam tests. The charging up effect is heavily dependent on the number of primary ionisation electrons liberated in the detection volume. A larger number effectively reduces the charging up time (see Fig. 3.13). A study by Kumar et al. [57] in an Ar-based gas mixture showed that a two orders of magnitude increase in the source rate reduced the charging up time by approximately two orders of magnitude. The increase in source rate directly translates to the increase in the number of ionisation electrons liberated. Similar observations were made during the test chamber studies. While using the 3α source the charging up time was found to be significantly less ($\approx$ 2 mins.) in both Ar- and He-based gas mixtures. This needs to be further quantified in future through a rate dependent charging up study of the μ-RWELL detector. In all the data reported in this chapter and also in Chapter 7, related to alpha source or beam tests, $\approx$ 3 hrs. of charging up time was considered. This approximation is sufficient, as for the alpha source and beam tests, the number of primary ionisation electrons liberated per second per pad was $\approx 10-10^4$ times higher compared to the ^{55}Fe source tests.

A pad dependent variation in the μ-RWELL response was also observed (see Fig. 5.14). The primary sources of the variation were identified to be the structural effects of the μ-RWELL and differences in the preamplifier channels. Thus, in order to improve the energy resolution achievable with the μ-RWELL detector used, a gain normalisation is required. This becomes more relevant for particle identification in TACTIC. By using the ^{55}Fe source and selecting the highly localised single pad events (see Fig. 5.15), it is possible to perform a gain normalisation across the anode pads as well as a reliable energy calibration. However, this was outside the scope of this work and is subject to future studies.

Chapter 6

TACTIC: experimental considerations

6.1. TRIUMF

TRIUMF is Canada's national laboratory for nuclear and particle physics research and can be considered as a world leading facility of post-accelerated radioactive ion beams (RIBs), important for experimental nuclear science [78]. The ISAC (Isotope Separation and Acceleration) facility has a beam production section consisting of an off-line ion source (OLIS) [77] for production of stable beams and a ion source station located in an underground vault for the production of RIBs. Radioactive ion beams are created by making use of TRIUMF's main cyclotron which is capable of producing a beam of 500 MeV protons. The primary negative hydrogen ion beam is then accelerated and stripped to bare protons and sent to the ISAC target hall. The ISOL (Isotope Separator Online) technique is then used to extract the desired radioactive fragments created from the collision between a target and the protons.

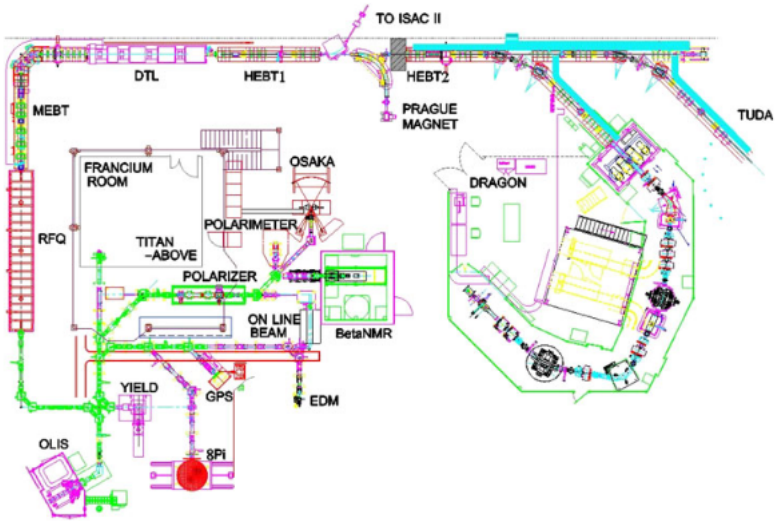

Figure 6.1: Technical drawing of ISAC I experimental hall where OLIS supplies beams from stable isotopes to various experiments. The ISAC II experimental hall is not shown in the picture. During the in-beam experiments, TACTIC was positioned at the HEBT3 beamline in place of TUDA [77].

After the extraction and the separation of the desired radioactive fragments, the ions are then transported to ISAC accelerator chain (Fig. 6.1), which consists of the RFQ (Radio Frequency Quadrupole), the MEBT (Medium Energy Beam Transport), a DTL (Drift Tube Linear accelerator) and finally the SC-LINAC (Super-Conducting Linear Accelerator). The RFQ accelerates the ions, which fall within the acceptance limit A/q < 30 (A: atomic mass; q: charge state). The beam is then transported along the MEBT, where a carbon stripper foil is used to increase the charge state of the beam. Afterwards the beam is sent to a DTL, which is capable of further accelerating the beam up to 1.8 MeV/u. The final acceleration stage is the SC-LINAC, which can increase the beam energies to 6 MeV/u or higher.

6.1.1. OLIS facility

Beams of stable nuclei are produced using the OLIS facility [77], which consists of a high voltage terminal containing a microwave cusp ion source, a surface ion source or a hybrid surface-arc discharge ion source and a multi-charge ion source. These sources are capable of providing stable ion beams with charge state +1 or +n up to A/q = 32, which can be injected into the ISAC accelerator chain for experiments and for tuning the beam lines. The ^{23}Na beam used to study the ^{23}Na (α, p)^{26}Mg reaction with TACTIC (discussed in the chapter 7) was produced at the OLIS facility using the surface ion source (SIS).

6.2. TACTIC

6.2.1. General setup

TACTIC [7, 11, 12] is a cylindrical time projection chamber with radial drift field. It is also classified as an active target detector (discussed in Section 3.11). The length and the radius of the detection region are 251.9 mm and 50 mm, respectively. TACTIC was designed in a way that the beam enters the field-free gas target region through a window (typically aluminised mylar) at the upstream end. The target region is separated from the active detection region by a cathode cage assembly at a radius 12 mm (Fig. 6.2). Scattered beam particles, recoils and ejectiles come out of the field-free target region and enter the detection region, where they can be tracked and identified. The gas target length/thickness can be adjusted by changing the position of the entrance and exit windows.

The nuclear interactions take place inside the field-free target region inside the cathode cage. The reaction products (recoils, ejectiles) or the scattered particles emerge out of the cathode cage and ionise the gas in the active detection region. The ionisation electrons move radially outwards under the influence of the drift field and undergo gas multiplication at the μ-RWELL. The field guide rings just outside the detection region are used to make the drift field between the outer cathode wires and the μ-RWELL uniform over the length of the detection region. The design of the rings were finalised based on a study by Kirchner [79]. The multiplied electrons induce a signal at the anode pads. The working principle of the μ-RWELL is discussed in section the 3.9.3. For TACTIC in-beam experiments, the energy deposited on each anode pad by the charged particles can have a large dynamic range, i.e., from tens of keV to a few MeV. The light ejectiles, e.g., protons, deposit very small

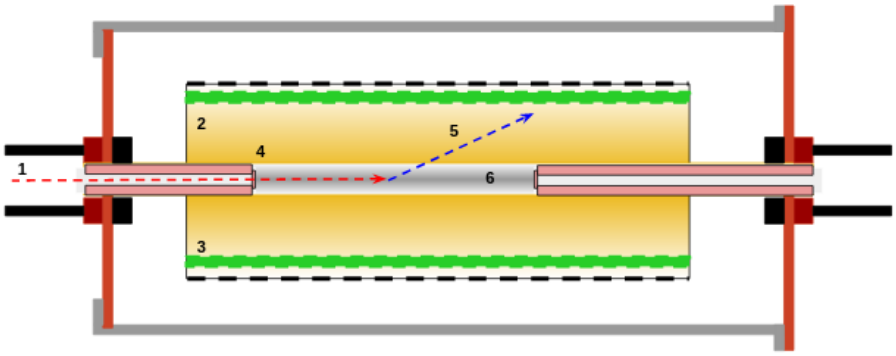

Figure 6.2: Schematic diagram of TACTIC. Key features, 1: ion beam, 2: detection region, 3: μ-RWELL, 4: entrance window, 5: reaction or scattering product, 6: target region.

amount of energy in the gas, thus the ionisation electrons in such cases need to be multiplied to produce large enough signal at the anode to distinguish them from the electronic noise associated with the setup. The high gas gain achievable with the μ-RWELL as discussed in Section 5.3.3, makes them suitable for this purpose. The signals produced at the anode pads by the electrons are amplified by charge sensitive preamplifiers and fed into the data acquisition system, which records the raw signals for analysis. The two important active region components, i.e., the cathode cage and the μ-RWELL are discussed in detail below.

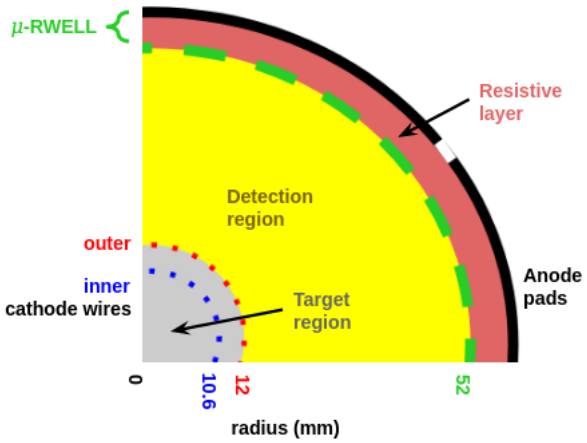

Figure 6.3: Schematic cross-section of TACTIC. The drift field in the detection region is is created by the potential difference between the outer cathode wires and the μ-RWELL.

The cathode cage

The cathode cage assembly around the target region as shown in the Fig. 6.4 is designed to prevent the beam-induced electrons in the target region from diffusing into the detection region, as well as providing the necessary drift field. The assembly consists of two concentric and annular sets of 32 gold-plated tungsten wires, each

with thickness ≈ 20 μm, running along the length of the detection region parallel to the central beam axis (Fig. 6.3). The inner wires, at a radius of ≈ 10.6 mm act as the electron cage. The outer wires, at a radius of ≈ 12.0 mm provides the drift field in conjunction with the μ-RWELL. The inner and the outer sets of wires are connected through a resistor, in a way that the inner wires are at a positive potential compared to the outer wires. This arrangement crates a suitable potential gradient, which prevents the escape of the beam-induced ionised electrons from the target region. Both sets of wires are held in place by an aluminium flute, which includes three support beams running parallel to the beam axis at a radius of ≈ 8.8 mm. Each of these support beams are 15° wide and effects the detection efficiency of TACTIC, which is discussed in Section 6.2.2.

The design of the cathode cage assembly was conceived in order for TACTIC to work with high beam intensities by suppressing the beam-induced ionisation. However, the cathode cage also renders the initial part of the ion track undetectable inside the target region, which includes the vertex of the nuclear interaction. This implies that the energy measured is always a fraction of the total energy of the ion. The undetectable fraction of energy depends on the track angle, the track length and the energy loss (dE/dx) characteristics of the ion.

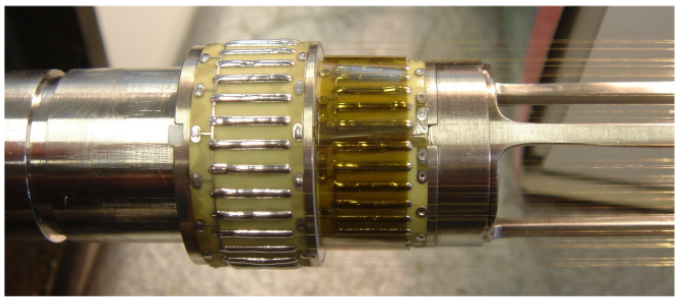

Figure 6.4: Picture of one end of the cathode flute. The aluminium flute consists of three beams and keeps the cathode wires under tension. The inner and outer cathode wires are also visible [7].

The μ-RWELL

The μ-RWELL structures in TACTIC were made by utilising thin flexible PCB boards, with bending tolerance up to radius ≈ 50 mm. During their installation, two μ-RWELL structures were bent in a semi-cylindrical shape in order to fully cover the cylindrical geometry of TACTIC. Each μ-RWELL structure included 240 segmented copper anode pads in 4 rows with 60 pads each on the readout PCB plane, an active area of 139.0×251.9 mm^2 and a resistive layer (sheet resistance ≈ 45 MΩ/□). The anode pad dimensions were 4.1 mm×34.7 mm with pitch 0.1 mm. TACTIC readout consists of a total 480 anode pads, divided into 8 rows with 60 pads each. Each row is called a sector, these are numbered from 0 to 7 (Fig. 6.5). The sectors are further divided into two parts, i.e., upstream and downstream, with respect to the direction of the beam. The anode pads and the readout PCB boards were connected through standard 30-core flat flexible cables (FFC) with pitch 0.5 mm.

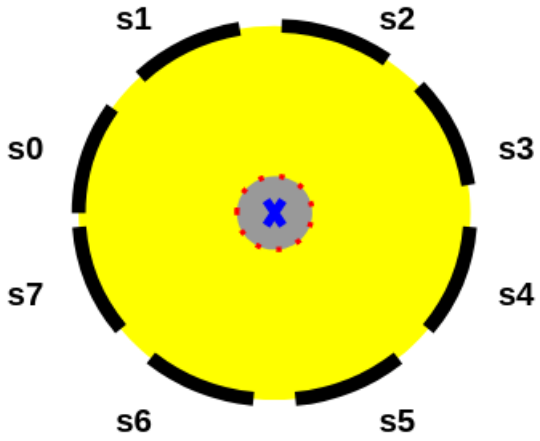

Figure 6.5: Schematic diagram of TACTIC cross section: each black segment of the outer boundary represents a sector. There are finite gaps between two consecutive sectors. The red dotted line and the blue cross in the middle represents the outer cathode wires and the beam axis, respectively. Eight sectors are divided among the two halves of TACTIC, i.e., group 1: s6, s7, s0, s1 and group 2: s2, s3, s4, s5.

6.2.2. Geometric acceptance

The tracking of a charged particle inside TACTIC is limited to the detection region, as illustrated in Fig. 6.2 and 6.3. The limits of the detection region in the z (beam) direction is determined by the width and the pitch of the 60 anode pads in each sector:

$$-126\,\text{mm} \leq z \leq 126\,\text{mm}. \tag{6.1}$$

The radial limits of the detection region are determined by the position of the outer cathode cage and the μ-RWELL structure. The inner radial limit is not well defined and has an azimuthal angle ϕ dependence [7]:

$$12\,\text{mm} \lesssim r \lesssim 50\,\text{mm}. \tag{6.2}$$

The outer radius of the cathode cage ≈ 12 mm was chosen to prevent the majority of the beam from straggling into the detection region. The geometrical limitations determines the maximum detectable track lengths in upstream (l_{us}), downstream (l_{ds}) and radial directions (l_r). For any given track angle, θ, the tracks will be shorter than l_{us}, l_{ds} and l_r. The maximum track lengths can be expressed as,

$$l_{us} = \frac{d/2 + z_0}{\cos(180 - \theta)}, \tag{6.3}$$

$$l_{ds} = \frac{d/2 - z_0}{\cos\theta}, \tag{6.4}$$

$$l_r = \frac{r_{max}}{\sin\theta}, \tag{6.5}$$

where $r_{max} = 50$ mm, is the maximum radius, $d = 252$ mm, is the total length (z direction) of the detection region and z_0 is the vertex position with respect to the centre of the detection region.

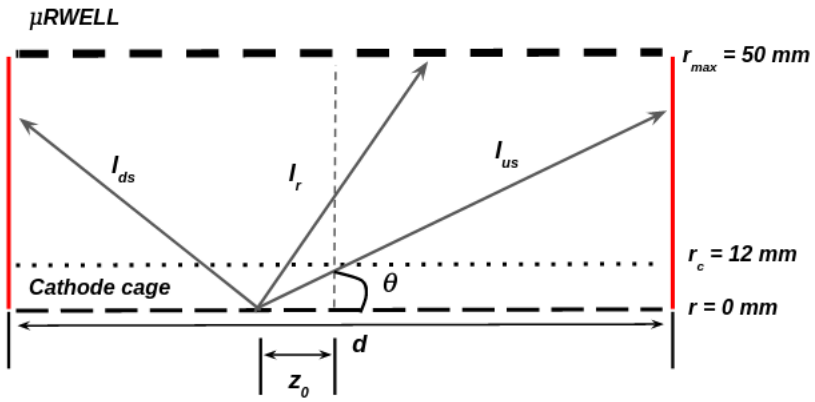

Figure 6.6: Geometric limitations to detectable track lengths in TACTIC: maximum detectable track lengths are given by the outer boundaries of the drift region (red solid lines and the μ-RWELL).

Ideally, the 8 sectors of TACTIC should entirely cover the total 360° ϕ-range with each sector covering a ϕ-range ($\Delta\phi$) of 45°. However, the construction of TACTIC in two halves, the cathode cage wires and the support beams on the cathode flute reduces the total ϕ coverage of the sectors ($\Delta\phi'$) and concurrently the geometrical detection efficiency of the detector (η_{geo}). The geometrical efficiencies of each sector (η_{sector}) listed in table 6.1 was obtained by,

$$\eta_{sector} = \eta_{CWC} \cdot \frac{\Delta\phi'}{360°}, \tag{6.6}$$

where $\eta_{CWC} = 98.19\%$ is the reduced efficiency due to the shading effect of the cathode cage wires [7].

Table 6.1: Geometric efficiencies corresponding to TACTIC sectors [7]. The total geometric efficiency was calculated to be, $\eta_{geo} = 69.5$.

Sector	$\Delta\phi'$ **(degrees)**	η_{sector} (%)
0	37.48	10.22
1	22.48	6.13
2	37.48	10.22
3	29.98	8.18
4	29.98	8.18
5	37.48	10.22
6	22.48	6.13
7	37.48	10.22
Sum	254.84	69.50

6.2.3. Electronics

High voltage supply

All voltages are delivered to the different TACTIC components, i.e., the cathode cage, the μ-RWELLs, the guide rings, from a single high voltage supply through a resistor chain (Fig. 6.7). The resistor chain is housed inside a dedicated high voltage distribution box outside the chamber and connected to TACTIC through 25-pin LEMO connectors. A few modifications were made to the resistor chain in order to accommodate the μ-RWELL structures as highlighted in Fig. 6.8, which replaced the previously used GEMs [7], i.e., R_6 was removed so the drift field steps down correctly, and 8 GEM HV connections were replaced by 4 HV (mesh) and 4 ground connections. The two important voltages, V_{drift} and V_{mesh} are determined by the variable resistor R_7 and the voltage applied to the resistor chain, V_{in}.

$$V_{drift} = V_{in} \cdot \frac{R_{rest}}{R_7 + R_{rest}}, \tag{6.7}$$

$$V_{mesh} = V_{in} \cdot \frac{R_7}{R_7 + R_{rest}}, \tag{6.8}$$

where $R_{rest} = 5.8 \pm 0.2$ MΩ is the total resistance of the unlabelled resistors in the chain. V_{drift} is the drift voltage determining the drift field inside the detection region and V_{mesh} is the voltage applied to the top copper layer (also called the mesh) of the μ-RWELL facing the cathode cage.

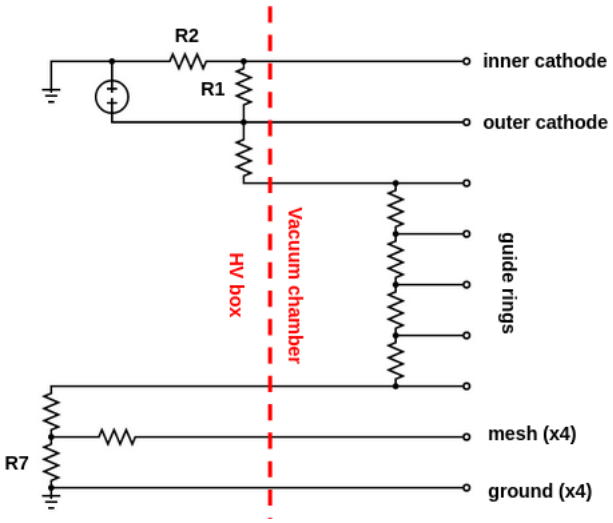

Figure 6.7: Simplified high voltage distribution circuit for TACTIC. Resistors R_1 and R_2 are usually kept at a fixed value. R_7 can be varied as required.

Preamplifiers

The TACTIC preamplifiers were adapted from a design originally developed for the Liquid Xenon PET project at TRIUMF by Leonid Kurchaninov [80]. These charge-sensitive preamplifiers have 32 channels on one PCB and are powered by a ± 6V custom-made power unit. Also, they are shielded by two aluminium sheets to reduce the pickup noise. These preamplifiers exhibited a gain ≈ 8 mV/fC. The equivalent

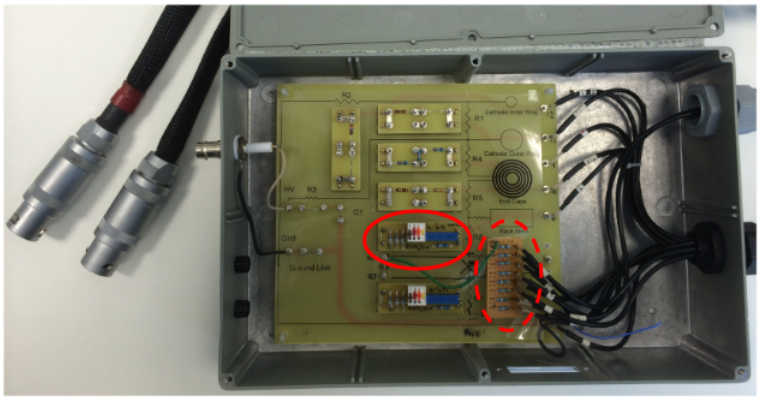

Figure 6.8: The high voltage distribution box. The voltage is provided to the resistor chain through the SHV connection on the left. The two modifications are highlighted, i.e., R_6 was removed so the drift field steps down correctly (solid red line), 8 GEM HV connections were replaced by 4 HV (mesh) and 4 ground connections for the μ-RWELL (dashed red line).

noise charge (ENC) was 600-800 electrons RMS, which translates to $\approx$ 1 mV [81]. Over the course of time, the TACTIC preamplifiers have gone through a few major modifications. The modifications were made on the basis of the SPICE model of the preamplifier circuit by S. P. Fox (Fig. 6.9) and are listed below:

I. The capacitor C288 = 200 pF was removed to eliminate the CR shaping of the pulse for a more detailed study of the timing information, i.e., rise time, fall time, and trigger time. The timing information of a pulse as discussed in Section 6.4 is important for track angle estimation and concurrently, vertex reconstruction.

II. The value of the capacitor C334 was reduced from 56 pF to 0.1 pF, which practically eliminated the CR shaping.

III. The value of the resistor R594 was changed from $\approx 51\Omega$ to 650Ω, which reduced the gain value to $\approx$ 2.3 mV/fC. As a result, the electronic noise level also decreased proportionally. This modification was made in order to utilise the relatively higher gas gain provided by the μ-RWELL compared to the standard GEM (Fig. 3.13).

6.3. Experimental arrangement

TACTIC was installed at the HEBT3 beam line located inside the ISAC-I experimental hall at TRIUMF. The chamber was placed on a cradle with a tripod atop a support frame. The cradle allows fine vertical and horizontal position adjustments for alignment with the beam line. For the experiments with the on-line beam, two beam tubes were inserted from both the upstream and downstream ends. Depending on the desired target thickness, the beam tube lengths can be selected. As the name suggests, the beam tube is used to guide the beam into the target region. The beam enters the target region through a window mounted at the end of the upstream beam

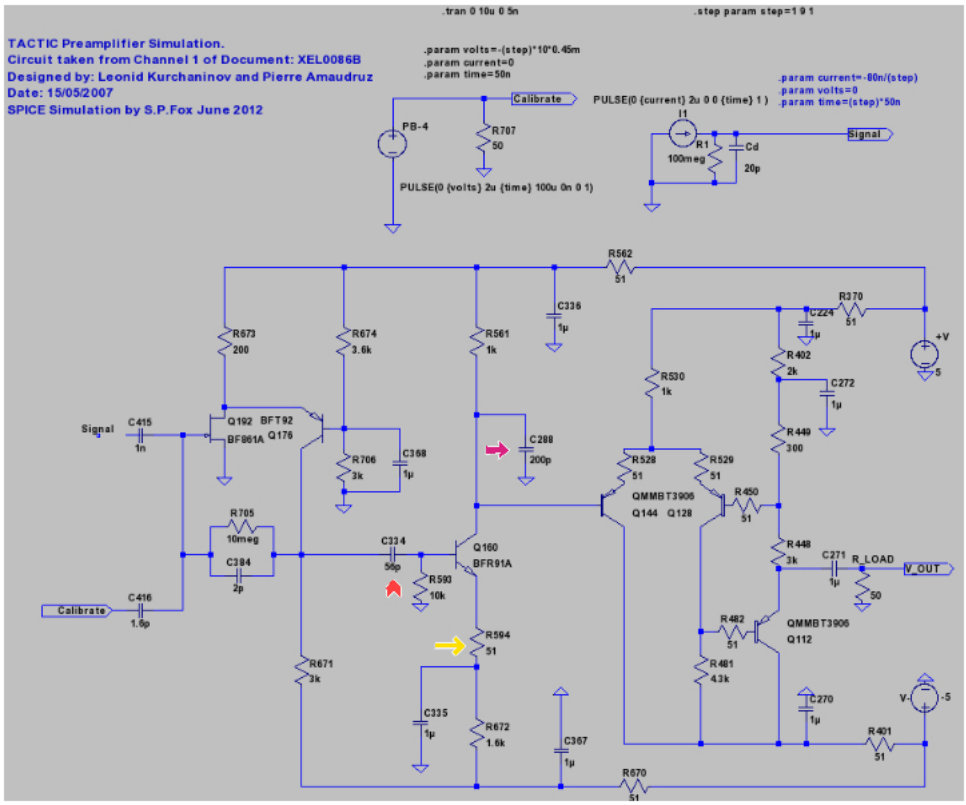

Figure 6.9: SPICE model for a single unmodified TACTIC preamplifier channel [81]. The red, magenta, and yellow arrows indicate the positions of the modified circuit components, i.e., C334, C288, and R594, respectively.

tube inside the chamber. The window was made of aluminised-mylar material with thickness ≈ 2.5 μm, which also separated the beam line vacuum (P $\approx 10^{-6}$ Torr) from the target gas inside the chamber (P $\approx$ 760 Torr). The downstream beam tube had an 10 mm aperture without a window, as a physical volume separation was not necessary between the target region and the Faraday cup. The chamber was connected to a diagnostics box on the upstream end and a Faraday cup on the downstream end through standard KF-16 flanges on the beam tubes and KF-16 bellows, as illustrated in the Fig. 6.10. The upstream diagnostics box had a target ladder in place with apertures of 3 mm, 5 mm, 10 mm and was predominantly used for beam tuning in conjunction with the Faraday cup. The 5 mm aperture with zinc sulphide coating on the edges was also used during the in-beam tests to monitor beam transmission through to the chamber. Both convectron and ion gauges were also installed on the diagnostics box to monitor the beam line vacuum.

Similar to the test chamber setup (discussed in Section 5), TACTIC gas flow and in-situ gas mixing for the target and the detection volume were controlled with MKS 647C MGC (Multi Gas Controller) and 1179A mass-flo Controller modules [70, 71]. The gas pressure inside the chamber was monitored using a MKS Baratron manometer. Among the total 480 anode pads, only 60 were connected through the feed-through PCBs to their own preamplifier channels (discussed in Section 6.2.3) due to the lack of DAQ resources. The output channels of the preamplifiers were connected to a 64-channel CAEN V1740 digitiser [14] via two standard 32-channel ribbon cables. The digitiser was used to record full traces of the raw pulses for each

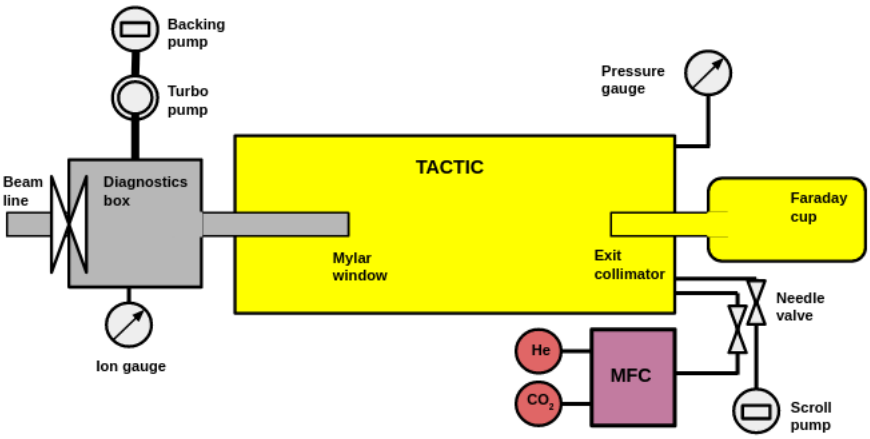

Figure 6.10: Schematic diagram of TACTIC experimental arrangement. The grey and the yellow regions indicate the beam line vacuum and TACTIC vacuum, respectively.

channel.

For the source tests, the chamber was decoupled from the upstream diagnostics box and the Faraday cup. Also, a combination of a source holder and a blank was used to replace the beam tubes. The source holder and source position measurement inside TACTIC are discussed in Appendix B. The rest of the setup, e.g., the gas handling system, the preamplifiers, and the digitiser, were kept the same.

6.4. Experimental method

6.4.1. Measurement of reaction cross section

Unlike detectors like MUSIC [66], MAYA [83], TACTIC does not have the advantage of being able to detect the point at which the differential energy loss ($-dE/dx$) changes at the reaction vertex. As discussed in Section 6.2.1, the target region in TACTIC is shielded by the cathode cage. However, identifying the reaction vertex is important in order to estimate the reaction energy. TACTIC was conceived upon the concept that the unobserved reaction vertex at $r \approx 0$ mm would be reconstructed by extrapolating the trajectory of a reaction product in the detection region ($12 \lesssim r \lesssim 50$ mm). The methods utilised to reconstruct the reaction vertex and the related uncertainty are discussed in Sections 6.4.2 and 6.4.4. Once a reaction vertex has been acquired, the particle track must be analysed for identification, which is required to ascertain if the particle was a product of the reaction of interest. The number of reaction products of interest (yield) corresponding to specific reaction vertices allows for the estimation of the excitation function.

6.4.2. Reconstruction of reaction vertex

In the detection region, the particle track can be reconstructed by measuring the relative drift times of the ionisation electrons liberated by the interaction between

the charged particle and detector gas. Measurement of the electron drift times and identification of the anode pads where the signals are measured, can be used to obtain the corresponding track radius (r_d) and track base (z_d) in the detection region, respectively. The track angle (θ) and the end position of the track, z_f (corresponding to a pad p_f) can also be measured with a given uncertainty that arises from the width of the anode pads ($p_w = 4.2$ mm). As illustrated in Fig. 6.11, a part of the track inside the cathode cage ($r < 12$ mm) remains undetected; therefore the part of the track in the detection region is extrapolated to obtain the reaction vertex (v_z). The vertex and related important parameters for the reconstruction can be calculated using the equations below:

$$z_d = p_w \cdot m_{track}, \tag{6.9}$$

$$\theta = \arctan\left(\frac{r_d}{z_d}\right), \tag{6.10}$$

$$r_{track} = r_c + r_d \quad , \tag{6.11}$$

$$z_{track} = \frac{r_{track}}{\tan\theta}, \tag{6.12}$$

$$v_z = z_f \pm z_{track}, \tag{6.13}$$

where m_{track} is the track multiplicity, i.e., the number of pads above detection threshold, $r_c \approx 12$ mm is the radius of the cathode cage, and z_f is the z-coordinate of p_f. r_d can be calculated by estimating the trigger time difference between p_i and p_f, i.e., t_i'. The detailed radius calculation procedure, and error propagation related to different parameters are discussed in Section 6.4.3, and 6.4.4, respectively. The drift time difference directly translates to the trigger time difference from the DAQ between the first and final pad of a track. The track radii were estimated using Eq. 6.11 under the assumption that all the tracks get detected in the immediate vicinity of the cathode cage and the vertex position is at $r = 0$ mm. A careful approach is required to understand the results obtained under this assumption, which can give rise to anomalous vertex estimations. Some discrepancies are to be expected as the detection of a track is dependent on the energy thresholds used as well as the radial deviation of v_z from the central axis ($r = 0$ mm) due to the radial straggling of the beam or the dimension of the active area of the calibration source (see Appendix A).

6.4.3. Calculation of track radius

Both tracking inside the detection region and reconstruction of the reaction vertex require a robust calculation of track radius. The radii can be calculated from the drift times of the ionisation electrons collected by each pad in a track. Garfield [28] was used to model the electric field strength and to calculate the drift times inside the cylindrical TACTIC geometry. For a specific geometry, the electron drift time varies for different gases or gas mixtures, and for a given gas, it is dependent on the electric field strength and pressure (discussed in Section 3.7). Garfield uses the

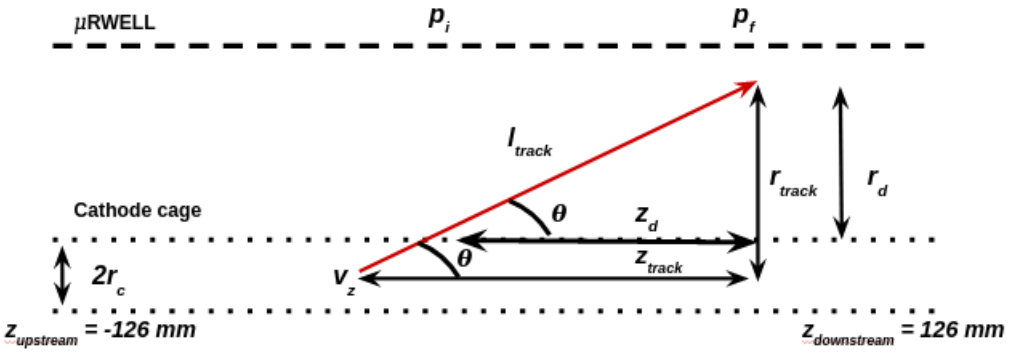

Figure 6.11: A schematic diagram of TACTIC illustrating a charged particle track (red line) with track length l_{track}, track base (z_{track}), track radius (r_{track}) and track angle (θ). The detected part of the track has a track base z_d and track radius r_d. The first and the final pad positions in the track are p_i and p_f, respectively.

Magboltz [84] program, which has an extensive database of electron interaction cross sections for different gases, to calculate drift velocities. The Garfield calculations were made under the assumption that the gas pressure is equal and the gas mixture is homogeneous throughout the chamber. The assumption should hold good, as the tests were performed using a constant gas flow rate ≈ 100 sccm (Standard Cubic Centimetre) to address the potential separation of the gas mixture constituents inside the chamber. For a constant gas pressure, the drift times are primarily dependent on the variation in the electric field strength along the electron drift path. Therefore, a precise measurement of the electron drift time, along with knowledge of the geometry dependent variation of drift velocity allowed the calculation of the radius, i.e., the position inside the chamber from which the electron originated. Any given electron drift time can be associated with a radius value (r). In TACTIC, each pad in a track had a unique drift time and a radius value associated with it.

The electric fields for the Garfield calculations were chosen based on a range of expected operational electrode voltages. The electric field calculation inside TACTIC is complicated, as the chamber is not exactly symmetrical in ϕ. The pitch of the inner and outer cathode wires is not fine enough to be considered uniform; therefore the electric field in the cathode cage region cannot be assumed to be identical in ϕ. The field between the wires was found to be distorted by the contribution from adjacent wires in the gap between the inner and outer cathode wires [8]. This asymmetry of the electric field in ϕ leads to a variation of drift times, affecting the radius estimation. In order to address this asymmetry, an approximation was made that can justifiably represent the majority of drift electrons [8]. It was found that the variation of drift times with ϕ is small and confined to the region in the immediate vicinity of the cathode wires ($r < 13$ mm) [7]. Therefore, a drift time calibration can be adopted sufficiently by using Garfield, which is independent of the variations in drift time with ϕ. Garfield was used to simulate and calculate the electric field strength and electron drift times along a radial line equidistant between the outer cathode cage wires ($r \approx 12$ mm) and the μ-RWELL ($r \approx 50$ mm). The simulations used are the analytical simulation of a

single drifting electron (DRIFT_MICROSCOPIC_ELCTRON) and re-ionisation (MICROSCOPIC_AVALANCHE). The calculations take into account a number of experimental variables, e.g., TACTIC geometry, the gas mixture, the pressure, and the drift field. Electrons were simulated to be released and drift from different positions within the range of 12 mm $\lesssim r \lesssim$ 50 mm in 100 steps. The results are shown in Fig. 6.12. In principle, the fit function from the plot in Fig. 6.12 can be used to calculate the origin radius of any drift electron inside the drift volume. However, since TACTIC is self-triggering, it measures relative drift times instead of absolute drift times (t_d). The relative drift time measured for each anode pad (t'_{di}) in a track is the time elapsed since the first pad triggered in an event (t_0), i.e., the pad closest to the μ-WELL. The first pad triggered in a track, which also describes the end position of the ion, is considered to be at $t = 0$, and acts as the trigger signal for the data acquisition system. The relative drift times for each pad in a track (t'_{di}), were assigned with respect to t_0.

$$t'_{di} = t_i - t_0, \tag{6.14}$$

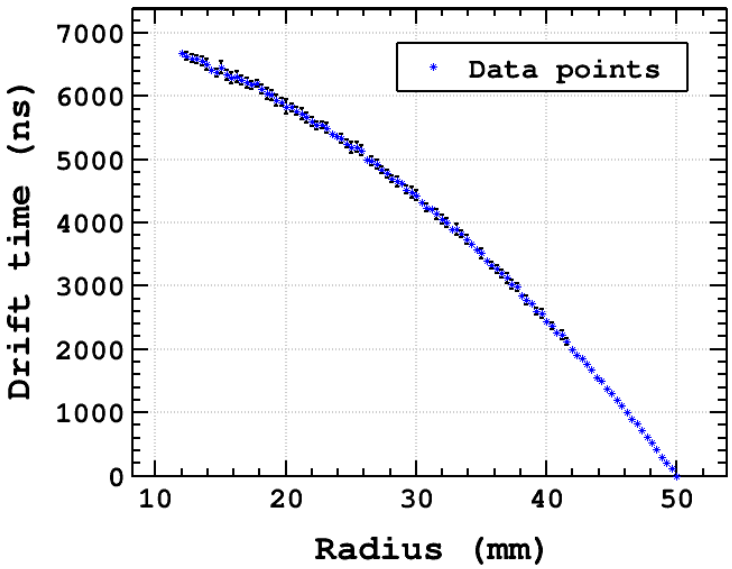

Figure 6.12: The drift times (t_d) of electrons originating from equally spaced points within the range 12 mm $\lesssim r \lesssim$ 50 mm along the drift path for the drift voltage (V_{drift}) = -800 V. For this Garfield simulation, the gas mixture was He:CO_2 90:10 at 1 bar.

where t_i are the trigger times of individual pads in a track. In order to obtain the relative drift times, an assumption was made that the longest time measured with respect to $t = 0$, is in fact the longest possible drift time (t_{full}) for a specific run containing multiple events, and a specific operating condition determined by the gas mixture, the gas pressure, and the drift voltage. t_{full} was calculated using Garfield and corresponds to the time taken by an electron to drift from the cathode cage to the μ-RWELL. In Fig. 6.12, $t_{full} \approx 6.5$ μs. The data in the Fig. 6.12 was then transformed by subtracting the absolute drift times (t_d) from t_{full} and also the corresponding r-values using the equations 6.15 and 6.16. This process yields

a series of theoretical t_{dr} values for specific radius differences (r_d) as illustrated in Fig. 6.13.

$$t_{dr} = t_{full} - t_d(r_i). \tag{6.15}$$

$$r_d = r_i - r_c, \tag{6.16}$$

where $r_i > 12$ mm and $r_c = 12$ mm. The data in Fig. 6.13 was fitted using a polynomial function,

$$r_d = p_0 + p_1 \cdot t_{dr} + p_2 \cdot t_{dr}^2 + p_3 \cdot t_{dr}^3. \tag{6.17}$$

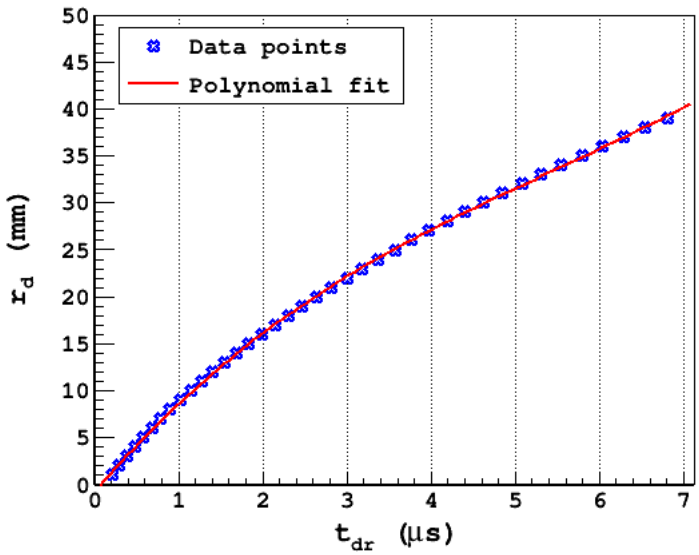

Figure 6.13: A plot of the theoretical t_{dr} values, i.e., the time taken for an electron to drift from the outer cathode cage to a greater r-value, up to the radius of the μ-RWELL. The maximum t_{dr} value is the same as $t_{full} = 6.5$ μs, corresponds to the maximum $r_d \approx 38$ mm, which signifies the maximum drift radius inside the chamber.

For each track inside TACTIC, the largest measured trigger time difference, t'_i, was determined by transforming the corresponding t'_{di} value,

$$t'_i = t_{full} - t_{max} + t'_{di}; \qquad t'_i \leq t_{max}, \tag{6.18}$$

where t_{max} is the maximum possible value of t'_i for a specific detector setup. For a real measurement, t_{dr} values can be replaced by t'_i in Eq. 6.17,

$$r_d = p_0 + p_1 \cdot t'_i + p_2 \cdot t'^2_i + p_3 \cdot t'^3_i. \tag{6.19}$$

The above equation and Eq. 6.11 were used to calculate r_d associated with a measured t'_i and the track radius (r_{track}) under the assumption discussed in Section 6.4.2.

Due to the ϕ-asymmetry in the electric field calculation, the value of t_{full} calculated by Garfield was not fully trusted. Instead, the actual data was used for the normalisation of the relative drift times for a specific experimental setup. As long as some of the events contain tracks that hit the μ-RWELL, the maximum value of t_i', i.e., t_{max} should be in good agreement with t_{full}. Fig. 6.14 shows the calculated track radii from ^{23}Na beam runs with He:CO_2 90:10 as the target gas mixture. The majority of the tracks corresponding to t_{max} were protons from the (α, p) and alphas from the $(\alpha,\ \alpha)$ interactions. The drift field, the gas mixture, and pressure used were similar to the aforementioned Garfield calculations. The half-height point of the falling edge was considered as the value of $t_{max} = 6.8 \pm 1.1$ μs, which agrees with $t_{full} \approx 6.5$ μs. Furthermore, the maximum track radius obtained was found to be in reasonable agreement with the expected upper limit of $r \approx 50$ mm. The Garfield calculations were repeated for different voltages but not for different gas pressures, as it is known from Eq. 3.11 that the drift velocity depends on the electric field to gas pressure ratio. Fig. 6.15 shows t_{full} and t_{max} for the different V_{drift}/P values.

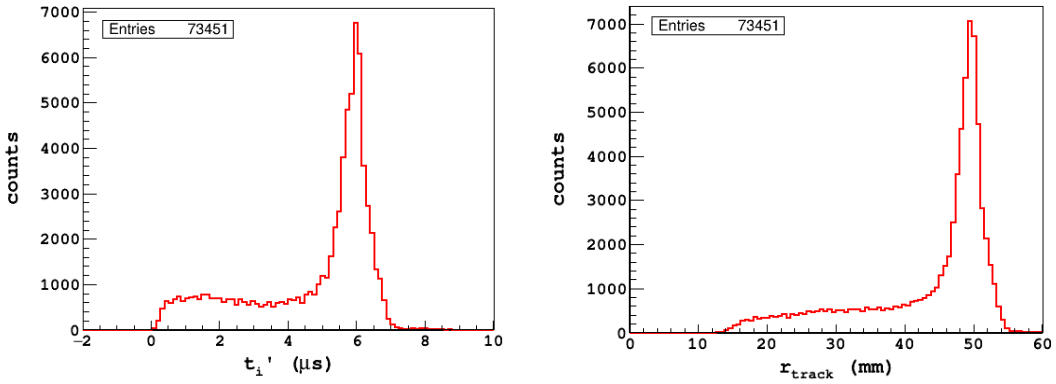

Figure 6.14: [**Left**]: Relative drift times, or the differences between the earliest and latest signals for stable beam runs 61, 64, and 65 (discussed in Section 7.2) and alpha run 26073 (discussed in Section 7.1.4). The highest value of t_i' is $t_{max} = 6.8 \pm 1.1$ μs, estimated at the half-height point of the falling edge. [**Right**]: Calculated track radii for multiple events. The majority of the tracks in the data set corresponding to t_{max}, terminate at the μ-RWELL ($r \approx 50$ mm). A Gaussian fit of the peak yielded, $r_{track} = 49.3 \pm 1.9$ mm.

6.4.4. Uncertainty in vertex estimation

The vertex reconstruction discussed in Section 6.4.2 is subject to uncertainties. The main contributions were identified to be from the diffusion of drift electrons, the width of the anode pads, the statistical uncertainty from the track itself, the radial straggling of the beam, or the source diameter for the calibration source measurements. However, it was shown using Magboltz calculations that in the TACTIC geometry the influence of diffusion in the detector gas towards the vertex uncertainty is negligible compared to the other factors [8]. It was found that the diffusion coefficients decrease with electric field strength and increase with pressure, so the maximum diffusion will occur when in the experimental setup the cathode voltage is at its highest limit and the pressure is at its lowest. The cathode voltage and the

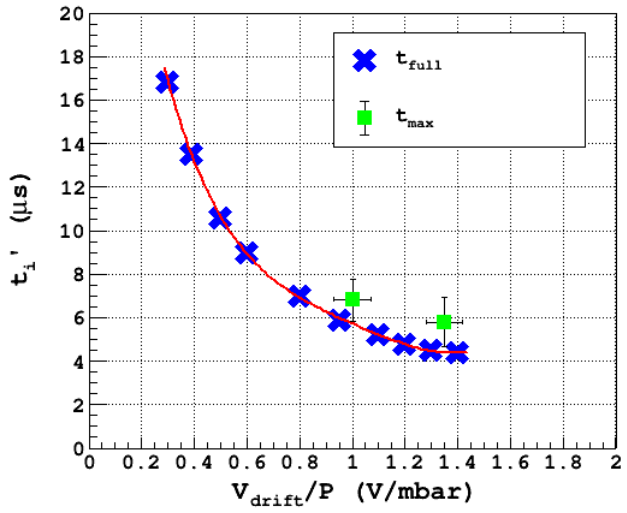

Figure 6.15: Maximum drift time for different parameter settings in He:CO_2 90:10. Experimentally obtained t_{max} shown in green, vertical error bars were estimated from the widths of the falling edge. Blue points represent t_{full} calculated using Garfield and agree well with t_{max} within error limits.

gas pressure used for most of the tests discussed in Chapter 7 were -1600 V and 1 bar, respectively. The maximum contribution from the transverse and longitudinal diffusion for similar voltage and pressure values in TACTIC was estimated to be $\lesssim$ 0.4 mm (see Fig. 6.16), which can be considered negligible compared to the uncertainty in the track radius (r_{track}) estimation.

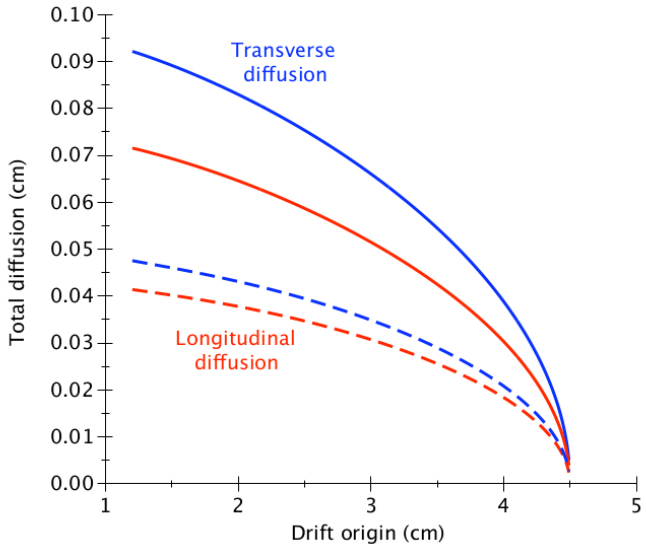

Figure 6.16: The total longitudinal and transverse electron diffusion against the origin in r of the drifting electrons at two different TACTIC operating cathode voltage and pressure. Dotted lines represent diffusion at a pressure of 1 bar and -1800 V on the cathode; solid lines represent 0.1 bar and -900 V on the cathode. The maximum diffusion takes place at the drift origin $r \approx 12$ mm [8].

If a total measurement Z is a function of individual measurements x, y, ..., where

$Z = f(x, y, ...)$ the general formula for the propagation of errors can be written as,

$$\Delta Z = \sqrt{\left(\frac{\partial Z}{\partial x}\right)^2 \Delta x^2 + \left(\frac{\partial Z}{\partial y}\right)^2 \Delta y^2 + ...}, \tag{6.20}$$

where ΔZ, Δx and Δy are the uncertainties in the measurements of Z, x and y. In order to estimate the vertex position (v_z) using Eq. 6.13, the uncertainty in the measurements of z_f, r_c, r_d and θ needs to be taken into account. The uncertainty in v_z can be estimated from the uncertainty in the measurements of z_f (Δz_f) and z_{track} (Δz_{track}) by using the standard propagation of errors method.

$$\Delta v_z = \sqrt{\Delta z_f^2 + \Delta z_{track}^2}. \tag{6.21}$$

The estimation of Δz_f is straightforward. The z-coordinate of the first and the last anode pad in a track was selected randomly within the pad width of 4.2 mm by considering a flat distribution. This results in an effective uncertainty of $2 \cdot p_w/\sqrt{12}$, i.e., $\pm$ 2.4 mm. Δz_{track} was estimated from the definitions in the Eqs. 6.11 and 6.12,

$$\frac{\Delta z_{track}}{z_{track}} = \sqrt{\frac{\Delta z_d^2}{z_d^2} + \frac{\Delta r_d^2}{r_d^2} + \frac{\Delta r_c^2}{r_c^2}}, \tag{6.22}$$

where,

$$z_{track} = f(z_d, r_d, r_c), \tag{6.23}$$

$$z_{track} = z_d\left(1 + \frac{r_c}{r_d}\right). \tag{6.24}$$

Also it follows from Eqs. 6.11 and 6.12,

$$\Delta r_{track} = \sqrt{\Delta r_c^2 + \Delta r_d^2}. \tag{6.25}$$

As expressed by Eq. 6.10, θ is a function of r_d and z_d, therefore $\Delta\theta$ can be estimated from the slope ($s = r_d/z_d$) of a track. The uncertainty in s (Δs) can be expressed as,

$$\Delta s = s\sqrt{\frac{\Delta r_d^2}{r_d^2} + \frac{\Delta z_d^2}{z_d^2}}, \tag{6.26}$$

$$\Delta\theta = \sqrt{\frac{\Delta r_d^2}{z_d^2}\cos^2\theta + \frac{\Delta z_d^2}{z_d^2}\sin^2\theta}. \tag{6.27}$$

where, $\Delta z_d = \pm$ 2.4 mm, i.e., the same as Δz_f. following from Eq. 6.9. The Eq. 6.21 can be used to obtain the theoretical estimates of Δv_z. The second term has significant contributions from estimates of both r_c and r_d. Δr_c originates from the radial straggling of the beam and the size of the beam spot ($\Delta r_c \approx 4.0$ mm) or the active radius of the calibration source used ($\Delta r_c \approx 2.0$ mm). Δr_d can be estimated by using Eq. 6.17.

Chapter 7

TACTIC: results

This chapter contains a comprehensive study of the recently modified TACTIC setup was conducted at TRIUMF between May 2022 and September 2023. The study included a series of alpha source measurements and stable beam tests, focusing on a number of key areas:

- Tracking accuracy: reaction vertex reconstruction resolution.
- Particle identification capability.
- Verification of the cylindrical symmetry.
- Low energy ($<$ 100 keV) detection capability.
- Characterisation of the novel μ-RWELL in cylindrical geometry.

The tests were aided by NPTool simulation, discussed in the chapter 4. The motivation for the tests detailed in this chapter was to achieve a detailed characterisation of the detector setup and its commissioning. The source test results discussed in Section 7.1 were ultimately used in conjunction with the stable beam tests detailed in Section 7.2 in order to study the aforementioned areas of focus.

7.1. Alpha source studies

Alpha source measurements are important for the characterisation of a charged particle detector like TACTIC, as they offer a high degree of reproducibility and precise knowledge of position and energy. Furthermore, the source tests were used to verify the experimental method discussed in Section 6.4 and the accuracy of the detector simulation. The alpha source used for the tests consisted of a dot of radioactive material (^{148}Gd) on a metal backing. The source details and its position inside TACTIC are discussed in App. A and B.

7.1.1. Tracking

The alpha source at a fixed position (z_s = -16 $\pm$ 2 mm) was used to test the accuracy of the method for vertex and reconstruction described in Section 6.4. The alpha events recorded by the CAEN V1740 digitiser were analysed and a set of TACTIC coordinates (r, z, θ) were extracted for individual events or tracks, comprising

of a specific number of triggered anode pads. Each triggered pad in an event can be specified by a point inside TACTIC coordinate space. A group of consecutive points lying in a straight line was assumed to be a track. If the group contains less than three points, two special cases arise. For events with only one point in them, one has to assume an infinite slope, which leads to incorrect estimation of the track parameters. Two-point tracks are on the other hand provide the minimum number of points to calculate the slope from, therefore the accuracy can not be estimated. Thus, one and two-point tracks were ignored in analysis. For statistically sound estimates of track parameters, tracks with five points or more ($m_{track} \geq 5$) were considered in analysis. This choice of multiplicity becomes more relevant for the vertex reconstruction using stable beam data (discussed in Section 7.2.2).

For track reconstruction, multiple track parameters, i.e., r_d, z_d, θ, need to be extracted from an event. As discussed in Section 6.4.3, the track radius (r_{track}) was calculated using Eqs. 6.11 and 6.17. Fig. 7.1 shows the track radii obtained from an alpha run in He:CO_2 90:10 at 0.5 bar pressure. The gas pressure was chosen in a way that the majority of the alpha tracks terminate at the μ-RWELL, which provided a robust measurement of the maximum drift time (t_{max}) in the detection region. The maximum electron drift time (t_{full}) for the same drift voltage and gas pressure calculated using Garfield (see Fig. 6.15) was found to be ≈ 5.2 μs, which agrees with $t_{max} = 5.8 \pm 0.7$ μs within uncertainties. The tracks with $t_i' \geq 5.1$ μs were considered to have terminated at the μ-RWELL (discussed in Section 6.4.3). The drift voltage (V_{drift}), i.e., the voltage difference between the outer cathode wires and the μ-RWELL, for the study was kept constant (see Table 7.1).

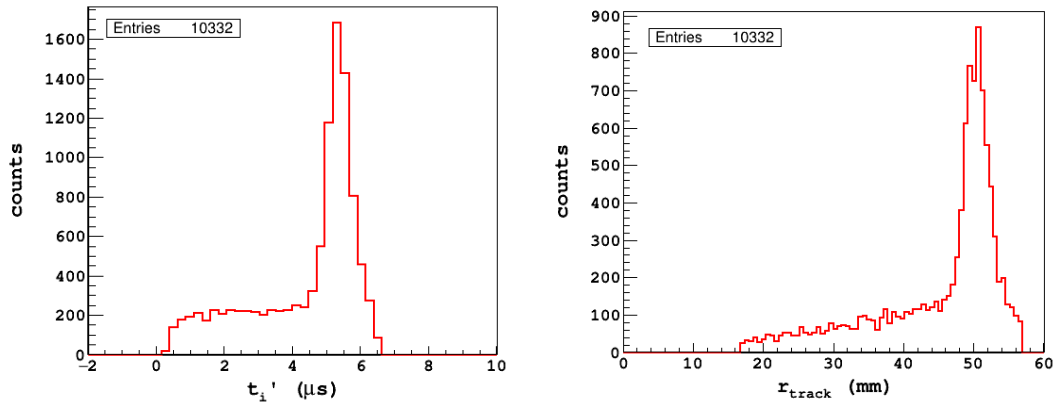

Figure 7.1: [**Left**]: Relative drift times or the trigger time differences between earliest and latest signals for each event in alpha run 02085. The highest value of t_i' is $t_{max} = 5.8 \pm 0.7$ μs, estimated at the half-height point of the falling edge (discussed in Section 6.4.3). [**Right**]: Calculated track radii for multiple events. Majority of the tracks in the data set corresponding to t_{max} as expected, terminate at the μ-RWELL ($r \approx 50$ mm). Gaussian fit of the peak yielded the maximum value of $r_{track} = 50.2 \pm 2.3$ mm.

The calculated value of r_{track} and the multiplicity (m_{track}) were then used to derive the other important parameters necessary for track reconstruction, e.g., z_d, z_{track}, θ, by using Eqs. 6.9-6.12. Every point in a track has an unique pad number (p_i) and a t_{di}' value (defined in Eq. 6.14) associated with it. The t_{di}' values can be

Table 7.1: Experimental details of alpha run 02085.

Parameters	**He:CO_2 90:10**
Pressure	0.5 bar
Drift voltage (V_{drift})	-750 V/cm
μ-RWELL bias (ΔV)	-460 V

substituted in Eq. 6.19 to calculate the corresponding r-coordinate in the detection region. Fig. 7.2 shows a reconstructed alpha track.

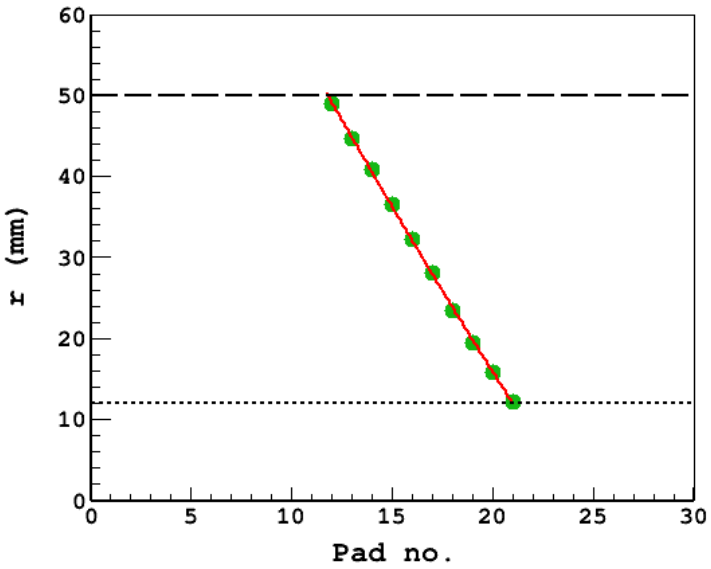

Figure 7.2: A reconstructed alpha track from alpha run 02085 (event number: 45; sector number: 1). The track starts at the cathode cage ($r \approx 12$ mm) and terminates at the μ-RWELL ($r \approx 50$ mm), thus, traversing the entire r-range of the detection region. Track parameters: t_i' ($\approx t_{max}$) = 5.6 $\pm$ 0.6 μs, m_{track} = 10, $\theta \approx 40°$. A second order polynomial fit yielded: p_0 = 105.71 $\pm$ 2.98, p_1 = -5.05 $\pm$ 0.34, p_2 = 0.03 $\pm$ 0.01. The value of p_2 can be used as a measure of the straightness of a track. For an ideal straight track, p_2 should have a value of 0.

Consecutiveness

In order to estimate z_d by using Eq. 6.9, the track multiplicity (m_{track}) needs to be obtained correctly. If a track has one or more missing points, it leads to an inaccurate estimate of m_{track}, which in turn introduces an additional systematic uncertainty to the reconstructed vertex. A parameter consecutiveness (c_{track}) was used in the analysis to identify tracks with non-consecutive points or pad hits. The analysis code identifies the anode pad positions (p_i) triggering above a set threshold and the difference between the consecutive pad positions (c_i) as defined in Eq. 7.1 for each event. As an example, an event with m_{track} = 5 will yield four individual c_i values. The maximum c_i value in an event was defined as the consecutiveness.

$$c_i = p_{i+1} - p_i; \quad 1 \leq i \leq 60. \tag{7.1}$$

The missing points in a track can have various origins: electronic noise, detection threshold set at the digitiser for the individual channels, interference from the background, crossover events where parts of single track getting detected by two or more sectors. Fig. 7.3 includes a few such examples. For a continuous event with no missing pads between the first and the final pad, $c_{track} = 1$. Fig. 7.4 shows the c_{track} values for the events with $m_{track} \geq 5$, for alpha run 02085. Majority of the events ($\approx 99.6\%$) in the run were found to be consecutive. The events with $c_{track} = 1$ were chosen for vertex reconstruction. It is noteworthy that an event selection criteria based on consecutiveness alone, does not address the tracks with missing points at their extremities but, together with the assumption that all tracks begin at the cathode cage (discussed in Section 6.4.2) and by selecting events which traverse the entire detection region (see Fig. 7.2), a reliable estimate of the vertex position can be obtained (see Section 7.1.3).

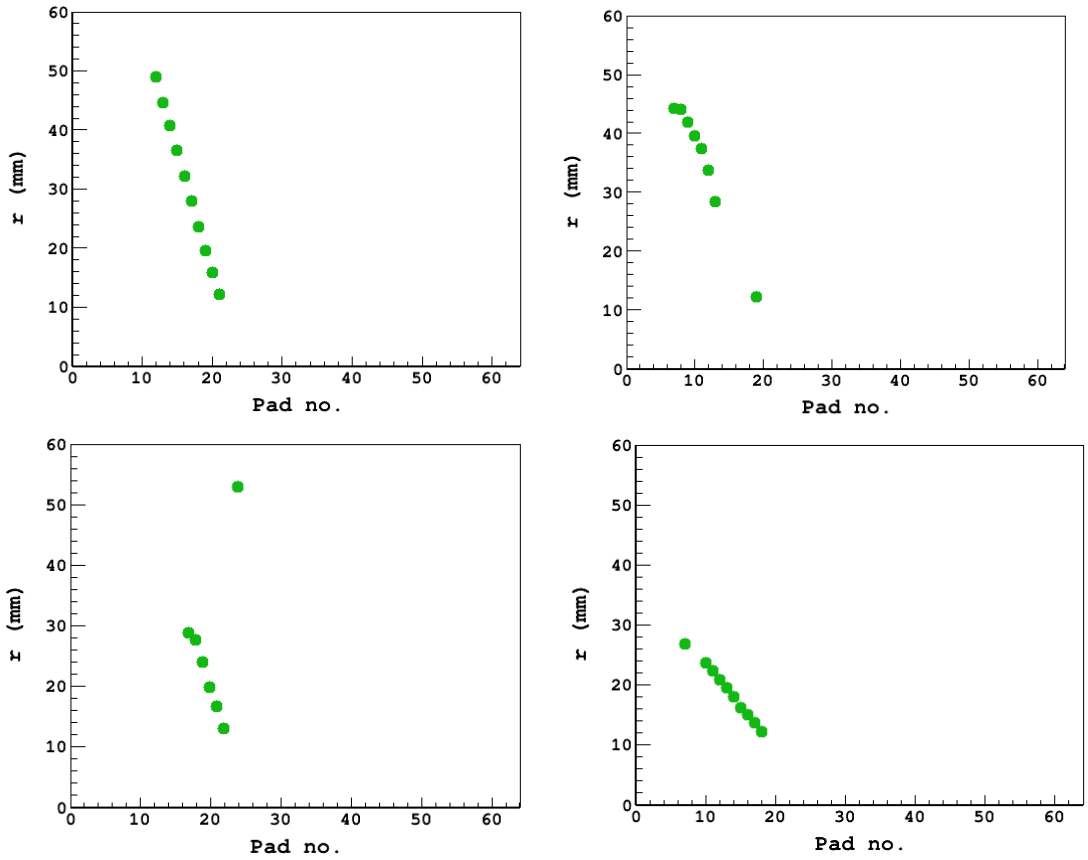

Figure 7.3: Reconstructed tracks from alpha run 02095. [**TL**]: $c_{track} = 1$; the track details are in fig, 7.2. [**TR**]: $c_{track} = 6$; the missing pads in the middle were believed to be below the detection threshold set at the digitiser. [**BL**]: $c_{track} = 2$; the single spurious point at r $>$ 50 mm was likely due to electronic noise. [**BR**]: $c_{track} = 3$; similar to the case shown in the TR plot.

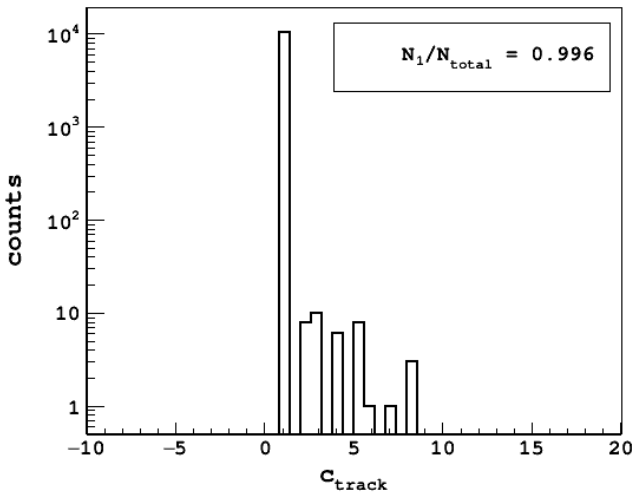

Figure 7.4: c_{track} for the events with $m_{track} \geq 5$, in alpha run 02085. N_1 and N_{total} are the number of events with $c_{track} = 1$ and the total number of events, respectively.

7.1.2. Comparison with simulation

In order to verify the accuracy of TACTIC tracking algorithm, calculated track parameters, e.g., angle (θ), radius (r_{track}), multiplicity (m_{track}) were compared with simulation (discussed in Chapter 4). As discussed in Appendix A, the ^{148}Gd calibration source used for the tests had an unknown protective layer, which causes energy straggling. In addition to this, the electron multiplication from μ-RWELL also introduces an energy resolution of $\approx 8\% - 30\%$ in He:CO_2 90:10 (see Sections 5.3.1 and 5.3.3). Thus, to make the simulation useful for comparison with real data, an energy resolution was added to the initial alpha energies. Instead of a single alpha energy, a normal distribution function was used in the simulations:

$$f(x) = \frac{1}{\sigma\sqrt{2\pi}} \cdot exp\left[-\frac{(x-\mu)^2}{2\sigma^2}\right], \tag{7.2}$$

where σ and μ are the standard deviation and mean of the energy distribution, respectively. A comparison between the simulation and the calculated parameters is shown in Fig. 7.5. The histograms show the relation between track angles and multiplicities. The ranges and distributions of both track angle and multiplicities were reproduced well in the simulation. TACTIC responses were not energy calibrated and thus, it was not possible to identify the minimum energy threshold from the source data. The agreement between the multiplicities was used to determine a minimum energy threshold. Without an energy threshold, the simulated multiplicities were found to be sensitive to very small energy depositions, especially at the end of the tracks (< 50 keV). Also, the simulation does not include the effect of the electronic noise. During the source tests, in order to avoid electronic noise, a minimum energy threshold was set at the digitiser. For a more realistic comparison, an energy threshold of 50 keV per pad was applied during the analysis of the simulated data. The relation between track angles and track radii was also studied. Fig. 7.6 shows that most tracks with $\theta > 28°$ terminate at the μ-RWELL ($r \approx 50$ mm), which was expected for the range of alpha particles in the gas mixture and the pressure used. The shallower tracks stop inside the gas volume. This is further investigated in Fig.

7.8. The range of parameters also agrees well with the simulation. The broader distribution in real data arises from the statistical uncertainties in r_d and θ. The uncertainties in θ were calculated using Eq. 6.27 (see Fig. 7.7). The z-resolution of the anode pads leads to a larger uncertainty for steep tracks and since smaller angles correspond to a larger number of track points, the estimations become more accurate. The maximum track angle uncertainty ($\Delta\theta$) was found to be $\approx 0.45°$ for $\theta \approx 60°$. It is noteworthy that $\Delta\theta$ is the statistical error in the estimation of θ and does not fully capture the effects of angular straggling. Even under ideal circumstances, the reconstructed angle will not accurately reproduce the emission angle at the vertex, which is mostly due to the straggling of the ion, i.e., deviations of the actual track from a straight line. This will be further discussed in Section 7.2.

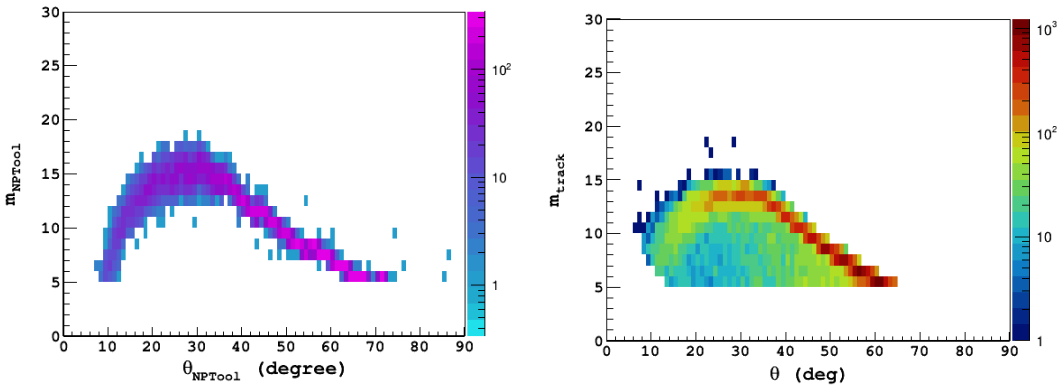

Figure 7.5: [**Left**]: Multiplicity versus track angle from the NPTool alpha source simulation with minimum energy threshold of 50 keV per pad. Range of parameters: $5 \leq m_{NPTool} \leq 16$, $5° \lesssim \theta_{NPTool} \lesssim 72°$. Data cuts used: $m_{NPTool} > 4$. [**Right**]: Multiplicity versus track angle for alpha run 02085. Range of parameters: $5 \leq m_{track} \leq 15$, $8° \lesssim \theta \lesssim 66°$. Data cuts used: $m_{track} > 4$, $r_d > 5$ mm.

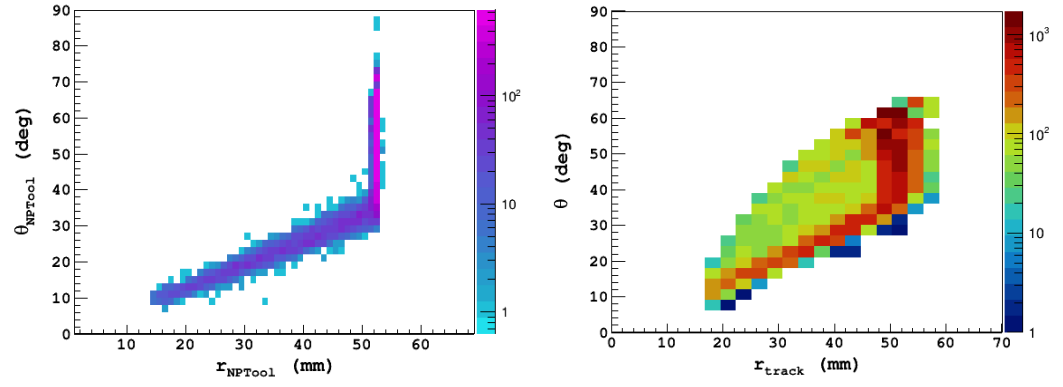

Figure 7.6: [**Left**]: Track angle versus track radius from the NPTool alpha source simulation with minimum energy threshold of 50 keV per pad. Range of parameters: 12 mm $\lesssim r_{NPTool} \lesssim$ 50 mm. Data cuts used: $m_{NPTool} > 4$. [**Right**]: Track angle versus track radius for alpha run 02085. Range of parameters: 17 mm $\lesssim r_{track} \lesssim$ 52 mm. The lower limit of $r_{track} \approx 17$ mm is due to the selection criteria $r_d >$ 5 mm, used in the analysis. This data cut was used to negate relatively high field uncertainties in small radius calculation using Garfield, as discussed in Section 6.4.3.

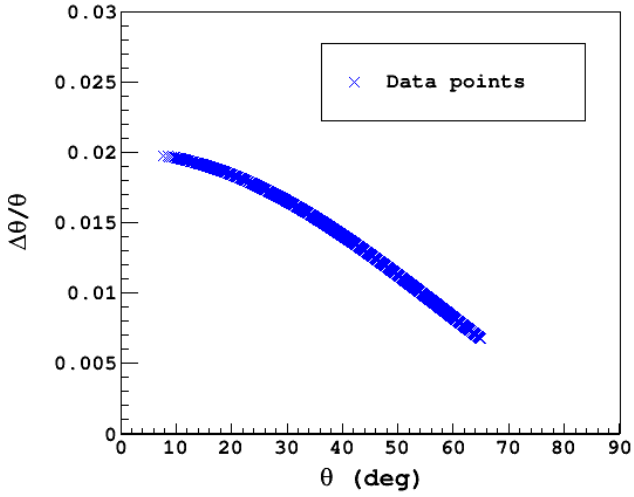

Figure 7.7: Relative systematic uncertainties in the estimation of track angle, θ, as per Eq. 6.27. The relative uncertainties are comparatively higher for shallower angles, which terminate inside the detection region.

Another important sanity-check for tracking is whether the geometric limits of TACTIC, as defined in Eqs. 6.3-6.5, are well reproduced in the simulated data and how it compares to real data. Fig. 7.8 shows the angular dependence of the detectable track length (l_d) for run 02085. The alpha source position (z_s) for the run was close to the centre of TACTIC and the pressure was chosen to be high enough to be able to stop some of the alpha tracks inside the detection volume and thus the limits l_{us} and l_{ds} are irrelevant in this case. Tracks were found to follow radial limit (l_r) well. For $\theta > 28°$, most tracks terminate at the μ-RWELL, which is in good agreement with the simulation. The range of the alpha particles for the specific run conditions (see table 7.1) was calculated using TRIM [32] to be, $l_{max} = 117.1 \pm 2.4$ mm. All the detectable track lengths were expected to be shorter than l_{max} due to the effect of the cathode cage, as was the case in both real and simulated data. Another important observation was that even in the simulation there is significant distribution of data points around the geometrical limits, especially for the tracks stopping inside the detection region ($\theta \lesssim 28°$). This is mainly because of θ_{NPTool} is determined in the first step of the track and l_{NPTool} is calculated as the distance between vertex and final point. Thus, l_{NPTool} is influenced by the angular straggling from the finite pad width, which also holds true for l_d values.

7.1.3. Vertex reconstruction

The calculated end points of alpha tracks are shown in Fig. 7.9. The bins on the horizontal axis were chosen to be 4 mm wide, so the resolution in the z-coordinate is approximately one pad. Starting at $r = 17$ mm, the locus containing the maximum number of events increases in r-value and plateaus at $r \approx 50$ mm, at which point the alpha tracks were expected to hit the μ-RWELL. This agrees with both TRIM predicted alpha range (l_{max}) and NPTool simulation as shown in Fig. 7.8. As expected, the majority of the tracks terminate at the μ-RWELL and all tracks end within the range, 17 mm $\lesssim r \lesssim$ 50 mm.

The accuracy of the tracking algorithm can be estimated by investigating how

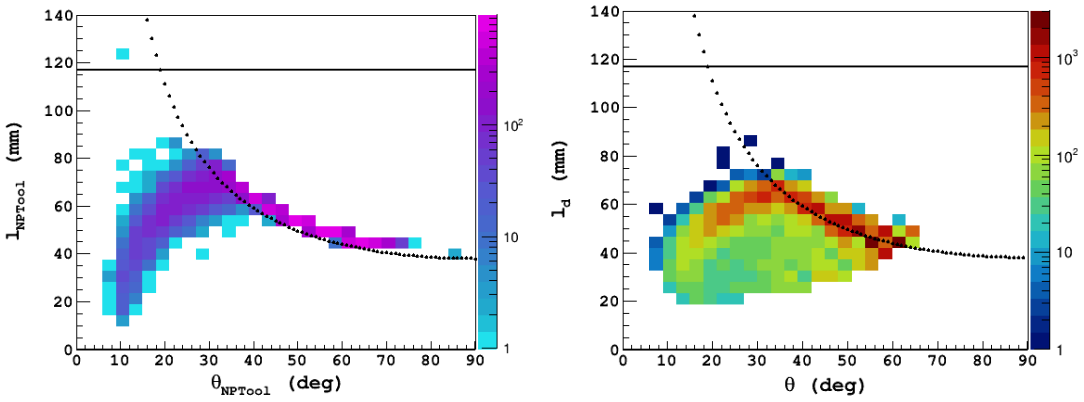

Figure 7.8: [**Left**]: Track length versus track angle from the NPTool alpha source simulation with minimum energy threshold of 50 keV per pad. [**Right**]: Track length versus track angle for alpha run 02085. TRIM predicted range (l_{max}) and the geometric limit imposed by the μ-RWELL (l_r) are represented by solid and dotted black lines, respectively.

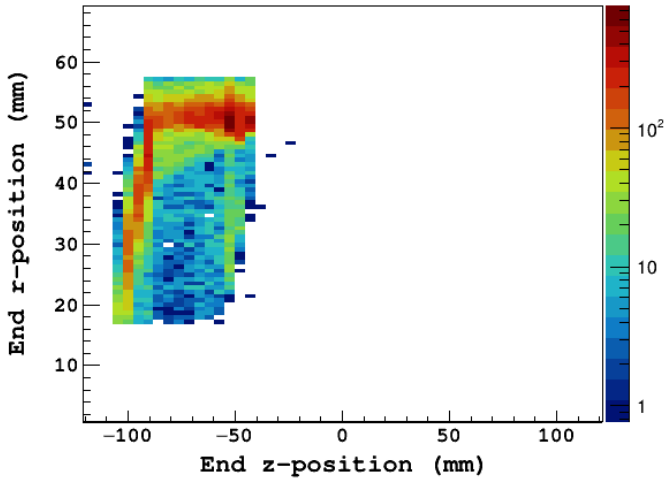

Figure 7.9: The end points of alpha tracks from run 02085. The source was positioned at z_s = -16 ± 2 mm. Data cuts used: $0 < t_i' \leq 6.5$ μs, $r_d > 5$ mm, $m_{track} \geq 5$, $c_{track} = 1$.

well the known position of the alpha source can be reproduced by the track vertex position v_z. Fig. 7.10 shows the relation between track angle and vertex position. The vertex positions were estimated using the method discussed in Section 6.4.2. A good agreement between the measured vertex position (z_s) and the mean v_z from Fig. 7.11, was observed for the majority of tracks ($\approx 98\%$) within uncertainties, i.e., the calculated vertex positions for most tracks agree with the known position of the source. The distribution of v_z was found to be more spread out for steeper angles, which can be attributed to the higher systematic errors associated with steeper angles (see Fig. 7.7). The uncertainty in v_z for shallow tracks ($\theta < 20°$) was dominated by higher degree of angular straggling (discussed in Section 3.5.1). According to Eq. 3.7, angular straggling increases with a decrease in energy towards the end of the tracks. Thus, shallower tracks, which terminate inside the detection region were more susceptible to the effect of angular straggling. In order to improve the ver-

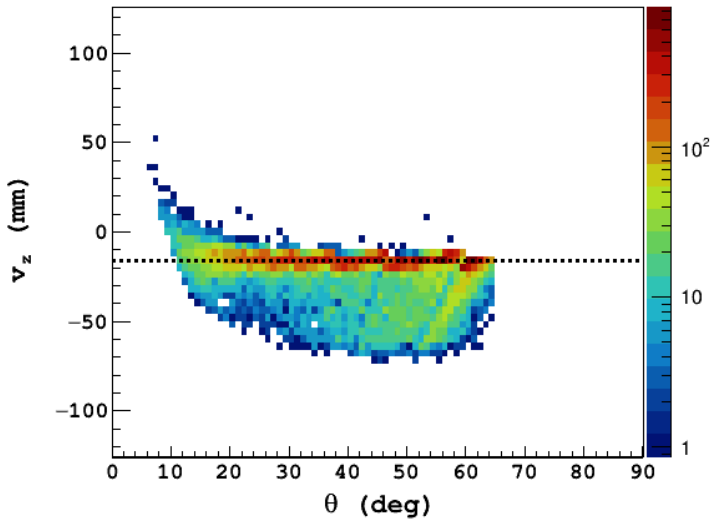

Figure 7.10: Detected vertex position of alpha tracks in relation to track angle for run 02085. Data cuts used: $0 < t_i' \leq 6.5$ μs, $r_d > 5$ mm, $m_{track} \geq 5$, $c_{track} = 1$. The black dashed line represents the real source position as calculated from the source holder and chamber dimensions (see Appendix B).

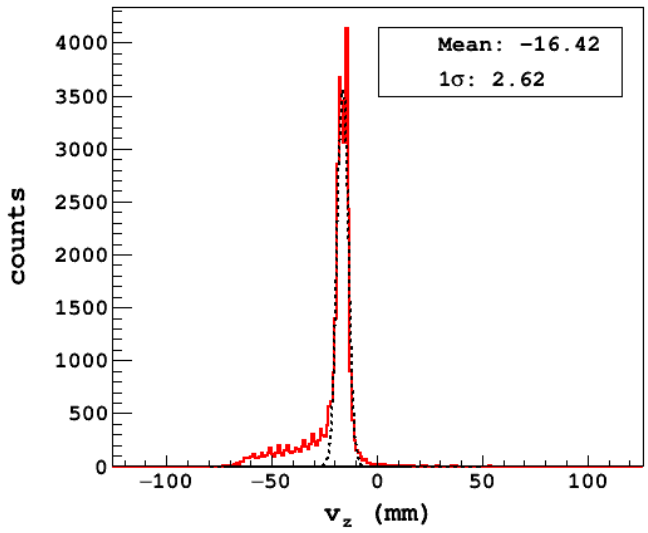

Figure 7.11: Projection of vertical axis from Fig. 7.10. The black dotted line is a Gaussian fit to the detected vertex positions.

tex estimation, an additional time cut ($t_i' > 5.1$ μs) was placed on the data, which selects only the tracks terminating at the μ-RWELL (see Fig. 7.1) following the discussion in Section 7.1.1. Fig. 7.12 shows that placing the time cut on the data removed the shallow tracks with $\theta \lesssim 32°$ and affected the detection efficiency, which reduced by $\approx 45\%$, as per the analysis. Conversely, the uncertainty in the vertex estimation improved by $\approx 26\%$, from 6.1 mm (FWHM) to 4.6 mm (FWHM). Thus, using consecutive tracks terminating at the μ-RWELL significantly improves the vertex reconstruction, which has major implications, especially for the estimation of reaction energy from vertex position. This will be further discussed in Section 7.2. The selection of tracks for vertex reconstruction based on the cuts applied in Fig. 7.12 did not fully address the higher uncertainty in v_z at steeper angles. The

accuracy of the vertex reconstruction method discussed in Section 6.4.2 relies on the assumption that all tracks get detected in the immediate vicinity of the cathode cage and that the actual vertex position is always at $r = 0$ mm. Due to the active area dimension (radius $\approx$ 2 mm) of the calibration source and detection thresholds used, an overestimation of the calculated r_{track} for some tracks was expected. Furthermore, a track can deviate from its straight path due to angular straggling, which becomes more relevant for the shallower tracks that terminate inside the detection volume (see Section 3.5.1). This can also affect the calculation of r_{track} and θ. As shown in Fig. 7.13, the overestimation of track radius was believed to have affected the vertex estimates of tracks outside the FWHM of the distribution, i.e., the region $v_z \lesssim$ -21 mm in Fig. 7.13. According to Eqs. 6.12 and 6.13, an inaccuracy in the calculation of v_z can arise from the overestimation of r_{track}. However, the majority ($\approx$ 94%) of the reconstructed v_z fall within the FWHM of the fitted distribution in Fig. 7.13, with the mean agreeing well with the real source position (z_s). Thus, the degree of accuracy of the vertex reconstruction for most tracks suggests that the aforementioned assumptions and the straight line approximation for tracking inside TACTIC hold good.

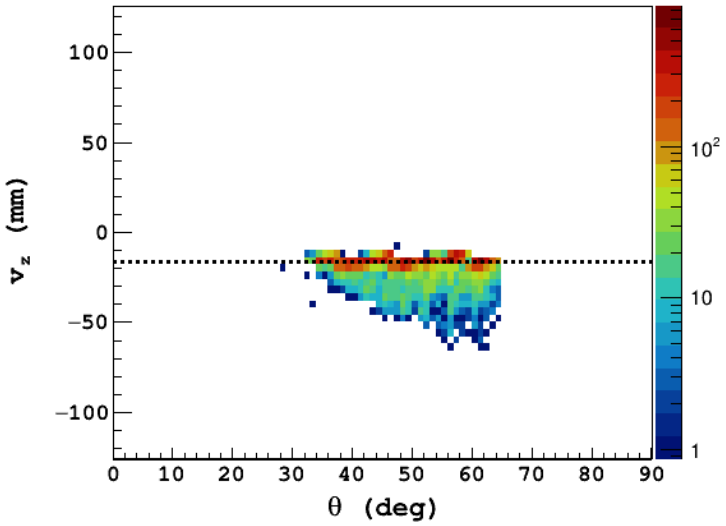

Figure 7.12: Detected vertex position of alpha tracks in relation to track angle for run 02085. Data cuts used: $5.1 < t_i' \leq 6.5$ μs, $r_d > 5$ mm, $m_{track} \geq 5$, $c_{track} = 1$. The black dashed line represents the real source position as calculated from the source holder and chamber dimensions (see Appendix B).

Another way to investigate the accuracy of track angle calculation and vertex reconstruction is to study the dependence of track angle on the position of emergence of a track outside the cathode cage (z_{first}). The value of z_{first} for a track was determined by the first pad in a track (p_i). Fig. 7.14 shows that $v_z - z_{first}$ decreases with angle and assumes a minimum of $\approx$ 10 mm at the maximum calculated angle of $\theta \approx 66°$. This was expected as the shallower alpha tracks will emerge out of the cathode cage at a later point further from the source position, compared to steeper tracks. The base of the track inside the cathode cage (z_{dc}) can be calculated using:

$$z_{dc} = \frac{r_c}{\tan\theta}. \tag{7.3}$$

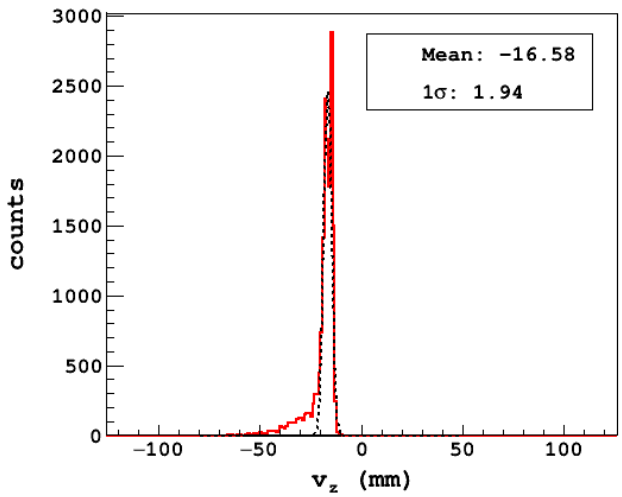

Figure 7.13: Projection of vertical axis from Fig. 7.12. The black dotted line is a Gaussian fit to the detected vertex positions. The overestimation of track radius affected the vertex estimates of tracks outside the FWHM of the distribution.

The value of z_{dc} (5.3 ± 3.1 mm) for the maximum calculated angle agree with the minimum value of $v_z - z_{first}$ = 9.9 ± 3.3 mm within uncertainties (see Fig. 7.14). This result along with the observed accuracy of vertex reconstruction using the alpha source, signify that the vertex reconstruction method and the associated assumptions discussed in the previous chapter are sound and hold good for the majority of the tracks. They were therefore further implemented in the analysis of the stable beam data (discussed in Section 7.2.2).

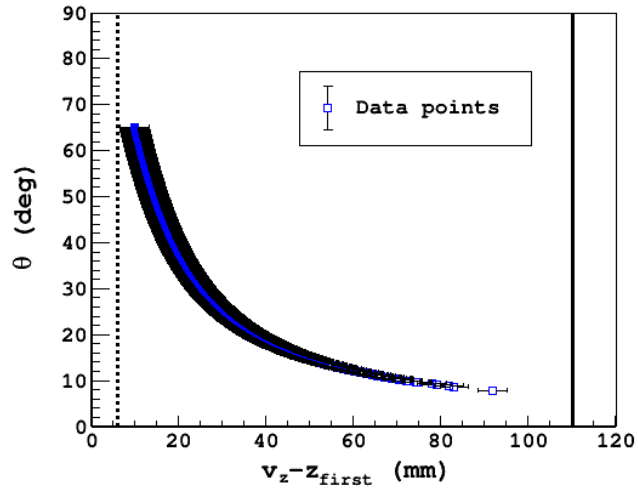

Figure 7.14: Calculated track angles in relation to z_{first} for alpha run 02085 (sector 1). Data cuts used: $0 < t_i' \leq 6.5$ μs, $r_d > 5$ mm, $m_{track} \geq 5$, $c_{track} = 1$. The black dotted and solid lines represent z_{dc} for $\theta = 66°$ and the maximum geometrically possible value of $v_z - z_{first}$, respectively.

7.1.4. Pulse height

An absolute energy calibration was not performed on the TACTIC data. The preamplifiers used for TACTIC tests were identical to the test chamber preamplifiers discussed in Section 5.2. As shown in Fig. 5.6, a systematic variation between the preamplifier channels was present, therefore an energy calibration using a pulser was not reliable. As discussed later in this section and Section 7.2.3, the ^{148}Gd alpha source was used to obtain the conversion of pulse heights to energy. It is noteworthy that in TACTIC, due to the presence of the cathode cage, an accurate energy calibration using the alpha source is also complicated as a fraction of energy is always lost. Thus, in order to achieve a detailed understanding of such geometrical effects on the energy parameters, the NPTool simulation was used. As discussed in Section 7.1.2, a good agreement between the simulation and alpha run analysis results was achieved in terms of the track parameters. It was therefore decided to use the equivalence between the simulated energy deposited per pad and the pulse heights solely as an approximation in order to further study the detector characteristics and aid in particle identification for the in-beam experiment, discussed in Section 7.2.3. Fig. 7.15 shows the trace of a single TACTIC pulse. The raw pulse height (PH_{raw}) was considered to be the peak of the negative pulse, i.e., -150 ADC. The horizontal axis (x_i) was converted from the raw ADC values to time (μs) unit using the conversion formula,

$$x_i(\mu s) = \frac{x_i(ADC)}{n} \cdot t, \tag{7.4}$$

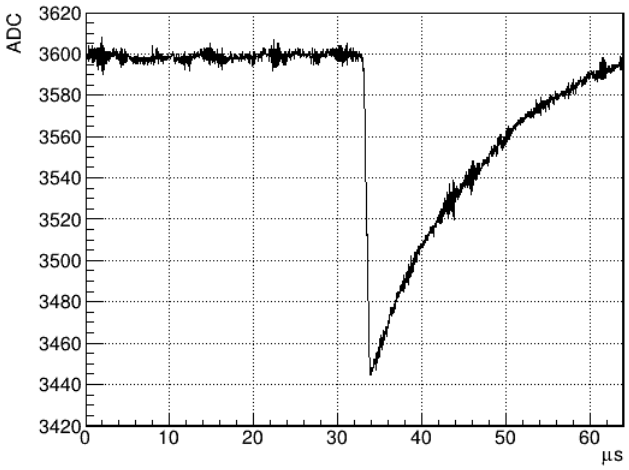

Figure 7.15: Trace of single pulse from alpha run 02085 (event no. 45) from a CAEN V1740 digitiser channel corresponding to a specific anode pad. Set digitiser range on the horizontal axis (time axis): $0 \leq n \leq 4096$ ADC or $0 \leq t \leq 64$ μs and on the vertical axis (amplitude axis): $0 \leq y \leq 4000$ ADC.

where n and t are the record length in ADC channel and equivalent μs units, respectively, set at the digitiser. In order to obtain a good statistical estimate of the pulse height, the standard pulse processing method of moving window deconvolution [82] was used to transform the raw pulse according to Eq. 7.5. The pulse height after the transformation (PH) was used for further analysis.

$$PH(k) = \frac{\sum_{i=j}^{j+4} PH_{raw}(i)}{5}; \quad k = 1, 2, 3, \cdots, j = 1, 6, 11, \cdots, n-4, \tag{7.5}$$

where $\mathrm{PH}_{raw}(i)$ is the pulse amplitude at the i-th position on the time axis. Fig. 7.16 shows the pulse heights across the anode pads triggering above a set threshold for alpha run 02085 (see table 7.1). A Bragg peak signature (see Fig. 3.2) in the region $PH > 120$ ADC was observed between pads 10 to 15, which was expected for shallower tracks with $\theta \lesssim 28°$ (see Fig. 7.6), that terminate inside the detection region. The shorter steep tracks ($\theta > 28°$) mostly terminate at the μ-RWELL (see Fig. 7.8). Thus, most of these tracks were not expected to show the Bragg peak signature. In Fig. 7.16, the pulse height distribution $20 \leq PH \leq 180$ ADC between pads 15 to 25 is representative of the plateau region of the energy loss curve. These trends are also visible in Fig. 7.17, which shows the angular dependence of the maximum pulse height (PH_{max}) in a track. Between pads 15 to 25, some steep tracks ($\theta > 50°$) were found to deposit energies higher than the believed Bragg peak energy corresponding to $180 \leq PH_{max} \leq 260$ ADC. This can be explained by the angular dependence of the track length under a single pad (l_{pad}) in TACTIC geometry (see Eq. 7.6). For steeper tracks, l_{pad} will be higher compared to shallower tracks, which translates to a higher energy loss ($-dE/dx$). This effect can also be observed in Fig. 7.17.

$$l_{pad} = \frac{p_w}{\cos\theta}, \tag{7.6}$$

$$l_{pad} \propto DE, \tag{7.7}$$

where p_w is width of the anode pads and DE is the total energy loss over a pad.

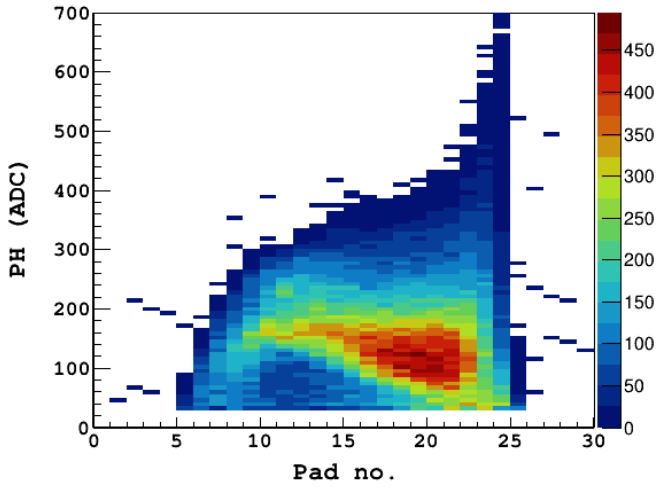

Figure 7.16: Pulse heights across anode pads for alpha run 02085 (sector 1) for all tracks ($m_{track} \geq 1$). The range of alpha particles observed $\approx$ 21 pads or 88.6 mm agree with the NPTool predicted range (see Fig. 7.8). The alpha source position approximately corresponds to pad number 26.

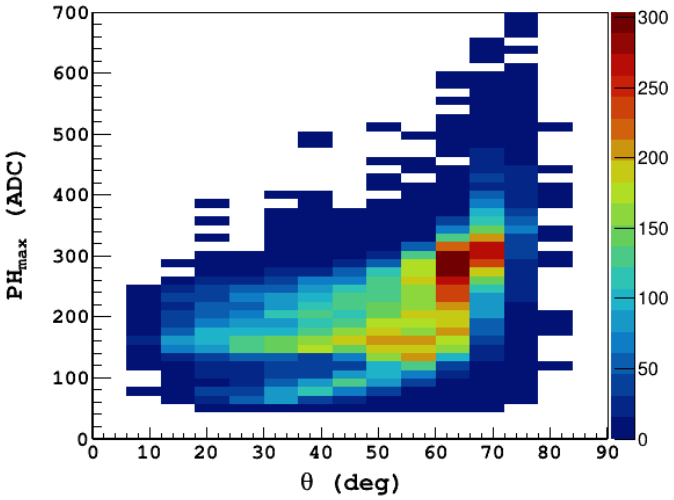

Figure 7.17: Maximum pulse height in a track versus track angle for alpha run 02085 (sector 1). Data cuts used: Data cuts used: $0 < t'_i \leq 6.5$ μs, $r_d > 5$ mm, $m_{track} \geq 1$, $c_{track} = 1$. Maximum pulse heights show a downward trend with decreasing angle as a result of the angular dependence of differential energy loss over l_{pad} (see Eq. 7.6).

In Section 5.3.1, PH_{sum} was defined as the sum of the pulse heights from all triggered pads in a track,

$$PH_{sum} = \sum_{i=1}^{m_{track}} PH(i), \tag{7.8}$$

where $PH(i)$ are the pulse heights of individual pads and m_{track} is the multiplicity. PH_{sum} is representative of the total energy deposited (E) by an ion inside the detection volume. Fig. 7.19 illustrates the comparison of the angular dependence of the summed pulse height from an alpha run and the simulated total energy deposited in a track. The simulation parameters used, e.g., gas mixture, pressure, etc., were kept the same as the alpha run. The energy resolution in the simulation mainly arises from the effects of the cathode cage always shielding a part of the ion track from detection and the steeper tracks terminating at the μ-RWELL, which led to a fraction of the total alpha energies being detected. The simulation shows two main distributions in total energy. The higher energy distribution ($E > 1.7$ MeV) is mainly from the shallow tracks ($20° < \theta < 40°$), implying the shallow tracks terminate and deposit most of their energy in the detection region. On the other hand, mostly the steep tracks ($\theta > 40°$) terminating at the μ-RWELL contribute to the lower energy distribution ($E \leq 1.7$ MeV). Fig. 7.18 shows that the steep tracks deposited relatively more energy per pad, as discussed earlier; the total energy deposited was less compared to the shallow tracks as shown in Fig. 7.19. A lower total energy deposition was expected as the majority of the steep tracks were found to be shorter in comparison (see Fig. 7.5). The simulation was found to be in good agreement with the data from the alpha run analysis, especially in the trends and angular distributions. The detection efficiency for the steeper tracks was found to be comparatively higher (discussed further in Section 7.1.5). In addition to the effect of the cathode cage, the energy resolution from the μ-RWELL also impacts the pulse height distributions. The resolution was estimated to be $\approx 8\%$ in the He:CO_2 90:10 gas mixture (see Section 5.3.1). Furthermore, the lack of energy calibration makes

the pulse heights susceptible to the gain variation between the preamplifier channels used.

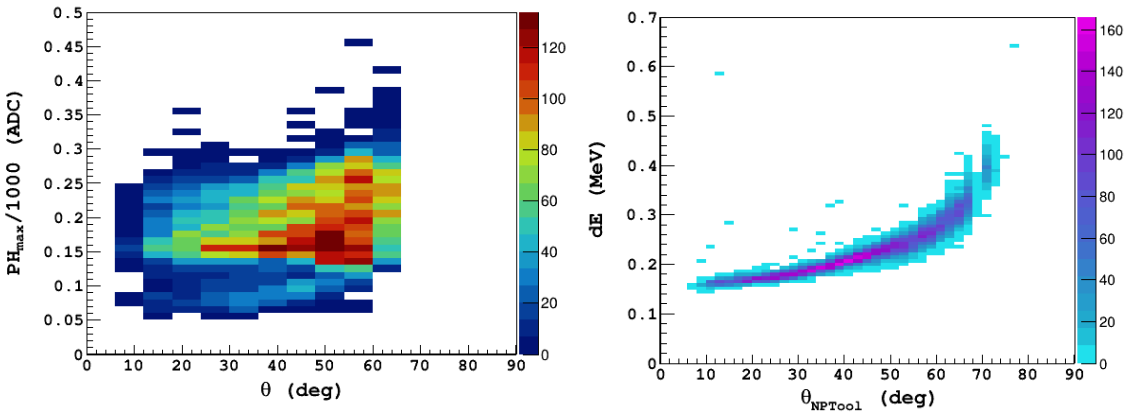

Figure 7.18: **[Left]:** PH_{max} versus track angle for alpha run 02085 (sector 1). Data cuts: $0 < t_i' \leq 6.5$ μs, $r_d > 5$ mm, $m_{track} \geq 5$, $c_{track} = 1$. **[Right]:** Simulated maximum differential energy loss in a track (dE) versus angle for ^{148}Gd alpha energy = 3.1 $\pm$ 0.1 MeV. Data cuts: $r > 12$ mm, multiplicity ≥ 5. Furthermore, an energy threshold of 50 keV per pad was used.

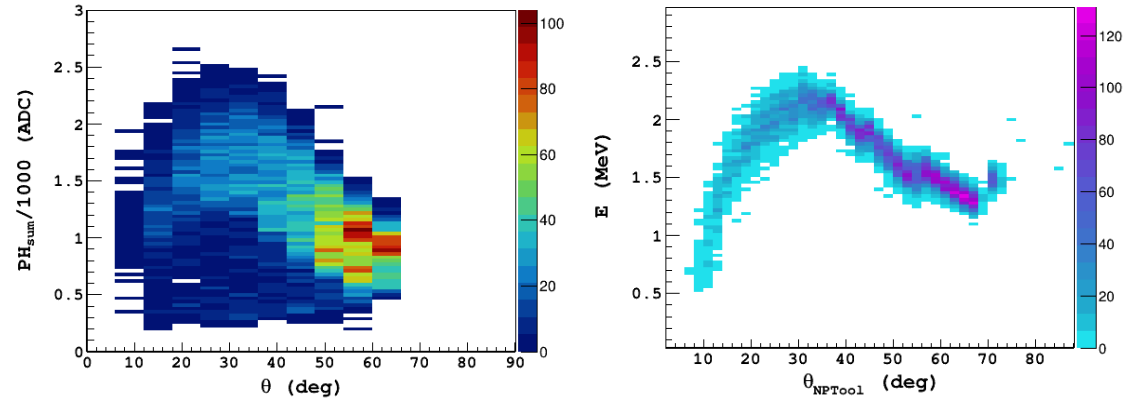

Figure 7.19: **[Left]:** PH_{sum} versus track angle for alpha run 02085 (sector 1). Data cuts: $0 < t_i' \leq 6.5$ μs, $r_d > 5$ mm, $m_{track} \geq 5$, $c_{track} = 1$. **[Right]:** Simulated total energy (E) versus track angle for ^{148}Gd alpha energy = 3.1 $\pm$ 0.1 MeV. The cuts and energy thresholds used were similar to the ones in Fig. 7.18.

In order to further investigate the equivalence between the pulse heights and simulated energies, source studies were extended to a different gas pressure. The higher gas pressure and the μ-RWELL bias compared to run 02085 were chosen by taking the stable beam tests into consideration (discussed in Section 7.2). Fig. 7.20 shows the maximum pulse heights from run 26073. The run parameters are listed in Table 7.2. Some signal saturation was observed at the digitiser channels, which was expected as the μ-RWELL was operating a high gain of $\approx$ 4500 (see Fig. 5.17). Compared to the maximum pulse heights of $\approx$ 700 from run 02085 (see Fig. 7.17), at least a 5-fold increase was observed. A correlation was drawn between the ranges of the simulated energy parameters and their pulse height equivalents, as the effect of saturation was found to be negligible. Plots in Fig. 7.21 show a similar upward

trend. The simulation parameter ΔE_{NPTool}, the maximum differential energy loss in a track, is equivalent to PH_{max}. The ranges of the parameters from Fig. 7.21 are listed in Table 7.3. It must be noted that the equivalence between the pulse height and energy from alpha run 26073 was used for the energy calibration in Section 7.2.

Table 7.2: Experimental details of alpha run 26073.

Parameters	**He:CO_2 90:10**
Pressure	1.0 bar
Drift voltage (V_{drift})	-990 V/cm
μ-RWELL bias (ΔV)	-590 V

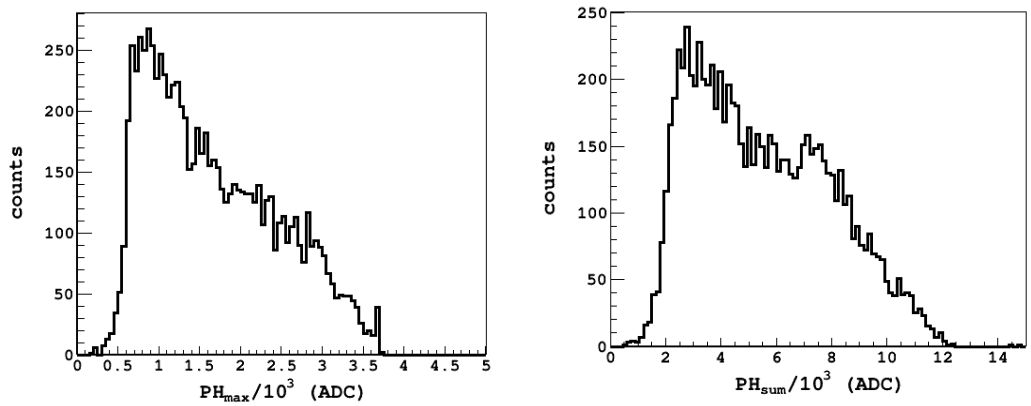

Figure 7.20: Maximum and summed pulse heights (scaled) for alpha run 26073 (sector 1). Data cuts used: $0 < t_i' \leq 7.5$ μs, $r_d > 5$ mm, $m_{track} \geq 5$, $c_{track} = 1$. The upper limit of t_i' was chosen based on the maximum calculated drift time for the specific experimental conditions (see Fig. 6.15). Signal saturation at the digitiser channels was observed for $PH_{max} > 3600$ ADC.

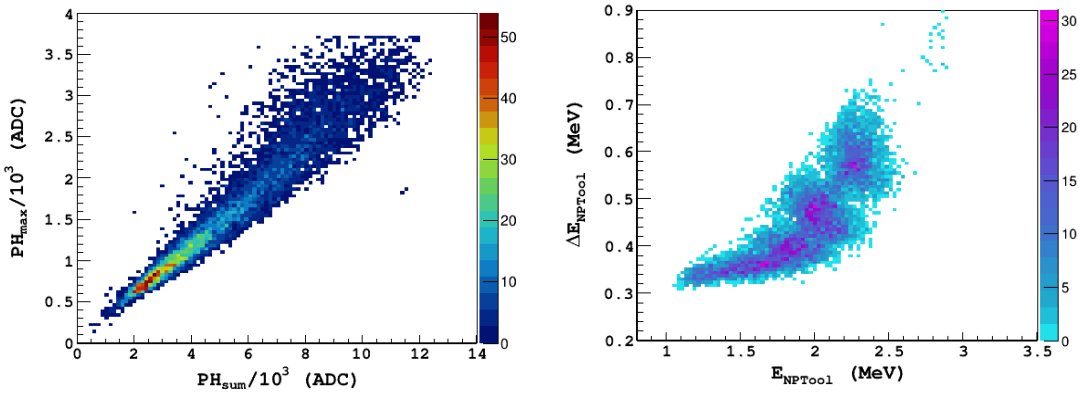

Figure 7.21: **[Left]:** PH_{max} (scaled) versus PH_{sum} (scaled) for alpha run 26073 (sector 1). Data cuts used: $0 < t_i' \leq 7.5$ μs, $r_d > 5$ mm, $m_{track} \geq 5$, $c_{track} = 1$. **[Right]:** Simulated dE versus E for ^{148}Gd alpha energy = 3.1 $\pm$ 0.1 MeV. Data cuts: $r > 12$ mm, multiplicity ≥ 5. Furthermore, an energy threshold of 20 keV per pad was used.

Table 7.3: Approximate ranges of simulated and measured parameters from Fig. 7.21.

Parameters	**Range**	**Parameters**	**Range**
E_{NPTool} (MeV)	1.1 - 2.6	PH_{sum} (ADC)	(2-12)$\times 10^3$
ΔE_{NPTool} (MeV)	0.3 - 0.7	PH_{max} (ADC)	(0.5-3.7)$\times 10^3$

7.1.5. Sector response comparison

The intrinsic structural differences from the manufacturing process between the two μ-RWELL detectors inside TACTIC and the tolerances of the high voltage distribution box resistors, through which the bias is supplied, can introduce a potential variation in gas gains between the sectors. Furthermore, the tolerances of the preamplifier electronic components result in a gain variation between the channels. Additionally, the μ-RWELL axis in one half of TACTIC was misaligned with respect to the cathode cage axis during the assembly procedure as illustrated in Fig. 7.22. As a result, the pad alignment relative to the position of the source and the tracks was also affected, as the anode pads are included in the μ-RWELL structure. A maximum offset of ≈ 1.8 mm (Δr) was measured on the upstream end of the half which included sector 2, with respect to the central axis. This misalignment translated to an additional contribution to the uncertainty Δr_{track}, defined in Section 6.4.4, and had a relatively larger impact on the particle tracking using the upstream anode pads as well as their responses. As another immediate consequence, the track length under a single pad (l_{pad}) defined in Eq. 7.6 gets affected and must be redefined.

$$l'_{pad} = \frac{p_w}{\cos\theta'}, \tag{7.9}$$

where $\theta' = \theta - \lambda$ is the modified track angle relative to the misaligned anode pads, and λ is the deviation of sector 2 from the original pad plane as a result of the misalignment as shown in Fig. 7.22.

$$\tan\lambda = \frac{\Delta r}{d}, \tag{7.10}$$

where $d = 252$ mm, i.e., the length of the detection region.

In order to isolate μ-RWELL-related variations from the electronic variations, an investigation of the pulser spectra should have been sufficient. However, the test input circuits that distribute the pulser signal to the preamplifier channels give rise to systematic variation as to what pulse height each channel outputs as depicted in Fig. 5.6. Thus, it was decided to study the combined variations in channel and sector response by using the source data. The distribution of pulse heights across the anode pads and the reconstructed vertex positions should sufficiently capture variations from all the potential sources. Fig. 7.23 shows a comparison of pulse heights across the pads between sectors 1 and 2. Sector 1 shows an overall high gain compared to sector 2 across all pads. One of the major contributions was believed to be from the different gas gains of the sectors. A difference in the bias supplied to

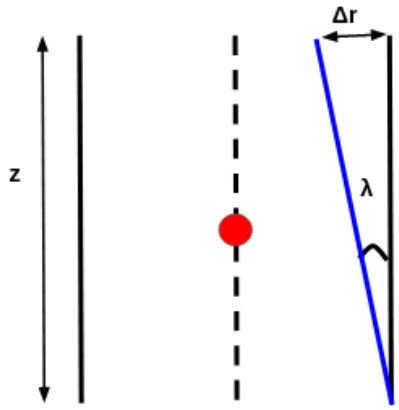

Figure 7.22: Schematic drawing of the misalignment of the μ-RWELL axis (blue) in sector 2 with respect to the cathode cage axis (black dashed). The red circle depicts the approximate source position. The maximum deviation of the anode pad axis Δr = 1.8 $\pm$ 0.1 mm was measured on the upstream end. The length of the detection region was, d = 252 mm, and $\lambda = 0.4°$.

the μ-RWELLs (ΔV) on opposite halves of TACTIC can arise from the tolerances of the supply resistor chain. Since gas gain has an exponential dependence on the applied bias (ΔV) (see Fig. 5.17), small differences in ΔV ($\sim$ few volts) can potentially lead to a substantial variation in gas gain and concurrently the output signals. It is noteworthy that the range of triggered pads was found to be similar for both sectors, which implies the source positions detected by the sectors agree well within uncertainties. This was further investigated later in the section, i.e., Fig. 7.26 shows that the reconstructed vertex positions of the alpha tracks are in good agreement with the position of the source.

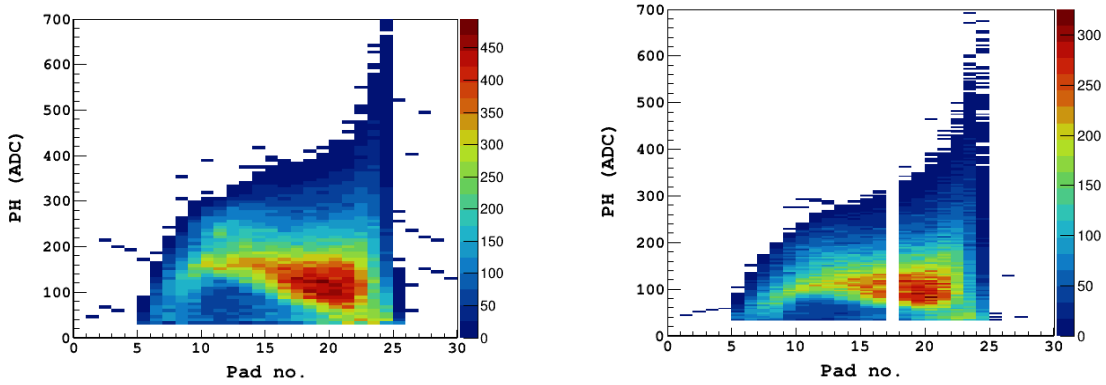

Figure 7.23: **[Left]:** Pulse heights across anode pads for alpha run 02085 (sector 1). **[Right]:** Pulse heights across anode pads for alpha run 02085 (sector 2). The sector positions are illustrated in Fig. 6.5. A more detailed comparison between individual pads from both sectors are shown in Fig. 7.24. Pad no. 17 in sector 2 was found unresponsive. A similar behaviour was also observed in the test chamber (see Fig. 5.7).

The differences in the pulse height spectra between the sectors were further investigated by comparing a subset of individual pads (see Fig. 7.24). The overall

distribution of pulse heights, i.e., a peak followed by a high energy tail, for each pad within a sector was found to be similar. The maximum pulse heights between pads showed a variation of $\approx 14\%$ for both sectors, decreasing gradually away from the source position. The gradual decrease indicates that the effect of the gas gain and energy dependence dominates over the electronic gain variation between the preamplifier channels. This can be explained by the relatively higher number of shallow angle tracks reaching the later pads. The shallower tracks deposit less energy per pad in comparison to the steep tracks, according to Eq. 7.6 and the discussion in Section 7.1.4. A clear shift in the mean of the distributions was observed between the sectors. The difference was found to become clearer in the pads towards the end of the shallower alpha tracks (pad no. 10 to 13), where the energy deposition per pad or the number of primary electrons liberated is higher. This made the gas gain difference between the two sectors more prominent.

The misalignment could have also potentially affected the energy detected by the pads in sector 2, in addition to the differences in gas gain and preamplifier gain between the sectors. The pad positions relative to the tracks changed as a result of the misalignment, which in turn reduced the effective l_{pad} for a given θ as per Eq. 7.9 and consequently the energy deposition ($l'_{pad} \propto DE$). A track angle of $\theta = 40°$ gets modified to $\theta' \approx 39.6°$ (see Eq. 7.10) as a result of the misalignment. Therefore, using Eqs. 7.6 and 7.9, it can be shown that l_{pad} reduced by a very small amount, i.e., $\approx 1\%$. Therefore, the effect of misalignment did not contribute majorly in the sector response variation. It must be further noted that the alpha source used was not mono-energetic; therefore, some additional statistical variations in the energy loss between the pads and sectors were present. In order to sufficiently address all the potential sources of variation, gain matching using a mono-energetic X-ray source is required. This was outside the scope of this work and needs to be studied in the future. Since the majority of results reported in this chapter involve only sector 1, the misalignment and the gain variation between the sectors did not have any impact.

Two important tracking parameters, i.e., calculated track angle and reconstructed vertex position, were also compared between sectors 1 and 2. The track angle distributions were found to be in good agreement between the sectors. Fig. 7.25 illustrates the comparison between calculated and simulated angular distributions. The minor discrepancies at the extremities of the distributions can be attributed to associated systematic uncertainties in the calculation of θ (see Fig. 7.7). Furthermore, the comparison between the reconstructed vertices is shown in Fig. 7.26. The disagreement in the mean value as well as the standard deviations from the Gaussian fits was believed to be a result of the misalignment of the μ-RWELL axis corresponding to sector 2 (see Fig. 7.22). The additional uncertainty (≈ 1.5 times higher) arises from the modified pad positions with respect to the cathode cage axis. As the misalignment will add to the uncertainty, Δr_{track}, which in turn affects the calculation of v_z. The reconstructed vertex position was found to be in better agreement with the measured source position, z_s, for sector 1, which does not have the same alignment issues. The estimated uncertainties from the Gaussian fits include the effects of misalignment and any deviation of the source position from the cathode cage axis. For future studies, the μ-RWELL structure of concern will be realigned or replaced.

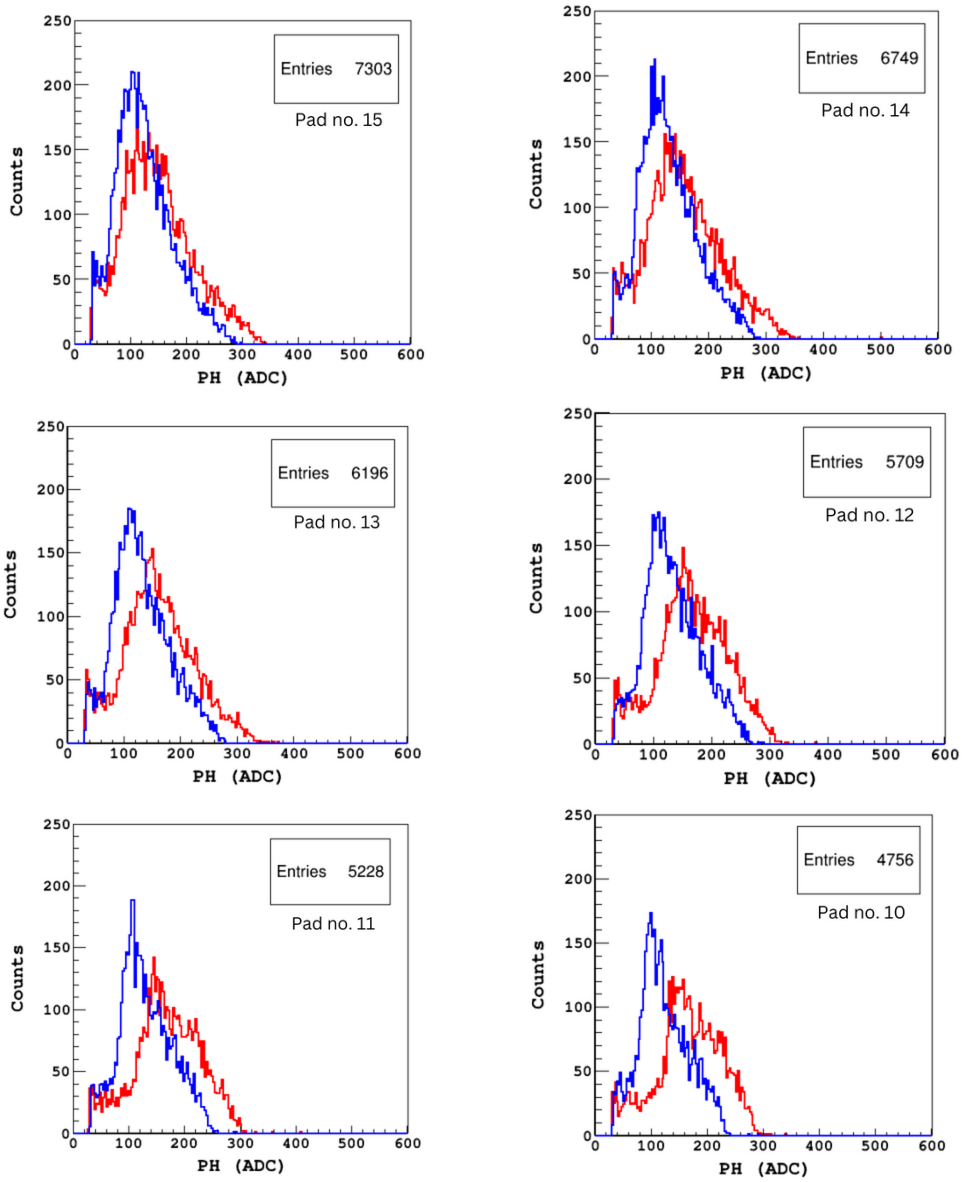

Figure 7.24: Pulse height spectra for individual pads from sector 1 (red) and sector 2 (blue) for alpha run 02085.

7.2. Stable beam studies

The first in-beam tests of the TACTIC setup post modifications took place in July and November 2022. A ^{23}Na beam and a He:CO_2 90:10 gas target were used to study the $^{23}\mathrm{Na}(\alpha,p)^{26}\mathrm{Mg}$ reaction in the astrophysically important energy region ($E_{cm} = 1.0 - 5.1$ MeV) in inverse kinematics. The goal of these initial in-beam tests was also to investigate the achievable vertex position resolution and the associated reaction energy resolution, as well as the particle identification capability and the performance of the dedicated data analysis codes. The detailed experimental arrangement is discussed in Section 6.3.

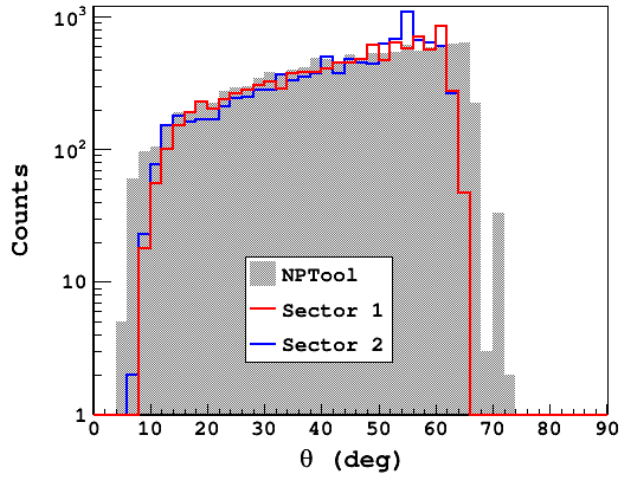

Figure 7.25: Angular distribution of alpha tracks for sectors 1 and 2 (run 02085) compared to NPTool simulation.

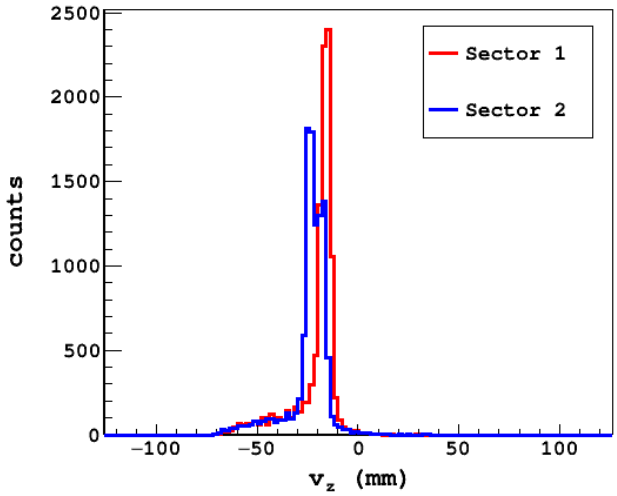

Figure 7.26: Reconstructed vertex or source positions for sectors 1 (mean = -16.6 mm, σ = 2.6 mm) and 2 (mean = -21.6 mm, σ = 3.9 mm) from alpha run 02085. The measured source position, z_s = -16 ± 2 mm (see Appendix B), agrees well with the reconstructed vertices within uncertainties.

7.2.1. ^{23}Na beam

An 1.7 MeV/u ^{23}Na (6^+) beam was used for the in-beam tests and was delivered to TACTIC from the OLIS facility (see Section 6.1). It entered the target region through a 2.5 μm-thick aluminised-mylar window (see Fig. 6.2). The entrance window and exit collimator were positioned at $z = -49 \pm 3$ mm (see Appendix B) and $z = 84 \pm 3$ mm, respectively, for the tests. Thus, the gas target thickness was $\approx 133 \pm 3$ mm. Fig. 7.27 shows the TRIM simulation of the ^{23}Na beam in the entrance window and the gas target. The initial spike in the energy loss curve is due to the presence of the window. According to the predicted range of 74 ± 2 mm (equivalent to ≈ 18 anode pads), the beam stops inside the target region. The TRIM predicted range was found to be in agreement with the simulated range of 72 ± 2 mm (see Fig. 7.28) from NPTool. In both simulations, the energy loss of ≈ 4.8 MeV inside the entrance window was accounted for. A linear fit from the plot

in Fig. 7.28 was used to express the beam energy as a function of target depth in TACTIC coordinates (-126 $\leq z(\text{mm}) \leq$ 126):

$$E_b = 12.4 - (0.5 \cdot z), \tag{7.11}$$

$$\Delta E_b = 0.5 \cdot \Delta z, \tag{7.12}$$

where E_b is the beam energy in the lab frame corresponding to position z. z can be replaced by $v_{z,m}$ to obtain the beam energy at a certain vertex position. The linear fit holds good in the energy range: $6 \leq E_b(MeV) \leq 35$. The Geant4 simulation becomes inaccurate at low energies due to low energy scattering. Thus, only the beam energies above 6 MeV were considered in the analysis, which is sufficient for the energy region of interest ($>$ 1 MeV in the CM frame) for the study of the ^{23}Na$(\alpha, p)^{26}$Mg reaction. Eq. 7.12 can be used to estimate the associated beam energy uncertainty arising from the vertex position uncertainty, which follows from Eq. 6.20. While passing through the window and gas target, the beam ions will be subjected to radial straggling, which needs to be taken into account while estimating ΔE_b. The radial straggling or the deviation of the beam ions from the central cathode cage axis was estimated using NPTool simulation. From Fig. 7.29, the maximum radial straggling inside the target region was estimated to be $\approx$ 3.5 mm at the half-height point of the falling edge of the distribution, which was found to be consistent with the TRIM predicted value of 3.0 $\pm$ 0.1 mm. It is noteworthy that in both simulations, the ion beam was generated from a point source. However, in practice, a beam spot with finite dimensions needs to be considered. For TACTIC tests, a "pencil" beam with a "spot" size or diameter $\approx$ 4 mm was used, which also contributed to the radial straggling and the estimation of Δr_c (see Eq. 6.25), i.e., the uncertainty in the estimation of track radius inside the cathode cage.

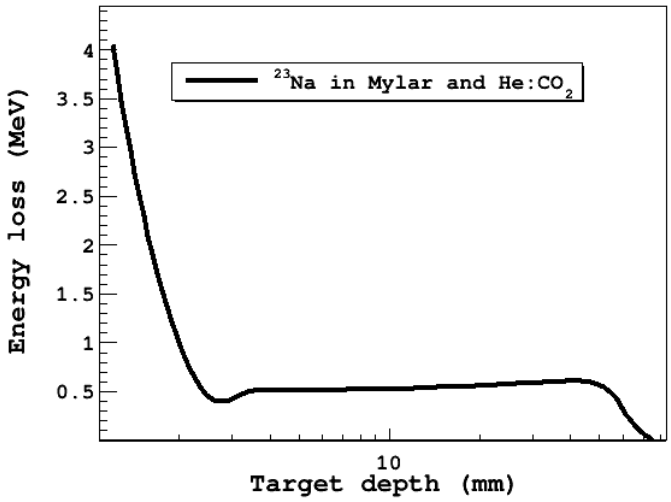

Figure 7.27: TRIM predicted energy loss of the ^{23}Na beam in He:CO_2 90:10 gas mixture at P = 1 bar, after passing through the entrance window. The log scale on the horizontal axis was used to highlight the energy loss inside the entrance window.

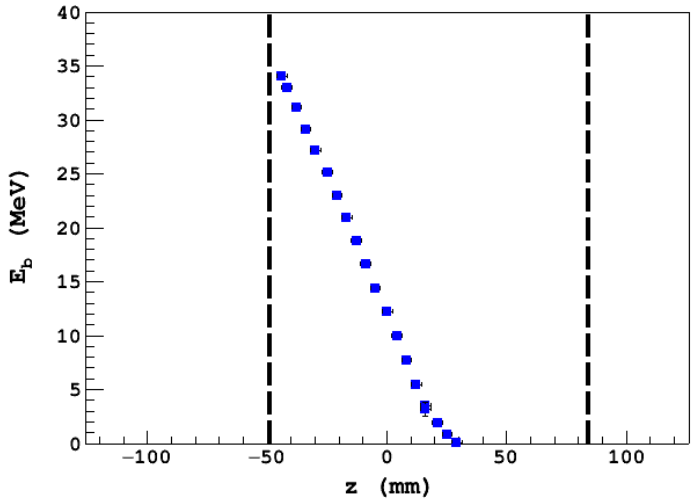

Figure 7.28: Simulated ^{23}Na beam energies in the lab frame versus He:CO_2 90:10 gas target (P = 1 bar) depth in TACTIC coordinates. The black dashed lines indicate the position of the entrance window and exit collimator.

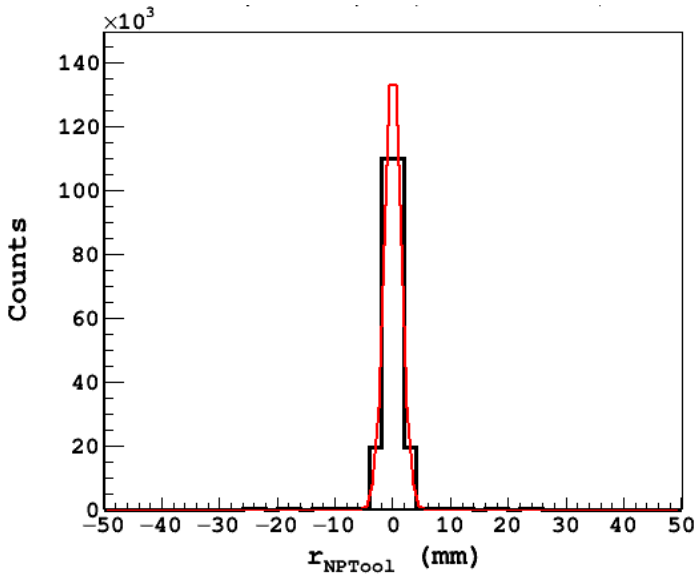

Figure 7.29: Simulated end radius of the ^{23}Na ions inside the target gas after passing through the window. The Gaussian fit parameters: $\mu = 0$ mm, $\sigma = 1.5$ mm. The value of σ provides a measure of the radial straggling of the beam.

7.2.2. Vertex energy resolution

One of the key parameters that needs to be estimated in order to obtain the excitation function for a reaction of interest is the reaction energy at the vertex as well as the associated energy resolution. For the in-beam experiments, TACTIC operates with an extended target, which means that over the range of the ion beam inside the gas target, multiple interactions will take place at different points corresponding to different energies. The accuracy of reconstruction of these points of interaction or reaction vertices must be estimated, and this was one of the key areas of focus for the in-beam tests.

Table 7.4: Experimental details of stable beam runs 61, 64 and 65.

Parameters	**He:CO_2 90:10**
Pressure	1.0 bar
Drift voltage (V_{drift})	-990 V/cm
μ-RWELL bias (ΔV)	-590 V

Fig. 7.30 shows the end points of tracks for the stable beam runs 61, 64 and 65. The run parameters are listed in Table 7.4. The majority of the tracks terminate at the μ-RWELL ($r \approx 50$ mm) as expected (also see Fig. 6.14). Some of the shallower tracks also escape the detection region on the downstream end ($z = 126$ mm). These tracks mostly correspond to protons and alphas from (p,p), (α,α), and (α,p) scattering and reaction channels. The (p,p) channel represents the elastic scattering of ^{1}H present in the window material due to their interaction with the beam. The heavier scattering products, e.g., ^{12}C, ^{16}O and ^{23}Na, mostly stop inside the detection region ($r < 50$ mm) or get shielded completely by the cathode cage (see Fig. 7.31). Together with the track selection criteria, i.e., $m_{track} \geq 5$, c_{track} =1, discussed in Section 7.1.1, only the tracks terminating at the μ-RWELL ($r_{track} \approx$ 50 mm) can be further selected to eliminate the majority of the elastic scattering products from the target gas and entrance window, as well as to improve the quality of vertex reconstruction (discussed in Section 7.1.3). However, this will also reduce the detection efficiency of the reaction protons of interest from the (α,p) reaction channel (see Table 7.5).

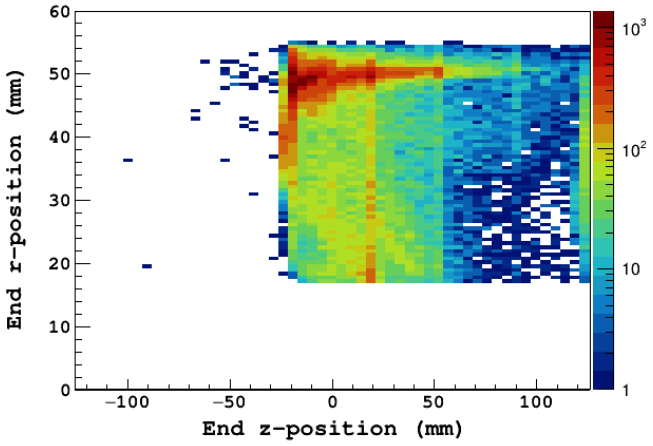

Figure 7.30: The end points of tracks from stable beam runs 61, 64 and 65. The entrance window was positioned at z_{uw} = -49 ± 3 mm. Data cuts used: $0 < t'_i \leq$ 7.9 μs, $r_d > 5$ mm, $m_{track} \geq 5$, $c_{track} = 1$.

Unlike the alpha source placed at a fixed position, the interactions between the beam and target nuclei take place at different points inside the target region. Thus, the vertex positions for the in-beam tests were estimated differently. Instead of using only the initial and final pad positions in a track, p_i and p_f, respectively (discussed in Section 6.4.2 and implemented in Section 7.1.3), the vertex position was calculated separately for each pad in a track ($v_{z,i}$) with respect to the final pad as the signal on the final pad (p_f) generates the trigger for an event. The mean ($v_{z,m}$) and the uncertainty (Δv_z) from the resulting vertex distribution for each track were

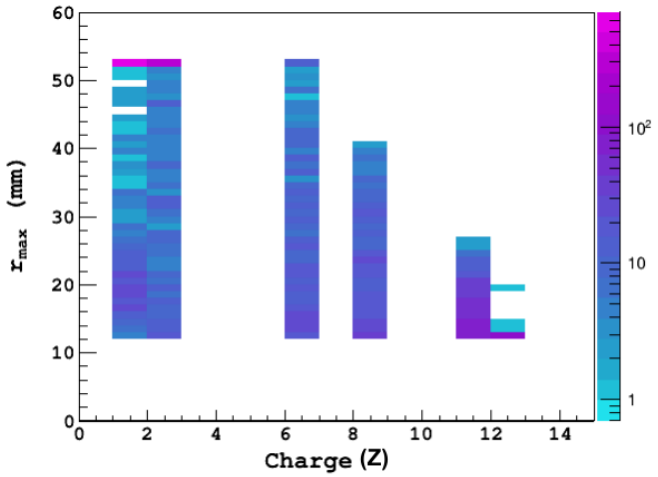

Figure 7.31: Simulated maximum track radius with no cuts of products from different nuclear interactions between ^{23}Na beam and the target gas mixture: $^{23}\mathrm{Na}(\alpha,p)^{26}\mathrm{Mg}$, $^{23}\mathrm{Na}(\alpha,\alpha)^{23}\mathrm{Na}$, $^{23}\mathrm{Na}(^{12}C,^{12}C)^{23}\mathrm{Na}$, $^{23}\mathrm{Na}(^{16}O,^{16}O)^{23}\mathrm{Na}$. Most of the heavy ions from elastic scattering and reactions (charge > 2), stop inside the detection volume ($r < 50$ mm). It is must be noted that the reaction and scattering cross sections used (flat.cs) in the simulation did not have an energy or angle dependence. Thus, the yields were artificially inflated, i.e., an equal number of reaction products were produced for all the simulated nuclear interactions.

Table 7.5: Simulated detection efficiencies (%) of different reaction products corresponding to different nuclear interactions between ^{23}Na beam and the target gas mixture: (α,p), (α,α), $(^{12}C,^{12}C)$, $(^{16}O,^{16}O)$ in inverse kinematics. The reduced detection efficiency with no cuts on the simulated data results solely from the presence of the cathode cage. The parameters m_{NPTool} and r_{max} represents track multiplicity and maximum track radius, respectively.

Sp.	**No cuts**	$m_{NPTool} \geq$ **3**	$m_{NPTool} \geq$ **5**	$m_{NPTool} \geq$ **5,** $r_{max} \geq$ **50 mm**
p	87.1	77.8	65.4	37.6
α	79.0	64.9	55.2	36.4
^{12}C	75.3	50.2	32.7	0.1
^{16}O	72.1	40.9	21.1	0.0
^{23}Na	52.8	27.7	11.8	0.0
^{26}Mg	10.0	0.0	0.0	0.0

obtained. The same procedure was followed to estimate the track angle and the associated uncertainty (see Fig. 7.32).

$$v_{z,m} = \sum_{i=1}^{i=m_{track}-1} \frac{v_{z,i}}{m_{track}-1}, \tag{7.13}$$

$$\theta = \sum_{i=1}^{i=m_{track}-1} \frac{\theta_i}{m_{track}-1}. \tag{7.14}$$

Fig. 7.33 shows the reconstructed vertices for the stable beam runs 61, 64, and 65. The majority ($\approx$ 94%) of the vertices were estimated to be within the ex-

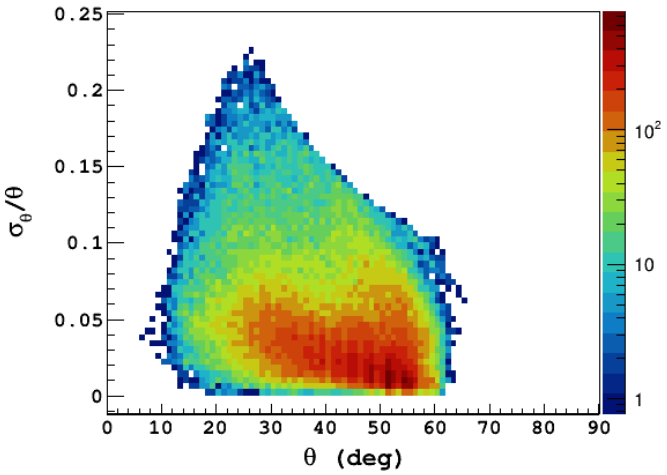

Figure 7.32: Calculated track angle versus associated relative uncertainties for stable beam runs 61, 64, and 65 (sector 1). The higher relative uncertainty at shallower angles results from angular straggling at the end of the track (see Section 3.5.1). The maximum uncertainty of $\approx 7.2°$ was calculated for $\theta \approx 30°$.

pected z-range, determined by the measured position of the entrance window at $z_{uw} = -49 \pm 3$ mm and the range of the ^{23}Na ion beam inside the gas target (see Fig. 7.28). As discussed in Section 6.4.2, the method employed for vertex reconstruction is based on certain assumptions. Any deviation from the assumptions impacts the estimation of the track parameters, i.e., radius, angle, and vertex position (see Eq. 6.13). In addition to this, the angular straggling at the end of a track also affects the radius calculation as it gives rise to inaccuracy in the measured t_i' values (see Eq. 6.19). These are believed to be the primary sources of the outliers in the calculated vertex position distribution. Selecting tracks that terminate at the μ-RWELL ($5.7 < t_i'(\mu s) < 7.9$) effectively eliminated most of the outliers (see Fig. 7.33). Such tracks traversed the entire detection region. Thus, the effect of angular straggling at the end of the shallower tracks (see Fig. 7.32) and undetected initial track segments due to the set energy threshold was minimised. However, this selection criteria reduces the detection efficiency by $\approx 50\%$, especially impacting the shallower tracks as expected (see Fig. 7.34). The reduction in detection efficiency was also supported by the simulation (see Table 7.5).

In Fig. 7.33, the maxima of the distribution in the vicinity of the entrance window position, followed by a gradual decrease in the yield inside the gas target, were observed. The density of the window material, i.e., Mylar, is 9.6×10^{22} atoms·cm^{-3}. Thus, considering the window thickness of 2.5 μm, an effective target thickness of 2.4×10^{19} atoms·cm^{-2} can be estimated. In a similar way, the effective target thickness of the target gas mixture was estimated to be 2.8×10^{20} atoms·cm^{-2}, over the entire target region defined by the range of the beam $\approx$ 72 mm (see Fig. 7.28). The effective thickness of the target gas was found to be approximately an order of magnitude higher than the entrance window. However, as most of the atoms in the window were closely packed, the reconstructed vertices of the elastic scattering interactions from the window were expected to be highly localised. This is reflected in the maxima with sharp drops on either side in Fig. 7.33. Another feature of interest in the vertex distribution is the second sharp drop at $z \approx 0$ mm, which

corresponds to the centre of mass energy, $E_{cm} \approx 1.7$ MeV, which was deduced using Eq. 7.11 and subsequently a conversion to the centre of mass frame. This significant decrease in the yield can be attributed to the steep drop in the (α, p) reaction cross section in the region below $E_{cm} \approx 2$ MeV (see Fig. 1.1) as well as the lower energy of the products from the elastic scattering interactions, diminishing their detection efficiency under the specific experimental (gas gain, gas pressure, etc.) and analysis (data cuts) considerations.

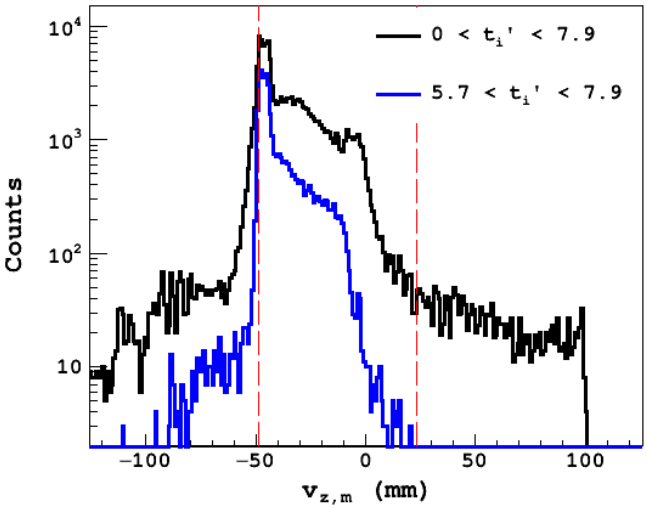

Figure 7.33: Reconstructed vertices from stable beam runs 61, 64, and 65 (sector 1). The red dashed lines represent the position of the entrance window and range of ^{23}Na beam in He:CO_2 90:10. In addition to the cuts placed on the minimum t_i' values, the data cuts used were: $r_d > 5$ mm, $m_{track} \geq 5$, $c_{track} = 1$. The maximum value of t_i' (μs) represents the maximum drift time of electrons in the detection region (see Fig. 6.14) under the experimental conditions.

Table 7.5 shows that most of background inside the target gas originates from the elastic scattering channels (α, α) and $(^{12}C, ^{12}C)$ for tracks with multiplicity of ≥ 5. By selecting tracks that terminate at the μ-RWELL, the majority of the heavy scattering products $(A > 4)$ can be excluded. The elastic scattering cross section has an angular dependence as per Eq. 2.24. The scattered α yield is expected to reduce with lab angle (see Fig. 2.1) for a given energy. Thus, the multiplicity (≥ 5) cut on the data eliminates most of the remaining α scattering yield from steeper angles ($\theta > 66°$). This also aids in the suppression of scattering background, which will be further discussed in Section 7.2.3.

The vertex positions ($v_{z,m}$) and associated uncertainties (Δv_z), as well as the uncertainties in track angles ($\Delta\theta$), were calculated for multiple tracks using the method discussed earlier in this section. Gaussian fits to the distributions in Fig. 7.35 showed that the resolution in the vertex position and track angle was 2.4 mm and 6.1°, respectively. These resolutions were calculated as the full width at half maximum (FWHM) of each distribution. By selecting the tracks that fall within the FWHM of the Δv_z distribution as shown in Fig. 7.35 and terminate at the μ-RWELL, all the outliers in Fig. 7.33 can be eliminated (see Fig. 7.36). It is noteworthy that the vertex position resolution was found to be less than the width of

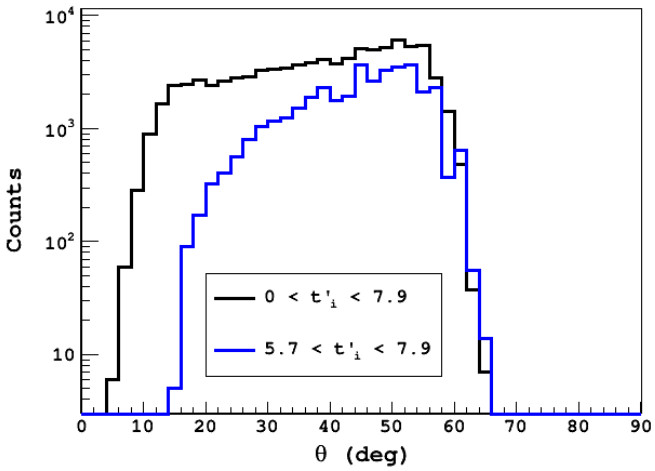

Figure 7.34: Calculated track angles from stable beam runs 61, 64, and 65 with and without the minimum cut in t_i' following Fig. 7.33. As expected, a reduction in the number of smaller angles was observed in the angular distribution of the tracks terminating at the μ-RWELL.

a single anode pad, the quantum for tracking inside TACTIC. This suggests that the assumptions made regarding the vertex reconstruction and tracking (see Section 7.1.1) work sufficiently well for the majority of the tracks. Using Eq. 7.12 and the calculated Δv_z values, the vertex energy resolution were obtained. Gaussian fit to the distribution in Fig. 7.37 yielded a resolution of 153 keV (FWHM) in the centre of mass frame or, 45 keV/u in the lab frame. The centre of mass energy was calculated with respect to helium in inverse kinematics. This is an important result and was used to obtain the excitation function for the reaction of interest in Section 7.2.4.

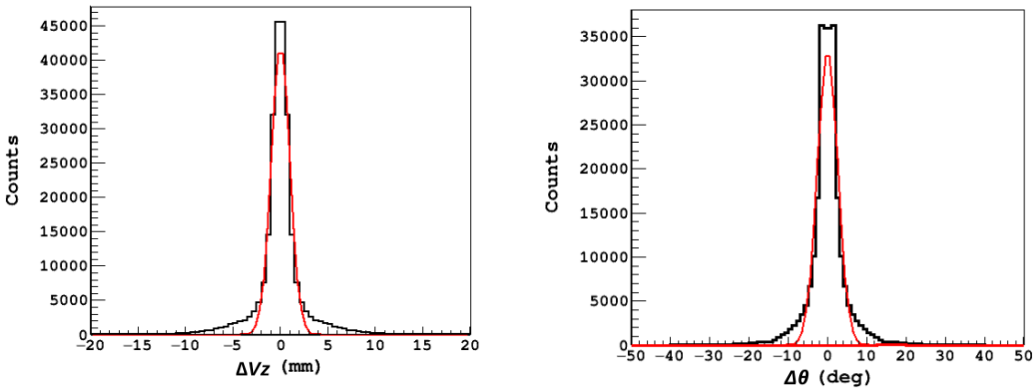

Figure 7.35: Uncertainties in vertex position and track angle from stable beam runs 61, 64, and 65 (sector 1). Data cuts used: $r_d > 5$ mm, $m_{track} \geq 5$, $c_{track} = 1$, $0 < t_i'(\mu s) < 7.9$. For a track, multiple vertex position and track angle values were calculated using each point in the track with respect to the final point. Subsequently, the corresponding uncertainties were obtained from the resulting distributions.

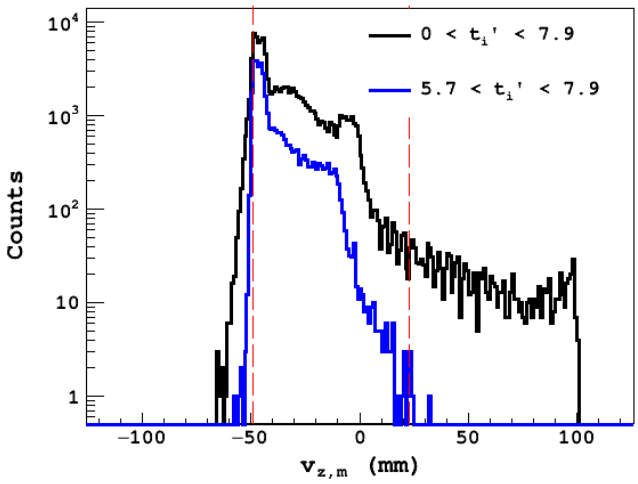

Figure 7.36: Reconstructed vertices from stable beam runs 61, 64, and 65 (sector 1). The red dashed lines represent the position of the entrance window and range of ^{23}Na beam in He:CO_2 90:10. In addition to the cuts placed on the minimum t'_i values, the data cuts used were: $r_d > 5$ mm, $m_{track} \geq 5$, $c_{track} = 1$, $\Delta v_z < 2.4$ mm, $\Delta\theta < 6.1°$.

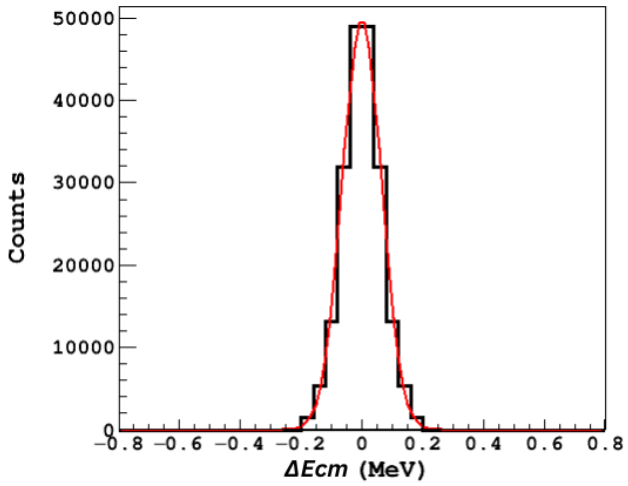

Figure 7.37: Uncertainties in the vertex energy from stable beam runs 61, 64, and 65 (sector 1). Data cuts used: $r_d > 5$ mm, $m_{track} \geq 5$, $c_{track} = 1$, $0 < t'_i(\mu s) < 7.9$, $\Delta v_z < 2.4$ mm, $\Delta\theta < 6.1°$.

7.2.3. Particle identification

In order to separate out the reaction products of interest from the background, the identification of particles inside TACTIC is required. As discussed in Section 7.2.2, the majority of the background arises from the elastic scattering interactions between the beam ions and the target gas as well as the entrance window material. Fig. 7.38 shows the reconstructed vertex positions for the tracks that terminate at the μ-RWELL. The elastic scattering at the entrance window gives rise to the initial peak in the vertex position distribution, which can be completely eliminated by only selecting tracks with vertex positions inside the target gas. For this only the tracks outside 4σ ($v_{z,m} \geq$ -38.3 mm) of the Gaussian fit of the "window scattering" peak

were considered for particle identification in the gas target region.

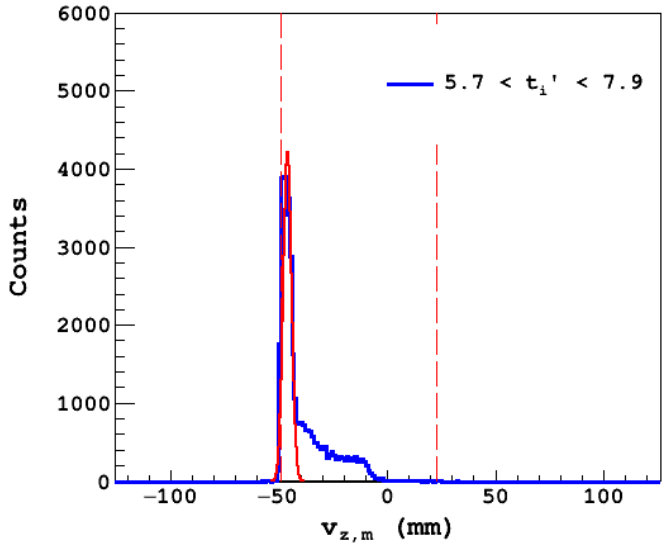

Figure 7.38: Reconstructed vertices from stable beam runs 61, 64, and 65 (sector 1). The red dashed lines represent the position of the entrance window and range of ^{23}Na beam in He:CO_2 90:10. The data cuts used: $5.7 < t_i'(\mu s) < 7.9$, $r_d > 5$ mm, $m_{track} \geq 5$, $c_{track} = 1$. The Gaussian fit parameters from the "window scattering" peak: μ = -46.0 mm, σ = 1.9 mm.

Following the comparative study between the simulation and source test results (discussed in Section 7.1.2), NPTool was further used to investigate particle identification schemes for the in-beam tests. In the simulation, a 1.7 MeV/u ^{23}Na beam was sent through TACTIC and the entrance window position was set at z = -49 mm in accordance with the measured window position (see Appendix B). The energy attenuation in the entrance window was also accounted for in the simulation. A He:CO_2 90:10 gas mixture at pressure 1 bar was used as the target and detection volume. The (α, p) reaction cross section was artificially inflated to produce a similar amount of reaction and elastic scattering events. The reaction and elastic scattering channels simulated:

1. $\alpha(^{23}\text{Na}, p)^{26}\text{Mg}$
2. $\alpha(^{23}\text{Na}, \alpha)^{23}\text{Na}$
3. $^{12}\text{C}(^{23}\text{Na}, ^{12}\text{C})^{23}\text{Na}$
4. $^{16}\text{O}(^{23}\text{Na}, ^{16}\text{O})^{23}\text{Na}$

Fig. 7.39 shows the relationship between the simulated track length and track angle for different reaction and scattering products. The protons and alphas were predicted to have the longest track lengths, and a majority of them reach the μ-RWELL. The plots also show that even after the selection of tracks that reach the μ-RWELL, distinguishing the protons from alphas is kinematically challenging under the specific experimental conditions. The recoils from the reaction (^{26}Mg) and scattered beam particles (^{23}Na) were not included in the plots, as all of them will

either get shielded by the cathode cage, stop inside the detection volume (see Table 7.5) or cause the digitiser channels to saturate as a result of high differential energy loss in the gas.

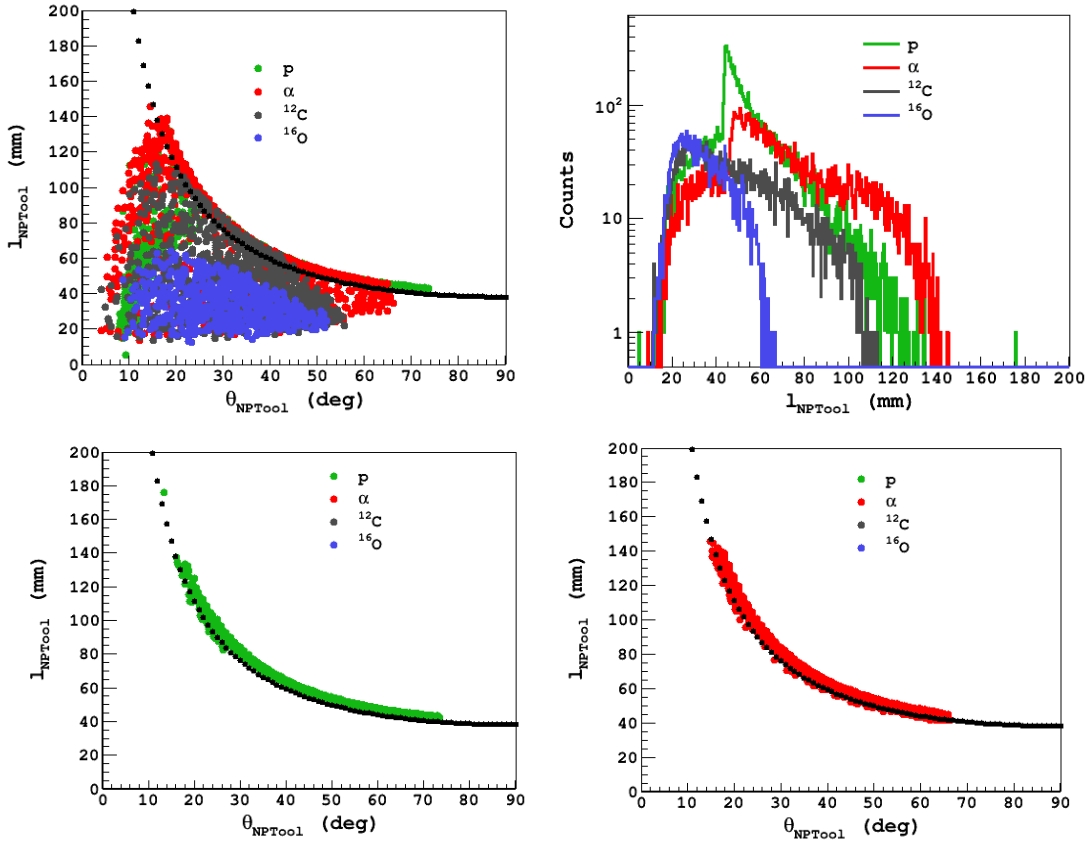

Figure 7.39: Simulated track length versus track angle for the particles produced by the simulation. The dotted black line on the left plot indicates l_r (see Eq. 6.5). The bottom plots show the angular dependence of track length for reaction protons and scattered alphas terminating at the μ-RWELL separately. Data cut used: $m_{NPTool} \geq 5$. A 20 keV per pad energy threshold was used in the analysis.

The reaction and the elastic scattering products possess different charges, and Eq. 3.3 shows that the differential energy loss in a medium is highly dependent on the charge of an ion. Thus, different energy parameters were further utilised to investigate the particle identification capability of TACTIC. The plots in Fig. 7.40 show that the simulated energy parameters can be used effectively to distinguish between protons and heavier scattering products. The mean energy ($E_{mean,NPTool}$) deposited in a track was calculated by,

$$E_{mean,NPTool} = \frac{E_{NPTool}}{m_{NPTool}}, \tag{7.15}$$

where E_{NPTool} and m_{NPTool} are the total energy deposited in the detection volume and multiplicity, respectively. Both scattered ^{12}C and ^{16}O can be easily eliminated by using the energy parameters, as they were found to deposit significantly higher energy compared to protons and alphas in the detection volume. The remaining

scattered alphas and protons were found to be well separated in terms of E_{NPTool} with a minor overlap. The majority ($\approx$ 99%) of events with the simulated total energy deposited in a track, $E_{NPTool} < 0.8$ MeV and simulated maximum energy deposited in a track, $\Delta E_{NPTool} < 0.15$ MeV can be identified as reaction protons (see Fig. 7.41). It is noteworthy that all simulated ΔE_{NPTool} values are higher than the calculated values in Table 7.6, as expected. The table values represent the lower limit of maximum differential energy loss in TACTIC for a track angle of 0°. The energy loss will increase with angle, as per Eq. 7.7.

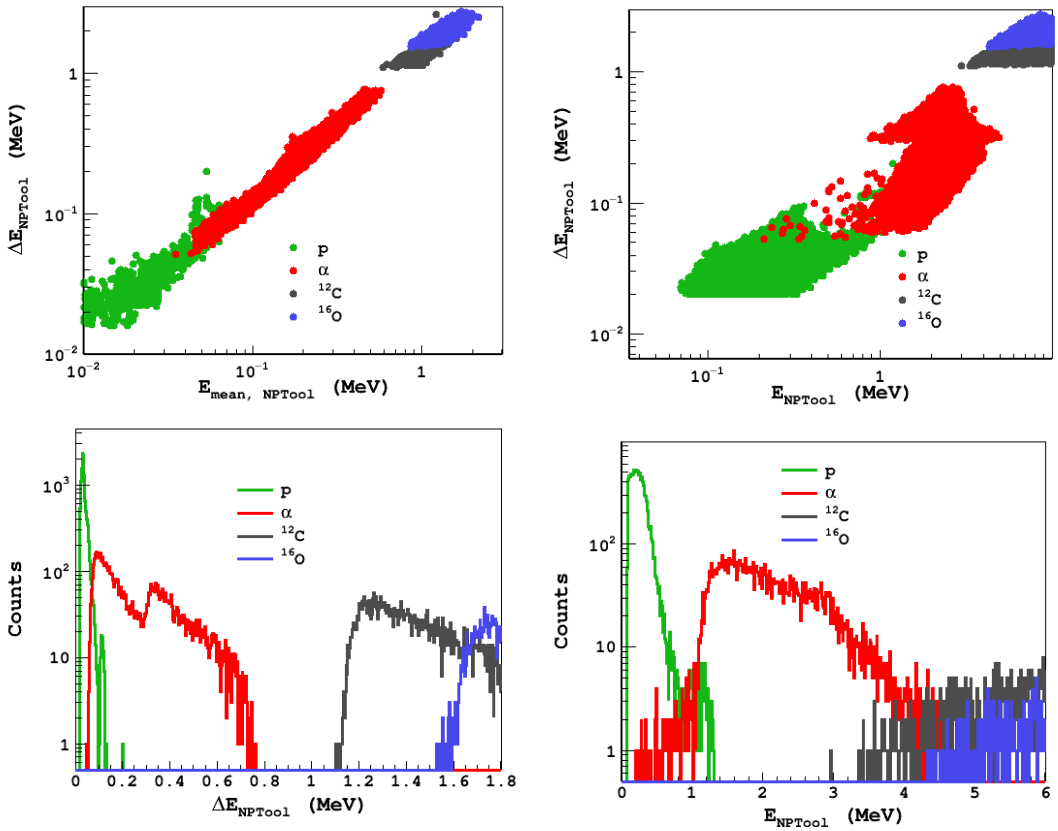

Figure 7.40: **[TL]:** Simulated maximum energy versus mean energy deposited in a track. **[TR]:** Simulated maximum energy versus total energy deposited in a track. **[BL]:** Projection of vertical axis from the TR plot. **[BR]:** Projection of horizontal axis from the TR plot. Data cut used: $m_{NPTool} \geq 5$. A 20 keV per pad energy threshold was used in the analysis.

Fig. 7.42 shows the maximum and summed pulse height of the particle tracks from the stable beam runs. Only the tracks with vertex positions inside the gas target region ($v_{z,m} \geq 38.3$ mm) were selected to eliminate the elastic scattering from the window. Signal saturation at the digitiser channels was observed for the maximum pulse height in the output channels, $\text{PH}_{max} > 3600$ ADC. The plot parameters are defined in Section 7.1.4. Throughout the stable beam runs, a low-frequency ($\approx$ 5 Hz) fixed pulser signal was applied to all the preamplifier channels used. This provided an independent monitor of the electronic gain and the means to correct any potential gain drifts. Fig. 7.43 shows that the pulser signals with an amplitude of 2710.6 $\pm$ 3.5 ADC appear in all 64 channels read out. No significant gain drift was observed as the pulser signal across the channels (PH_{max}) was well resolved (0.1% at

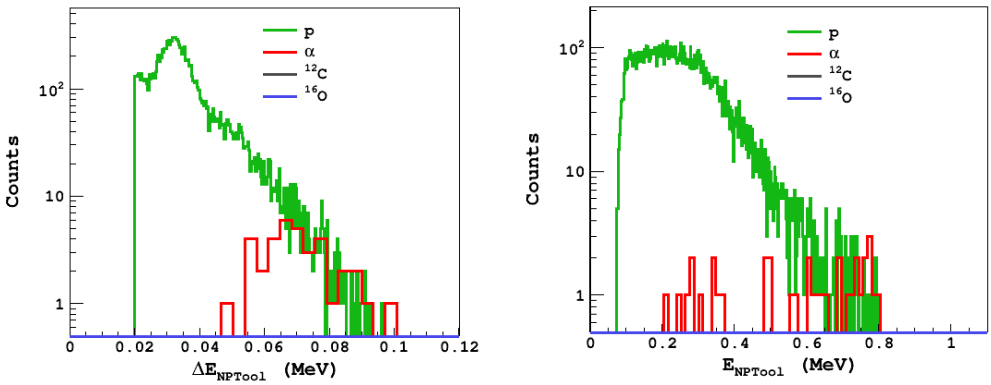

Figure 7.41: Simulated maximum and total energy deposited in the detection volume. Data cut used: $m_{NPTool} \geq 5$, $E_{NPTool} < 0.8$ MeV, $\Delta E_{NPTool} < 0.15$ MeV. A 20 keV per pad energy threshold was used in the analysis.

Table 7.6: Maximum and minimum energies (MeV) of different scattering and reaction products from the target gas and the window were calculated using CATKIN [85] and SRIM [32]. The corresponding lower limit of differential energy losses were calculated over the width of a single anode pad (p_w) and for $\theta = 0°$. The angular range ($5° < \theta < 70°$) considered for the calculations followed from the experimentally obtained range of angles (see Fig. 7.34). Energy loss of the scattering products ($^{23}Na_{wC}$, $^{23}Na_{wO}$, p_w, $^{12}C_w$, $^{16}O_w$) inside the 2.5 μm thick mylar window was also considered in the calculations.

Particle species	$\mathbf{E}_{max}$	$\mathbf{E}_{min}$	$\mathbf{dE}_{E_{max}}$	$\mathbf{dE}_{E_{min}}$
p_g	13.1	7.0	0.004	0.008
^{26}Mg	31.1	25.7	2.5	2.7
p_w	6.1	0.3	0.008	0.084
$^{23}Na_{wp}$	×	×	×	×
α	17.2	1.2	0.050	0.3
$^{23}Na_{\alpha}$	32.6	17.8	2.1	2.5
$^{12}C_g$	30.6	2.1	0.9	1.3
$^{23}Na_{gC}$	33.6	3.4	2.1	1.7
$^{16}O_g$	32.8	2.2	0.7	1.3
$^{23}Na_{gO}$	33.7	1.1	2.1	0.7
$^{12}C_w$	33.8	×	0.6	×
$^{23}Na_{wC}$	34.2	0.3	2.2	0.3
$^{16}O_w$	33.4	×	1.3	×
$^{23}Na_{wO}$	34.0	×	2.1	×

FWHM). By selecting the events with summed pulse height, $PH_{sum} < 8{\times}10^4$ ADC, the contribution from the pulser was completely eliminated from the analysis.

In Fig. 7.42, the uncalibrated parameters PH_{max} and PH_{sum} can be considered analogous to ΔE and E, i.e., the maximum energy and the total energy deposited by a particle track inside the detection volume, respectively. Although several features, e.g., distribution of data points in the PH_{max}-PH_{sum} space, saturation etc., were identifiable in the plot, an energy calibration was required to develop a re-

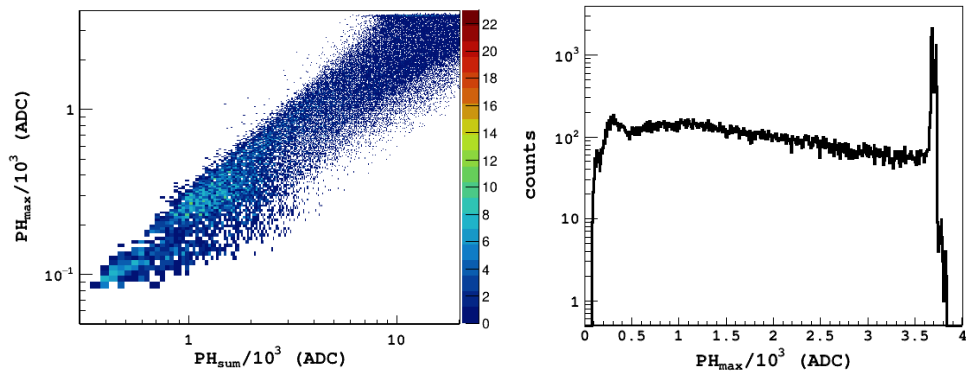

Figure 7.42: **[Left]:** PH_{max} versus PH_{sum} (scaled) from stable beam runs 61, 64, and 65 (sector 1). Data cuts used: $0 < t'_i \leq 7.5$ μs, $r_d > 5$ mm, $m_{track} \geq 5$, $c_{track} = 1$, $\Delta v_z < 2.4$ mm, $\Delta\theta < 6.1°$, $v_{z,m} > -38$ mm, $PH_{sum} < 8 \times 10^4$ ADC. **[Right]:** Projection of the vertical axis from the left plot.

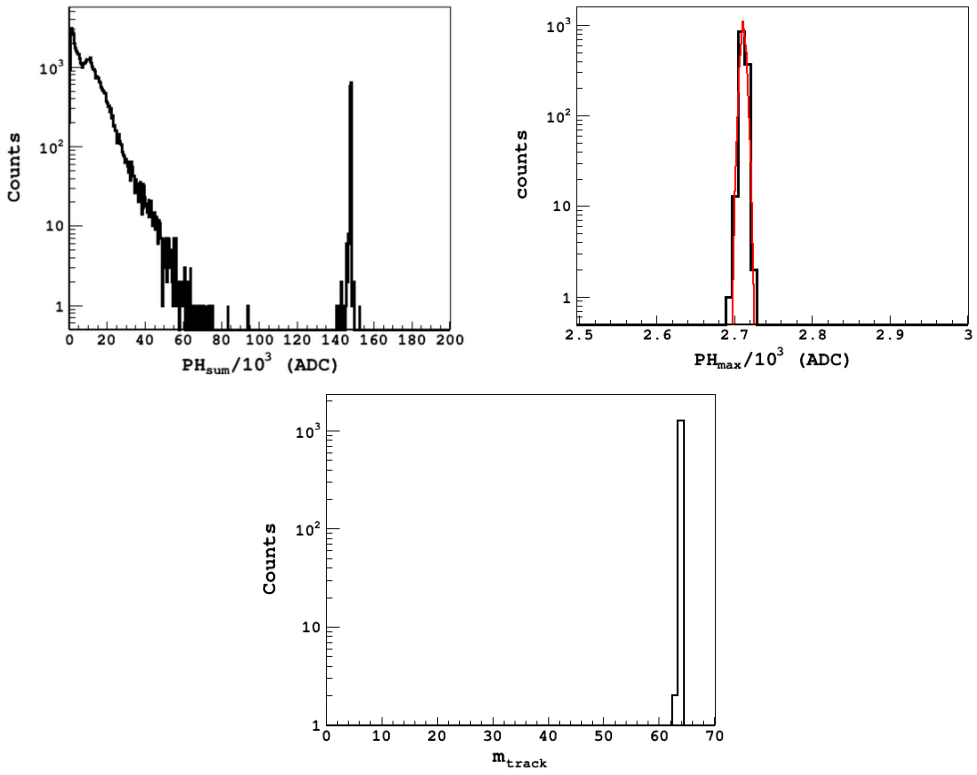

Figure 7.43: **[TL]:** PH_{sum} distribution from stable beam runs 61, 64, and 65 (sector 1). Pulser signal peak at $PH_{sum} = 15 \times 10^4 \pm 9e0$ ADC. Data cuts used: $0 < t'_i \leq 7.5$ μs, $m_{track} \geq 5$. **[TR]:** PH_{max} distribution from stable beam runs 61, 64, and 65 (sector 1). Data cuts used for top plots: $0 < t'_i \leq 7.5$ μs, $m_{track} \geq 5$, $PH_{sum} > 8 \times 10^4$ ADC. The Gaussian fit parameters: $\mu = 2710.6$ ADC, $\sigma = 3.5$ ADC. **[Bottom]:** Multiplicities for from stable beam runs 61, 64, and 65 (sector 1). Data cuts used: $0 < t'_i \leq 7.5$ μs, $m_{track} \geq 5$, $PH_{sum} > 8 \times 10^4$ ADC.

liable particle identification scheme based on the energy parameters. The energy calibration was performed using alpha run 26073. The conditions for the alpha run were similar to those for the stable beam runs (see Tables 7.2 and 7.4). Fig. 7.44 illustrates the comparison between different experimental and simulated parameters.

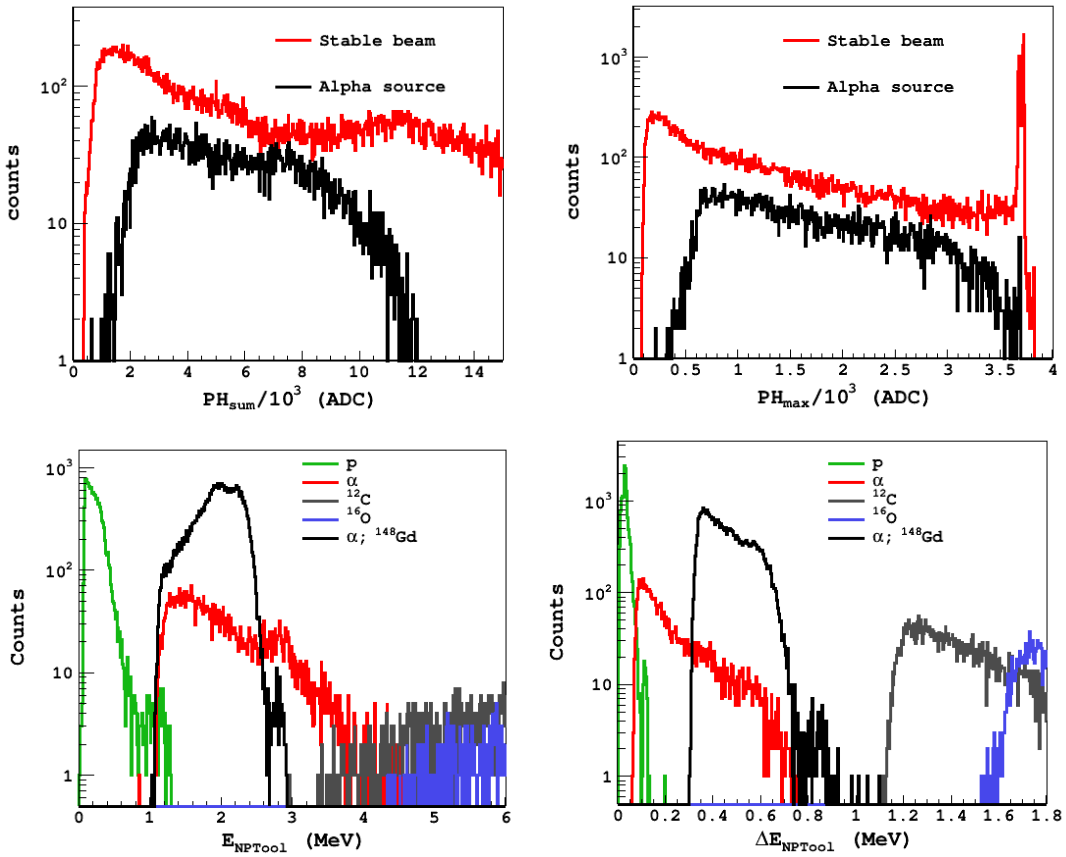

Figure 7.44: **[TL]:** PH_{sum} distribution from stable beam runs 61, 64, and 65 and alpha run 26073 (sector 1). Data cuts used: $0 < t_i' \leq 7.5$ μs, $r_d > 5$ mm, $m_{track} \geq 5$, $c_{track} = 1$, $\Delta v_z < 2.4$ mm, $\Delta\theta < 6.1°$, $\mathrm{PH}_{sum} < 8 \times 10^4$ ADC. **[TR]:** PH_{max} distribution from stable beam runs 61, 64, and 65 and alpha run 26073 (sector 1). Data cuts used: $0 < t_i' \leq 7.5$ μs, $r_d > 5$ mm, $m_{track} \geq 5$, $c_{track} = 1$, $\Delta v_z < 2.4$ mm, $\Delta\theta < 6.1°$, $\mathrm{PH}_{sum} < 8 \times 10^4$ ADC. **[BL]:** Simulated total energy deposited in a track for different reaction and scattering products as well as the alpha particles from the calibration source. Data cut used: $m_{NPTool} \geq 4$. A 20 keV per pad energy threshold was used in the analysis. **[BL]:** Simulated maximum energy deposited in a track for different reaction and scattering products as well as the alpha particles from the calibration source. Data cut used: $m_{NPTool} \geq 5$.

The upper limits of the experimentally obtained parameters PH_{sum} and PH_{max} from the alpha run were identified to be 12.1×10^3 ADC and 3.7×10^3 ADC, respectively. These limits are comparable to the upper limits of the simulated alpha source energy parameters, i.e., $E_{NPTool} \approx 2.6$ MeV and $\Delta E_{NPTool} \approx 0.7$ MeV. The upper limits were chosen for a better estimate, as the lower limits of the experimental parameters are more susceptible to being affected by electronic noise. The alpha energies in the simulation were defined by Eq. 7.2. It is noteworthy that the effect of the cathode cage on the energy parameters was also considered in the simulation, which adds to the energy resolution of the detectable alpha energies. The comparison yielded a conversion of 0.2 keV/ADC. Fig. 7.45 shows the calibrated experimental energy parameters and a comparison with the equivalent simulated parameters. From the experimental data, a detectable energy range of 15-700 keV

per pad was identified. Furthermore, the comparison with the simulation revealed that most of the unsaturated events are either reaction protons or scattered alphas. Saturation at the DAQ channels was observed for the events with $\Delta E > 0.7$ MeV. The simulation indicated that some of the scattered ^{4}He and all scattered ^{12}C and ^{16}O will cause signal saturation at the DAQ channels. The simulation also suggested that only a small number of scattered ^{12}C and no ^{16}O will be detected as a result of the data cuts employed. The PH_{max} distribution in Figs. 7.44 and 7.45 for the stable beam runs shows a large number of saturated events. These predominantly originated from elastic scattering products. Fig. 7.46 shows that most of the saturated tracks with $\Delta E > 0.7$ MeV terminate inside the detection volume ($r_{track} < 50$ mm). This was expected for the scattering products (see Fig. 7.31). The black dashed lines in Fig. 7.45 represent the energy cuts for the separation between reaction protons and scattered alphas (see Fig. 7.41).

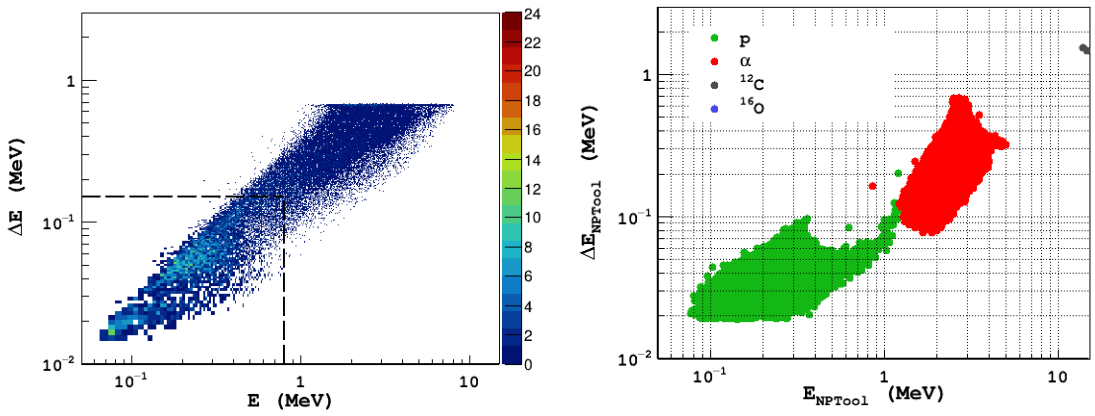

Figure 7.45: **[Left]:** ΔE versus E from stable beam runs 61, 64, and 65 (sector 1). Data cuts used: $0 < t_i' \leq 7.5$ μs, $r_d > 5$ mm, $m_{track} \geq 5$, $c_{track} = 1$, $\Delta v_z < 2.4$ mm, $\Delta\theta < 6.1°$, $\mathrm{PH}_{sum} < 8 \times 10^4$ ADC, $v_{z,m} >$ -38 mm. The black dashed lines represent the energy cuts for the identification of the reaction proton using the simulation as the reference (see also Fig. 7.41). **[Right]:** Simulated maximum energy versus total energy deposited in a track. Data cut used: $m_{NPTool} \geq 5$, $v_{z,NPTool} >$ -38 mm. A 20 keV per pad energy threshold was used in the analysis.

The reaction proton distribution in the $\Delta E - E$ space in the experimental data, further shows two sub-distributions around $\Delta E = 20$ keV and $\Delta E = 60$ keV (see Figs. 7.45, 7.46, 7.47). This can be explained by the angular dependence of energy deposition per pad (see Eq. 7.6) as discussed previously in Section 7.1.4. The steeper proton tracks ($\Delta E < 0.15$ MeV, $\theta > 45°$, $r_{track} \approx 50$ mm) that terminate at the μ-RWELL were found to deposit higher energy per pad compared to the shallower tracks ($\Delta E < 0.15$ MeV, $\theta \leq 45°$, $r_{track} < 50$ mm), which mostly escape the detection volume on the downstream end. Following the discussions in Sections 7.1.3 and 7.2.2, the tracks that terminate at the μ-RWELL were chosen for further analysis. The selection of such tracks allows a robust and reliable vertex reconstruction (see Fig. 7.36). It also provides a significant suppression of elastic scattering background (see Table 7.5). Fig. 7.48 shows the ΔE-E plot for the events that terminate at the μ-RWELL. Due to a significant reduction of the tracks with shallower angles (see Fig. 7.34), the proton distribution around $\Delta E = 20$ keV does not appear in the plot. Furthermore, during the selection of the maximum energy cut ($E < 0.8$ MeV) that

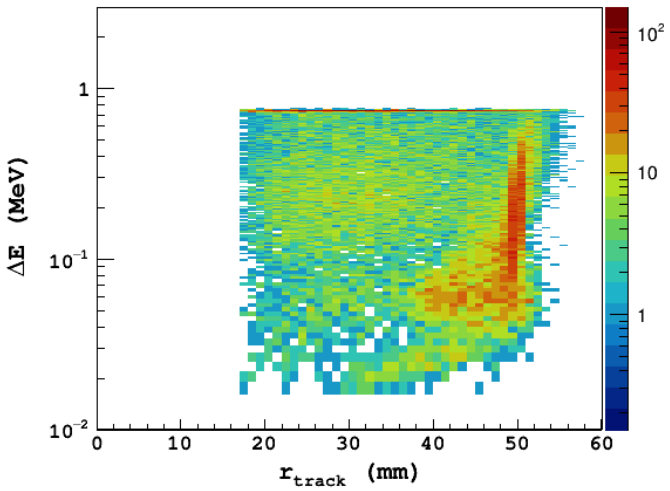

Figure 7.46: ΔE versus track radius from stable beam runs 61, 64, and 65 (sector 1). Data cuts used: $0 < t_i' \leq 7.5$ μs, $r_d > 5$ mm, $m_{track} \geq 5$, $c_{track} = 1$, $\Delta v_z < 2.4$ mm, $\Delta\theta < 6.1°$, $\mathrm{PH}_{sum} < 8 \times 10^4$ ADC, $v_{z,m} > -38$ mm.

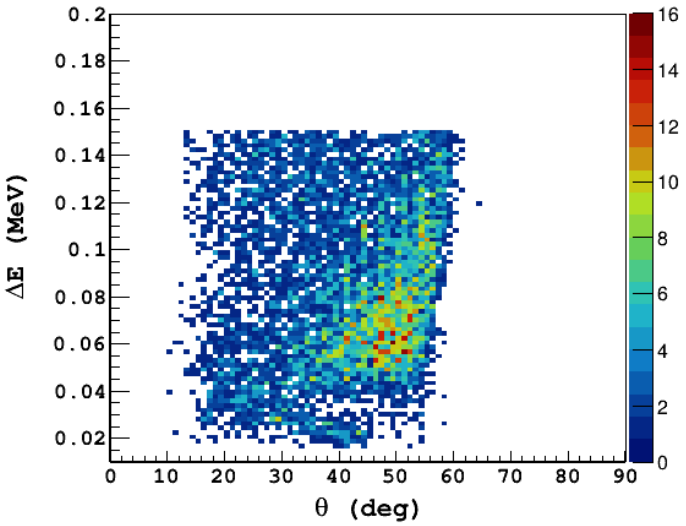

Figure 7.47: ΔE versus track angle from stable beam runs 61, 64, and 65 (sector 1). Data cuts used: $0 < t_i' \leq 7.5$ μs, $r_d > 5$ mm, $m_{track} \geq 5$, $c_{track} = 1$, $\Delta v_z < 2.4$ mm, $\Delta\theta < 6.1°$, $\mathrm{PH}_{sum} < 8 \times 10^4$ ADC, $v_{z,m} > -38$ mm, $\Delta E < 0.15$ MeV, $E < 0.8$ MeV.

was used to separate the reaction protons from scattered alphas, an energy resolution of 38% from the μ-RWELL in He:CO_2 90:10 gas mixture (see Fig. 5.18) was also taken into account. The simulated energy parameters did not include an energy resolution. In the experimental data, the limits of the total energy distribution for the protons and alphas will be affected by the detector resolution. As shown in Fig. 7.49, the lower limit of alpha distribution ($E_{NPTool} = 1.2$ MeV) can have a value as low as 0.7 MeV if a 38% energy resolution is taken into consideration. Thus, the total energy cut selected should sufficiently minimise any potential overlap between the proton and alpha distributions.

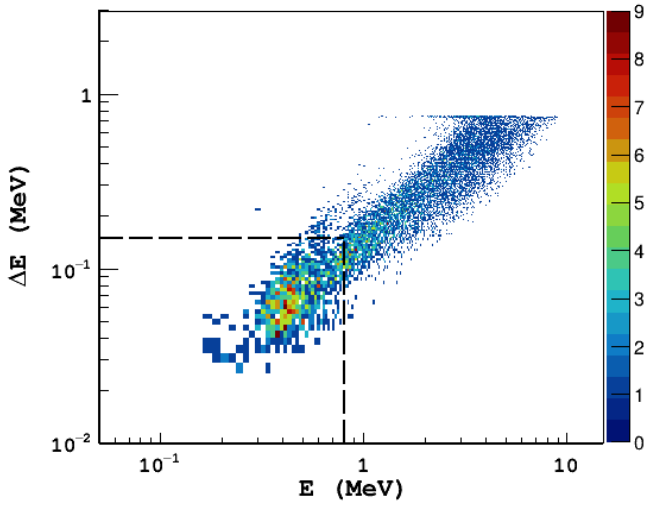

Figure 7.48: ΔE versus E from stable beam runs 61, 64, and 65 (sector 1). Data cuts used: $5.7 < t_i' \leq 7.5$ μs, $r_d > 5$ mm, $m_{track} \geq 5$, $c_{track} = 1$, $v_{z,m} >$ -38 mm, $\Delta v_z < 2.4$ mm, $\Delta\theta < 6.1°$, $\text{PH}_{sum} < 8 \times 10^4$ ADC. The black dashed lines indicate the selected cuts for the identification of the reaction proton using the simulation as the reference.

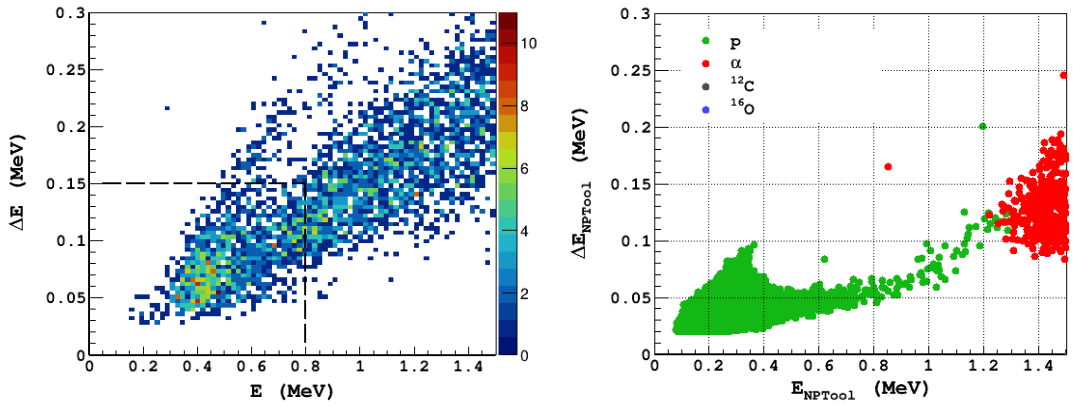

Figure 7.49: **[Left]:** ΔE versus E from stable beam runs 61, 64, and 65 (sector 1). Data cuts used: $5.7 < t_i' \leq 7.5$ μs, $r_d > 5$ mm, $m_{track} \geq 5$, $c_{track} = 1$, $v_{z,m} >$ -38 mm, $\Delta v_z < 2.4$ mm, $\Delta\theta < 6.1°$, $\text{PH}_{sum} < 8 \times 10^4$ ADC. The black dashed lines indicate the selected cuts for the identification of the reaction proton using the simulation as the reference. **[Right]:** Simulated maximum energy versus total energy deposited in a track. Data cuts used: $m_{NPTool} \geq 5$, $r_{max} \geq 50$ mm, $v_{z,NPTool} >$ -38 mm.

The vertex position-dependent variation of dE was also studied (see Fig. 7.50) for tracks terminating at the μ-RWELL. Vertex positions can be directly translated to ^{23}Na beam energy using Eq. 7.11. The energy of the reaction or scattering product reduces with beam energy, and conversely, the differential energy loss increases. It follows from Eq. 3.3,

$$-\frac{dE}{dx} \propto \frac{1}{v^2}. \tag{7.16}$$

Therefore,

$$-\frac{dE}{dx} \propto \frac{1}{E_k}, \tag{7.17}$$

where E_k is the kinetic energy of an ion. Although the experimental data are not as well resolved, the trends observed were found to be similar to those in the simulation. The two distributions in the simulation plot represent scattered alphas ($\Delta E_{NPTool} \gtrsim$ 0.08 MeV) and reaction protons ($\Delta E_{NPTool} \lesssim 0.08$ MeV). The scattered ^{12}C and ^{16}O do not appear in the simulation plot due to the specific data cuts used. Furthermore, alphas do not appear after the vertex position of 0 mm in the simulation. However, in the experimental data, some events ($< 1\%$) were observed after $v_{z,m} = 0$ mm, mainly due to the inaccurate vertex reconstruction or open fusion evaporation reaction channels, which were not considered in the simulation due to their relatively low cross section (in the order of $\sim \mu$b) for the energy region of interest (discussed further in Section 7.2.4) and the low CO_2 percentage in the target gas mixture. The range of vertices of reaction protons in the experimental data (-38 $\lesssim v_{z,m}$(mm) $\lesssim$ -10) did not agree with the simulation (-38 $\lesssim v_{z,m}$(mm) $\lesssim$ 26). This was expected as the flat cross section used for the (α, p) channel in the simulation did not have an energy and angle dependence. However, in practice the reaction cross section decreases with energy. The dependence of cross section on the vertex positions is further discussed in Section 7.2.4. For tracks with vertex positions ≤ 0 mm, the total energy cut of $E < 0.8$ MeV was found to provide a better separation between alphas and protons as shown in Fig. 7.51. The simulation predicts little ($< 2\%$) to no overlap even when an energy resolution of 38% is considered. Furthermore, for tracks with vertex positions > 0 mm, a zero background from elastic scattering was predicted by the simulation considering the specific data cuts in place. This provides a significant advantage in terms of cross section measurements at lower energies and will be discussed in the later sections.

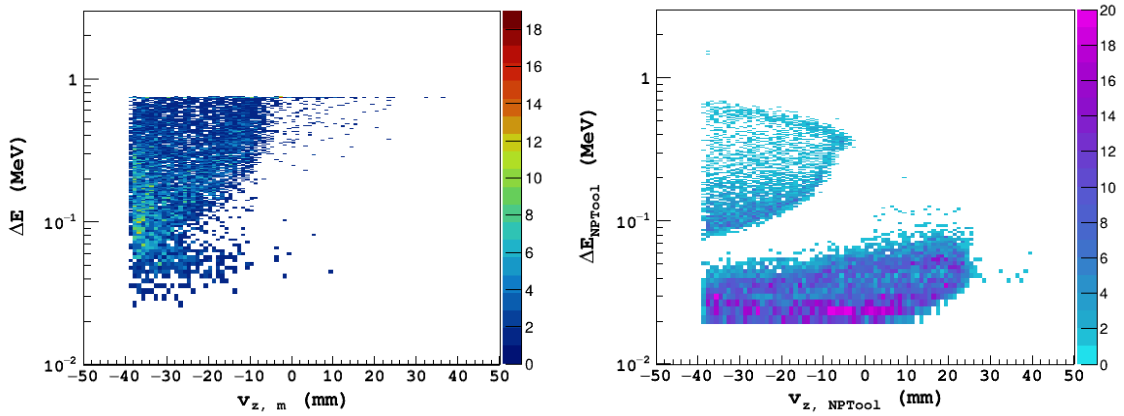

Figure 7.50: **[Left]:** ΔE versus $v_{z,m}$ from stable beam runs 61, 64, and 65 (sector 1). Data cuts used: $5.7 < t_i' \leq 7.5$ μs, $r_d > 5$ mm, $m_{track} \geq 5$, $c_{track} = 1$, $v_{z,m} >$ -38 mm, $\Delta v_z < 2.4$ mm, $\Delta\theta < 6.1°$, $\text{PH}_{sum} < 8 \times 10^4$ ADC. **[Right]:** Simulated maximum energy deposited in a track versus vertex positions. Data cuts used: $m_{NPTool} \geq 5$, $r_{max} \geq 50$ mm, $v_{z,NPTool} >$ -38 mm. The upper and lower ΔE_{NPTool} distributions represent the scattered alphas and protons, respectively.

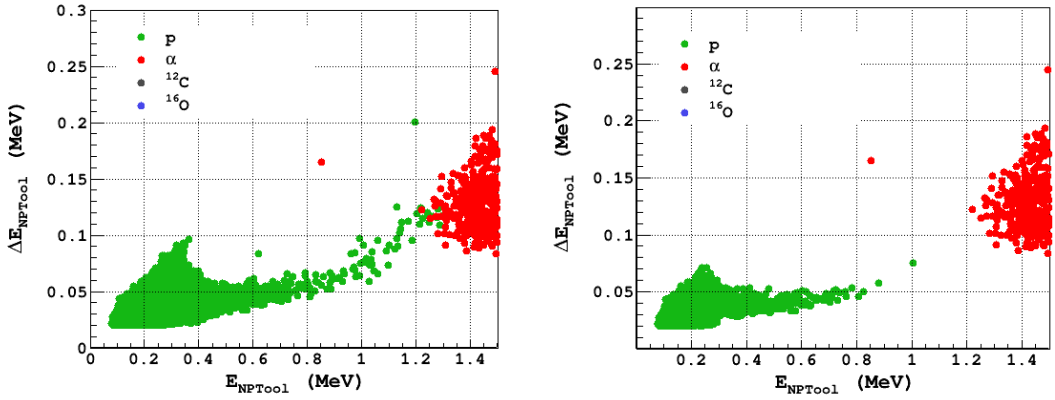

Figure 7.51: Simulated maximum energy versus total energy deposited in a track. Data cuts used (**left**): $m_{NPTool} \geq 5$, $r_{max} \geq 50$ mm, $v_{z,NPTool} >$ -38 mm. Data cuts used (**right**): $m_{NPTool} \geq 5$, $r_{max} \geq 50$ mm, -37.4 $\leq v_{z,NPTool}$(mm) $\leq$ -2.6. A minimum energy threshold of 20 keV per pad was also used in both cases.

Table 7.7: Simulated detection efficiencies (%) of the reaction products from different nuclear interactions corresponding to different data cut combinations between ^{23}Na beam and the target gas mixture: (α, p), (α, α), $(^{12}C,^{12}C)$, $(^{16}O,^{16}O)$ in inverse kinematics following Table 7.5.

Sp.	$m_{NPTool} \geq$ **5,** $r_{max} \geq$ **50 mm** $v_{z,NPTool} \geq$ -38 mm	$m_{NPTool} \geq$ **5,** $r_{max} \geq$ **50 mm,** -37.4 $\leq v_{z,NPTool}$(mm) $\leq$ -2.6
p	37.6	21.6
α	36.4	36.2
^{12}C	0.1	0.1
^{16}O	0.0	0.0
^{23}Na	0.0	0.0
^{26}Mg	0.0	0.0

7.2.4. ^{23}Na$(\alpha, p)^{26}$Mg: cross section measurement

The particle identification scheme discussed in the previous section was used to identify the reaction protons and determine the cross sections for the ^{23}Na$(\alpha, p)^{26}$Mg reaction at different vertex energies. Table 7.7 shows that the background from the elastic scattering arises from ^{4}He only. Additional background can also arise from the fusion evaporation reaction, discussed later the present section. It must also be noted that most of the heavy recoil ^{26}Mg from the reaction either got shielded by the cathode cage, caused saturation at the digitiser channels, or did not satisfy the track selection criteria discussed in the previous sections. Thus, the cross section measurement depends solely on the detection efficiency of the reaction protons. Fig. 7.52 shows the vertex distributions of the reaction protons ($E <$ 0.8 MeV) and scattering products ($E >$ 0.8 MeV). The vertex distribution or yield of protons was found to fall off sharply with increasing vertex position and conversely decreasing ^{23}Na beam energy. This was found to be consistent with the calculated yield using the theoretical Hauser-Feshbach cross sections (see Fig. 7.53). In comparison with the theoretical yields, two proton counts were observed in the distribution corresponding to the reaction protons in the region $v_{z,m} > 0$ mm. The potential sources were identified as the variance in the experimental parameters and the vertex posi-

tion resolution. These were not included in the theoretical yield calculations, as the Hauser-Feshbach cross sections were only used as a reference. The elastic scattering yield was found to be at least two times higher the proton yield. Fig. 7.52 also shows a gradual increase at lower energies consistent with Rutherford scattering formula (see Eq. 2.24) followed by a sharp drop in the corresponding distribution at $v_{z,m} = 0$ mm was observed. The sharp drop was due to the data cuts used. A similar trend was also observed in the simulated data (see Fig. 7.50), i.e., the vertex positions corresponding to the scattered alphas were within the limit $v_{z,NPTool} = 0$.

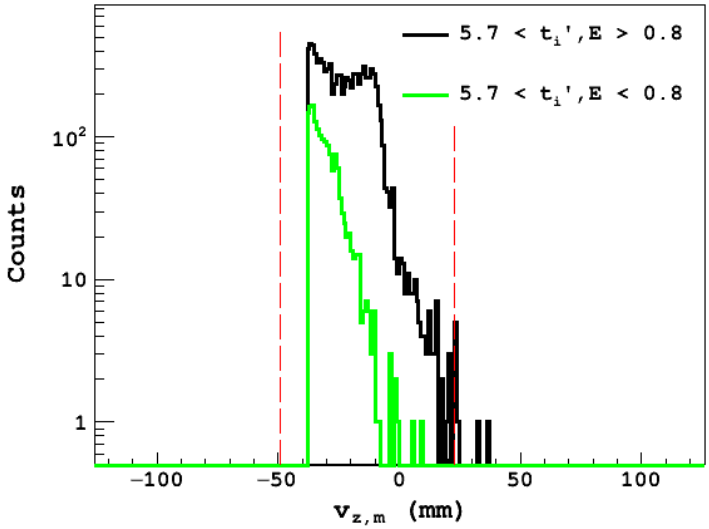

Figure 7.52: Reconstructed vertices from stable beam runs 61, 64, and 65 (sector 1). The distributions of the reaction proton (green) and scattered particles (black) are overlaid. The red dashed lines represent the position of the entrance window and range of ^{23}Na beam in He:CO_2 90:10. Data cuts used: $5.7 < t_i' \leq 7.5$ μs, $r_d >$ 5 mm, $m_{track} \geq 5$, $c_{track} = 1$, $v_{z,m} >$ -38 mm, $\Delta v_z <$ 2.4 mm, $\Delta\theta < 6.1°$, $PH_{sum} <$ 8 $\times 10^4$ ADC. The additional energy cuts were applied based on the discussions in Section 7.2.3 to identify the reaction protons and scattered alpha particles.

Table 7.8: Experimental details for stable beam runs 61, 64, and 65 in addition to Table 7.4. Following from Table 7.7, the simulated proton detection efficiency listed here was calculated over the vertex range of $-37.4 \leq v_{z,NPTool}(\text{mm}) \leq -2.6$, taking into consideration, an energy threshold of 20 keV per pad.

Parameters	**Values**
Beam intensity	6×10^6 pps
Transmission efficiency	80 ± 10%
Run time	2 hrs. 53 mins.
Target thickness	0.5 cm
Target density	3.5×10^{19} atoms cm^{-3} (He)
Target composition	He:CO_2 90:10
Geometrical efficiency, η_{geo}	6.1% (sector 1)
Proton detection efficiency (simulation), η_{sim}	21.6%

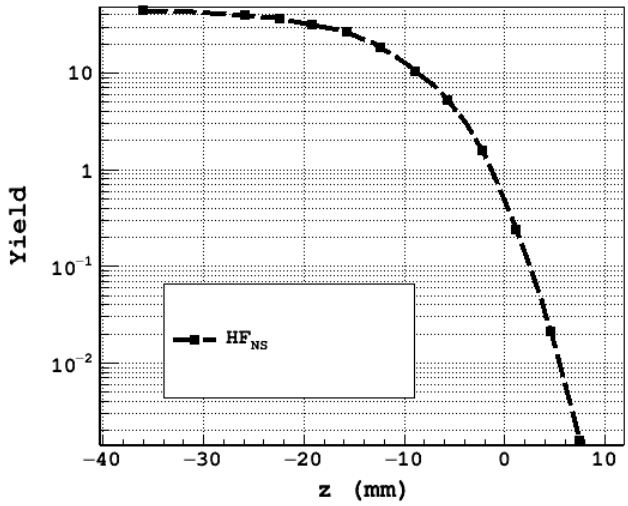

Figure 7.53: Calculated proton yields at different vertex positions using Hauser-Feshbach calculated cross sections [89] and experimental parameters listed in Table 7.8. The parameter z is equivalent to the experimentally obtained vertex position $v_{z,m}$.

Beam normalisation

The beam intensity mentioned in Table 7.8 is an approximate value. During the total run time, the beam intensity increased by $\approx 19\%$ between runs 61 and 65. This was taken into account during the calculation of the reaction cross section. Although similar beam intensities were measured before and after each run using the beam-line Faraday cup just upstream of TACTIC, it did not account for any fluctuations during the runs. In order to address this, the alpha scattering yield for each run was used for a more accurate beam normalisation. The run conditions and data cuts employed to identify the scattered alphas were almost identical for runs 61, 64, and 65. Thus, the alpha scattering yields for the individual runs were expected to agree within the uncertainty, arising mainly from the transmission efficiency ($\approx 10\%$). A dimensionless quantity, ξ, was used for this purpose.

$$\xi = \frac{Y_\alpha}{t \cdot N_b} \tag{7.18}$$

where Y_α and t are the alpha scattering yield and duration of each run, respectively. N_b is the measured beam intensity before the start of each run. Fig. 7.54 shows that the calculated values of ξ agree well for runs 64 and 65. However, for run 61 a discrepancy of $\approx 30\%$ was observed in the mean value of ξ compared to the other two runs. As all the experimental parameters remained the same, the disagreement was believed to arise from a decrease in the beam intensity during run 61. Thus, N_b for the run was adjusted accordingly. The normalisation technique employed must be considered approximate, as it relies on the agreement and accuracy of ξ obtained from runs 64 and 65. Ideally, the Rutherford scattering yields need to be calculated and used as a reference for better and robust beam normalisation. Due to the target thickness (≈ 72 mm) and non-isotropic track angle distribution (see Fig. 7.55) in TACTIC, the calculation of the elastic scattering cross section is not straightforward

and was outside the scope of this work. The most efficient approach for this will be to implement the Rutherford scattering cross section in the existing simulation in place of the isotropic or flat cross section used in this work.

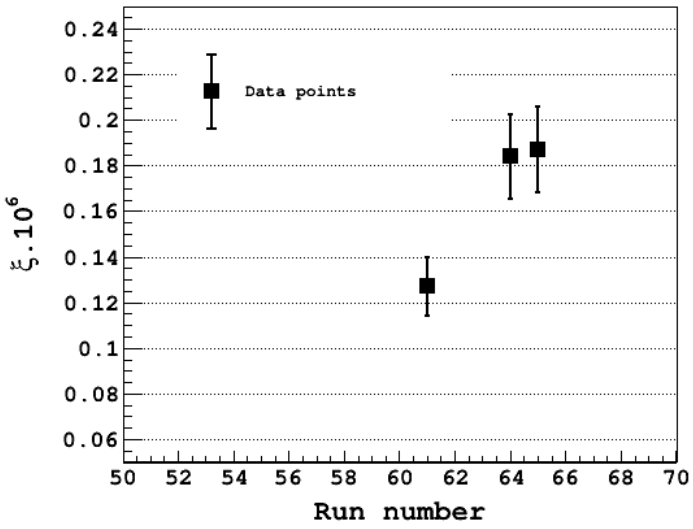

Figure 7.54: Calculated values of ξ for stable beam runs 61, 64, and 65.

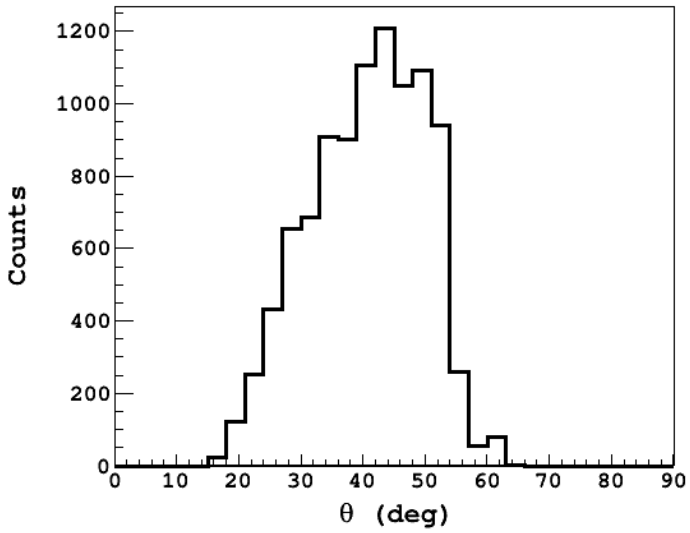

Figure 7.55: Track angle distribution of scattered alphas from stable beam runs 61, 64, and 65. Data cuts used: $5.7 < t_i' \leq 7.5$ μs, $r_d > 5$ mm, $m_{track} \geq 5$, $c_{track} = 1$, $v_{z,m} >$ -38 mm, $\Delta v_z < 2.4$ mm, $\Delta\theta < 6.1°$, $\mathrm{PH}_{sum} < 8 \times 10^4$ ADC, $E > 0.8$ MeV, $\Delta E > 0.15$ MeV.

In order to obtain the reaction cross section, the total detection efficiency needs to be calculated. The total detection efficiency (η) was obtained from the geometrical (η_{geo}) and analysis efficiency (η_{ana}). The geometrical efficiency of each TACTIC sector is listed in Table 6.1. The analysis efficiency, η_{ana}, is a combination of the ratio of events accepted by the offline analysis to the actual number of events (η_o) and the proton detection efficiency from the simulation (η_{sim}), taking into account

all the data cuts employed in the offline analysis. The analysis efficiency for the reaction protons was found to be $\approx 21.6\%$ for the detection of reaction protons over the z-range, $-37.4 \leq v_{z,NPTool}(\text{mm}) \leq -2.6$.

$$\eta_{ana} = \eta_{sim} \cdot \eta_o, \tag{7.19}$$

where η_{sim} is the proton detection efficiency obtained from the simulation as listed in Table 7.8, and $\eta_o \approx 97\%$ is the efficiency from the offline analysis. In order to obtain a precise position dependent proton detection efficiency, the target region illustrated in Fig. 7.50 was divided into 7 segments in the z-range, $-37.4 \leq v_{z,NPTool}(\text{mm}) \leq -2.6$. As shown in Fig. 7.56, for each of these segments an individual proton detection efficiency was calculated by running the simulation for 2×10^4 events. The η_{sim} value for each segment was used in the calculation of their individual analysis efficiency (η_{ana}) for the reaction protons, and finally, the energy dependent reaction cross sections discussed later in this chapter.

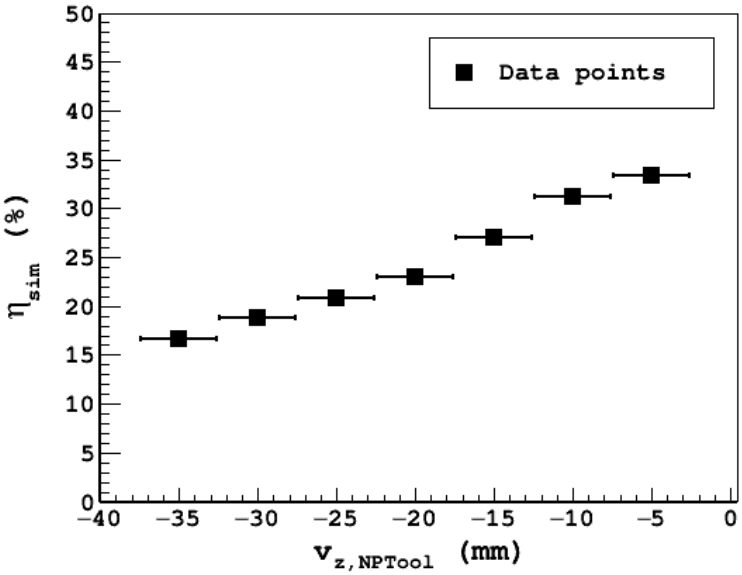

Figure 7.56: η_{sim} versus $v_{z,NPTool}$ for the reaction protons from the simulation. The vertex positions were selected based on the target region of interest as well as the vertex position uncertainty of 2.4 mm as shown in Fig. 7.35. Data cuts used: $m_{NPTool} \geq 5$, $r_{max} \geq 50$ mm. An energy threshold of 20 keV per pad was also considered.

In addition to the geometrical and analysis efficiencies, the dead time of the data acquisition system also impacts the total efficiency as it leads to a potential loss of true events. Thus, a dead time sensitive efficiency, η_d was also considered and was defined as the ratio of the number of events recorded to the number of events read by the data acquisition system. For the stable beam runs 61, 64, and 65, η_d had a value of 85±15%. Thus, a total proton detection efficiency (η) of $1.5 \pm 1.0\%$ can be calculated for stable runs 61, 64, and 65 using Eq. 7.20. This can be significantly improved in the future to $\approx 18\%$ by instrumenting all TACTIC sectors.

$$\eta = \eta_{geo} \cdot \eta_{ana} \cdot \eta_{d}. \tag{7.20}$$

Another important parameter for the cross section measurement, target thickness in Table 7.8 was defined by the smallest division of the z-range in TACTIC (see Section 6.2.2). Also, the target density was calculated using SRIM. As discussed in Section 7.2.1, Eq. 7.12 was used to obtain the vertex energy resolution. The uncertainty in the vertex position (see Section 7.2.2) directly translates to the uncertainty in the vertex energy. The vertex position uncertainty accounts for the radial straggling of the beam, which leads to an incorrect track radius calculation. However, a position-dependent energy straggling must also be taken into consideration. The energy straggling depends on the specific vertex positions inside the target region as well as the corresponding statistical uncertainties ($\approx$ 2.4 mm, discussed in Section 7.2.2). Ideally, if all the beam particles were parallel to the central axis, the energy loss would simply follow the Bethe formula (see Eq. 3.3). However, in reality, due to the radial straggling of the beam, the energy deposition corresponding to each vertex position will have an additional statistical uncertainty. Fig. 7.57 shows the simulated uncertainties in the beam energy ($\Delta E_{b,es}$) corresponding to different vertex positions for the energy range of interest ($E_b > 6$ MeV). The energy resolution gets worse with the decrease in beam energy as expected. The uncertainties ΔE_b (see Eq. 7.12) and $\Delta E_{b,es}$ were combined to obtain the position dependent vertex energy resolution:

$$\Delta E_{b,t} = \sqrt{\Delta E_b^2 + \Delta E_{b,es}^2}. \tag{7.21}$$

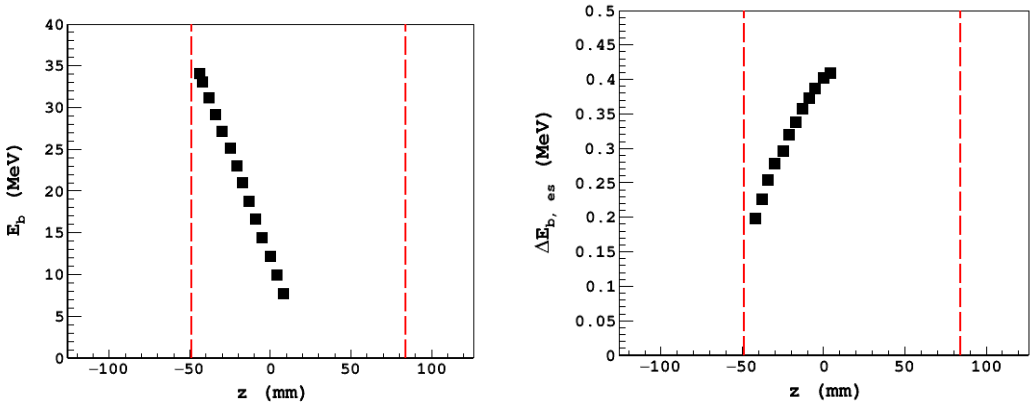

Figure 7.57: **[Left]:** Simulated ^{23}Na beam energies in the lab frame versus He:CO_2 90:10 gas target (P = 1 bar) depth in TACTIC coordinates. **[Right]:** Simulated ^{23}Na beam energy uncertainties in the lab frame versus He:CO_2 90:10 gas target (P = 1 bar) depth in TACTIC coordinates. The uncertainties arise from the energy straggling. The second order polynomial fit parameters: $p_0 = 0.399$, $p_1 = 0.003$, p_2 = -5e-5. The dashed red lines indicate the positions of the entrance window and exit collimator, for both plots.

In order to calculate the total cross sections for the ^{23}Na$(\alpha, p)^{26}$Mg reaction, Eq.

2.1 was used. The said equation can be modified to account for the detection and beam transmission efficiencies,

$$\sigma(E) = \frac{Y}{N_{b,norm} \cdot T \cdot (\Delta z \cdot N_t) \cdot \eta}, \tag{7.22}$$

where $N_{b,norm}$ is the normalised total number of incident beam ions, T is the beam transmission efficiency factor (had a value of 0.8 ± 0.1), Δz is the target thickness, N_t is the target density (see Table 7.8) and Y is the proton yield from a specific z-range defined by the vertex position and the corresponding uncertainty. The target density can be considered constant throughout the run duration as a stable gas flow was used. Seven vertex positions, ≈ 5 cm apart were chosen, for which the corresponding ^{23}Na beam energy and cross sections were calculated by using Eqs. 7.11 and 7.22, respectively. The choices of vertex position were made by taking into consideration the corresponding uncertainties to avoid any potential overlaps. Fig. 7.58 shows the calculated ^{23}Na$(\alpha, p)^{26}$Mg reaction cross sections at different ^{23}Na vertex energies. The vertex energies were converted from the lab frame to the centre of mass frame by using Eq. 7.23.

$$E_{cm} = E_b \cdot \frac{m_t}{m_t + m_p}, \tag{7.23}$$

where m_t and m_p are the masses of the target and projectile in amu. E_{cm} is the vertex energy in the centre of mass frame. The uncertainty in the calculated cross section originated from the uncertainties in the transmission efficiency ($\Delta T \approx 10\%$) and detection efficiency ($\Delta\eta \approx 15\%$). The uncertainty in the transmission efficiency was considered in order to account for any minor fluctuations in the beam intensity during the runs. The calculated ^{23}Na$(\alpha, p)^{26}$Mg reaction cross sections at higher energies ($E_b \geq 29.0$ MeV) were found to be significantly affected by fusion evaporation reactions, which contributed to the proton yield of interest. For $E_b \geq 29.0$ MeV, the fusion reaction channel between ^{23}Na and ^{12}C was found to be relevant (see Fig. 7.59) and thus, the fusion-evaporation cross sections (σ_{FE}) were estimated using the PACE4 code [90] for the first three vertex positions corresponding to higher energies, i.e., $\sigma_{FE} \approx 240$ mb, 98 mb, and 16 mb, respectively. These values were combined with the lower uncertainties of the measured ^{23}Na$(\alpha, p)^{26}$Mg reaction cross sections. It is noteworthy that at the entrance window position, the fusion evaporation cross sections were found to be at least an order of magnitude higher. Thus, it is important to identify and completely eliminate the fusion evaporation background from the window and following gas target region where the beam energy is above the Coulomb barrier heights corresponding to ^{12}C+^{23}Na and ^{16}O+^{23}Na fusion channels. In this work, the vertex positions for the desired cross section measurements were chosen carefully ($z >$ -38.0 mm) to avoid any major contribution to the reaction cross section measurement from the proton background arising from the fusion evaporation reactions as well as the elastic scattering from the window. The fusion evaporation cross sections were found to be small, i.e., in the order of μb, below the respective Coulomb barriers. Therefore, their impact on the cross section measurements below $E_b = 29.0$ MeV (corresponds to $E_{cm} < 3.5$ MeV in Fig. 7.58), can be considered negligible ($\lesssim 1\%$).

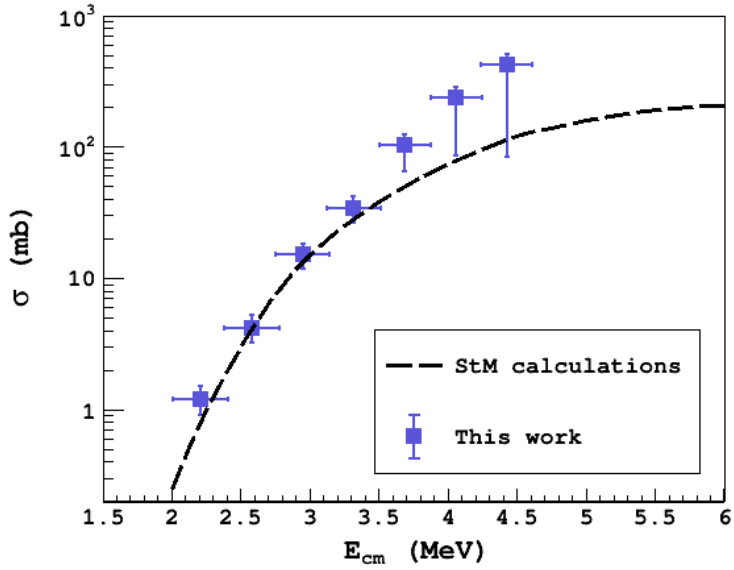

Figure 7.58: Calculated cross sections for ^{23}Na$(\alpha,p)^{26}$Mg using runs 61, 64, and 65. The black dashed line represents the theoretically calculated cross sections by P. Mohr [91], which agrees with the Hauser-Feshbach predicted cross sections [89] within 5%. The three higher energy cross sections are significantly affected by fusion evaporation reaction.

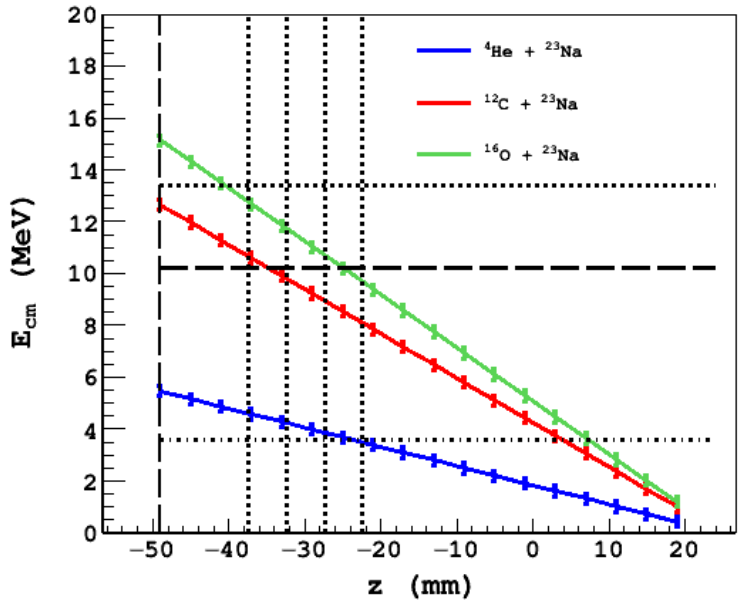

Figure 7.59: ^{23}Na vertex energies with respect to target gas components in the centre of mass frame as a function of z-position in TACTIC coordinates. The vertical dashed line represents the position of the entrance window. The vertical dotted lines represent the maximum of the four higher energy bins defined by the vertex positions selected and the corresponding uncertainties for the cross section calculation. The horizontal dashed, dotted, and dotted-dashed lines represent the height of the Coulomb barrier between ^{12}C+^{23}Na, ^{16}O+^{23}Na, and ^{4}He+^{23}Na, respectively. The maximum energies (CM) corresponding to the first two vertex positions are over and in the immediate vicinity of the ^{12}C+^{23}Na Coulomb barrier height.

The ^{23}Na$(\alpha,p)^{26}$Mg reaction cross section measured with TACTIC was compared to several previous measurements as shown in Fig. 7.60. The TACTIC measurement covered a wide angular range of $\theta = 20-60°$ ($\theta_{cm} = 22-82°$) as depicted in Fig. 7.47. Furthermore, it must be noted that an isotropic angular distribution was assumed for the calculation of the total cross section. In the astrophysically important energy range, $E_{cm} \approx$ 1.7-3.4 MeV, the TACTIC measurement was found to be consistent with both statistical model calculations (StM calculations) and the measurements by Avila et al. (ANL-2016) [66] within 20%. However, compared to the measurement by Tomlinson et al. (TRIUMF-2015) [92] the cross sections were found to be consistently lower by a factor of 2. This was due to the comparatively small angular coverage of the experimental setup used for the TRIUMF-2015 measurement. The data from the TRIUMF-2015 measurement was re-analysed and corrected by Hubbard et al. [9], which reduced the discrepancy to 30% compared to the other existing measurements and Hauser-Feshbach calculations. It was not possible to extend the TACTIC measurement to low centre of mass energies below 2.0 MeV due to time and the maximum beam intensity restrictions, both of which can be addressed in the future. The TACTIC measurement re-establishes the good agreement between the theoretical model and results from the past experiments in the centre of mass energy range relevant to explosive Ne/C burning in massive stars, i.e., E_{cm} =1.7 - 3.4 MeV. A future TACTIC experiment will be extremely useful for extending this study to the lower centre of mass energy region, which lacks experimental data.

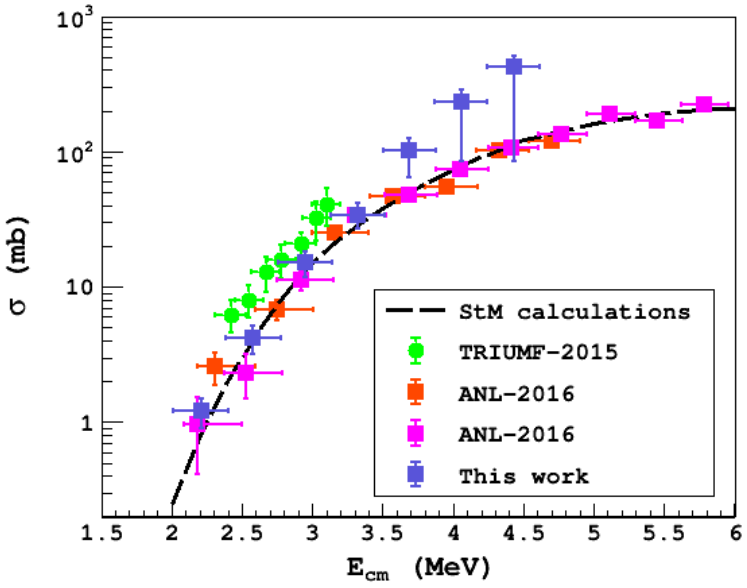

Figure 7.60: Cross sections measured with TACTIC for the ^{23}Na$(\alpha,p)^{26}$Mg reaction (blue) and comparison with published cross sections from Avila et al. (2016) [66], Tomlinson et al. (2015) [92] and statistical model calculations by P. Mohr [91]. The two sets of data points from Avila et al. are from measurements with two different energies.

The ^{23}Na$(\alpha,p)^{26}$Mg reaction produces an ^{27}Al compound nucleus in an excited state, which decays to ^{26}Mg and emits a proton as a result. If ^{26}Mg is produced in the ground state, the emitted proton is called the p_0 proton. For the production of ^{26}Mg in the first excited state, the emitted proton is termed as p_1 protons and

so on, as illustrated in Fig. 7.61. The proton yield from the reaction is, however, dominated by p_0 and p_1 protons. The cross section measurement included in this work considers the total proton yield (p_{tot}), i.e., the combined contribution from the proton decay of ^{27}Al to all the energy states of ^{26}Mg. The investigation of individual proton channels was outside the scope of this work. This will most certainly be addressed in the future analysis.

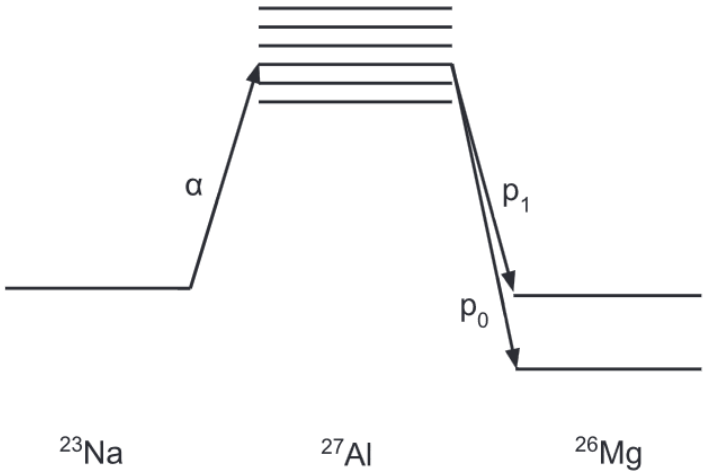

Figure 7.61: Schematic of the ^{23}Na$(\alpha, p)^{26}$Mg reaction. Alpha particles react with ^{23}Na to form ^{27}Al in an excited state, which then decays to ^{26}Mg emitting a proton (p_0, p_1, ...) [9].

7.2.5. Discussion

A series of tests with an alpha source and ^{23}Na beam were performed with TACTIC, aiming at the commissioning of the detector. The alpha source tests were used to verify the accuracy of the tracking algorithm and consistency with the simulation framework developed for TACTIC. The essential tracking parameters, e.g., multiplicity, track radius, track angle, and track length, were found to be consistent with their simulated analogues. This was an important result towards benchmarking the dedicated simulation, which later aided the analysis of the stable beam data.

The source tests were also used to formulate a robust vertex reconstruction technique. It was found that the consecutive ($c_{track} = 1$) "full" tracks, i.e., tracks that start at the cathode cage and terminate at the μ-RWELL (see Fig. 7.2), provide $\approx 26\%$ better vertex position resolution compared to the tracks that terminate inside the detection volume. The full tracks are also independent of the track radius calculation using Garfield, which is a highly parameterised procedure and is also susceptible to the accuracy of the knowledge of the electric field inside TACTIC. Past studies [8, 12] have shown that in the immediate vicinity of the cathode cage, the electric field is non-uniform due to the unequal separation of the cathode wires. Furthermore, the cylindrical geometry of TACTIC is not perfect. Small submillimeter imperfections mostly arise during the assembly procedure and also the smoothness of the μ-RWELL surface. It is difficult to make precise measurements of such imperfections. Thus, the Garfield simulation for TACTIC which assumes a perfect cylindrical symmetry will always produce incorrect drift times. This inaccuracy needs to be quantified and studied further in order to effectively include the tracks that terminate inside the detection region in the analysis. Garfield calculations also does not take into account the angular straggling of an ion, especially at the end of track. This also adds to the inaccuracy in the track parameters obtained using the Garfield drift times. Using the full tracks completely addresses both of these potential sources of inaccuracy. For such tracks, an accurate and independent measurement of the maximum drift time (t_{max}) can be performed. The uncertainties in this drift time accounts for the imperfections in the cylindrical symmetry as well as any non-uniformity in the electric field inside. The full tracks are also less susceptible to the effect of the angular straggling as they terminate at the μ-RWELL. Furthermore, the stable beam tests also showed that by only using the full tracks in the analysis, a significant amount of elastic scattering background can be suppressed. Gating on these tracks, however, reduces the detection efficiency and impacts the flexibility in the selection of experimental conditions. However, in this work, only full tracks were chosen to obtain the reaction cross sections, in light of the obvious advantages they offer.

A comparative study between two TACTIC sectors was also performed. The study showed a disagreement in terms of the maximum pulse height observed. The disagreement could have originated from multiple sources, e.g., the difference in the gas gains from the two different μ-RWELL detectors used corresponding to the sectors in question, variation in the electronic gain between the preamplifier channels, or a combination of both. The effect of the variation in the electronic gain should be more relevant within a sector. In addition to this, the misalignment in one of the μ-RWELL detectors during installation (corresponding to sector 2, 3, 4, and

5), could have also affected the consistency in the observed pulse heights between the sectors. Apart from this comparison study, most of the measurements with TACTIC presented in this work utilised sector 1. Thus, the difference in the sector responses did not affect the quality of the results. However, in the future, a robust gain normalisation technique must be formulated for the simultaneous use of multiple sectors. A gain normalisation with a mono-energetic source should sufficiently address the gain variation across the anode pads as well as the sectors.

The stable beam tests were also used to verify the accuracy of the tracking algorithm and the effectiveness of the related assumptions. A significant improvement in the accuracy of the vertex reconstruction from gating on the full tracks was found in accordance with the alpha source test results. The uncertainties in the vertex reconstruction and the corresponding energy in the lab frame were also calculated, i.e., $\Delta v_{z,m} = 2.4$ mm (FWHM) and $\Delta E_b = 45$ keV/u (FWHM). The mean vertex position ($v_{z,m}$) and the associated uncertainty were obtained from the mean and standard deviation of the vertex position distribution originating from the vertex positions for each point in a track. Thus, only the tracks with a multiplicity of 5 or higher were considered to make the calculations statistically sound. In order to develop a robust particle identification scheme to measure the ^{23}Na$(\alpha, p)^{26}$Mg reaction, an energy calibration was performed using a ^{148}Gd alpha source. The simulations showed that the main background in the detection of the reaction protons arises from the scattered alphas, once the contribution from the entrance window is removed. Furthermore, the reaction protons and scattered alphas were found to be kinematically similar in terms of the range of track angles and track lengths. Thus, the difference in their characteristic differential energy loss was utilised to successfully separate out the reaction product of interest. The most effective energy parameters were found to be the maximum (ΔE), mean (E_{mean}), and total (E) energy deposited in a track. Another major contributor to the background was found to be the elastic scattering and fusion evaporation reaction products from the entrance window. In order to address this, the window position was identified, and any potential effect of it on the reaction proton yield was completely eliminated based on the corresponding vertex position.

The ^{23}Na$(\alpha, p)^{26}$Mg reaction cross sections were calculated in the energy range $E_{cm} = 2.0$-5.0 MeV. At higher energies $E_{cm} > 4.0$ MeV, the measured reaction cross sections were found to be significantly affected by the proton background from the fusion evaporation reaction involving ^{23}Na and ^{12}C. However, in the energy region $E_{cm} < 4.0$ MeV, the cross section measurements were found to be consistent with the statistical model calculations and other existing measurements. In this centre of mass energy region the contribution from the fusion evaporation cross section was found to be relatively small (on the order of μb). Table 7.9 shows a summary of the different experimental parameters from the measurement of the ^{23}Na$(\alpha, p)^{26}$Mg reaction cross section documented in this work and by Avila et al. [66], which utilised the MUSIC detector setup (discussed in Section 3.11). For the measurement of the same reaction in inverse kinematics, a three order of magnitude higher beam intensity (N_b) was used for the TACTIC measurement. The comparison highlights that a significantly higher rate capability can be achieved with TACTIC alongside $\approx 10-50\%$ better vertex energy resolution. The difference in the vertex energy resolution (ΔE_{cm}) was found to be more evident at the lower centre of mass energies for

this particular comparison. However, MUSIC has a higher detection efficiency (η). It must also be noted that the TACTIC measurement reported in this work only utilised one sector out of eight. Therefore, the geometrical efficiency was reduced to $\eta_{geo} = 6.1\%$ which can be improved significantly up to $\approx 70\%$ in the future by instrumenting more channels and implementing minor modifications to the internal structure [7]. The comparison shows that TACTIC fairs well compared to the cross section measurement capabilities of MUSIC. It must also be noted that TACTIC offers significant advantage in terms of the beam intensity that can be used, which is important for low cross section measurements (< 1 mb).

Table 7.9: Summary of different parameters related to the cross section measurement of ^{23}Na$(\alpha, p)^{26}$Mg reaction in inverse kinematics with TACTIC and MUSIC [66]. The efficiency stated for TACTIC is the geometrical efficiency.

Exp.	N_b (pps)	ΔE_{cm} (MeV)	η (%)	**Run time** (hrs.)	**PID method**
MUSIC	5×10^3	0.16 - 0.29	$\approx$ 100	36	Ion track analysis
TACTIC	6×10^6	0.18 - 0.19	$\approx$ 6.1	3	Ion track analysis

Chapter 8

Conclusions

This thesis presents the first successful cross section measurement with TACTIC and details of the development work leading up to it. Since its conception in 2007, numerous experimental campaigns have been undertaken towards the characterisation and implementation of the detector. However, these studies revealed a number of shortcomings and limitations in multiple aspects of the detector setup, e.g., the degree of inaccuracy in the vertex position reconstruction, non-uniform preamplifier response, low gas gain from the GEM (Gas Electron Multipliers) previously used as the gas multiplication stage, and the lack of optimisation of the data acquisition system. Learning from the rigorous studies in the past, several major changes and modifications were made to the detector. TACTIC was initially designed to study (α, n) reactions, through detection of the heavy recoils. The newly developed simulation showed that the detection of heavy recoils is not optimal in the TACTIC geometry due their small forward angles and the presence of the cathode cage. The combination of both alongside the lack of neutron detection capability, results in reduced detection efficiency, making the cross section measurements challenging. Thus, a new approach was conceived in order to fully utilise the capabilities of TACTIC after recent modifications. The simulations indicated that the cross section measurements of (α, p) reactions can be performed by efficiently detecting the reaction protons utilising the low energy ($\sim$ few keV) detection capability of TACTIC.

For charged particle detection by means of the differential energy loss in the detection medium, TACTIC relies solely on the gas multiplication from the μ-RWELL detectors. This thesis also includes the test chamber studies involving the novel μ-RWELL detector before its installation in TACTIC. The primary focus of these tests was to characterise the μ-RWELL detector in helium-based gas mixtures, which serve as the target gas for cross section measurements of alpha-induced reactions with TACTIC. The low energy detection capability was examined using a monoenergetic ^{55}Fe X-ray source. The gas gain, energy resolution, and charging up effect studies in the helium-based gas mixtures were also important, as no previous experimental data existed. In addition, a series of optimisation studies concerning different experimental parameters, e.g., quench gas (CO_2) percentage and gas pressure, were performed in preparation for the TACTIC measurements. The test results showed that high gas gains in the order of $\approx 8 \times 10^3$ can be achieved in He:CO_2 gas mixtures, allowing the detection of small energy depositions in the gas volume ($\approx$ 5.9 keV/pad). This indicated that the gas gain from the μ-RWELL detector should be sufficient to detect protons from the ^{23}Na$(\alpha, p)^{26}$Mg reaction. Furthermore, the

results obtained from the test chamber studies in different Ar- and He-based gas mixtures have the potential to be useful for future developments of the μ-RWELL technology and dark matter physics. A part of these results was published [13], and a more detailed future publication is planned.

Based on the test chamber studies, two μ-RWELL detectors were installed in TACTIC. The ensuing source and stable beam tests bear particular significance in terms of the very first integration of the μ-RWELL detectors in a cylindrical geometry and also a tracking detector. The alpha source tests were found to be consistent with the simulation. The source tests also showed that the vertex reconstruction method employed produces a high degree of accuracy, i.e., a disagreement of $\approx 3\%$ within uncertainties for sector 1 with respect to the measured source position. It was possible to further improve the uncertainty in the vertex reconstruction by using "full" tracks. The vertex reconstruction uncertainty from the stable beam test yielded an energy resolution of 153 keV (FWHM) in the centre of mass frame. The other contribution to the vertex energy resolution was from the energy straggling of the beam ions in the target gas, which was calculated using the NPTool simulation. Thus, the combined energy resolution was found to be $186 - 198$ keV in the centre of mass frame. In principle, the vertex position uncertainty can be improved in the future by making the existing anode pad widths ($p_w = 4.2$ mm) smaller and will require a complete restructuring of the anode pad layout. Also, it will increase the number of readout channels while simultaneously increasing the required instrumentation resources. The energy staggering of the beam ions can also be reduced by using lower gas pressures to achieve a better vertex energy resolution. However, a gas pressure of 1 bar was chosen to provide the maximum stopping for efficient proton detection. Lowering the gas pressure will lower the deposited energy by protons and, in turn, the detection efficiency of the same. The gas gain from the μ-RWELL can be further increased, conversely lowering the detection threshold in order to account for the lower energy deposition, as the maximum achievable gas gain was not utilised during the stable beam tests reported in this work. Thus, an optimisation study can be performed in the future to potentially find a better combination of experimental parameters to improve the vertex energy resolution. It is noteworthy that the stable beam tests showed that the energy threshold was ≈ 20 keV/pad, which was set at the digitiser in ADC channel units to avoid electronic noise. A higher gas gain from the μ-RWELL will have little to no effect on the electronic noise, while at the same time it will increase the signal induced at the anode pads and, concurrently, the detection efficiency of the protons.

For a more detailed study of the $^{23}\mathrm{Na}(\alpha, p)^{26}\mathrm{Mg}$ reaction, it will be optimal if the p_0 and p_1 protons can be identified separately. The p_1 protons will deposit higher energies per pad in the detection volume compared to p_0 protons due to their respective energy profiles. Investigation of the individual proton channels was outside the scope of this work. However, they can be potentially separated based on different energy parameters used for particle identification, e.g., E, ΔE, etc. In order to identify the individual proton yields separately, a low energy threshold and a sufficient energy resolution are required. Both test chamber and TACTIC studies showed that the energy resolution achieved in this work can be improved upon by performing a gain normalisation between the readout channels across all the sectors using a mono-energetic ^{55}Fe X-ray source. This will be an important study in the

future, as this method will also provide a more precise energy calibration as the energies deposited by the reaction protons in the detection medium are similar to the energy of the K_α X-ray. This was outside the scope of this work due to time constraints and the lack of data acquisition resources. It must be noted that the energy calibration method employed in this work using the ^{148}Gd alpha source necessitated an extrapolation down to energies at least an order of magnitude lower for protons.

The analysis of the stable beam data showed that the elastic scattering and fusion evaporation reaction at the entrance window produce the majority of the background. The entrance window position was successfully identified, and based on the corresponding vertex position, the background arising from it was eliminated. However, this background puts an unwanted burden on the readout, which did not affect the performance of the digitiser for the study reported in this work. At higher beam intensities ($N_b > 10^7$ pps), the background from the window can significantly increase the dead time of the digitiser and concurrently affect the proton detection efficiency. In order to stop the entrance window background from entering the detection volume, a window shield with a certain length protruding into the target region can be used for future tests. Calculations based on Fig. 8.1 indicate that a shield of length (L_s) and diameter ($2r_s$) of 10 mm and 8 mm, respectively, should restrict the angle of the background from the window to 21.8°. Together with the choice of full tracks, the remaining shallow tracks can be completely eliminated.

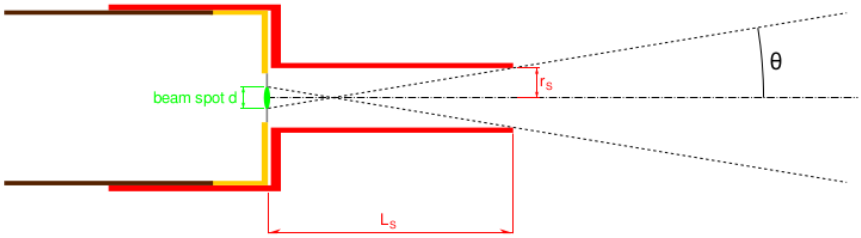

Figure 8.1: Schematic of the proposed entrance window shield [7]. The angle θ here represents the minimum angle a track must have to escape the window shield. The typical beam spot size for the tests included in this work was $d = 4$ mm.

Another constraint for achieving higher beam intensities was identified from the stable beam tests. During the beam runs, several entrance window failures were observed, especially for beam intensities higher than 10^7 pps. A potential reason could have been the quality of the window material (Mylar), which lost its integrity due to oxidization. In addition to this, the depletion of the window material over time due to its interaction with beam ions, mainly elastic scattering, also contributed to the loss of integrity. This needs to be addressed in the future, especially for the low cross section (< 1 mb) measurements with high beam intensities. A different window material, i.e., kapton, kevlar, etc., or a thicker window can potentially be considered.

The simulation and the analysis also suggested that the particle identification capability of TACTIC improves significantly at lower energies for the ^{23}Na$(\alpha, p)^{26}$Mg reaction. However, due to constraints in the run time and maximum beam intensity

acceptable, the cross section measurement in this work was limited to the lowest energy of $E_{cm} = 2.2$ MeV. It was not possible to obtain enough statistics in the region below $E_{cm} = 2.0$ MeV, as the reaction cross section drops sharply. Although multiple measurements and the statistical model calculations agree within 30% in the region above $E_{cm} = 1.7$ MeV, there still exist inconsistencies and a lack of experimental data in the lower energy region. Both the exisiting measurements by Almaraz-Calderon et al. [23] and Tomlinson et al. [92] only provided the upper limit of the cross section at $E_{cm} \approx 1.3$ MeV. The energy region of $E_{cm} \approx 1.2 - 2.4$ MeV, is important for the ^{26}Al production during the convective shell C/Ne burning in massive stars. Thus, a future measurement with TACTIC can be aimed at constraining the existing cross section measurements by extending the current studies to lower centre of mass energies.

To summarise, the results from the stable beam tests clearly show that TACTIC is capable of measuring reaction cross sections of (α, p) nuclear reactions. The (p, α) reactions can also potentially be studied, as the detection of reaction alphas will be easier compared to protons in terms of the energy deposited in the detection medium. The feasibility of such measurements needs to be explored in the future. Furthermore, the studies, scope of improvements, and observations documented in this work represent the crucial final steps prior to the successful commissioning of TACTIC.

Appendices

Appendix A

Characteristics of alpha source

The ^{148}Gd alpha source (R-00076) used for the TACTIC tests was manufactured at TRIUMF. An undocumented protective layer was placed on the radioactive material, which was expected to affect the energy of emitted alpha particles. Therefore, a spectroscopic 3α source was used to verify and calibrate for the effects of the protective layer on the well-established ^{148}Gd alpha energy of 3.27 MeV [86].

Angular distribution Alpha particles are emitted isotropically only into the forward half-space, i.e., the ranges of ϕ and θ are 0°-360°and 0°-90°. For TACTIC the source holder might limit the upper θ value to an angle smaller than 90°.

Energy The test setup at TRIUMF, that was used to study the ^{148}Gd alpha energies consisted of a vacuum chamber, a silicon surface barrier (SSB) detector [87], a single-channel preamplifier and a CAEN DT5724 digitiser [88]. The test setup was constantly pumped on to maintain the quality of the vacuum inside. The alpha energies from a standard 3α source (^{239}Pu, ^{241}Am, ^{244}Cm) was used for the energy calibration of the digitiser channels, which yielded an ADC channel to energy conversion of 14.3 keV/ADC. The energy loss in the dead layer ($\approx$ 70 keV) of the SSB detector was also corrected for. The alpha energy from the ^{148}Gd source was estimated using the energy calibration. It was found to be 3.1 $\pm$ 0.1 MeV, which was obtained from a Gaussian fit of the calibrated spectrum (see Fig. A.2).

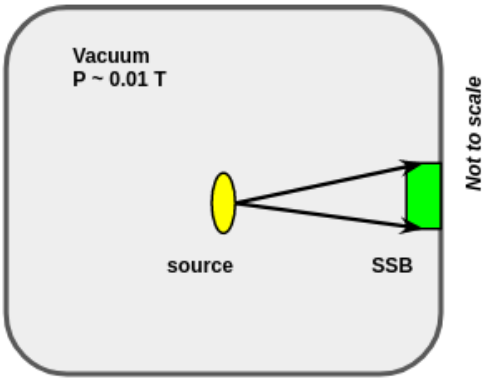

Figure A.1: Schematic diagram of the alpha test setup. The source under study was placed on a mount with its active region facing the SSB detector.

A low energy tail in the ^{148}Gd spectrum was observed. This was expected as the energy degradation from the protective layer increases with the alpha emission angle, i.e., the alphas pass through more material prior to their detection for higher angles. It is noteworthy that the protective layer did not affect the alpha energies significantly. The calculated alpha energy is in good agreement with the literature value within uncertainties. Thus, the protective layer used must have been very thin (< 1 μm).

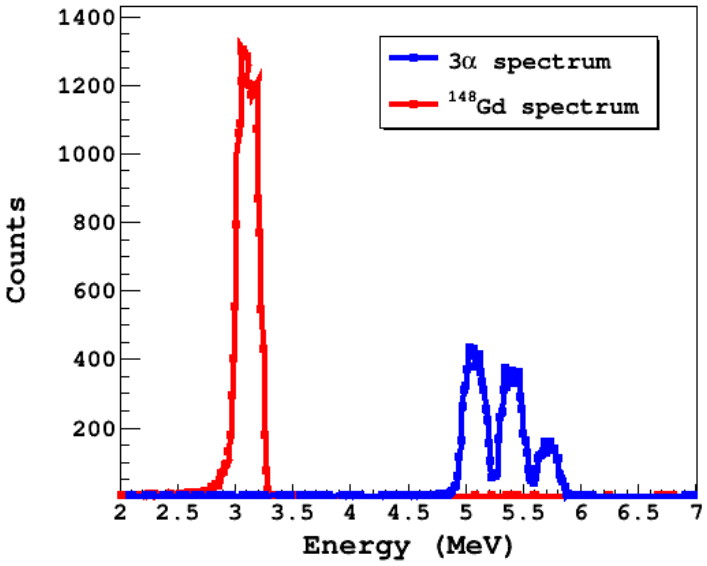

Figure A.2: Calibrated ^{148}Gd and 3α spectra. The 3α peaks are within the energy range of 5.0 to 6.0 MeV after being corrected for the energy loss in the dead layer.

Appendix B

Source and entrance window positions

The source holder is a cylindrical plastic rod that can be inserted in the detector from either the upstream or the downstream end. A brass nut and rubber o-ring mechanism creates the vacuum seal at the chamber entrances. Fig. B.1 shows the distance of the o-ring position inside the brass nut on the holder from the centre of the detection region ($z = 0$ mm). The dimensions of the source holder rod used for the source tests detailed in Section 7 is illustrated in Fig. B.2. The source position was determined by the holder being fully inserted, i.e., the edge of the "handle" resting against the brass nut. The "handle" is defined by the portion of the holder with the larger radius. The source position is determined by estimating the length protruding inside TACTIC, i.e., the distance between the end of the holder and the o-ring inside the brass nut.

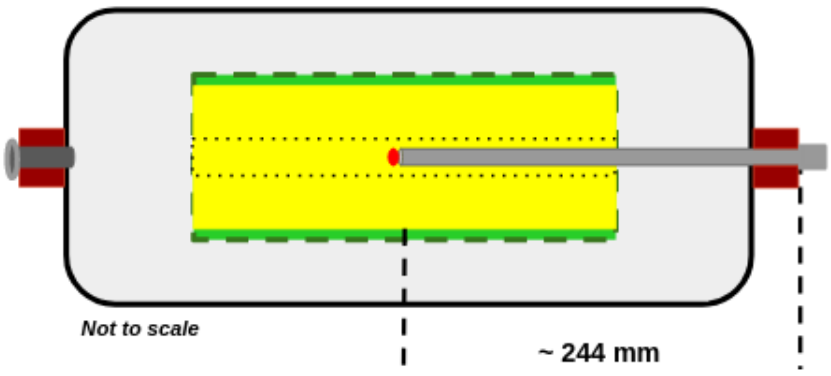

Figure B.1: Schematic diagram of TACTIC with the source holder rod (grey) inserted from the downstream end. A blank (dark grey) provides the vacuum seal on the upstream end. The distance of the o-ring position inside the brass nut on the holder from the centre of the detection region (z_{sh}) is $\approx$ 244 mm.

Two observations were made while physically determining the position of the source inside TACTIC chamber. First, the source was mounted on the end of the holder, without a precise measure of of how far it gets screwed in, so its measured length can vary by 1-2 mm. Second, the vacuum seal between the source holder and

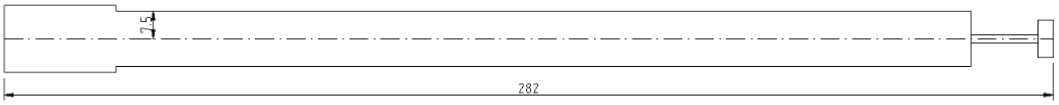

Figure B.2: Schematic drawing of the alpha source holder. The assembly has two different radii. The portion with the larger radius is called the "handle". The longer portion with the smaller radius protrudes inside by ≈ 260 mm.

the chamber is obtained by tightening a brass nut on a rubber o-ring. The edge of the brass nut moves inwards during this process. This can make the length of the rod protruding the chamber vary by 1-2 mm. These two factors gives rise to a source position uncertainty of 2 mm to 4 mm, which is also true for the window positions during the beam tests. For the instance where the source holder rod was fully inserted from the downstream end, the source position (z_s) was -16.0 ± 2.0 mm.

$$z_s = 244(1) - 260(1) \quad mm \tag{B.1}$$

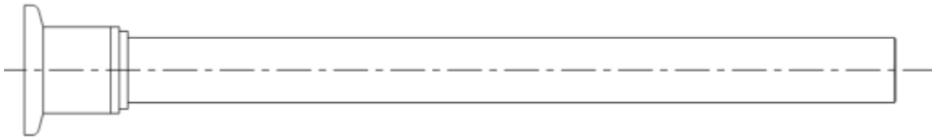

Figure B.3: Schematic drawing of the window tube. The assembly has two different radii. The portion with the larger radius is the aluminum tube with a KF-16 flange at the end. The longer portion with the smaller radius protrudes inside by ≈ 195 mm.

The entrance window was mounted on top of the end collimator of the beam tube assembly. The assembly physically connected TACTIC to the upstream diagnostics box during the in-beam tests (see Fig. 6.10). The removable beam tube assembly consisted of a tube made of G-10 composite material, which was glued into an aluminum tube machined at the end into a KF-16 flange. The KF-16 flange provides the interface between the chamber and the upstream diagnostics box. The beam tube protrudes inside TACTIC by 195 ± 1 mm. The measurement was made from the o-ring position on the flange to the collimator position on the other end. The window tube was connected to the upstream diagnostics box through standard KF-16 bellow tubes, the length of which gets affected by the differential pressure between the chamber and the diagnostics box, affecting the position of the window inside TACTIC. A constrictor was put in place in order to minimise this effect. However, a slight movement of ≈ 3 mm towards the upstream end was observed under test conditions, which was added to the estimated position of the entrance window, i.e., z_{uw} = -49 ± 3 mm.

$$z_{uw} = -244(1) + 195(3) \quad mm \tag{B.2}$$

Bibliography

[1] C. Iliadis, *Nuclear Physics of Stars (2007).*

[2] S. Engel et al., *Development of detection systems for low-energy heavy ions at DRAGON*, Nucl. Phys. A, 701 (2002).

[3] TUDA webpage (Date accessed: 27/07/2023).

[4] TRIUMF webpage (Date accessed: 30/11/2023).

[5] FRIB webpage (Date accessed: 27/07/2023).

[6] TACTIC webpage (Date accessed: 30/11/2023).

[7] L. Martin, *TACTIC: the TRIUMF Annular Chamber for Tracking and Identification of Charged particles*, PhD thesis (2015).

[8] P. Mumby-Croft, *TACTIC: A New Detector for Nuclear Astrophysics*, PhD thesis (2009).

[9] N. J. Hubbard et al., *New Experimental $^{23}Na(\alpha, p)^{26}Mg$ Reaction Rate for Massive Star and Type Ia Supernova Models*, The Astrophysical Journal 912:59 (9pp) (2021).

[10] C. Iliadis et al., *The effects of thermonuclear reaction rate variations on ^{26}Al production in massive stars: a sensitivity study*, The Astrophysical Journal, 193:16 (2011).

[11] A. M. Laird et al., *Status of TACTIC: A detector for nuclear astrophysics*, Nuclear Instruments and Methods in Physics Research A 573 (2007) 306–309.

[12] L. Martin et al., *TACTIC: the TRIUMF Annular Chamber for Tracking and Identification of Charged particles*, Journal of Physics: Conf. Series 940 (2018) 012048.

[13] S. Chakraborty et al., *Performance study of novel micro-Resistive WELL (μ-RWELL) detector in different gas mixtures*, JINST 18 C06006 (2023).

[14] CAEN website (Date accessed: 12/06/2023).

[15] K. S. Krane, *Introductory Nuclear Physics (1988).*

[16] H. P. Trautvetter and C. Rolfs, *Direct capture in the $^{24}Mg(p, \gamma)^{25}Al$ reaction*, Nuclear Physics A 242 (1975) 519-532.

[17] C. E. Rolfs and W. S. Rodney, *Cauldrons in the cosmos (1988).*

[18] M. Wiescher et al., *Break-out reactions from the CNO cycles*, J. Phys. G 25, R133 (1999).

[19] D. Groombridge et al., *Breakout from the hot CNO cycle via the $^{18}Ne(\alpha, p)^{21}Na$ reaction*, Phys. Rev. C 66, 055802 (2002).

[20] W. Bradfield-Smith et al., *Breakout from the hot CNO cycle via the $^{18}Ne(\alpha, p)^{21}Na$ reaction*, Phys. Rev. C 59, 3402 (1999).

[21] P. J. C. Salter et al., *Measurement of the $^{18}Ne(\alpha, p_0)^{21}Na$ reaction cross section in the burning energy region for X-Ray bursts*, Phys. Rev. Lett. 108, 242701 (2013).

[22] P. Mohr, A. Matic, *Examination and experimental constraints of the stellar reaction rate factor $NA\langle\sigma v\rangle$ of the $^{18}Ne(\alpha, p)^{21}Na$ reaction at temperatures of X-ray bursts*, Phys. Rev. C 87, 035801 (2013).

[23] S. Almaraz-Calderon et al., *Direct Measurement of the $^{23}Na(\alpha,p)^{26}Mg$ Reaction Cross Section at Energies Relevant for the Production of Galactic ^{26}Al*, PRL 112, 152701 (2014)

[24] G. Knoll, *Radiation detection and measurement (2000).*

[25] W. R. Leo, *Techniques for Nuclear and Particle Physics Experiments (1987).*

[26] H. O. Wyckoff and F. H. Attix, *Design of Free-Air Ionisation Chambers, National Bureau of Standards Handbook 64 (1957).*

[27] L. F. Curtiss, *Detection of radioactive contamination, using Geiger-Muller counters, Journal of Research of the National Bureau of Standards 23 (1939).*

[28] Garfield website (Date accessed: 30/11/2023).

[29] H. Bethe, *Zur Theorie des Durchgangs schneller Korpuskularstrahlen durch Materie*, Annalen der Physik (1930).

[30] W. H. Bragg, R. Kleeman, *XXXIX. On the α particles of radium, and their loss of range in passing through various atoms and molecules*, The London, Edinburgh, and Dublin Philosophical Magazine and Journal of Science 10 (1905) 318.

[31] J. F. Ziegler, J. F. Manoyan, *The stopping of ions in compounds.* Nuclear Instruments and Methods B 35 (1988) 215.

[32] SRIM website (Date accessed: 30/11/2023).

[33] G. R. Lynch, O. I. Dahl, *Approximations to multiple Coulomb scattering*, Nuclear Instruments and Methods in Physics Research Section B (1991) 58.

[34] Gamma interaction in matter (Date accessed: 15/09/2023).

[35] L. Sabbatucci, F. Salvat, *Theory and calculation of the atomic photoeffect*, Radiation Physics and Chemistry 121 (2016) 122.

[36] S. Ramo, *Currents Induced by Electron Motion*, Proceedings of the IRE 27 (1939) 584.

[37] V. Radeka, *Low-noise techniques in detectors*, Ann. Rev. Nud. ParI. Sci. 38 (1988) 217.

[38] O. R. Frisch, *Isotope analysis of uranium samples by means of their α-ray groups. British Atomic Energy Report, BR-49, (1944).*

[39] F. Sauli, *Principles of Operation of Multiwire Proportional and Drift chambers in Experimental techniques in high energy physics (1987).*

[40] H. Raether, *Electron Avalanches and Breakdown in gases, Butterworth, London U.K. (1964).*

[41] B. D. Ramsey, P. C. Agarwal, *Quench gases for xenon- (and krypton-) filled proportional counters*, Nuclear Instruments and methods A 273 (1988) 326.

[42] A. Sharma, *Properties of some gas mixtures used in tracking detectors*, ICFA Instrumentation Bulletin 16 (1998).

[43] F. Sauli, *Gaseous Radiation Detectors*, Cambridge University Press (2015).

[44] G. Charpak, R. Bouclier et al., *The use of multiwire proportional counters to select and localize charged particles*, Nuclear Instruments and Methods 62 (1968) 262.

[45] A. Breskin, G. Charpak et al., *Recent observations and measurements with high-accuracy drift chambers*, Nuclear Instruments and Methods 124 (1975) 189.

[46] M. Capeans, *Aging and materials: lessons for detectors and gas systems*, Nuclear Instruments and Methods A 515 (2004) 73.

[47] A. Oed, *Position-sensitive detector with microstrip anode for electron multiplication with gases*, Nuclear Instruments and Methods A 263 (1983) 351.

[48] F. Sauli, A. Sharma, *Micropattern gaseous detectors*, Annual Review of Nuclear and Particle Science 49 (1999) 341.

[49] M. Titov, *New developments and future perspectives of gaseous detectors*, Nuclear Instruments and Methods A 581 (2007) 25.

[50] A. V. Klyachko et al., *Dose Imaging Detectors for Radiotherapy Based on Gas Electron Multipliers*, Nuclear Instruments and Methods A 628 (2011) 434.

[51] M. Hohlmann et al., *Design and Construction of a First Prototype Muon Tomography System with GEM Detectors for the Detection of Nuclear Contraband*, IEEE Nucl. Sci. Symp. (2009).

[52] F. Sauli, *The gas electron multiplier (GEM): Operating principles and applications*, Nuclear Instruments and Methods A 805 (2016) 2.

[53] F. Sauli, *GEM: A new concept for electron amplification in gas detectors*, Nuclear Instruments and Methods A 386 (1997) 531.

[54] B. Ketzer, *Micropattern gaseous detectors in the COMPASS tracker*, Nuclear Instruments and Methods A, 494 (2002) 142.

[55] B. Blank et al., *A time projection chamber for the three-dimensional reconstruction of two-proton radioactivity events*, Nuclear Instruments and Methods A 613 (2010) 65.

[56] P. Hauer et al., *Study of Charge-Up Processes in Gas Electron Multipliers*, J. Phys.: Conf. Ser. 1498 012029 (2020).

[57] V. Kumar et al., *Studies on charging-up of single Gas Electron Multiplier*, 2021 JINST 16 P01038

[58] G. Bencivenni et al., *The micro-Resistive WELL detector: a compact spark-protected single amplification-stage MPGD*, 2015 JINST 10 P02008.

[59] G. Bencivenni et al., *High space resolution μ-RWELL for high particle rate*, Nuclear Instruments and Methods A 958 (2020) 162050.

[60] G. Bencivenni et al., *The μ-RWELL layouts for high particle rate*, arXiv:1903.11017.

[61] S. Bachmann et al., *Discharge studies and prevention in the gas electron multiplier (GEM), CERN-EP/2000-151 (2000).*

[62] D. Fancher et al., *Performance of a time-projection chamber*, Nuclear Instruments and Methods 161 (1979) 383.

[63] C. E. Demonchy et al., *First results of the new active target MAYA*, J. Phys. G: Nucl. Part. Phys. 31 (2005) S1831–S1835 .

[64] P. F. F. Carnelli et al., *Multi-Sampling Ionization Chamber (MUSIC) for measurements of fusion reactions with radioactive beams*, Nuclear Instruments and Methods A 799 (2015) 197.

[65] M. L. Avila et al., *Experimental study of the astrophysically important $^{23}Na(\alpha, p)^{26}Mg$ and $^{23}Na(\alpha, n)^{26}Al$ reactions*, PHYSICAL REVIEW C 94, 065804 (2016).

[66] J. Bradt et al., *Commissioning of the Active-Target Time Projection Chamber*, Nuclear Instruments and Methods A 875 (2017) 65.

[67] J. S. Randhawa et al., *First Direct Measurement of $^{22}Mg(\alpha, p)^{25}Al$ and Implications for X-Ray Burst Model-Observation Comparisons*, PHYSICAL REVIEW LETTERS 125, 202701 (2020).

[68] Y. Giomataris et al., *MICROMEGAS: a high-granularity position-sensitive gaseous detector for high particle-flux environments*, Nuclear Instruments and Methods A 376 (1996) 29.

[69] E. Martin, *Cross Section Measurements for Low Energy Nuclear Astrophysics Reactions in Supernovae*, PhD thesis (2014).

[70] Multi Gas Controller (MGC) Type 647C (Date accessed: 27/07/2023).

[71] Mass Flo Controller Type 1197a (Date accessed: 27/07/2023).

[72] Mesytec MHV-4 (Date accessed: 27/07/2023).

[73] M. Oreglia, *A Study of the Reactions $\psi' \to \gamma\gamma\psi$. PhD thesis, SLAC (1980).*

[74] A. Matta et al., *NPTool: a simulation and analysis framework for low-energy nuclear physics experiments*, Journal of Physics G: Nuclear and Particle Physics 42 (2016).

[75] Geant4 website (Date accessed: 30/11/2023).

[76] ROOT website (Date accessed: 30/11/2023).

[77] K. Jayamanna et al., *Off-line ion source terminal for ISAC at TRIUMF*, The Review of scientific instruments 79 (2008).

[78] M. S. Smith and K. E. Rehm, *Nuclear astrophysics measurements with radioactive beams*, Annual Review of Nuclear and Particle Science Vol. 51:91-130 (2001).

[79] T. Kirchner, *Investigations on the design of the tactic detector for the $^{8}Li(\alpha, n)^{11}B$ reaction*, TRIUMF internal publication (2005).

[80] P. A. Amaudruz et al., *Investigation of liquid xenon detectors for PET: Simultaneous reconstruction of light and charge signals from 511 keV photons*, Nuclear Science Symposium Conference Record (2007).

[81] S. P. Fox, *Status of TACTIC preamplifiers*, Internal report, Department of Physics, University of York (2012).

[82] A. Georgiev et al., *An analog-to-digital conversion based on a moving window deconvolution*, IEEE Transactions on Nuclear Science (1994) 41.

[83] C. Rodriguez-Tajes et al., *First inverse-kinematics fission measurements in a gaseous active target*, Nuclear Physics A (2017).

[84] Magboltz website (Date accessed: 30/11/2023).

[85] CATKIN website (Date accessed: 30/11/2023).

[86] NNDC website (Date accessed: 30/11/2023).

[87] S. Gotoh, Z. Takagi, *Silicon Surface Barrier Detector*, Journal of Nuclear Science and Technology (1964) 1.

[88] CAEN website (Date accessed: 27/07/2023).

[89] T. Rauscher, F. Thielemann, *Astrophysical Reaction Rates from Statistical Model Calculations*, Atomic Data and Nuclear Data Tables 75, 1–351 (2000).

[90] PACE4 website (Date accessed: 30/11/2023).

[91] P. Mohr, *Cross sections of α-induced reactions for targets with masses $A \approx 20$–50 at low energies*, Eur. Phys. J. A (2015) 51: 56.

[92] J. R. Tomlinson, *Measurement of $^{23}Na(\alpha, p)^{26}Mg$ at Energies Relevant to ^{26}Al Production in Massive Stars*, PRL 115, 052702 (2015).